Transcriptional Profiling to Identify Therapeutic Targets Influencing Skeletal Muscle Atrophy

Thesis submitted in accordance with the requirements of

The University of Liverpool

for the degree of

Doctor in Philosophy

by

Andrew Fisher, MRes, BSc (Hons)

September 2012

DECLARATION

I declare that this thesis is the result of my own work and has not been submitted in any form for another degree or diploma at any univerisyt or other instiution. Inofmration derived from published or unpublished work of others has been acknowledged in the text and a list of references is given.

The research was carried out in the Department of Musculoskeletal Biology at The University of Liverpool

ACKNOWLEDGEMENTS

There are many people who have contributed towards my work whom I would like to thank.

Firstly, I would like to acknowledge my supervisors, Dr. Jonathan Jarvis and Dr. Judy Coulson for their guidance and support in both practical and written aspects of my research over the last four years.

I would also like to thank members of Musculoskeletal Biology II, who have provided a supportive and encouraging working environment as well as training in *in vivo* surgical procedures. *In vitro* work was made possible through the generous support of members of Professor Jim Gallagher's lab as well as the kind donation of myotube cell lines from Dr. Aphrodite Vasilaki.

I started my PhD as a graduate anatomist, with no prior knowledge of biostatistics. In my early attempts at microarray analysis a great deal of assistance was provided within the group. However, the statistical analysis contained within this thesis would not have been possible without the expertise of Alex Gutteridge at Pfizer, Cambridge who trained and guided me in use of all the analysis software.

Lastly, I would like to acknowledge the continuing dedicated support of my wife and colleague Lauren. Without her there would be no thesis.

ABSTRACT

Skeletal muscle atrophy is characterised by a loss of muscle weight and volume involving a reduction in muscle fibre diameter in the absence of degenerative changes and/or a reduction in the actual number of fibres. In humans there are a wide range of stimuli for skeletal muscle atrophy including bed rest, extreme training, malnutrition and cancer. The underlying cellular and molecular mechanisms governing the process of atrophy are beginning to be elucidated. However, there remains much to be learnt to allow the development of rational therapeutic interventions.

A miniature neuromuscular stimulator was used to impose artificial levels of activity on the rat T*ibialis anterior* muscle *in vivo*. Continuous electrical stimulation at a frequency of 20 Hz for 7 days resulted in a 12% (+/- 2%) decrease in muscle weight. Foxo1 is known to play a central role in skeletal muscle atrophy. Therefore transcriptional changes in 12 Foxo1 target genes were measured following artificial *in vivo* stimulation and compared with changes in the same genes in published *in vitro* models of muscle atrophy. The standard *in-vitro* models used were treatment of C2C12 myotubes for 24 hours with glucose free media, giving a 56% (+/- 2%) decrease in myotube diameter, or 24 hours treatment with 1μM dexamethasone (Dex), which we found produced no significant change in myotube diameter. Marked transcriptional differences were observed between *in vivo* and *in vitro* atrophy models. These differences highlighted the need to develop a model based on muscle inactivity that more clearly reflected muscle behaviour *in vivo*.

A tetrodotoxin (TTX) nerve cuff was used to block all efferent impulse activity in the common peroneal nerve, and therefore to induce progressive disuse atrophy in the dorsiflexors over a period of 14 days. This resulted in a maximal 51% (+/-1%) loss in mass of the treated T*ibialis anterior* muscle compared to that in the untreated control limb. This atrophy was achieved in the absence of any histological signs of damage or degeneration of the muscle fibres. It was therefore possible to block muscle activity for 14 days, and then reverse the blockade, allowing the same muscle fibres to recover without detriment over the subsequent 7 days.

Microarray analysis was used to compare genome-wide transcript changes following 3, 7 and 14 days of nerve blockade, 14 days of nerve block with 7 days of recovery, or 7 days electrical stimulation at 20Hz. Following quality control and normalisation of data

(*n*=4), systematic bioinformatics analysis including GO-term enrichment revealed key signalling pathways involved in the process of disuse atrophy. A working hypothesis was developed which centres on the transcriptional control of myogenin (Myog) through a sensory role of the neuromuscular junction. This involves both class II histone deacetylases (Hdac4/5) and the *janus kin*ase and *signal transducer and activator of transcription* (Jak/Stat) pathway, and influences potential downstream Myog targets including the ubiquitin E3 ligases Trim63 and Fbxo32, as well as genes involved in neuromuscular junction formation. Quantitative reverse transcription polymerase chain reaction (qRT-PCR) was used to confirm the temporal profiles for expression of key genes central to this model. These included a 33-fold increase in Myog mRNA after 3 days nerve block, and a 180-fold increase in transcript for the alpha subunit of the nicotinic acetylcholine receptor after 14 days of nerve blockade.

To establish whether our findings were transferable to atrophy induced by other mechanisms, and to examine potential chemical interventions, we returned to the C2C12 *in vitro* model. The transcript levels of the same key genes were measured in myotubes following treatment with glucose-free media as well as media containing chemical inhibitors of the signalling pathways central to our hypothesis: the class II Hdac inhibitor MC1568, the Stat3 inhibitor S3I-201, and in addition to the Class I Hdac inhibitor MGCD0103. Differences were again observed in the patterns of change in transcript levels between *in vivo* and *in vitro* treatments as well as between *in vitro* treatment groups. The atrophy associated with glucose starvation was a 56% (+/- 2.%) reduction in myotube diameter relative to cells grown in normal media. While MC1568 and S3I-201 treatment reduced this *in vitro* atrophy by a small amount (to 42% +/- 4% and 21% +/- 6%, respectively, relative to cells grown in normal media), surprisingly the class I Hdac inhibitor MGCD0103 markedly blunted starvation atrophy with a decrease in myotube diameter of only 3% (+/- 7%).

The discovery of therapeutic targets that could alleviate skeletal muscle atrophy is an exciting and potentially productive avenue of research. Skeletal muscle atrophy has wide ranging causes and debilitating consequences for patients. This project represents a starting point in the systematic development of drugs that could benefit these patients by improving quality of life and decreasing morbidity.

LIST OF ABBREVIATIONS

Ach	Acetyl Choline
Bcl2l11	Bcl-2-interacting mediator of cell-death
CaMKII	Calcium/calmodulin-dependent protein kinase
Ccnb1	Cyclin B
Ccnd2	Cyclin D2
Cdkn1b	Cyclin-dependent kinase inhibitor 1B
Chrna1	Nicotinic Acetyl Choline Receptor Subunit Alpha 1
CSA	Cross Sectional Area
Dach2	Dachsund 2
Dex	Dexamethasone
dNTPs	Deoxynucleotide Triphosphates
DTT	Dithiothreitol
EIF3f	Eukaryotic Initiation Factor
Fbxo32/Atrogin-1/ MAFbx	F-Box Protein 32
FCS	Foetal Calf Serum
Foxo	Forkhead Box 01 Transcription Factor
G6pc3	Glucose-6-phosphatase
GO	Gene Ontology
Hdac	Histone Deacetylase
HS	Horse Serum
IGF	Insulin-Like Growth Factor
Jak	Janus Kinase
Lpl	Lipoprotein Lipase
MHC	Myosin Heavy Chain
Mitr	Hdac 9 Splice Variant
mTOR	Mammalian Target of Rapamycin
Myog	Myogenin
nAChR	Nicotinic Acetyl Choline Receptor
NCBI	National Centre for Biotechnology Information
NMJ	Neuromuscular Junction
Pdk4	Pyruvate dehydrogenase kinase 4
PI3K	Phosphatidylinositol-3-Kinase
Plk1	Polo-like Kinase
Polr2a	RNA polymerase II polypeptide A
qRT-PCR	Quantitative Reverse Transcription Polymerase Chain Reaction
Rn18S	18S ribosomal RNA
SAGE	Serial Analysis of Gene Expression
Socs3	Suppressor of Cytokine Signalling 3
Sod2	Manganese superoxide dismutase
Stat	Signal Transducer and Activator of Transcription
TA	Tibialis Anterior
Tgfb2	Transforming growth factor β-2
Trim63/MuRF1	Tripartite Motif Containing 63 / Muscle RING-Finger Protein 1
TTX	Tetrodotoxin
Ub	Ubiquitin

LIST OF FIGURES

LIST OF TABLES

APPENDICES

TABLE OF CONTENTS

Chapter 1: Introduction

1.1 Motivation For The Project

Progressive muscle wasting or muscle atrophy is a debilitating and life-threatening disorder. It is a pathological aspect of many diseases including cancer, diabetes, chronic obstructive pulmonary disease (COPD), and AIDS and is a natural consequence of the inactivity associated with ageing, when it is known as sarcopenia (Holecek, 2012). Loss of muscle mass in elderly patients may affect quality of life by increasing risk of falling and fractures, as well as the risk of surgical complications (Aversa et al., 2011). Weight loss in cancer cachexia patients causes reduced mobility and quality of life. Studies suggest that in patients with nonresectable pancreatric cancer, a 25-30% loss of body weight has been reported upon death (Tisdale, 2009). Critical illness requiring care in the intensive care unit (ICU) and prolonged ventilatory support is associated with muscle wasting as a combined result of the underlying condition, bed rest, muscle inactivity and mechanical ventilation (Callahan and Supinski, 2009, Khan et al., 2008). Patients in intensive care can lose about 2% of their muscle mass per 24 hours and some patients lose up to 50% of their total muscle mass during their stay in the ICU (Khan et al., 2008). Some critically ill patients develop acute quadriplegic myopathy caused by a specific and pronounced depletion of muscle myosin (Larsson et al., 2000).

The underlying cellular and molecular mechanisms governing the process of atrophy are beginning to be elucidated. However, there remains much to learn before these mechanisms are clarified sufficiently to allow the development of rational therapeutic interventions. The discovery of therapeutic targets that could alleviate skeletal muscle atrophy is an exciting and potentially productive avenue of research. This project represents a starting point in the systematic development of drugs that could benefit these patients by improving quality of life and decreasing morbidity.

1.2 Skeletal Muscle Structure

1.2.1 Gross Anatomy

Skeletal muscle is a form of striated muscle capable of contractions, generally within a limited range. If a larger range of movement is required it is achieved through the amplification provided by the lever systems of the skeleton, which muscles attach to via

bundles of collagen fibres known as tendons. Skeletal muscle is under control of the somatic nervous system, implying voluntary control. However, this is an inadequate term as many of the movements in which it participates, such as breathing and swallowing, are not usually under conscious control. Muscles vary considerably in size, shape and arrangement of fibres depending on the function for which it is required. An individual muscle is made up of many individual cells known as muscle fibres (myofibres), which are bundled together into fascicles, each surrounded by a layer of connective tissue called the perimysium. Many fascicles combined make up a muscle, and a connective sheath called the epimysium surrounds the muscle and provides a pathway for blood vessels and nerves (Figure 1) (Salmons, 1995).

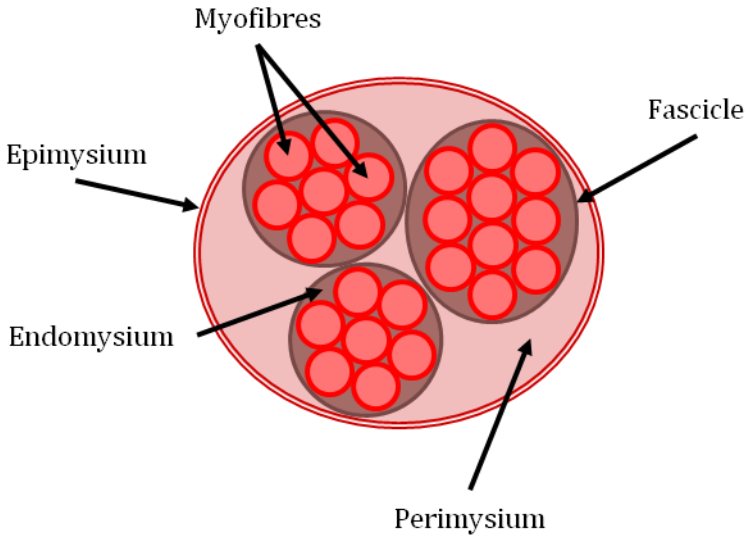

Figure 1 Diagrammatic Representation of the Organisation of Skeletal Muscle
Skeletal Muscle is composed of numerous myofibres that are bundled together into fascicles surrounded by the perimysium

The myofibres are composed of myofibrils, which are cylindrical structures of about 1μm in diameter. These are the dominant ultra-structural feature of an electron micrograph and give the striated appearance of skeletal muscle. The myofibrils are mainly composed of the proteins actin and myosin. Primarily these form thin (actin) and thick (myosin) filaments, which overlap to some extent when the muscle is at rest. These filaments repeat along the length of the myofibril in sections known as sarcomeres, which form the basic functional unit of the muscle fibre. Muscles contract by ATP-driven conformational changes in the myosin head.

The nuclei of mammalian myofibres are entirely postmitotic and cannot replace themselves (Charge and Rudnicki, 2004, Moss and Leblond, 1971, Snow, 1978); consequently the contribution of another, precursor cell type is required for growth and injury-induced regeneration (Collins and Partridge, 2005). Satellite cells form a small population of quiescent muscle precursor cells which reside beneath the basal lamina of each myofibre (Charge and Rudnicki, 2004, Mauro, 1961). In response to muscle injury, satelite cells are activated, proliferate and differentiate, at which time they fuse together to repair or replace damaged myofibres (Charge and Rudnicki, 2004).

1.2.2 Nervous Control of Skeletal Muscle

Every skeletal muscle is supplied by one or more nerves. Muscle nerves are frequently referred to as motor nerves, but they contain both motor and sensory components. The major motor component consists of the large, myelinated axons that supply the muscle fibres; these α-efferents, or α-motor axons are among the fastest-conducting nerve fibres in the body (Finsterer et al., 2011). Within muscles, nerves follow the connective sheaths, coursing in the epimysial and perimysial septa before entering the fine endomysial tissue around the muscle fibres. A specialised synpase, the neuromuscular junction, is formed where the terminal branch of an α-motor axon contacts the muscle fibre (Deschenes, 2011). The axon terminal gives off several short, curling branches over an elliptical area, the motor end plate (Salmons, 1995). The arrival of an action potential at the motor end plate causes acetylcholine (ACh) to be exocytosed from synaptic vesicles into the synaptic cleft that separates the nerve ending from the sarcolemma (figure 2).

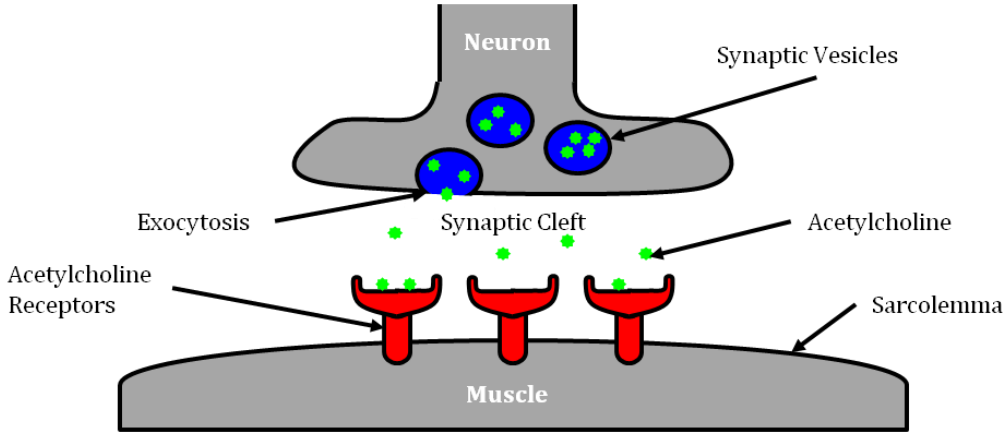

Figure 2 Diagrammatic Representation of the Neuromuscular Junction
Acetylcholine exocytosed from the neuron moves over the synaptic cleft to bind to acetylcholine (Ach) receptors, increasing sarcolemma permeability, and hence conductance.

The ACh is rapidly bound by nicotinic acetylcholine receptors, or nAChRs on muscle. These receptors are made up of five subunits, arranged symmetrically around a central pore (Purves, 2008, Deschenes, 2011). Each subunit comprises four transmembrane domains with both the N- and C-terminus located extracellularly. In vertebrates, nicotinic receptors are broadly classified into two subtypes based on their primary sites of expression: muscle-type nicotinic receptors and neuronal-type nicotinic receptors. In the muscle-type receptors, found at the neuromuscular junction, receptors are either the embryonic form, composed of α1, β1, δ, and γ subunits in a 2:1:1:1 ratio, or the adult form composed of α1, β1, δ, and ε subunits in a 2:1:1:1 ratio (Purves, 2008). Binding of ACh to these receptors triggers an almost instantaneous increase in the permeability, and hence conductance, of the postsynaptic membrane. This generates the end-plate potential, a local depolarisation, which is normally several times larger than is needed to initiate an action potential in the surrounding sarcolemma. This ensures that excitation is passed with high security to the muscle so that, except under conditions of extreme fatigue, a muscle action potential is generated for each nerve impulse. The action potential propagates along the length of the muscle fibre and spreads into its interior along the T-tubules, initiating contraction (Salmons, 1995).

1.2.3 The Sliding Filament Theory

The sarcomere consists of a central bidirectional thick filament (myosin) flanked by two actin filaments, orientated in opposite directions (figure 3).

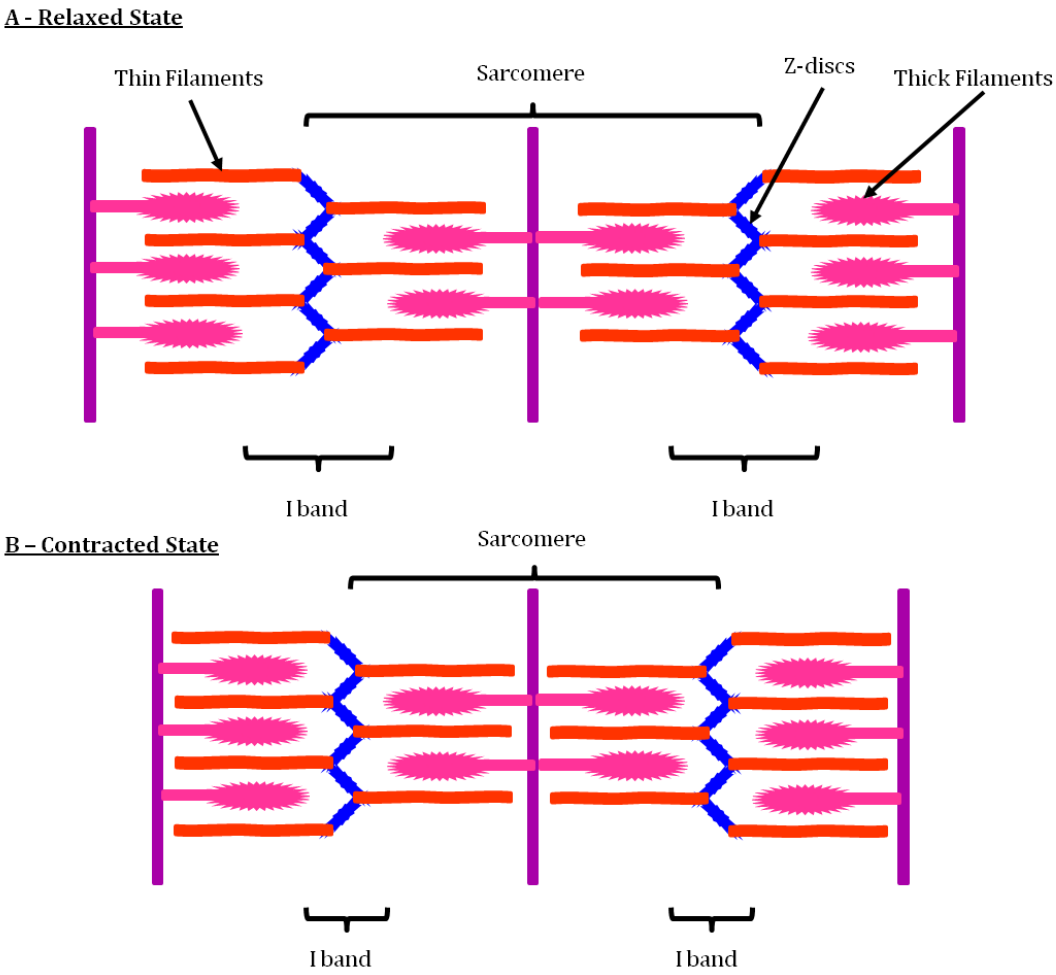

Figure 3 Diagrammatic Representation of the Sarcomere and Sliding Filament Theory
Upon contraction from the relaxed state (A) the thin and thick filaments slide over each other to shorten the I band and overall sarcomere length (B).

Myosin is the principal contractile protein in muscle. It is a heterohexamer with a molecular size of about 520 kilodaltons (kD) (Rayment et al., 1993), and is composed of two myosin heavy chains (MHCs), the carboxy-terminal portions of which associate to form an α-helical coiled-coil rod or 'myosin tail' (Schiaffino and Reggiani, 1994). The myosin tail accounts for the self association of myosin at low ionic strength and forms

the backbone of the thick filaments (Rayment et al., 1993). The amino portions of the MHCs are separated to form two elongated, globular domains known as the 'myosin heads', which act as an actin-based molecular motor to convert chemical energy released from the hydrolysis of adenosine tri phosphate (ATP) into mechanical force (Weiss et al., 1999). At the head-tail junction each MHC associates with two myosin light chains (MLCs).

Following the binding of ACh to the nAChRs the resulting action potential spreads through the muscle fibres network of T-tubules, depolarizing the inner portion of the muscle fibre. The depolarization activates L-type voltage-dependent calcium channels (dihydropyridine receptors) in the T tubule membrane, which are in close proximity to calcium-release channels (ryanodine receptors) in the adjacent sarcoplasmic reticulum. Activated voltage-gated calcium channels physically interact with calcium-release channels to activate them, causing the sarcoplasmic reticulum to release calcium. The calcium binds to the troponin C present on the actin-containing thin filaments of the myofibrils (Gillis et al., 2007). The troponin then allosterically modulates the tropomyosin. Under normal circumstances, the tropomyosin sterically obstructs binding sites for myosin on the thin filament; once calcium binds to the troponin C and causes an allosteric change in the troponin protein, troponin T allows tropomyosin to move, unblocking the binding sites (Gillis et al., 2007). Myosin has ADP and inorganic phosphate bound to its nucleotide binding pocket, and is in a ready state to bind to the newly uncovered binding sites on the thin filament, which is very tightly coupled to the release of inorganic phosphate. Myosin is now bound to actin in the strong binding state. The release of ADP and inorganic phosphate are tightly coupled to the power stroke, which is a conformational change in the myosin head. Actin acts as a cofactor in the release of inorganic phosphate, expediting the release. This will pull the Z-bands towards each other, thus shortening the sarcomere and the I-band (figure 3 panel B).

ATP binds myosin, allowing it to release actin and be in the weak binding state (a lack of ATP makes this step impossible, resulting in the rigor state characteristic of rigor mortis). The myosin then hydrolyzes the ATP and uses the energy to move into the 'cocked back' conformation. ATP binds to myosin as long as it is available and calcium is present on the thin filament (Gillis et al., 2007). While the above steps are occurring, calcium is actively pumped back into the sarcoplasmic reticulum. When calcium is no longer present on the thin filament, the tropomyosin changes conformation back to its previous state so as to block the binding sites again. The myosin ceases binding to the thin filament, and the contractions cease (Salmons, 1995). When a muscle fibre

contracts, all sarcomeres contract simultaneously because of the spread of excitation along the plasma membrane and the t-tubukes, so that force is transmitted to the fibre ends.

1.2.4 The Cellular Process of Atrophy

Under normal physiological conditions, muscle mass is maintained at a relatively constant level by a balance between protein synthesis and protein degradation. This balance is highly important in situations where for example more power is needed from the muscle (hypertrophy) or in periods when food sources are limited and protein breakdown is required to produce energy (atrophy). When this balance is perturbed so that protein breakdown rates exceed the rates of protein synthesis, loss of muscle mass occurs. Muscle mass or muscle atrophy involves a reduction in muscle fibre diameter in the absence of degenerative changes or a reduction in the actual number of fibres. It can be caused by reduced protein synthesis, increased protein breakdown or a combination of these changes, the balance of which is probably determined by the cause of the atrophy (Aversa et al., 2011). The regulation of protein synthesis is complex, but reduced anabolic signalling through the PI3K/Akt pathway with altered downstream signalling through mTOR, GSK-3β, and Foxo is an important factor in muscle wasting that at least in part accounts for reduced protein synthesis (Glass, 2010). Proteolytic pathways involved in the degradation of proteins in atrophying muscle include the ubiquitin-proteasome pathway.

1.2.5 The Ubiqutin-Proteasome System

The ubiquitin proteosome pathway and specific ubiquitin pathway enzymes have been directly implicated in the progression of muscle atrophy (Eddins et al., 2011, Sandri et al., 2004, Stitt et al., 2004). Ubiquitin is a small 76-residue protein that is highly conserved among all living organisms (Hershko and Ciechanover, 1998, Eldridge and O'Brien, 2010). Ubiquitin is used as a post-translational lysine modification on proteins affecting stability, activity and/or localisation of the target protein (Hershko and Ciechanover, 1998, Pickart, 2001, Pickart and Eddins, 2004, Sun and Chen, 2004). The co-ordinated action of three enzymes (E1, E2 and E3) facilitate the conjugation of the c-

terminal glycine of ubiquitin to the ε-amino group of a specific lysine on the target protein (Eldridge and O'Brien, 2010) (figure 4). Ubiquitin (Ub) and ubiquitin-like proteins are activated for transfer by the E1 ubiquitin-activating enzyme. Activated ubiquitin is then transferred in thioester linkage from the active-site cysteine of E1 to the active-site cysteine of an E2 ubiquitin-conjugating enzyme. The E2Ub thioester next interacts with an E3 ubiquitin ligase, which effects transfer of Ub from E2Ub to a lysine residue of a substrate. Monoubiquitinated, the substrate can either dissociate from the E3 or can acquire additional Ub modifications in the form of multiple single attachments.

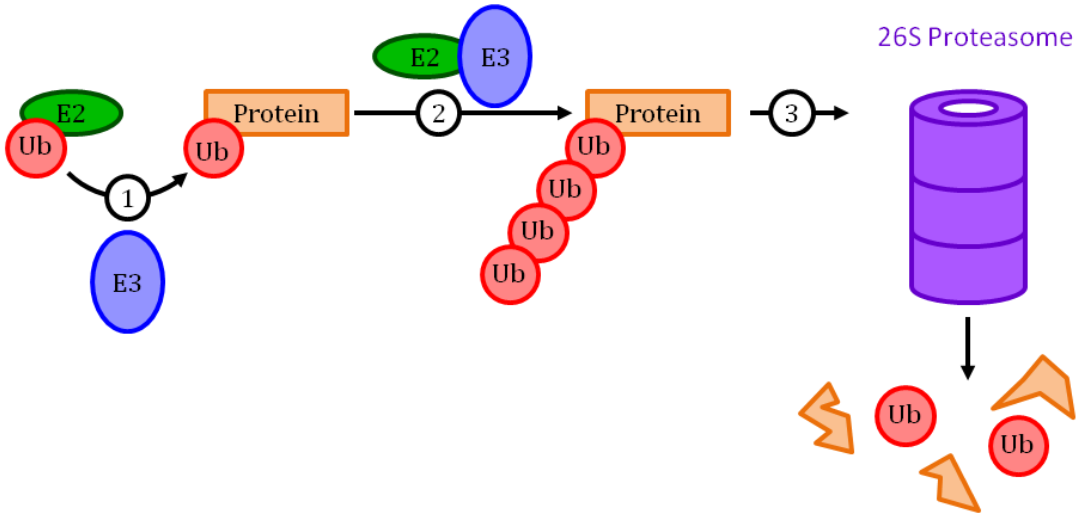

Figure 4 Ubiquitin Ligases & The Proteasome
Ubiquitin (Ub) and ubiquitin-like proteins are activated for transfer by the E1 ubiquitin-activating enzyme. The E2Ub thioester interacts with an E3 ubiquitin ligase, which effects transfer of Ub from E2Ub to a lysine residue of a substrate (1). Monoubiquitinated substrate can either dissociate from E3 or additional ubiquitins can be attached (2). The substrate protein may be moved to the 26S proteasome for degradation into short oligopeptides and releases free ubiquitin (3).

In addition to the conjugation of a ubiquitin (monoubiquitylation) to a target substrate protein, additional ubiquitins can be attached to one of the seven lysines on each ubiquitin (polyubiquitination) (Hershko and Ciechanover, 1998, Sun and Chen, 2004). This affords an extraordinary amount of signalling diversity for proteins that are modified by ubiquitin. Of these seven lysines on ubiquitin, lysine 48 is the modification that has been the most studied (K48-linked polyubiquitination) (Eddins et al., 2007). This modification generally targets the substrate protein to the 26S proteasome for

degradation. The 26S proteasome hydrolyses the polypeptide into short oligopeptides and releases free ubiquitin (figure 4) (Eddins et al., 2007).

Targeting of ubiquitin to a substrate protein's lysine is accomplished by an E3 ubiquitin ligase. E3's provide the majority of substrate recognition and selectivity. There are over 600 E3 ligases that target cellular proteins (Deshaies and Joazeiro, 2009). Each E3 ligase has very specific protein substrates. There are two major classes of E3s; RING E3s and HECT domain containing E3s (Deshaies and Joazeiro, 2009, Scheffner and Staub, 2007). The two major E3 ligases that have been implicated in skeletal muscle atrophy are Trim63, also known as MuRF1 and Fbxo32, also known as Atrogin-1 or MAFbx. Trim63 is upregulated in at least 13 different models of atrophy (Clarke et al., 2007) and has been shown to be the E3 required for the degradation of myosin heavy and light chain proteins (Clarke et al., 2007, Cohen et al., 2009). Clarke *et al* demonstrated a physical interaction *in vitro* between Trim63 and MHC by immune precipitation of epitope-tagged Trim63 protein, which co-immunoprecipitated MHC protein. The study went on to show that the loss of MHC induced by the treatment of cultured myotubes with the cachectic glucocorticoid dexamethasone (dex) was blocked by siRNA-mediated depletion of Trim63. Furthermore, MHC was found to be spared in $Trim63^{-/-}$ mice in comparison to wild-type mice under dex-induced atrophy conditions (Clarke et al., 2007). Fbxo32 has been implicated in muscle atrophy and was originally thought to also degrade myofibrillar proteins (Bodine et al., 2001). However, more recent studies have suggested that the role of Fbxo32 is to regulate protein synthesis via the degradation of alternative substrates, the transcription factor MyoD (Tintignac et al., 2005) and the eukaryotic initiation factor EIF3f (Lagirand-Cantaloube et al., 2008).

The activation and proliferation of satellite cells, followed by their differentiation and fusion with myotubes, is believed to be essential for hypertrophy of adult skeletal muscle (Hawke and Garry, 2001, Rosenblatt et al., 1994) and MyoD has been shown to be upregulated prior to satellite cell proliferation (Charge and Rudnicki, 2004). EIF3f is a regulatory subunit that plays a major role in muscle hypertrophy through its actions in the insulin-like growth factor (IGF)/ mammalian target of rapamycin (mTOR) pathway (Csibi et al., 2010).

1.3 Transcriptional Regulation of Skeletal Muscle Atrophy

1.3.1 Transcriptional Regulation

One of the mechanisms by which skeletal muscle changes in response to the demands placed upon it, i.e. increased activity or decreased nutrient supply, is through the regulation of gene transcription. Transcriptional regulation controls when, and how much RNA is produced by RNA polymerase. There are several regulatory mechanisms, including a role for transcription factors, which position RNA polymerase at the start of a protein-coding sequence of DNA and then release the polymerase to transcribe mRNA. Transcription factors can be regulated pre- or post-transcription.

Foxo and Myogenin are transcription factors that have been implicated in skeletal muscle atrophy, through their role in the upregulation of genes encoding the E3 ubiquitin ligases Trim63 and Fbxo32. Whilst it is the activation of Foxo which determines its activity, control of myogenin activity occurs through transcriptional expression. Myogenin has been shown to be indirectly regulated by the action of Histone deacetylases (Hdacs). Histones are proteins found in eukaryotic cell nuclei that package and order the DNA into structural units called nucleosomes. They are the chief protein components of chromatin, acting as spools around which DNA winds. Acetylation of histones decreases their affinity for DNA (Hong et al. 1993), resulting in a change in nucleosomal conformation (Norton et al. 1989) and thus an increase the accessibility of transcriptional regulatory proteins to chromatin templates (Lee et al. 1993; Vettese-Dadey et al. 1996). Hdacs are a class of enzymes that remove acetyl groups on a histone, returning them to their original conformation and thus lending them to reduce transcription (Choudhary et al., 2009).

1.3.2 Foxo Transcription Factors

In differentiated myotube cultures both dex treatment and calorific restriction have been reported to induce atrophy, accompanied by increased expression of Fbxo32 and Trim63 (Sandri et al., 2004, Stitt et al., 2004). This was antagonised by simultaneous treatment with IGF-1, that acts through the phosphatidylinositol 3-kinase (PI3K)/Akt signalling pathway (Sandri et al., 2004, Stitt et al., 2004). These studies demonstrated a novel role for Akt as, in addition to stimulating skeletal muscle hypertrophy (Rommel

et al., 2001), Akt stimulation could dominantly inhibit the induction of atrophy signalling. This link between IGF, Fbxo32 and Trim63 was confirmed *in vivo*. Lee *et al* showed that the expression levels of the E3 ubiquitin ligases, measured by northern blotting, increased the atrophy induced by diabetes in the rat. Here too, IGF-1 blocked the transcriptional upregulation of E3 ligases (Lee et al., 2004). Stitt *et al* showed that activation of the PI3K/Akt pathway using C2C12 lines that stably expressed constitutively active forms of PI3K or Akt, was sufficient to block dex-induced upregulation of Fbxo32 and Trim63 (Stitt et al., 2004). The mechanism by which Akt inhibited the expression of these E3s was demonstrated to involve the Forkhead (Foxo) family of transcription factors (Sandri et al., 2004, Stitt et al., 2004).

Foxo transcription factors were first discovered more than 10 years ago in Drosophila and are characterized by a shared 100 amino acid DNA-binding motif, termed the "winged helix" or "forkhead" domain (Tzivion et al., 2011). Conserved forkhead domains have been identified in eukaryotic organisms from yeast to humans. The human genome contains more than 40 FOX genes, the Foxo family members; Foxo1, Foxo3 and Foxo4 are all expressed in skeletal muscle (Furuyama et al., 2002). The forkhead transcription factors have been shown to play diverse roles in development, metabolism, immunology, cancer, and cell-cycle control (Tuteja and Kaestner, 2007). Sandri *et al* demonstrated a role for Foxo during calorific restriction and dex-induced atrophy in myotubes. Foxo transcription factors, particularly Foxo1, are excluded from the nucleus when phosphorylated by Akt, resulting in an association with 14-3-3 sequestered proteins (Van Der Heide et al., 2004, Tzivion et al., 2011). Upon dephosphorylation they are translocated to the nucleus, where activation of Foxo transcription factors was shown to be required for upregulation of Fbxo32 and Trim63 (figure 5).

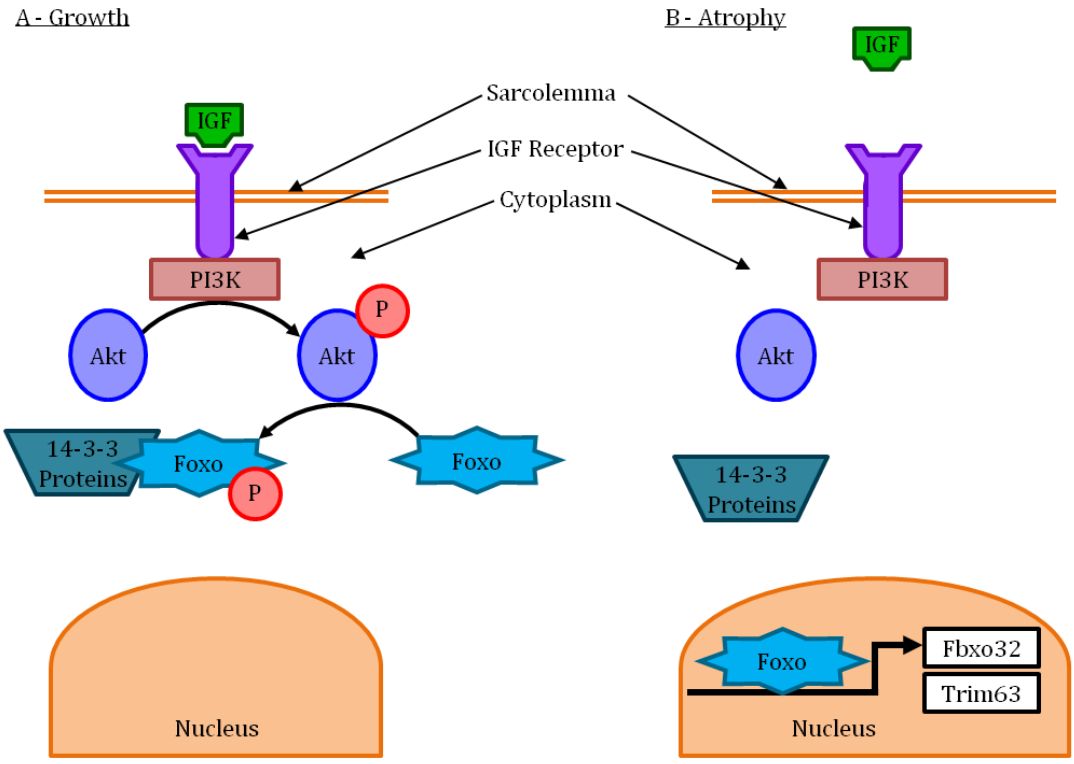

Figure 5 A role for Foxo Transcription Factors During Muscle Growth and Atrophy
In normal growth conditions IGF-1 activates its receptor, resulting in the activation of downstream targets and the consequent phosphorylation of Foxo. Foxo associates with the 14-3-3 proteins and is sequestered in the cytoplasm (Panel A). During atrophic conditions IGF-1 does not bind to the cellular receptors and therefore neither the receptor, or its downstream, targets are activated. As a consequence of the inactive signalling cascade Foxo remains unphosphorylated causing it to dissociate from the 14-3-3 proteins and translocate to the nucleus where it activates transcription of Trim63 and Fbxo32 (Panel B).

These findings have subsequently been confirmed *in vivo*. Transgenic over-expression of Foxo1 resulted in an atrophic phenotype in mouse; showing smaller muscle mass, reduced muscle fibre cross sectional area and impaired skeletal muscle function (Kamei et al., 2003). Senf *et al* demonstrated using a limb casting model of inactivity in rat that expression of a dominant-negative Foxo3a in rat soleus muscle, introduced by injection and electroporation, was able to block muscle fibre atrophy by over 40% (Senf et al., 2010).

1.3.3 Hdac Regulation of Myogenin and Its Role in Muscle Atrophy

Myogenin (Myog) is a basic helix-loop-helix (bHLH) transcription factor essential for skeletal muscle development. Transgenic mice homozygous for a targeted mutation in the Myog gene survive foetal development but die immediately after birth and show a severe reduction in the mass of all skeletal muscle (Hasty et al., 1993). During normal development, Myog expression is downregulated in skeletal muscle postnatally, but can be reinduced in response to denervation in mouse (Macpherson et al., 2011, Tang et al., 2009). Curiously, in view of its role in development, Myog has also been shown to bind the promotor regions of the Fbxo32 and Trim63 genes (Moresi et al., 2010), activating their expression (Macpherson et al., 2011, Moresi et al., 2010), and linking Myog as having an important role in the control of muscle atrophy. Consequently, control of Myog expression is highly relevant when looking at the mechanisms behind skeletal muscle atrophy.

Hdacs have been shown to play an important role in the regulation of Myog expression. Hdacs are classified into four classes (I, IIa & b, III and IV) depending on sequence identity and domain organization. The class II Hdacs (HDAC4, 5, 6, 7, 9, and 10) are able to shuttle in and out of the nucleus depending on their phosphorylation state (de Ruijter et al., 2003). Hdac inhibitors, a class of compounds that interfere with the function of Hdacs have recently been used in studies which have shown an important role for Hdacs in the regulation of Myog, and ultimately in muscle atrophy. The class IIa Hdacs, Hdac4 and Hdac5, which act as transcriptional repressors (Haberland et al., 2009, McKinsey et al., 2000, Potthoff et al., 2007), are upregulated in skeletal muscle upon denervation and repress the expression of Dach2 and Mitr, two negative regulators of Myog (Cohen et al., 2007, Tang et al., 2009) (figure 6).

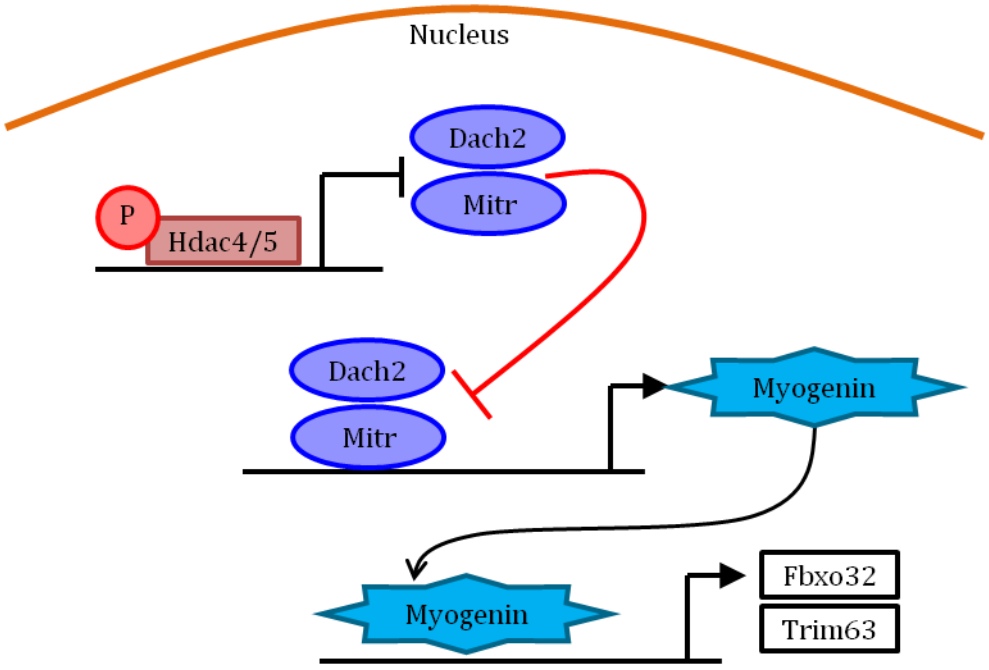

Figure 6 The Role of Myogenin in Skeletal Muscle Atrophy
Hdac4 and Hdac5 repress the expression of Dach2 and Mitr; the negative regulators of myogenin. Myogenin expression increases which promotes the expression of Fbxo32, Trim63 and acetylcholine receptors.

1.4 Experimental Models of Skeletal Muscle Atrophy

Muscle wasting is a pathological condition of many diseases ranging from cancer to AIDS and is also a natural consequence of muscle inactivity and age-related sarcopenia. Experimental models used to investigate muscle atrophy are equally wide ranging, and the relationship between the model used and the resulting data should be taken into account when making comparisons between studies.

1.4.1 *In Vitro* Models of Skeletal Muscle Atrophy

Myoblast cultures provide important and convenient mechanistic models of the signalling and molecular pathways potentially employed by skeletal muscle *in vivo* to regulate hypertrophy and atrophy. These myoblast models use either primary skeletal muscle cells derived from human or animal biopsies or, more frequently, established cell lines such as the mouse C2C12 or rat L6 myoblast cells (Sharples and Stewart, 2011). Myoblast cell lines may be cultured to allow differentiation into multinucleate

myotubes. Calorific restriction of myotubes or treatment with a corticosteroid, such as dexamethasone, can induce atrophy in cultured myotubes and are commonly used in studies of muscle atrophy (Sandri et al., 2004, Stitt et al., 2004). While these models are relatively simple to establish and have been very useful in beginning to unravel the mechanisms underlying skeletal muscle atrophy, there are several disadvantages of *in vitro* muscle cultures when compared with *in vivo* models. The limitations of an *in vitro* model include reduced differentiation capacity with passage, an inability to sustain myotubes for extended periods in culture and the environment of two-dimensional monolayer that lacks biomimicity, thus making direct comparisons with muscle in vivo difficult (Sharples and Stewart, 2011). Thus while these models can continue to be useful in highlighting some of the mechanisms involved, the study of the *in vivo* response is vital in directing research towards a therapeutic target for muscle atrophy. This thesis contains data from both types of model, highlighting some of the weaknesses of work bases *in vitro*, and some of the complexities that arise when dealing with the neuromuscular system as a whole.

1.4.2 *In Vivo* Models of Skeletal Muscle Atrophy

There are several *in vivo* animal models which adopt different methods of inducing atrophy, reflecting specific clinical causes of muscle wasting. Animal models of disease where muscle atrophy is one of the symptoms include induction of diabetes by selective destruction of the insulin-producing B-cells of the pancreas with a single, rapid injection of streptozotocin (STZ), a glucose moiety with a very reactive nitrosourea group from the mould Streptomyces guiseus (Wei et al., 2003). Cancer studies include several genetically engineered rodent models which were recently reviewed in detail by Holecek *et al* (Holecek, 2012), an example of which would be the Lewis lung carcinoma murine model described by Busquets *et al* in 2004 (Busquets et al., 2004). However, these models have the added symptoms of the disease itself, which may complicate the investigation of muscle atrophy specifically. Furthermore, the idea that systemic inflammation may be the primary cause of muscle wasting in ageing populations, and that muscle wasting is not entirely attributable to disuse, is an indication of the complexity of numerous factors that contribute to muscle wasting in different conditions leading to atrophy (Degens and Alway, 2006). Gaining an understanding of the molecular and cellular pathways that govern muscle atrophy without the interference of a diseased state is fundamental in understanding the

process of muscle wasting without confounding pathology. In order to achieve this goal models of muscle disuse atrophy have been developed. These include denervation, joint immobilisation and tail suspension.

Denervation studies either cut (van der Meer et al., 2011) or remove a section of the motor nerve supplying the muscle to be studied (Tang and Goldman, 2006), or crush the nerve so that it becomes damaged (Gigo-Benato et al., 2010). The advantage of this technique is the ability to compare denervated and innervated (contralateral) hindlimb muscles. Recent studies have shown a rapid onset of muscle atrophy in both young and old rats after just 1-2 weeks of denervation (van der Meer et al., 2011). However there are several disadvantages including the debate as to whether the lack of neurotrophic factors plays a role in the atrophy process as well as the lack of neuronal impulses (Midrio, 2006). Furthermore, this model provides a very limited option to look at the recovery from atrophy. Reinnervation is possible following a crush injury but requires a period of remodelling of axons and endplates (Varejao et al., 2004). Analysis of recovery is vital to see whether the pathways that lead to muscle atrophy are reversible, a key factor when considering the clinical implications.

Hindlimb suspension, where elastic tail casts are used to suspend the hindlimbs of the animal from the cage is another *in vivo* model which is used commonly in studies of atrophy. This technique unloads the muscles but does not restrict the movement of the limbs themselves. Consequently it has been suggested that this model is more suited to studies on microgravity during spaceflight than on muscle disuse (Holecek, 2012). Indeed, direct comparisons of the hindlimb suspension model have concluded that for certain muscles of the hindlimb the model shows no evidence of muscle disuse (Michel and Gardiner, 1990).

Joint immobilisation, such as limb casting, where the muscles of the limb are not prevented from contracting, but the limb is unable to move, has been shown to cause systemic stress responses and alterations, which may interfere with changes induced on the muscle by immobilisation (Holecek, 2012). The technique of limb immobilisation has also been used in human studies, where volunteers had one leg immobilised using a standard knee brace for up to 14 days (Yasuda et al., 2005). This approach may bypass the problems of translating findings from animal models but also has the added problems of increased ethical considerations and the availability of volunteer subjects. The issue of inter-individual variability also becomes more

important when looking at human studies, where it is difficult to control other components, such as diet and sleep patterns, which may contribute to the results.

1.4.3 Functional Atrophy: a Novel Method of Inducing Muscle Atrophy

The use of miniature implantable stimulators to alter the activity pattern in a muscle has been used to study changes in the contractile properties of skeletal muscle, such as muscle fibre types (Jarvis et al., 1996), as well as changes in mitochondrial biogenesis and metabolism (McMullen et al., 2011). Continuous electrical stimulation of the *Tibialis anterior* muscle was found to decrease muscle mass first in rabbit (Jarvis and Salmons, 1991, Mayne et al., 1991) and later in rat (Jarvis et al., 1996). The mechanisms behind this change in muscle size were not fully investigated as both studies focussed primarily on muscle fibre type, but a significant decrease in muscle weight was observed nonetheless. A study by Joplin and Salmons showed that increased muscle activity resulted in an increase in protein synthesis (Joplin et al., 1987). However, in certain types of activity, such as those mimicking endurance-type training, the level of protein degradation increases even further, resulting in muscle atrophy. This is ultimately the principle behind the model of functional atrophy, where one could perhaps say 'over use' of the muscle is the driving force behind the change in muscle size. However, whilst it is possible to use electrical stimulation of muscle to induce atrophy *in vivo*, whereby the change in muscle size is clearly an adaptive response to extreme activity, the physiological state of the muscle does not reflect the conditions that are linked with muscle wasting in diseased states, and is completely different from a disuse atrophy state.

1.4.4 Tetrodotoxin (TTX) nerve block to produce muscle atrophy.

A model employing the use of tetrodotoxin (TTX) to block action potentials in nerves is an interesting alternative to the other models of disuse atrophy, such as denervation or limb casting. TTX works by binding to the voltage-gated, fast sodium channels in nerve cell membranes, essentially preventing any affected nerve cells from firing by blocking the channels used in the process. The binding site of this toxin is located at the pore opening of the voltage-gated Na+ channel (Hwang and Noguchi, 2007). Such a toxin has

great potential for use in a muscle atrophy study as the ability to block specific nerve activity means that a particular muscle can be targeted and studied following a period of complete inactivity. Furthermore, as the toxin is reversible and does not permanently damage the nerve there is still the potential for neurotrophism. Studies that have used nerve block with TTX in rat models to look for changes in the contractile properties of muscle (Buffelli et al., 1997) or fibre type changes (Dupont Salter et al., 2003) have reported a decrease in muscle weight with this treatment. Thus TTX nerve block can be said to be an effective and clinically relevant model for muscle atrophy. However, there is currently no study which has focussed on the molecular and cellular signalling pathways which are involved in muscle atrophy using an *in vivo* TTX nerve block.

1.5 The Transcriptomics of Muscle Atrophy

There are several methods in place with which differential expression of a large number of genes can be identified and analysed. Analysis of the transcriptome is an exciting new tool with which the signalling pathways and molecular mechanisms controlling skeletal muscle atrophy can be further explored and delineated.

1.5.1 Methods for Transcriptome Analysis

Current high-throughput profiling technologies have enabled a more in depth approach to investigating interactions between multiple components within a signalling pathway. The more common methods used in studying muscle atrophy are serial analysis of gene expression (SAGE) and DNA microarray. SAGE allows the quantitative and simultaneous analysis of a large number of transcripts by producing a snapshot of the messenger RNA (mRNA) population in a sample of interest in the form of small tags that correspond to fragments of those transcripts. The SAGE technique does not require specific probes for transcripts and thus provides the potential for identifying novel changes in gene expression. The alternative approach employs the use of Affymetrix GeneChip microarray analysis, a technique that was originally developed by Maskos *et al* (Maskos and Southern, 1992). A DNA microarray is a collection of microscopic DNA probes attached to a solid surface that are used to measure the

expression levels of large numbers of genes. Probe-target hybridization is usually detected and quantified by detection of fluorophore-, silver-, or chemiluminescence-labelled targets to determine relative abundance of nucleic acid sequences in the target. The latter technique has been established for longer and thus there is a greater body of data available for comparison when considering muscle atrophy.

1.5.2 Transcriptome Analysis of muscle atrophy

Transcriptome analysis of the response of muscle to various models of muscle atrophy has been much improved with recent technological advances. SAGE analysis was used by St-Amand *et al* to investigate gene expression changes following 12 days of limb immobilisation in rat (St-Amand et al., 2001). More recent analyses have used Affymetrix GeneChips for microarray analysis. For example, several studies have looked at the transcriptional response to hind limb unloading following 12 hours (Bey et al., 2003), 21 days (Stein et al., 2002) or over a time course (Stevenson et al., 2003). There have also been studies combining many different data sets (meta-analysis) to look for common molecular signals over several different types of atrophy (Calura et al., 2008). We have used a combination of a the clinically accurate *in vivo* model of atrophy with the complex and accurate technology of Affymetrix GeneChip microarray analysis. The data presented here is key to understanding in greater detail the molecular mechanisms underlying the atrophy process, and the recovery from disuse atrophy to the normal active state.

1.5 Summary

The molecular mechanisms that lead to muscle atrophy have been studied using a variety of techniques *in vitro* and *in vivo*. *In vitro* myoblast cultures provide key mechanistic models of the signalling and molecular pathways potentially employed by skeletal muscle *in vivo* to regulate atrophy. However, the limitations of such models, such as the inaccurate physiological conditions, have led to the development of *in vivo* models which can look at the molecular response to atrophy at the level of muscle tissue as opposed to the cellular level.

The importance of looking at the *in vivo* response is vital in directing research towards a therapeutic target for muscle atrophy. There are currently several *in vivo* animal models which adopt different methods of inducing atrophy, reflecting specific clinical causes of muscle wasting. These include denervation, joint immobilisation and tail suspension. While each of these techniques has its place in the study of muscle atrophy, there are disadvantages associated with each model.

The development of a new model of atrophy, referred to as 'functional atrophy', where electrical stimulation of muscle results in a decrease in muscle size was a promising advancement in the field. With very little evidence of muscle damage, and the ability of the animal to continue using the muscle in the usual manner, this model of atrophy can provide more accurate information about the muscular response to atrophy and not the response to damage or unloading, However, clinical cases of atrophy are generally the result of disuse of a muscle rather than the continuous or over use that produces functional atrophy, much like the response of endurance training in athletes. Consequently, it has become apparent that a more clinically relevant *in vivo* model of atrophy was required. Such a model would enable direct comparisons between use and disuse atrophy to look for common pathways in both that would have the potential for therapeutic and enhancement targets.

The use of TTX to block nerve action, resulting in muscle disuse is an exciting avenue in the search for a more clinically and physiologically relevant model of muscle atrophy. The advantages associated with the *in vivo* models over the *in vitro* models, as well as the accuracy of the treatment to the muscle suggests that this model could be the future to beginning to elucidate the molecular mechanisms involved.

The most suitable and effective way of analysing the response in this model is to make a genome wide analysis of the transcriptional output of the muscle. Analysis of numerous transcripts may highlight potential pathways involved in the process of muscle atrophy, providing possible areas to focus on for therapeutic targets to either prevent muscle atrophy or induce hypertrophy. Our studies have highlighted a central role for the Foxo transcription factors and Myog, a transcription factor known to regulate genes involved in the control of muscle size. A better understanding of the expression of these transcription factors in muscle atrophy, as well as the signalling pathways in which they are involved, may begin to elucidate the mechanisms governing muscle size.

1.6 Aims

The aims of this thesis were to investigate the cellular and molecular mechanisms that govern skeletal muscle atrophy. Specifically,

- To compare changes in transcripts associated with muscle atrophy using *in vitro* models of skeletal muscle atrophy with an *in vivo* model of functional atrophy induced by electrical stimulation.
- To establish an *in vivo* model of atrophy that better represented the physiological state in disuse atrophy. An *in vivo* model using a TTX nerve block would be developed to induce progressive muscle atrophy, sampling at 3, 7 and 14 days without detriment to the muscle. In further groups, the nerve block would then be removed and the muscle allowed to recover for 7 days.
- In order to gain a better understanding of the cellular and molecular basis of atrophy and with the aim of generating a hypothesis of the pathways involved, the muscle from this model would be analysed, and compared with the electrical stimulation model of functional atrophy using DNA microarray. Following systematic and rigorous statistical analysis of the data, comparisons of transcriptional changes would be made between the two *in vivo* models of atrophy and the temporal effects of the nerve blockade and recovery to original active state.
- The final aim was to determine whether these findings were transferable to models of atrophy currently in use in the literature, and to examine potential chemical interventions. To accomplish this aim we would return to the C2C12 *in vitro* model. Chemical inhibitors of the signalling pathways identified by microarray analysis would be used and the degree of atrophy following chemical treatment, as well as the associated transcriptional changes would be measured to assess the effect of these inhibitors and the pathways they affect.

Chapter 2: Materials & Methods

2.1 C2C12 Myotube Cell Culture

C2C12 is a mouse myoblast cell line. C2C12 cells were originally obtained by Yaffe and Saxel through serial passage of myoblasts cultured from the thigh muscle of C3H mice after a crush injury (Yaffe and Saxel, 1977). Given the correct conditions, they are capable of differentiation into myotubes from the fusion of myoblasts into multi-nucleated cells. In this latter form they were used in this study as an in-vitro model of mature muscle cells.

2.1.1 Routine Culture of Myoblasts and Myotubes

C2C12 mouse myoblasts (gifted by Dr Vasilaki, The University of Liverpool) were cultured on BD Falcon 10 cm petri dishes (Scientific Lab Supplies Ltd, Hessle, UK) in Dulbecco's Modified Eagle Medium (Gibco, Paisley, UK) (DMEM) supplemented with 10% Foetal Calf Serum (FCS) and antibiotics (50U/ml penicillin and 50µg/ml streptomycin) at 37°C, 5% CO_2 until the cells reached 80% confluence. The medium was then replaced with DMEM supplemented with 2% horse serum (Gibco, Paisley, UK) (HS) and antibiotics and incubated for seven days, replenishing the media at three or four days, to induce myotube formation before any experimental treatments were started.

2.1.2 Myotube Starvation & Dexamethasone Treatment

Cultured myotubes obtained by methods outlined in 2.1.1 were treated by replacing the culture media with DMEM supplemented with 2% HS and antibiotics (Normal Media Control); DMEM, no glucose (Gibco, Paisley, UK) supplemented with 2% HS and antibiotics (Glucose Free Media); or DMEM supplemented with 2% HS, antibiotics and 1µM Dexamethasone (Sigma, Dorset, UK) (Dex Treated Media) and incubated for 24 hours at 37°C, 5% CO_2.

2.1.3 Myotube Treatment with Chemical Inhibitors

Each treatment group contained cultured myotubes obtained by methods outlined in 2.1.1. Each was treated by replacing the culture media with either DMEM supplemented with 2% HS and antibiotics or DMEM, no glucose supplemented with 2% HS and antibiotics. In some groups chemical inhibitors were added to the supplemented media, which replaced the culture media for 24 hours incubation at 37°C, 5% CO_2. 4 groups were treated with (a) the histone deacetylase (Hdac) Class I inhibitor MGCD0103 (Selleck, Houston, USA) at 10μM, (b) the Hdac class II inhibitor MC1568 (Selleck) at 10μM (c) the Signal Transducer and Activator of Transcription (Stat3) inhibitor S3I-201 (Selleck) at 50μM or (d) a combination of MC1568 and S3I-201. Concentrations were used as advised by Selleck and to ensure these were suitable for treatment of the cultured myotubes a CellTiter 96® Aqueous Non-Radioactive Cell Proliferation Assay (Promega, Southampton, UK) was performed as per manufacturer's instructions.

2.1.4 Myotube Diameter Measurement

An Olympus IMT-2 microscope was used to capture phase contrast photomicrographs of myotubes in culture using an Olympus c5050 digital camera. Photomicrographs were taken of five random fields over each plate before and after treatment. Using ImageJ 1.45i (http://rsbweb.nih.gov/ij/) each photograph was overlaid with an 8x8 grid. Running from top left to bottom right, at the first 10 points for which the grid intersections fell in a myotube its minimum diameter was measured using the the ImageJ software. The precise magnification of each section was determined using a stage graticule, photographed with the same settings, where each bar represents 100 μm. This allowed cross sectional areas to be calculated from precise diameter measurements.

2.1.5 First Stage RNA Extraction from Cultured Myotubes

The treatment media, described in 2.1.2 and 2.1.3 was removed following 24 hours incubation. The myotube cells were then washed twice with sterile 1X phosphate buffered saline (PBS). The cells were then lysed with 1 ml Tri Reagent (Sigma) and dislodged from the plate surface using a cell lifter. This suspension was then transferred to a 1.5 ml microcentrifuge tube and centrifuged at 14,000g for 10 minutes at 4°C. The supernatant was removed and transferred to a fresh 1.5 ml microcentrifuge tube. This crude extract was then processed as outlined in section 2.6.1.

2.2 Electrical Stimulation of Tibialis Anterior (TA) Muscle in Rats

Electrical stimulation of rat skeletal muscle by means of a miniature implantable stimulator was used to impose an atrophy inducing pattern of activity upon that muscle. In all studies the experimental subjects were male Wistar rats weighing between 350-450g. The Tibialis anterior (TA) muscle of the anterior compartment of the lower limb was chosen for stimulation because the common peroneal nerve, which supplies this muscle is largely motor in function; thus stimulation could be applied with little or no adverse sensory effects. Furthermore, the TA muscle acts to dorsiflex the foot at the ankle joint and thus activation of this muscle will have little effect on the normal movement of the animal. In all studies the left TA muscle was stimulated and the contralateral TA was used as an internal unstimulated control.

2.2.1 Miniature Implantable Stimulators

The stimulator was developed by Dr Jonathan Jarvis and Prof. Stanley Salmons (Jarvis and Salmons, 1991). It was used to deliver stimulation at a fixed frequency of 20Hz and could be switched on or off remotely by a defined sequence of light-flashes through the skin. The components of the stimulator were mounted by hand onto printed circuits and protected in a coating of biocompatible silicone rubber. A Dacron™ mesh extended from the silicone rubber to facilitate suturing *in-vivo* and help to prevent migration of the stimulators. Electrodes were PVC-insulated and made from multi-stranded

stainless steel, ending in uninsulated loops which could be sutured to the underlying muscle.

2.2.2 Implant Procedure

An anaesthetist was required to monitor animals for all implant procedures. The anaesthesia was adjusted accordingly to ensure a deep anaesthetic state throughout the procedure. All rats were anaesthetised by inhalation of isofluorane in conjunction with pure oxygen and nitrous oxide. Once anaesthetised, a subcutaneous injection of antibiotic (5mg/kg Baytril®) and an intramuscular injection of a semi-synthetic opioid Buprenorphine (0.05mg/Kg Temgesic) into the quadriceps femoris muscle of the right hind limb were administered. All implants were carried out under strict aseptic conditions using autoclaved instruments. The sterilised miniature implantable stimulator was submerged in sterile saline and inserted into the abdominal cavity via an incision through the skin and abdominal muscles of the flank on the left side of the animal. The stimulator was then sutured to the abdominal wall by way of the Dacron™ mesh. The electrodes were then tunnelled subcutaneously to the left hind limb. The abdominal muscles were closed using a running suture. Exposure of the common peroneal nerve, just proximal to the knee joint, was achieved by making a small, transverse incision in the biceps femoris muscle in the posterior compartment of the thigh. The electrodes were passed under the nerve using a 21 gauge needle and sutured in place with an attachment to the aponeurosis of the gastrocnemius muscle lying beneath. The electrodes were thus close to the nerve without actually being in contact. The biceps femoris muscle was then closed using a running stitch supplemented with several single interrupted stitches at two or three points along the line of the wound. External sutures were then used to close the skin. Prolene (Ethicon Ltd, Gargrave, UK) was used for all suturing, size 5-0 internally and externally. Animals were allowed to recover from the implant procedure for seven days before initiating stimulation, at which point both the muscle and skin had begun to heal and the effects of the anaesthetic had worn off.

2.2.3 Stimulation Protocol

The miniature implantable stimulators were pre-programmed to produce a stimulation pattern at a continuous frequency of 20 Hz for a period of 7 days. Stimulators were switched on remotely using a stroboscope to transmit a sequence of light pulses through the skin. Bi-directional communication by way of a sequence of flashes emitted from the stimulator indicated the stimulator had received the instructions. The stimulator could also be switched off when required with a single flash from the stroboscope. Rats undergoing stimulation were checked daily by palpating the front of the lower hind limb to ensure the frequency was correct. If signs of discomfort were evident or there was stimulation in the posterior compartment of the hind limb, known as co-contraction, stimulation was reduced in amplitude or terminated immediately. Full details of all implant experiments can be found in appendix 1.

2.3 Blockade of the Common Peroneal Nerve using a Nerve Cuff

A tetrodotoxin (TTX) nerve cuff was used to confer total blockade of all impulse activity reaching the muscle and induce progressive muscle atrophy over a period of 14 days. This atrophy was achieved in the absence of any histological signs of damage or degeneration to the muscle tissue. It was therefore possible to block muscle activity for 14 days, and then reverse the blockade, allowing the muscle to recover without detriment over the subsequent 7 days. TTX was delivered to a nerve cuff on the common peroneal nerve via an osmotic pump which was implanted sub-cutaneously. The common peroneal nerve was chosen because it is largely motor in function; thus nerve block could be applied with little or no adverse sensory effects. Furthermore, the muscles of the anterior compartment of the lower limb which are supplied by the common peroneal nerve, act to dorsiflex the foot at the ankle joint and thus blockade of these muscle had little effect on the normal movement of the animal. In all studies the experimental subjects were male Wistar rats weighing between 350-450g.

2.3.1 Implant Contents

The implant consists of a mini-osmotic pump which delivers TTX via a delivery tube to a nerve cuff which surrounds the *common peroneal nerve* at a rate of 0.5 µl/hour. The cuff allows the nerve to be bathed in TTX, which blocks action potentials in nerves by binding to the voltage-gated, fast sodium channels in nerve cell membranes.

The implanted system was prepared under sterile conditions. The mini-osmotic pumps (Alzet, Model 2002) were filled with calculated volumes of TTX solution (350 g/ml in sterile 0.9% saline) using a 1 ml syringe and blunt-tipped, 27 gauge filling tube to at least 90% potential volume to prevent unpredictable pumping rate fluctuations. This was confirmed by weighing the pump before and after filling. Attached to the flow moderator of the pump was a delivery-tube-and-nerve-cuff assembly (Figure 7), made in-house as a modification of the design used by Michel and Gardiner (Michel and Gardiner, 1990).

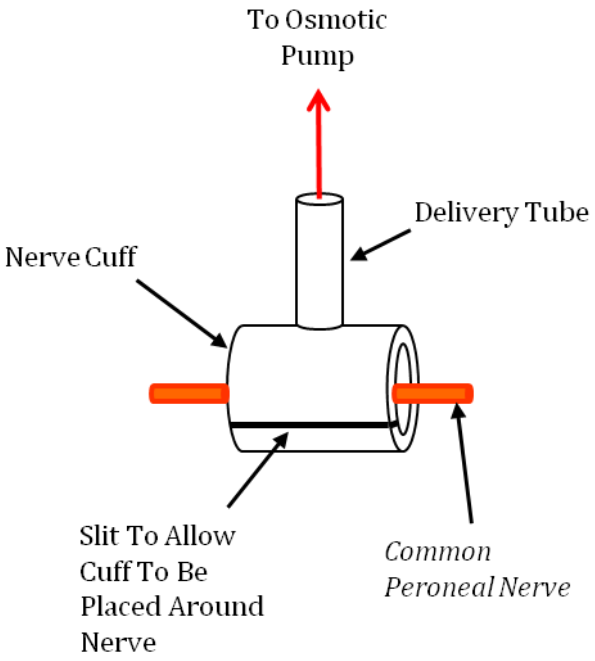

Figure 7 Schematic Representation of Nerve Cuff Assembly Showing The Common Peroneal Nerve In-Situ
Delivery tube and nerve cuff made from silastic tubing allows a continuous flow of TTX solution from the osmotic pump to surround the nerve.

The delivery tube was made from silastic tubing (Dow Corning) with outside diameter of 0.047 inches and internal diameter of 0.025 inches. The nerve cuff was made using silastic tubing with outside diameter 0.125 inches and internal diameter 0.078 inches with a slit made along the wall of the tubing, which allowed the cuff to be placed around the nerve. The delivery tube ran from the flow moderator of the osmotic pump to be attached using room temperature vulcanising (RTV) silicone rubber (Dow Corning) perpendicular to the nerve cuff. To ensure an uninterrupted flow from the pump, through the tubing and into the nerve cuff a 19 gauge needle was pushed through the wall of the nerve cuff and the tube threaded over this needle until it touched the outer surface of the nerve cuff. The RTV silicone rubber was then applied to the outside of the joint and allowed to set before removal of the needle. Once the osmotic pump was filled and attached to the delivery-tube-and-nerve-cuff assembly the whole implant was placed in sterile 0.9% saline and left overnight to prime the pump and allow the TTX solution to run through the delivery tube ready to be implanted.

2.3.2 Implant Procedure

The nerve cuff assembly was implanted along with the electrical stimulator described in 2.2.2. The stimulator was included to allow the nerve block to be checked. If the action of the nerve was fully blocked the electrical stimulator was unable to cause the TA muscle to contract. Figure 8 shows the schematic representation of the implant in-situ.

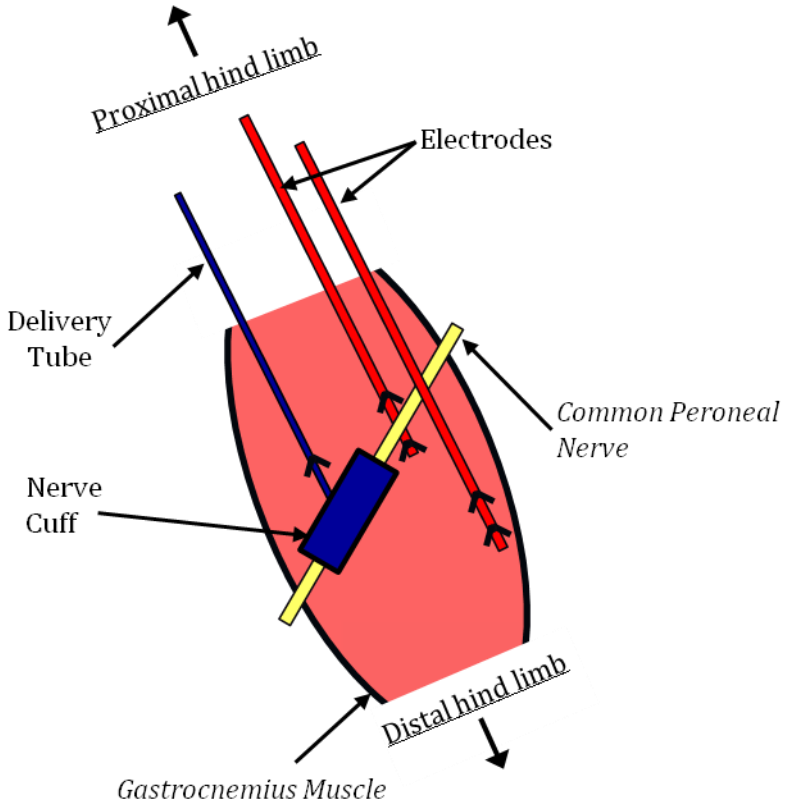

Figure 8 Schematic Representation of Nerve Cuff and Stimulator Electrodes In-Situ
The first electrode was tunnelled underneath the *common peroneal nerve* and sutured at either side to the underlying *Gastrocnemius muscle*. The second was sutured into the *Gastrocnemius muscle* near to the first electrode. The nerve cuff was placed around the nerve, downstream of the electrodes.

The nerve cuff in-situ is also shown in the photographs in figure 9 below.

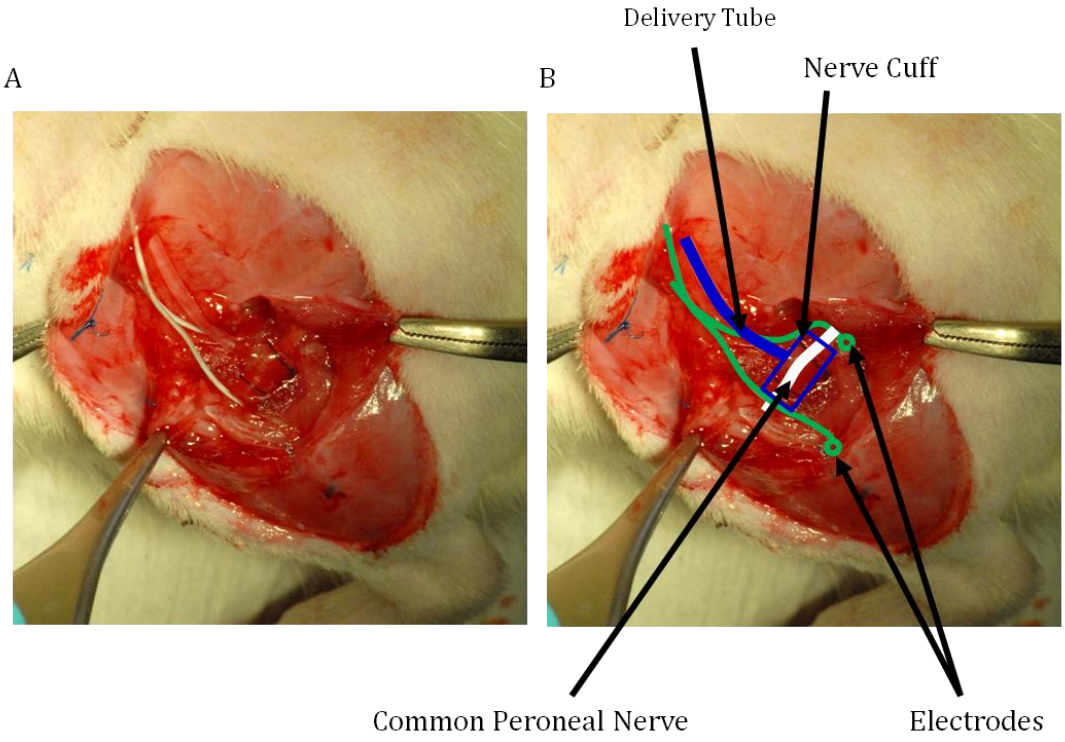

Figure 9 Photograph of Nerve Cuff and Stimulator Electrodes In-Situ
A. Photograph Showing Nerve Cuff In-Situ Prior to Closure of Wound. B. shows the same image with diagrammatic representation of constituent parts of the implant and nerve. The nerve cuff and delivery tube are represented in blue, electrodes in green and the common peroneal nerve in white.

An incision was made between the scapulae of the animal's back once the electrodes had been stitched into place in the hindlimb. The mini osmotic pump was positioned under the skin caudal to the incision on the back of the animal. The delivery tube was then tunnelled subcutaneously to the left lower limb. The common peroneal nerve was freed from the surrounding tissues taking great care not to stretch or touch the actual nerve as much as possible. The nerve cuff was then placed around the nerve and held in place by a suture at either end which ran around the cuff and into the underlying gastrocnemius muscle. A third suture was placed around the delivery cuff and into the biceps femoris approximately one centimetre from the nerve cuff ensuring not to restrict the diameter of the tube. As outlined in 2.2.2, the biceps femoris muscle was then closed using a running stitch aided with several single interrupted stitches at various points along the line of the wound. External sutures were then used to close the skin. Prolene (Ethicon Ltd.) was used for all suturing, size 5-0 internally and externally.

2.3.3 Nerve Block Protocol

The nerve block was effective as soon as the nerve cuff assembly was surgically implanted. The nerve block was left in place for 3, 7 and 14 days from the time of implant. Each day the animals were checked to ensure the nerve block was in place using the electrical stimulators. If signs of discomfort were evident or the block was not in place the experiment was terminated immediately. Another experimental group were subjected to 14 days of nerve block followed by 7 days of recovery. This was made possible as the pumps were known to deliver the TTX solution at a rate of 0.5µl per hour. Therefore if the pumps were filled with exactly 168 µl TTX solution this would run out after 14 days. The nerve block was checked at day 14 and its absence was confirmed on day 15 by turning on the electrical stimulators and palpating the contraction of the TA muscle in the anterior compartment of the left hind limb. Full details of all implant experiments can be found in appendix 1.

2.4 Muscle Tissue Processing for Extraction of RNA

2.4.1 Terminal Procedure and Muscle Harvesting

Rats were terminated by exposure to increasing concentrations of CO_2 followed by cervical dislocation, in accordance with Schedule 1 of the Animals (Scientific Procedures) Act 1986. Muscles were harvested using baked instruments and cut into sections on a sterile petri-dish using a sterile scalpel blade as shown in figure 10.

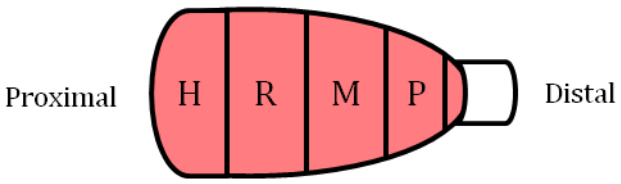

Figure 10 Segmentation of Rat TA Muscle For Analysis
Muscles were separated into samples to be analysed using histology (H), RNA extraction for qRT-PCR (R), RNA extraction for microarray analysis (M) and analysis of protein content (P)

The sections removed for RNA, microarray and protein analysis were approximately 100mg each. The samples were snap frozen in liquid nitrogen and stored at -80 °C. The remaining muscle from the proximal end of the muscle belly, for histological analysis, was mounted onto cork and frozen in melting isopentane above liquid nitrogen to prevent the formation of ice crystals. The samples were then stored at -80 °C.

2.4.2 First Stage RNA Extraction from Muscle Tissue

In order to prevent degradation of RNA by RNAses the instruments used for RNA extraction were baked overnight in an oven at 200°C. Frozen muscle samples (approximately 100 mg) were smashed under liquid nitrogen in the baked pestle and mortar and homogenised in 1 ml Tri Reagent (Sigma). Following centrifugation at 14,000g for 10 minutes at 4°C, the aqueous supernatant was removed, placed into a fresh 1.5 ml microcentrifuge tube and processed as outlined in 2.6.1.

2.5 Histological Analysis of Frozen Sections of Muscle Tissue

Examination of histological sections of both stimulated and unstimulated muscle tissue allowed evidence of nerve damage to be quantified as well as the measurement of fibre cross sectional area (CSA). A block of TA muscle was mounted onto a cork disc and immediately frozen in isopentane and snap frozen in liquid nitrogen. Samples were stored at -80°C. Serial sections (10 µm) were cut using a cryostat (Bright Instrument Company Ltd., Huntingdon, UK) and mounted onto subbed, glass slides (see appendix 2). The matched stimulated and unstimulated sections from each animal were placed on the same slide so that both were processed in parallel. Slides of sectioned muscle were stored at -80°C for future analysis by histological techniques.

2.5.1 Haematoxylin and Eosin Stain for Gross Fibre Morphology

Haematoxylin and eosin (H&E) staining was used to assess the general morphology of muscle fibres and look for signs of nerve damage following electrical stimulation and nerve block via the TTX nerve cuff (see appendix 3 for details of solutions used). H&E

staining causes muscle fibres to appear pink and nuclei blue. Before staining, sections were removed from the -80°C freezer and left for 30 minutes to adjust to room temperature. Sections were then dipped in tap water to rehydrate. Sections were then placed in Haematoxylin solution for 3 minutes before washing in warm, running tap water for 3 minutes. The sections were then placed in eosin for 1 minute before being dipped in running tap water for 10 seconds. The sections were then dehydrated through ascending grades of alcohol (50%, 70%, 90% and 100%), cleared in xylene and finally mounted in Di-N-Butyl phthalate in xylene (DPX)(BDH, Lutterworth, UK).

2.5.2 Fibre Cross Sectional Area Measurements

Using a Leitz Diaplan microscope photomicrographs were taken of histological sections of muscle tissue stained with H&E (outlined in 2.5.1). Images were captured using an Olympus c5050 digital camera. Photomicrographs were taken of five random fields over each section. Using ImageJ 1.45i (http://rsbweb.nih.gov/ij/) each photograph was overlaid with an 8x8 grid. Running from top left to bottom right, the first 10 points for which the grid intersections fell in a muscle fibre its diameter was measured using the ImageJ software. The precise magnification of each section was determined using a stage graticule, where each bar represents 100 µm. This allowed cross sectional areas to be calculated from precise diameter measurements.

2.6 mRNA Expression Analysis in Myotubes & Muscle Tissue

RNA was extracted from frozen muscle tissue, reverse transcribed into cDNA and the transcript levels of chosen genes were analysed using qRT-PCR. First stage extraction for myotubes (2.1.4) and frozen muscle tissue (2.4.2) produced an aqueous supernatant containing RNA which could be further treated in a common protocol as outlined below.

2.6.1 Second Stage RNA Extraction

0.2 mL chloroform (Sigma) was added to the aqueous supernatant containing RNA produced in 2.1.4 or 2.4.2. Each sample was shaken vigorously for 15 seconds and left to stand at room temperature for 15 minutes. The samples were then centrifuged at 14,000g at 4°C for 15 minutes. This separated the samples into three phases; an upper aqueous phase which contained the RNA, an inter-phase which contained the DNA, and an organic phase containing protein. The supernatant aqueous phase was transferred into a fresh 1.5 ml microcentrifuge tube and 0.5 ml isopropanol (Sigma) was added before each sample was left to stand at room temperature for 10 minutes. Samples were then centrifuged at 14,000g at 4 °C for 10 minutes. The supernatant was removed and the RNA pellet washed with 1 ml of 75% ethanol. Once the ethanol was removed, the RNA pellets were left to dry for 5 minutes at room temperature and then re-suspended in 50 µl diethylpyrocarbonate (DEPC) treated water (Sigma). RNA samples were stored at -80 °C.

2.6.2 Agarose Gel Electrophoresis

Agarose gel electrophoresis was used to assess the quality of RNA extracted in 2.6.1 and also to assess primer specificity (2.6.6). To produce a 1.5% gel; 1.5 g of agarose (Invitrogen, Paisley, UK) was dissolved in 100 ml of 0.5X tris-borate EDTA buffer (TBE) (Sigma) in double distilled water. 10 µl of 10 mg/ml ethidium bromide (Sigma) was added so that fragments could be visualised under ultra violet (UV) light. The gel was poured into a casting tray, which was fitted with well-forming combs and left to polymerise for 45 minutes. Once cooled, approximately 900 ml 0.5X TBE was added to the gel tank, ensuring the gel was well covered and the well-forming combs were removed. 5 µl RNA was mixed with 5 µl RNAse-free water and 2 µl of 6X DNA loading dye (30% glycerol, 0.05% bromophenol blue and 0.05% xylene cyanol) and loaded into a well. 5 µl of hyperladder IV DNA size marker (Bioline) was loaded into one well per gel so that the sizes of the RNA products could be determined. Following electrophoresis at 100 mV for 1.5 hours, the gel was visualised under UV light. A digital image was taken using the geneflash syngene bioimaging system (Syngene, Cambridge, UK). The prominence of 18S and 28S ribosomal RNA (18S rNA and 28S rRNA) bands

and lack of lower molecular weight smears indicated the quality (and yield) of RNA (see Appendix 4).

2.6.3 RNA Analysis using a Nanodrop

A precise estimation of the concentration and purity of the RNA extracted in 2.6.1 was made using a NanoDrop micro-volume spectrophotometer (Thermo Scientific, Loughborough, UK). The concentration was determined by measuring UV light absorbance at 260 nm of 1.5 µl of undiluted RNA. The ratio of absorbance at 260 nm v 280 nm was used to assess the purity of RNA with respect to protein contamination, since proteins absorb maximally at 280 nm. A ratio of 2.0 indicated high purity (for full Nanodrop results for each sample see Appendix 5).

2.6.4 First-Strand cDNA Synthesis

Based on the concentration determined in 2.6.3, 1 µg of total RNA was used for first strand cDNA synthesis in a 21 µl reaction; RNAse free water was added to 1 µg RNA to make a final volume of 12 µl. Following the addition of 1 µl oligo dT primer (Invitrogen) the samples were incubated at 70°C for 10 minutes. The samples were then snap cooled on ice to aid binding of the primer. A reaction mix consisting of 4µl of 5X buffer, 2 µl of dithiothreitol (DTT) and 1 µl of deoxynucleotide triphosphates (dNTPs) (Invitrogen) were added per RNA sample and incubated at 42°C for two minutes. 1µl of Superscript II Reverse Transcriptase (Invitrogen) was then added and the reaction mix incubated for a further 50 minutes at 42°C. The reaction was then inhibited by heating the mixtures to 70°C for 15 minutes. Each cDNA sample was stored at -80°C. For a control RNA sample prepared from both rat and mouse muscle tissue, a parallel reaction was performed which contained all the reaction components except the reverse transcriptase enzyme (RT-). Consequently the mRNA is not reverse transcribed into cDNA. These RT- samples were used as negative controls to confirm amplicons for each primer pair were derived from cDNA.

2.6.5 Design of Primers for Polymerase Chain Reaction (PCR)

Forward and reverse primers were designed to amplify the genes detailed in tables 1 and 2. Primers were designed using reference mRNA sequences for *Mus musculus* and *Rattus norvegicus*, which were available through the National Centre for Biotechnology Information (NCBI) database. Forward and reverse primers were designed to anneal to separate exons so that any amplification of contaminating genomic DNA could be distinguished from amplification of cDNA. All primers were 20 or 21bp in length, to ensure adequate specificity. Where possible the GC content of primers was 50-55%. Amplicons were designed to range from 112-297bp in length to ensure optimum amplification of the products during the PCR reaction. The software programme 'netprimer' (www.premierbiosoft.com/netprimer) was used to predict the efficiency of the primers. This estimated the probability of secondary structure formation produced by the inter-molecular on intra-molecular interactions such as self-priming and the formation of primer dimers or hairpins. Primers were synthesised by Invitrogen and resuspended as a 100 μM stock in Sigma-Water (Sigma).

Gene Name	Entrez Gene ID	Accession Number	Primer Sequence	Primer Length	Optimum Annealing Temperature	PCR Product Length
Rn18s	19791	NR_003278.1	F: 5' - TTGACGGAAGGGCACCACCAG - 3'	21	61	118
			R: 5' - GCACCACCACCCACGGAATCG - 3'	21		
Polr2a	20020	NM_009089.2	F: 5' - TAATGCAGAGAAGCTGGTCC - 3'	20	61	197
			R: 5' - TGTCTGTCTGAGGTAAGTGC - 3'	20		
G6pc3	68401	NM_175935.3	F: 5' - TACCTTCCTATTGGCAGTCG - 3'	20	61	161
			R: 5' - CCAGAGCAGTCAACCCATAA - 3'	20		
Pdk4	27273	NM_013743.2	F: 5' - GGATTACTGACCGCCTCTTT - 3'	20	61	188
			R: 5' - GTAGATGATAGCGTCTGTCC - 3'	20		
Lpl	16956	NM_008509.2	F: 5' - GCTCTCAGATGCCCTACAAA - 3'	20	61	248
			R: 5' - GAAGTAGGAGTCGCTTATCC - 3'	20		
Bcl2l11	12125	NM_207680.2	F: 5' - CAACACAAACCCCAAGTCCT - 3'	20	61	260
			R: 5' - CCTTCTCCATACCAGACGGA - 3'	20		
Tgfb2	21808	NM_009367.3	F: 5' - AAAAGCGAAGAGCTCGAGGC - 3'	20	61	127
			R: 5' - TTAGCAGGAGATGTGGGGTC - 3'	20		
Sod2	20656	NM_013671.3	F: 5' - CCGAGGAGAAGTACCACGAG - 3'	20	61	174
			R: 5' - GCTTGATAGCCTCCAGCAAC - 3'	20		
Ccnd2	12444	NM_009829.3	F: 5' - TTACCTGGACCGTTTCTTGG - 3'	20	61	240
			R: 5' - TGCTCAATGAAGTCGTGAGG - 3'	20		
Ccnb1	268697	NM_172301.3	F: 5' - GCTTCCTGTTATGCAGCACC - 3'	20	61	220
			R: 5' - ATGGTGCCAACTGCATCTGC - 3'	20		
Plk1	18817	NM_011121.3	F: 5' - GTGATGGCACGGAGTCCTAT - 3'	20	61	270
			R: 5' - GGGGGCACAGGATAAGTTTG - 3'	20		
Cdkn1b	12576	NM_009875.4	F: 5' - GGGTCTCAGGCAAACTCTGA - 3'	20	61	238
			R: 5' - TTTACGTATGGCGTCGAAGG - 3'	20		
Trim63	433766	NM_001039048.2	F: 5' - AGAAGAAGAGCGAGCTGCTGC - 3'	21	61	212
			R: 5' - GCCCTTGGAGGCTTCTACAAT - 3'	21		
Fbxo32	67731	NM_026346.2	F: 5' - ATCATGCAGAGGCTGAGTGACG - 3'	22	61	154
			R: 5' - CAGACAAGATCAAACGCTTGCG - 3'	22		
Myog	17928	NM_031189.2	F: 5' - GCCATCCAGTACATTGAGCG - 3'	20	61	267
			R: 5' - CATATCCTCCACCGTGATGC - 3'	20		
Stat3	20848	NM_213660.2	F: 5' - GCGAGAGCAGCAAAGAAGGA - 3'	20	61	193
			R: 5' - GGGTAGAGGTAGACAAGTGG - 3'	20		
Hdac4	208727	NM_207225.1	F: 5' - GCAGCCAAACTTCTCCAGCA - 3'	20	61	227
			R: 5' - CCCGTGAAAGCCATGTTGAC - 3'	20		
Hdac5	15184	NM_010412.3	F: 5' - CCAGCAAGCATTCTACAACG - 3'	20	61	231
			R: 5' - GGTGAGAACTCCTGGGCAAT - 3'	20		
Mitr	79221	NM_024124	F: 5' - GCGGTCCAGGTTAAAACAGA - 3'	20	61	203
			R: 5' - GAGCTGAAGCCTCATTTTCG - 3'	20		
Dach2	93837	NM_033605.2	F: 5' - CGTATCCAGGAGAAGCAGAT - 3'	20	61	248
			R: 5' - CCACTGTCACCAGATGTAGC - 3'	20		
Chrna1	11435	NM_007389.4	F: 5' - CGTCATCAACACACACCACC - 3'	20	61	270
			R: 5' - TCTGCAATGTACTTCACGCC - 3'	20		
Socs3	12702	NM_007707.3	F: 5' - GGAGATTTCGCTTCGGGACT - 3'	20	61	200
			R: 5' - CTCGCTTTTGGAGCTGAAGG - 3'	20		
Foxo1	56458	NM_019739.3	F: 5' - GCTATGGTAGGATGGGTGTC - 3'	20	61	297
			R: 5' - GGGTGAAGGGCATCTTTGGA - 3'	20		

Table 1 Primers for Real-Time RT-PCR (*Mus musculus*)

Rn18s; 18S ribosomal RNA, Polr2a; polymerase (RNA) II (DNA directed) polypeptide A, G6pc3; glucose 6 phosphatase catalytic 3, Pdk4; pyruvate dehydrogenase kinase isoenzyme 4, Lpl; lipoprotein lipase, Bcl2l11; BCL2-like 11 (apoptosis facilitator), Tgfb2; transforming growth factor beta 2, Sod2; superoxide dismutase 2 mitochondrial, Ccnd2; cyclin D2, Ccnb1; cyclin B1, Plk1; polo-like kinase 1, Cdkn1b; cyclin-dependent kinase inhibitor 1B, Trim63; tripartite motif-containing 63, Fbxo32; F-box protein 32, Myog; myogenin, Stat3; signal transducer and activator of transcription 3, Hdac4; histone deacetylase 4, Hdac5; histone deacetylase 5, Mitr; a histone deacetylase 9 splice variant, Dach2; dachshund 2, Chrna1; nicotinic cholinergic receptor nicotinic (alpha polypeptide 1), Socs3; suppressor of cytokine signaling 3, Foxo1; forkhead box O1.

Gene Name	Entrez Gene ID	Accession Number	Primer Sequence		Primer Length	Optimum Annealing Temperature	PCR Product Length
Rn18s	24723	X01117	F:	5' - TTGACGGAAGGGCACCACCAG - 3'	21	61	131
			R:	5' - GCACCACCACCCACGGAATCG - 3'	21		
Polr2a	363633	XM_001079162.1	F:	5' - CCGGAAGCTTACCATGGAAC - 3'	20	61	278
			R:	5' - TGTCTGTCTGAGGTAAGTGC - 3'	20		
G6pc3	303565	NM_176077.3	F:	5' - GCACCTTCCTATTGGCAGTC - 3'	20	61	200
			R:	5' - GAGCGTCCAATACATGAGGC - 3'	20		
Pdk4	89813	NM_053551.1	F:	5' - GGATTACTGACCGCCTCTTT - 3'	20	61	188
			R:	5' - GTAGATGATGGCATCTGTCC - 3'	20		
Lpl	24539	NM_012598.2	F:	5' - GCTCTCAGATGCCCTACAAA - 3'	20	61	248
			R:	5' - GAAGTAGGAGTCGTTCTTCC - 3'	20		
Bcl2l11	64547	NM_171988.1	F:	5' - CAACACAAACCCCAAGTCCT - 3'	20	61	192
			R:	5' - CCTCTCGGTAATCGTTTGCA - 3'	20		
Tgfb2	81809	NM_031131.1	F:	5' - GCTTTGGATGCCGCCTATTG - 3'	20	61	259
			R:	5' - TCAGTGGTTCCAGATCCTGG - 3'	20		
Sod2	24787	NM_017051.2	F:	5' - CCGAGGAGAAGTACCACGAG - 3'	20	61	174
			R:	5' - GCTTGATAGCCTCCAGCAAC - 3'	20		
Ccnd2	64033	NM_022267.1	F:	5' - TTACCTGGACCGTTTCTTGG - 3'	20	61	240
			R:	5' - TGCTCAATGAAGTCGTGAGG - 3'	20		
Ccnb1	25203	NM_171991.2	F:	5' - GCTTCCTGTGATGCAGCACC - 3'	20	61	216
			R:	5' - ATGGTGCCAACTGCATCTGC - 3'	20		
Plk1	25515	NM_017100.1	F:	5' - CAGTACATAGAGCGTGATGG - 3'	20	61	196
			R:	5' - TGCGGAACCATGTTCGTAGG - 3'	20		
Cdkn1b	83571	NM_031762.3	F:	5' - GGGTCTCAGGCAAACTCTGA - 3'	20	61	238
			R:	5' - TTTACGTCTGGCGTCGAAGG - 3'	20		
Trim63	140939	NM_080903	F:	5' - GGAGGAGTTTACTGAAGAGG - 3'	20	61	180
			R:	5' - GACACACTTCCCTATGGTGC - 3'	20		
Fbxo32	171043	NM_133521	F:	5' - CTTGTCTGACAAAGGGCAGC - 3'	20	61	184
			R:	5' - TGAAAGTGAGACGGAGCAGC - 3'	20		
Myog	29148	NM_017115.2	F:	5' - GCCATCCAGTACATTGAGCG - 3'	20	61	267
			R:	5' - CATATCCTCCACCGTGATGC - 3'	20		
Stat3	25125	NM_012747.2	F:	5' - AGTGAGAGCAGCAAGGAAGG - 3'	20	61	214
			R:	5' - CCTCCTCCTTGGGAATGTCA - 3'	20		
Hdac4	363287	XM_343629.4	F:	5' - GCAGCCAAACTTCTCCAGCA - 3'	20	61	212
			R:	5' - TTGACATTGAAACCCACGCC - 3'	20		
Hdac5	84580	NM_053450.1	F:	5' - GGTACAACGTAAATGTGGCG - 3'	20	61	112
			R:	5' - GGTGAGAACTCGTGGGCAAT - 3'	20		
Mitr	500642	XM_002729640.1	F:	5' - GCGGTCCAGGTTAAAACAGA - 3'	20	61	203
			R:	5' - GAACTGAAGCCTCGTTTTCG - 3'	20		
Dach2	302333	XM_228458.5	F:	5' - CGCATCCAGGAGAAGCAGAT - 3'	20	61	247
			R:	5' - CGCTGTCACCAGATGTAGCT - 3'	20		
Chrna1	79557	NM_024485.1	F:	5' - TGTCATCAACACACACCACC - 3'	20	61	269
			R:	5' - CTGCAATGTACTTCACACCC - 3'	20		
Socs3	89829	NM_053565.1	F:	5' - CCGACGGAACCTTCCTTTGA - 3'	20	61	202
			R:	5' - CTTTCTCATAGGAGTCCAGG - 3'	20		

Table 2 Primers for Real-Time RT-PCR (*Rattus norvegicus*)

Rn18s; 18S ribosomal RNA, Polr2a; polymerase (RNA) II (DNA directed) polypeptide A, G6pc3; glucose 6 phosphatase catalytic 3, Pdk4; pyruvate dehydrogenase kinase isoenzyme 4, Lpl; lipoprotein lipase, Bcl2l11; BCL2-like 11 (apoptosis facilitator), Tgfb2; transforming growth factor beta 2, Sod2; superoxide dismutase 2 mitochondrial, Ccnd2; cyclin D2, Ccnb1; cyclin B1, Plk1; polo-like kinase 1, Cdkn1b; cyclin-dependent kinase inhibitor 1B, Trim63; tripartite motif-containing 63, Fbxo32; F-box protein 32, Myog; myogenin, Stat3; signal transducer and activator of transcription 3, Hdac4; histone deacetylase 4, Hdac5; histone deacetylase 5, Mitr; a histone deacetylase 9 splice variant, Dach2; dachshund 2, Chrna1; nicotinic cholinergic receptor nicotinic (alpha polypeptide 1), Socs3; suppressor of cytokine signaling 3.

2.6.6 End-Point PCR & Agarose Gel Electrophoresis to Test Primer Specificity

Primer specificity was assessed using cDNA extracted from control TA muscle and cultured myotubes treated with normal media, using end-point RT-PCR with HotStar Taq Master Mix (Qiagen, Crawley, UK). The reaction for each primer pair was made up of 3 µl cDNA, 15 µl Hotstar Taq Master Mix, 1.5 µl each of 20 µM forward and reverse primers and 9 µl RNAse-free water totalling 30 µl. A negative control was performed in parallel using RT- control samples for each primer pair. End-point PCR reactions were set up in 0.5 ml microcentrifuge tubes and performed using a Px2 thermocycler (Thermo). The efficacy of primer sets at temperatures ranging from 55-65°C was assessed using a gradient annealing temperature programme to find an optimum annealing temperature (shown in tables 1 and 2). The standard PCR cycle used for all primer pairs is indicated in table 3 below.

Temperature (°C)	Time of Stage	Action	Number of Cycles
95	10 Minutes	Hotstart	1
94	30 Seconds	Denaturation	40
55-65	30 Seconds	Annealing	
72	1 Minute	Extension	
72	10 Minutes	Polishing	1

Table 3 Standard End-Point PCR Cycle

Agarose gel electrophoresis was used to assess the specificity of each primer set. A 2% gel was produced as outlined in 2.6.2, using 2 g of agarose instead of 1.5 g. 10 µl of the PCR reaction was mixed with 2 µl of 6X DNA loading dye (30% glycerol, 0.05% bromophenol blue and 0.05% xylene cyanol) and loaded into a well. 5 µl of hyperladder IV DNA size marker (Bioline) was loaded into one well per gel so that the sizes of the PCR amplicons could be determined. Following electrophoresis at 100 mV for 1.5 hours, the gel was visualised under UV light. A digital image was taken using the geneflash syngene bioimaging system (Syngene). The prominence of a clear band at the expected size indicated that the primer set worked efficiently at that temperature. All primer sets had an optimum annealing temperature of 61°C.

2.6.7 DNA Sequencing of PCR Amplicons

All sequencing was performed by Eurofins MWG Operon on 20 ng unpurified PCR product produced in 2.6.6 using the cycle sequencing technology (dideoxy chain termination / cycle sequencing) on ABI 3730XL sequencing machines. Analysis of the returned sequence was performed using the NCBI basic local alignment tool (BLAST) program (www.ncbi.nlm.nih.gov/BLAST) by means of a basic search against a nucleotide database for *Mus musculus* or *Rattus norvegicus*. Sequencing data for primer sets can be found in appendix 6. Due to low concentrations of some of the transcripts, sequencing was not successful for all the targeted transcripts.

2.6.8 Quantitative Reverse Transcription PCR (qRT-PCR)

qRT-PCR was used to quantitatively assess the transcript levels for genes of interest in RNA extracted from cultured myotubes and TA muscle tissue to evaluate changes in mRNA in response to a given treatment. The standard three-step reaction using an iQ5 Thermocycler (BioRad) is outlined in table 4 below.

Temperature (°C)	Time of Stage	Action	Number of Cycles
95	3 Minutes	Hotstart	1
94	30 Seconds	Denaturation	40
61	30 Seconds	Annealing	
72	30 Seconds	Extension	

Table 4 Standard qRT-PCR Cycle

Fluorescence levels were measured after each of the 40 PCR cycles. The reaction contained 3 µl cDNA, 3.96 µl RNAse-free water, 7.5 µl 2X SYBR Green Supermix (BioRad, Hemel Hempstead, UK) and 0.27 µl each of 20 µM forward and reverse primer totalling 15 µl. Reactions were carried out in triplicate on a 96-well plate and a negative control containing no cDNA was run with each primer set to assess the presence of contamination. Analysis was carried out by comparison of the cycle threshold (C_T) values for genes in untreated and treated samples. The C_T refers to the

cycle at which the fluorescence generated within the reaction exceeds a defined threshold and is thus related to the amount of starting template. The combined mean amplification of the Rn18s and Polr2a reference genes was used as a reference against which all data for genes of interest was normalised. These genes were chosen as a result of unpublished data by Dr Lauren Fisher, The University of Liverpool, showing that neither reference genes significantly change with electrical stimulation in muscle (Fisher, 2010). A melt curve analysis of the amplicons at every 1° for 36 cycles was used to look for primer dimer formation and amplification of other non-specific double-stranded products, as SYBR green binds non-specifically to all double stranded products. The relative expression for genes of interest was determined by the $2^{-\Delta CT}$ method, where differences between the mean reference gene C_T value and the target gene C_T value in each sample was quantified individually. Further analysis was by the $2^{-\Delta\Delta CT}$ method, where the expression differences between two samples was represented as a fold-change.

2.6.9 Analysis of The Efficiency of the qRT-PCR Assay

The need for efficiency analysis of a SYBR green based qRT-PCR assay is related to the fact that real-time quantification is based on the relationship between the starting template amount and the C_T value obtained during amplification. Three-step qRT-PCR reactions were performed as outlined in 2.6.8. Standard curves for all primer sets were generated using a 2-fold serial dilution of a control template cDNA with dilution factor plotted against the mean C_T value obtained during amplification. The standard curves for each primer set can be found in appendix 7. These curves were then used to assess the efficiency of amplification. Amplification efficiency (E) was calculated from the gradient of the standard curve using the following formula:

$$E = 2^{-1/slope}$$

in order to express amplification efficiency as a percentage the following equation was used:

$$\%E = (E-1) \times 100$$

An amplification efficiency of 90-105% indicated a robust, reproducible assay. The R^2 value, which is a statistical measure of how well a regression line approximates real data points, was used to assess confidence of the amplification efficiency calculated

from the gradient of the standard curve. An R^2 value of 1.0 indicates a perfect fit, values of over 0.95 were deemed acceptable.

2.7 Microarray Analysis

Microarray analysis was used to compare genome-wide transcript changes following 3, 7 and 14 days of nerve blockade, in addition to 14 days of nerve block with 7 days of recovery, or 7 days electrical stimulation at 20Hz. Using the GeneChip® Rat Genome 230 2.0 Array (Affymetrix, High Wycombe, UK) over 30,000 transcripts and variants from over 28,000 well-substantiated rat genes were measured. Frozen muscle samples, detailed in 2.7.1, harvested by methods outlined in 2.4.1, were sent as part of our collaboration with Pfizer Inc. to AROS Applied Biotechnology (Aarhus, Denmark) who carried out all RNA extraction, cDNA synthesis, chip hybridisation and fluorescence measurements. The data, in CEL file format was returned for subsequent analysis.

2.7.1 Details of Samples Subject to Microarray Analysis

Frozen muscle tissue samples were sent to AROS Applied Biotechnology for processing as detailed in table 5 below.

Animal Number	Sample Treatment	AROS Chip ID
1651	Untreated Contralateral Control	A958-02*
1656	Untreated Contralateral Control	A958-05*
1660	Untreated Contralateral Control	A958-07*
1661	Untreated Contralateral Control	A958-08*
1721	Sham Control Treated	A1236_06
1722	Sham Control Treated	A1236_08
1753	Sham Control Treated	A1236_11
1724	Sham Control Treated	A1236_20
1747	3 Days Atrophy	A1236_04
1745	3 Days Atrophy	A1236_13
1750	3 Days Atrophy	A1236_16
1746	3 Days Atrophy	A1236_19
1689	7 Days Atrophy	A1236_15
1688	7 Days Atrophy	A1236_17
1651	7 Days Atrophy	A958-01
1656	7 Days Atrophy	A958-06
1678	14 Days Atrophy	A1236_10
1677	14 Days Atrophy	A1236_14
1660	14 Days Atrophy	A958-03
1661	14 Days Atrophy	A958-04
1768	14 Days Atrophy with 7 Days Recovery	A1236_01
1770	14 Days Atrophy with 7 Days Recovery	A1236_03
1769	14 Days Atrophy with 7 Days Recovery	A1236_07
1772	14 Days Atrophy with 7 Days Recovery	A1236_18
1760	20Hz Electrical Stimulation 7 Days	A1236_02
1761	20Hz Electrical Stimulation 7 Days	A1236_05
1759	20Hz Electrical Stimulation 7 Days	A1236_09
1763	20Hz Electrical Stimulation 7 Days	A1236_12

Table 5 Details of Samples Subject to Microarray Analysis

Pilot study (Chip IDs beginning with A958) chips consisted of the untreated contralateral control TA muscle samples (A1236-02,05,07,08) and the treated samples (A1236-01,06,03,04). The untreated control samples (marked with *) were only included in the quality control stages of the microarray analysis and were excluded from subsequent analysis. Chips beginning with A1236 represent TA samples from the treated limbs of the animals indicated by number.

Untreated and treated muscle samples from a pilot study of four animals, two having the nerve bock in place for 7 days and two for 14 days, was initially sent for processing. These samples are indicated with the AROS Chip ID beginning with A958. The data was stored and analysed with the main study indicated by AROS Chip ID beginning with A1236. In the main study the treated muscle samples from each animal was analysed. The experimental groups included in the main study included a sham operated control group as well as animals treated with 3, 7 and 14 days of of nerve blockade, in addition to 14 days of nerve block with 7 days of recovery, or 7 days electrical stimulation at 20Hz. The untreated control samples from the pilot study (marked with *) were only included in the quality control stages of the microarray analysis and were excluded from subsequent analysis.

2.7.2 Details of Statistical and Bioinformatics Programmes Used in Microarray Analysis

All Statistical analysis of microarray data was carried out using the software R: A Language and Environment for Statistical Computing. version 2.13.1 (©2011, www.R-project.org). This is an open source programme developed by the R Development Core Team at the R Foundation for Statistical Computing, Vienna. Packages utilised within R included the Bioconductor project (Gentleman et al., 2004), which provides tools for the analysis and comprehension of high-throughput genomic data by using the R statistical programming language, and is open source and open development. These tools included: *affy* (Gautier et al., 2004); an extensible, interactive environment for data analysis and exploration of Affymetrix oligonucleotide array probe level data. *Limma* (Smyth, 2004); is a package for the analysis of gene expression microarray data, especially the use of linear models for analysing designed experiments and the assessment of differential expression. GOstats (Falcon and Gentleman, 2007) ; has extensive facilities for testing the association of Gene Ontology (GO) (Ashburner et al., 2000) terms to genes in a gene list.

Training for use of all statistical and bioinformatics software was undertaken under the supervision of Alex Gutteridge through the collaboration with Pfizer Inc.

Chapter 3: Comparison of Transcriptional Changes in Foxo1 Target Genes in *In Vitro*(C2C12 Myotube Culture) and *In Vivo* (20Hz Electrical Stimulation) Models of Atrophy

3.1 Introduction

Muscle atrophy is characterised by a loss of muscle weight and volume that involves a reduction in muscle fibre diameter in the absence of degenerative changes and/or a reduction in the actual number of fibres by apoptosis or necrosis (Glass, 2010). Atrophy of individual fibres may be due to either a reduction in protein synthesis, enhanced proteolysis, or both (Glass, 2010). A greater understanding of the molecular mechanisms that govern muscle atrophy is required in order to direct research towards a therapeutic target.

Increased ubiquitin-proteasome dependent proteolysis plays a key role on the control of muscle mass (Eddins et al., 2011, Sandri et al., 2004, Stitt et al., 2004). Myotube cell culture models of atrophy have shown that important atrophy-related ubiquitin ligases, Fbxo32 & Trim63, are induced following treatment with the corticosteroid Dexamethasone (Dex) (Sandri et al., 2004, Stitt et al., 2004) and during calorific restriction (Sandri et al., 2004), and that their expression is controlled by transcription factors of the foxo family (Sandri et al., 2004, Stitt et al., 2004). Foxo1, in particular has been implicated to have a central role in the control of muscle mass (Kamei et al., 2003).

There are currently numerous experimental models used to investigate muscle atrophy both *in vitro* and *in vivo*. To date, comparisons between these models in terms of the data produced have not been made, to determine whether it is viable to use different methods interchangeably. In order to compare the modes of action of different models of atrophy the transcriptional changes of known targets of Foxo1 transcription factors, identified from the literature (3.4.1), were measured following atrophy-inducing treatments (3.4). The models of atrophy to be compared included incubation of myotube cell cultures for 24 hours with media lacking glucose (calorific restriction) or media treated with Dex (3.2). These models would also be compared to the *in vivo* functional atrophy model involving the use of a miniature neuromuscular stimulator to impose artificially increased levels of activity on the rat *Tibialis anterior* muscle (3.3). The aim of this chapter is to compare and contrast these models and to better understand the similarities or differences in the molecular mechanisms underlying the atrophy produced. Thus the questions to be addressed here are to determine whether Foxo target genes other than the E3 ligases are induced during atrophy, and to compare the transcriptional responses of Foxo1 target genes, and other key genes linked with atrophy, to look for common or divergent models of atrophy.

3.2 Induction and Assessment of *In Vitro* Atrophy

C2C12 mouse myoblasts were cultured to induce myotube formation as outlined in 2.1.1. Myotubes were subject to three experimental conditions, replacing the culture media with either DMEM supplemented with 2% HS (Normal Media Control), glucose-free DMEM supplemented with 2% HS (Glucose Free Media) or DMEM supplemented with 2% HS and 1μM Dex (Dex Treated Media). Six plates were included in each group and incubated for 24 hours at 37°C, 5% CO_2.

The myotubes were visually assessed (3.2.1), the degree of atrophy determined by measuring changes in myotube cross sectional area (3.2.2) and RNA extracted to assess expression of foxo1 target genes (3.4).

3.2.1 Myotubes Show Little Apoptosis Following Atrophy Induction

Phase contrast microscopy was used to observe myotube cultures before and after treatment to ensure that cultures remained viable. Induction of apoptosis would result in abnormal numbers of free floating cells as well as aggregates of single cells. Figure 11 shows representative photomicrographs of the cell cultures, showing intact myotubes with little evidence of apoptosis at the time of harvest.

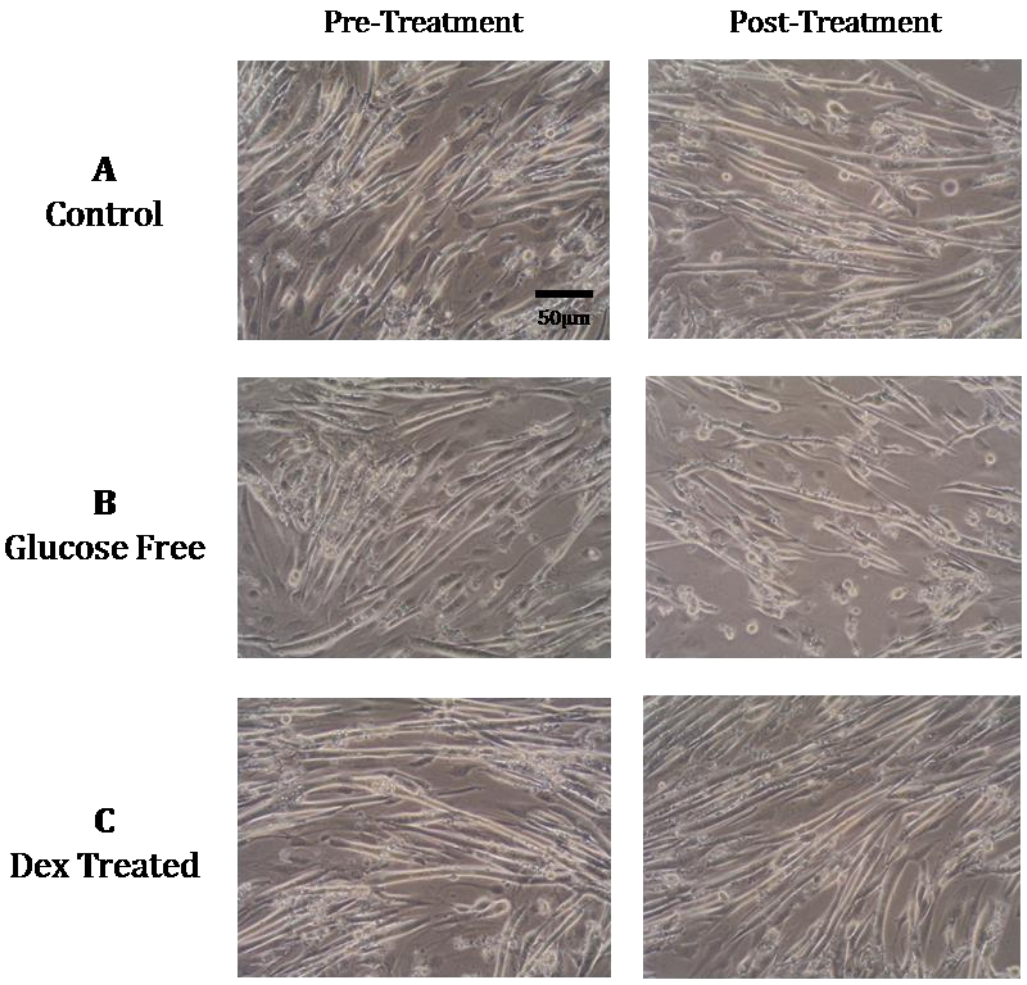

Figure 11 Phase Contrast Microscopy of Cultured C2C12 Myotubes Subject to Atrophic Conditions
Representative photomicrographs of control myotube cultures (A) and cultures before and after treatment with glucose-free media (B) and Dex (C). There was little evidence of apoptosis in all cultures.

3.2.2 Myotubes Cultured in Glucose-Free Media undergo Significant Atrophy

The cross sectional area (CSA) of the cultured C2C12 myotubes were measured before and after atrophic treatments, in order to measure the degree of atrophy produced by each treatment. The full method is provided in section 2.1.3.

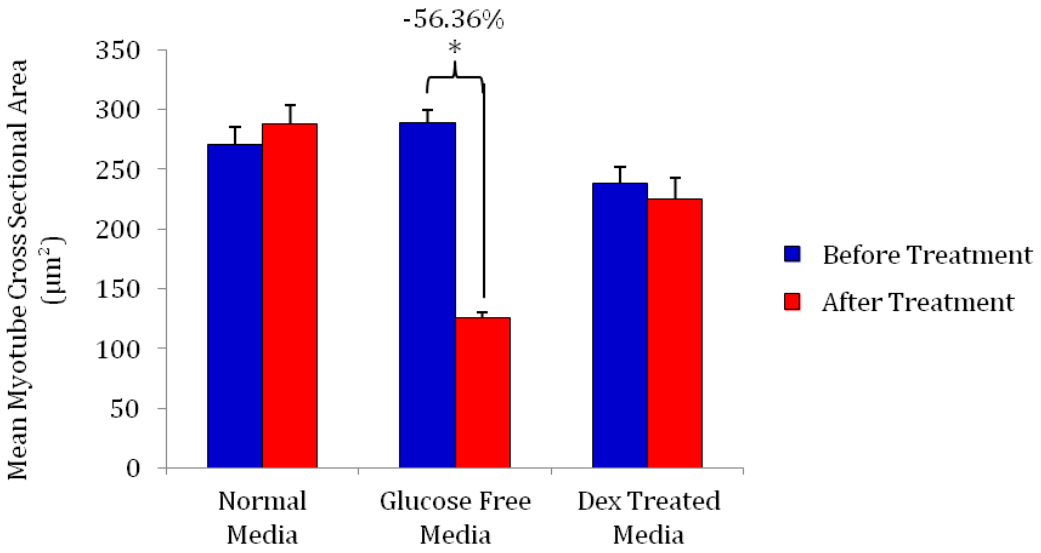

Figure 12 Mean Cross Sectional Area of Cultured Myotubes Decreased Following Treatment With Glucose-Free Media
Treatment of cultured C2C12 myotubes for 24 hours growth in normal media, glucose free media, or media containing 1μM Dex. CSAs were taken from photomicrographs of cells in culture. Glucose starvation resulted in a 56 % decrease in CSA. (n=6, *p<0.000001). Error bars indicate standard error of the mean (SEM).

Growth for 24 hours in glucose-free media produced a 56.36% decrease in mean CSA relative to that before the change of media (Figure 12), which was shown to be statistically significant following a t-test (p<0.000001). No significant change in mean CSA was found in control samples, cultured in normal media or in samples cultured in media containing Dex. The absence of atrophy on treatment with Dex was unexpected and is discussed in detail in 3.5.1.

3.3 Induction and Assessment of *In Vivo* Muscle Atrophy

Miniature neuromuscular stimulators were used to impose 20 Hz continuous electrical stimulation on the rat *Tibilais anterior* muscle for 7 days *in vivo* (n=6). Methods are outlined in 2.2. The degree of atrophy, determined by changes in muscle weight (3.3.2) and fibre CSA (3.3.3), was measured following stimulation. It is recognised in the literature that denervation of muscle due to damage to the motor axons also produces atrophy (Carlson, 2008), and in fact muscle denervation is used as a model of atrophy. In order to assess whether the electrical stimulation of muscle was able to produce atrophy that was not associated with nerve damage, histological analysis of muscle tissue was performed to look for evidence of nerve damage.

3.3.1 Histological Analysis Revealed Little Change in Muscle Tissue Indicative of Nerve Damage

It is possible to ascertain whether a nerve has been damaged through analysis of the fibres in the muscle that it supplies. Histological sections of stimulated and unstimulated, contralateral control muscle tissue were analysed to assess whether changes in muscle fibres were indicative of nerve damage. Frozen sections (10µm) were stained with Haematoxylin and eosin (See 2.5.1), which distinguishes between muscle fibres and nuclei. Any accidental nerve damage leading to denervation of the muscle would appear in the sections as the migration of nuclei from the periphery of the muscle fibres into the interior of the fibre (figure 13, panel C), as areas of small, non-uniformly shaped fibres, or the infiltration of inflammatory cells. Sections from muscles taken from each of the 6 animals, both stimulated and control, were assessed. Very little evidence of nerve damage was observed in any of the histological sections, with most sections containing no denervated fibres, in line with previous findings in rat (Jarvis et al., 1996). Figure 13 shows representative examples of the histological sections of the stimulated and control muscles samples.

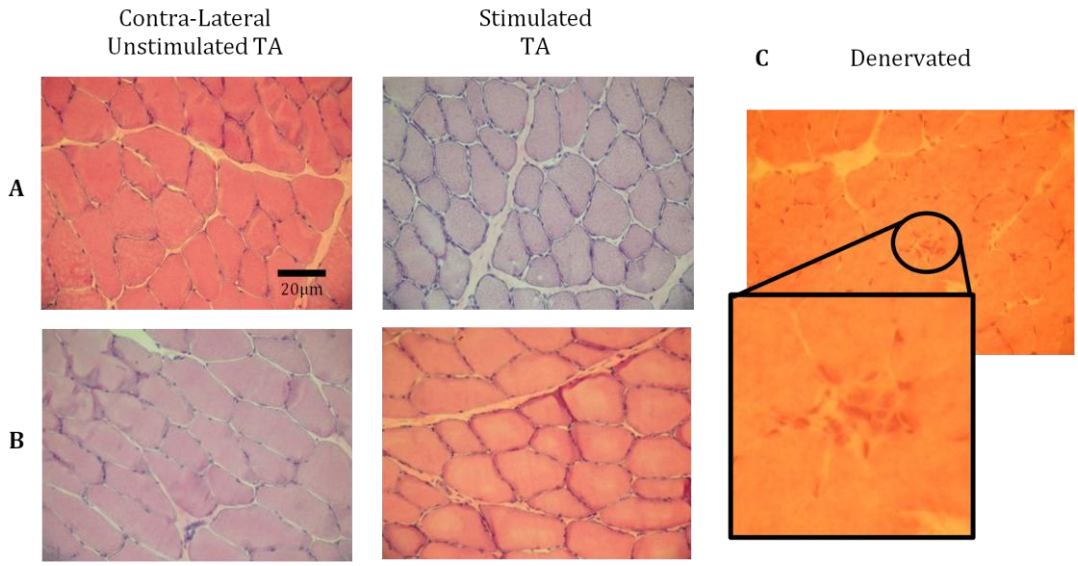

Figure 13 Representative Photomicrographs of Histological Sections of Control and Electrically Stimulated TA Muscle
Haematoxylin and eosin stain on sectioned muscle tissue (10µm) in control muscle and muscle that had electrical stimulation imposed on it for 1 week continuously at a frequency of 20Hz (A, B). An example of a single denervated muscle fibre is shown in panel C where nuclei are seen to infiltrate the fibre. Very few denervated fibres were observed in the experimental sections.

3.3.2 Electrical Stimulation for 1 week at 20Hz Significantly Reduced TA Muscle Weight

In order to assess the level of muscle atrophy produced by continuous electrical stimulation the weights of the control and stimulated TA muscles were measured immediately following harvesting, as outlined in section 2.4.1. Figure 14 shows the mean weight of the TA muscle from the untreated contralateral control limb and the limb that had been continuously electrically stimulated for 7 days, at a frequency of 20 Hz. The muscle weights are expressed as a percentage of the whole animal body weight to normalise the measurements to differing animal sizes. Electrical stimulation produced a 12.64% decrease in muscle weight when compared to the unstimulated contra-lateral control. This was shown to be statistically significant following a paired Ttest (p=0.016).

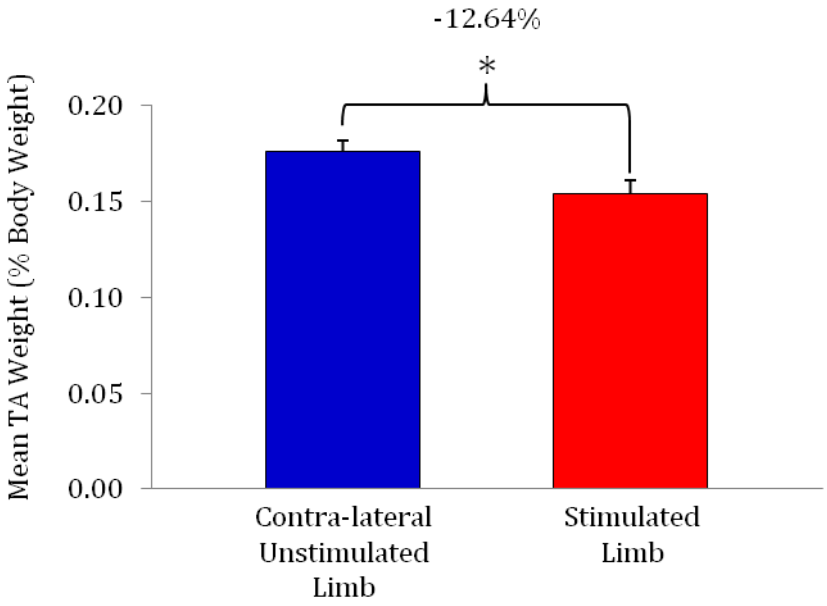

Figure 14 Mean Differences in TA Muscle Weight between The Electrically Stimulated and Unstimulated, Contralateral Control Limb
Muscle weight is expressed as a percentage of whole body weight to normalise measurements to differing animal sizes. Electrical stimulation was imposed at 20Hz continuously for 7 days and produced a significant 12.64% difference in electrically stimulated TA weight when compared to the unstimulated contralateral control. (*n*=6, *=p<0.05 following a paired Ttest). Error bars indicate SEM.

3.3.3 Electrical Stimulation *In Vivo* Decreased The Cross Sectional Area of Muscle Fibres

The CSA of fibres were measured from Haematoxylin and Eosin stained muscle sections as outlined in 2.5.2. Electrical stimulation produced a 17.18% decrease in mean fibre cross sectional area (Figure 15). This decrease was not found to be statistically significant following a paired t-test, with a p value of 0.153. However, when the individual animals are considered, five out of the six animals showed a decrease in fibre CSA ranging from 9 to a 46%. Only one animal showed an increase in fibre CSA (Rat 1759 - 21% increase). This large range in changes in CSA with an outlying result would account for the relatively high standard error and non significance of the result.

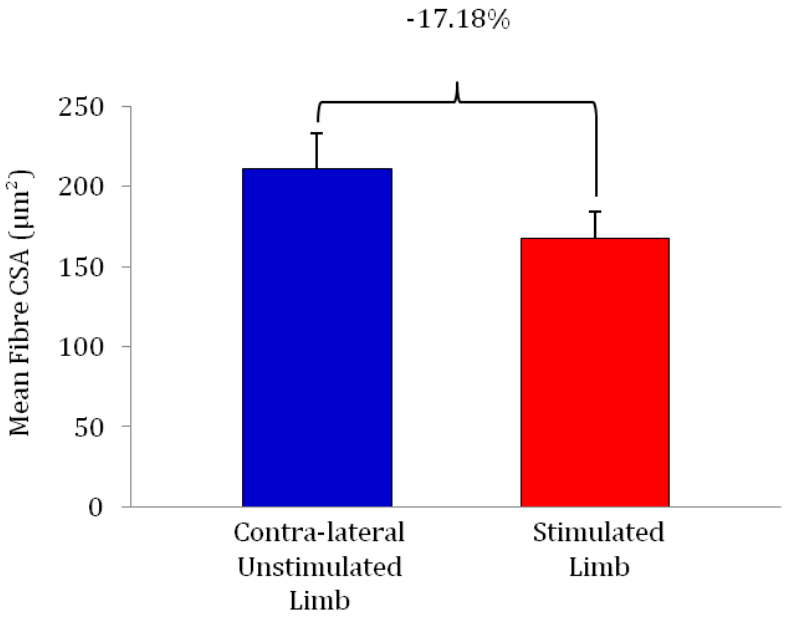

Figure 15 Mean Differences in TA Muscle Fibre CSA Between Electrically Stimulated And Unstimulated Contralateral Control
Fibre CSAs were taken from photomicrographs of Haematoxylin and eosin stained muscle sections (10µm). Electrical stimulation was imposed at 20Hz continuously for 7 days and produced a 17% difference in the mean values in electrically stimulated TA weight compared to the unstimulated contralateral control (*n*=6, p=0.153 following a paired Ttest). Error bars indicate SEM.

3.4 Transcript Changes of Foxo1 Target Genes in *In Vitro* & *In Vivo* Atrophy Models

In order to compare and contrast the molecular mechanisms involved in the *in vitro* and *in vivo* models of muscle atrophy, and to look for similarities or differences in their modes of action, the transcriptional changes of known Foxo1 target genes were measured following treatment *in vitro* and *in vivo* using qRT-PCR.

3.4.1 Identification of Foxo1 Target Genes

Having tested the two *in vitro* and one *in vivo* model of muscle cell atrophy, we wished to compare the transcriptional response of genes that have in common Foxo1 target sequences, knowing from previous literature that Foxo has been implicated as an important modulator in atrophy. A literature search was undertaken to identify Foxo1 target genes that are directly activated by this transcription factor. Ten genes were identified from studies where evidence for activation or direct binding of these genes by the Foxo1 transcription factor was reported. Details of the ten genes, a brief description of their function and the evidence for Foxo1 activation or binding are shown in tables 6, 7 and 8. The ten genes were separated into three biological processes; Metabolic Process (table 6), Programmed Cell Death (table 7) and Regulation of Cell Cycle (table 8). Fbxo32 and Trim63 were also included for analysis, as studies have shown these to be under the control of Foxo1 during muscle atrophy (Stitt et al., 2004).

METABOLIC PROCESS			
Target Gene	**Gene Function**	**Evidence of Activation or Binding**	**Reference**
Glucose-6-phosphatase (G6pc3)	Catalyses the hydrolysis of glucose-6-phosphatase to glucose, which is the terminal step of both gluconeogenesis and glycogen breakdown.	Labelled DNA probe binding Assay.	(Ayala et al., 1999)
Pyruvate dehydrogenase kinase 4 (Pdk4)	Kinase enzyme which acts to inactivate the enzyme pyruvate dehydrogenase, so participates in the regulation of the pyruvate dehydrogenase complex. This complex acts to convert pyruvate into acetyl-coA. and so the downregulation of the complex allows more pyruvate to be available for gluconeogenesis.	Luciferase Reporter Gene Assay	(Furuyama et al., 2003)
Lipoprotein Lipase (Lpl)	Hydrolyzes lipids in lipoproteins, such as those found in very low-density lipoproteins into three free fatty acids and one glycerol molecule.	Up-regulation of expression	(Kamei et al., 2003)

Table 6 Foxo1 Target Genes Involved In Metabolic Processes Included in Analysis

PROGRAMMED CELL DEATH			
Target Gene	**Gene Function**	**Evidence of Activation or Binding**	**Reference**
Bcl-2-interacting mediator of cell-death (Bcl2l11)	Forms hetero- or homodimers and act as anti- or pro-apoptotic regulators that are involved in a wide variety of cellular activities.	Electrophoretic Mobility Shift Assay (EMSA)	(Gilley et al., 2003)
Transforming growth factor β-2 (Tgfb2)	Known to inhibit cell proliferation and induce apoptosis in many cell types.	Transient Reporter Gene Assays	(Samatar et al., 2002)
Manganese superoxide dismutase (Sod2)	Transforms toxic superoxide, a byproduct of mitochondrial electron transport chain, into hydrogen peroxide and diatomic oxygen. This increase in protection from reactive oxygen species antagonizes apoptosis caused by glucose deprivation.	Chromatin Immuno-precipitation (ChIP)	(Adachi et al., 2007)

Table 7 Foxo1 Target Genes Involved In Programmed Cell Death Included in Analysis

REGULATION OF CELL CYCLE			
Target Gene	**Gene Function**	**Evidence of Binding**	**Reference**
Cyclin D2 (Ccnd2)	Forms a complex with and functions as a regulatory subunit of Cdk4 or Cdk6, whose activtiy is required for cell cycle G1/S transition.	Chromatin Immuno-precipitation (ChIP)	(Park et al., 2005)
Cyclin B (Ccnb1)	Cyclin B is a mitotic cyclin. The amount of cyclin B (which binds to Cdk1) and the activity of the cyclin B-Cdk complex rise through the cell cycle until mitosis completes, where they fall abruptly due to degradation.	Chromatin Immuno-precipitation (ChIP)	(Alvarez et al., 2001)
Polo-like Kinase (Plk1)	Plk1 modulates the ubiquitination of cyclin B, targeting it for degradation without affecting prior ubiquitination of anaphase inhibitors.	Chromatin Immuno-precipitation (ChIP)	(Alvarez et al., 2001)
Cyclin-dependent kinase inhibitor 1B (Cdkn1b)	p27Kip1 is a cdk inhibitor that associates with G1 cyclin/cdk complexes and inhibits their enzymatic activity leading to an arrest in the G1 phase of the cell cycle.	Chromatin Immuno-precipitation (ChIP)	(Adachi et al., 2007)

Table 8 Foxo1 Target Genes Involved In Regulation of The Cell Cycle Included in Analysis

3.4.2 End Point RT-PCR Validation of Primer Sets for Foxo1 Target Genes

Forward and reverse primers were designed for the selected Foxo1 target genes to enable analysis of mRNA transcripts by end-point RT-PCR and qRT-PCR in murine C2C12 myotubes and rat muscle. All primer pairs were tested using a gradient annealing temperature programme to find the optimum annealing temperature for each individual primer pair (data not shown). RT-PCR followed by 2% agarose gel electrophoresis (outlined in 2.6.6) confirmed that all primer pairs amplified a PCR product of the correct size at an annealing temperature of 61 °C (figure 16 A). An RT-template was tested with each primer pair and confirmed no amplification from genomic DNA by the primer sets (figure 16 B).

All PCR products were sequenced (method outlined in 2.6.7). The resulting sequences were subject to a BLAST search, which showed that the sequence derived for each PCR

product was specific to their target gene, further confirming primer specificity (sequencing data is compiled in appendix 6).

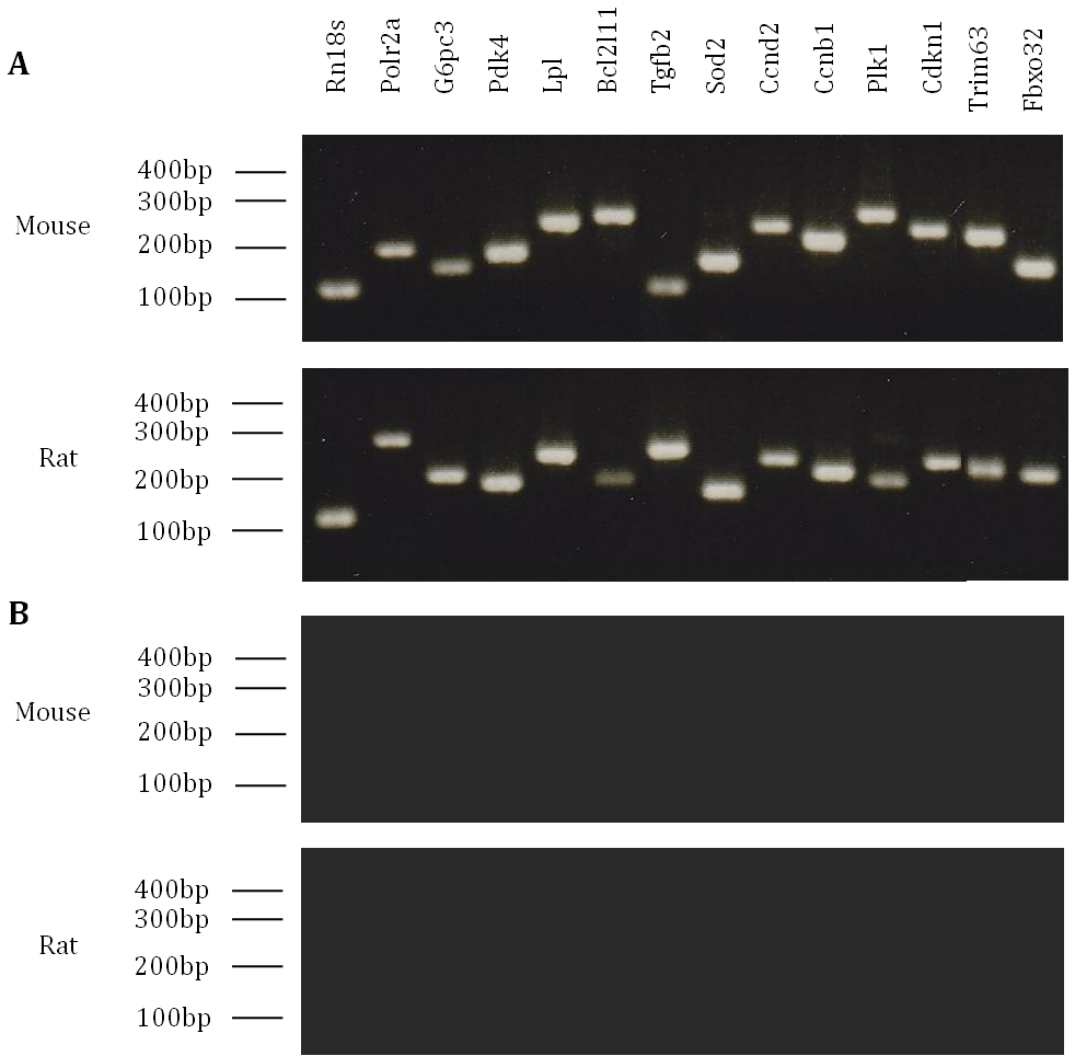

Figure 16 Specificity of Primer Sets for Foxo1 Target Genes
End-point RT-PCR Followed by 2% agarose gel electrophoresis shows single bands of the correct size for each of the primer pairs in mouse and rat (A). An RT- template was tested with each primer set to look for amplification of genomic DNA (B) and was negative in each case. A molecular weight hyperladder was run on each gel, whose band positions for 100-400 base pairs (bp) are shown.

3.4.3 Determination of Primer Efficiency in qRT-PCR

The amplification efficiency of all primer sets for Foxo1 target genes was assessed using qRT-PCR. As quantification is based on the relationship between the initial amount of template and the cycle threshold (C_t) value obtained during amplification, two criteria must be met to allow accurate and reproducible quantification of transcripts. Firstly, the amplification efficiency of the primer pairs must be determined to ensure that the template doubles with each cycle of the reaction, which is vital for the accurate analyses of the data. Secondly, amplification of a single product and not of any contaminating products or the formation of primer dimers was determined using a melt curve analysis since SYBR green binds non-specifically to double stranded DNA. 2-fold serial dilutions of a cDNA template were used to generate standard curves (method outlined in 2.6.9). Using the equation of the linear regression line, together with the coefficient of determination (R^2) the efficiency of the primers was calculated. The standard curves generated for each of the primer pairs can be found in appendix 7. The efficiency of all the primer sets was between 90 and 110%, as recommended for use in qRT-PCR by BioRad. The calculated efficiency for each primer set is shown in table 9.

Primer dimer formation or co-amplification of non-specific products was assessed by melt-curve analysis, where these would appear as additional peaks. Melt curve analysis showed no evidence of non-specific amplification by any of the primer sets. Melt curves for each of the primer sets can be found in appendix 8.

Primer Name	Efficiency %	Primer Name	Efficiency %
Mouse Rn18s	93.70	Rat Rn18s	92.22
Mouse Polr2a	102.62	Rat Polr2a	101.63
Mouse G6pc3	97.44	Rat G6pc3	103.31
Mouse Pdk4	99.88	Rat Pdk4	101.46
Mouse Lpl	99.12	Rat Lpl	103.10
Mouse Bcl2l11	103.65	Rat Bcl2l11	90.33
Mouse Tgfb2	97.48	Rat Tgfb2	102.14
Mouse Sod2	93.02	Rat Sod2	92.82
Mouse Ccnd2	104.88	Rat Ccnd2	104.09
Mouse Ccnb1	97.64	Rat Ccnb1	97.79
Mouse Plk1	102.17	Rat Plk1	104.58
Mouse Cdkn1b	98.81	Rat Cdkn1b	103.85
Mouse Trim63	94.12	Rat Trim63	98.44
Mouse Fbxo32	102.41	Rat Fbxo32	105.29

Table 9 Efficiency of Amplification During qRT-PCR for Foxo Target Gene Pairs
2-fold serial dilutions of a template cDNA (from control, untreated tissue) were used to generate a standard curve for each primer set. Amplification efficiency was calculated from the gradient of the linear regression line of these curves. For subsequent analysis an optimum efficiency of between 90 and 105% was required, and achieved for all primer pairs.

3.4.4 Changes in Transcript Levels of Foxo1 Target Genes with Atrophy

In order to compare the glucose starvation *in vitro* and functional atrophy *in vivo* models of atrophy, qRT-PCR was used to measure the transcript levels of Foxo1 target genes before and after treatment. The patterns of change in these transcripts would

give insight into whether the different methods of producing atrophy shared similar modes of action. Foxo1 target genes were chosen as this transcription factor has been shown to play a central role in skeletal muscle atrophy. Figure 17 shows the changes in transcript levels for each of the target genes following each atrophy inducing treatment. Relative transcript abundance was calculated using the $2^{-\Delta\Delta CT}$ method. The mean amplification of Rn18s and Polr2a was used as a reference against which all the results were normalised. Differences between the mean C_T value of the two reference genes and the target gene C_T value was quantified in each sample. The difference between two samples was then calculated as a fold-change. Genes were grouped according to their biological processes defined by associated Gene Ontology Terms; Metabolic Process (A), Programmed Cell Death (B), Regulation of Cell Cycle (C) and Ubiquitin-Protein Ligase Activity (D).

Changes in transcript within treatment groups were consistent, reflected in figure 17 by small standard errors, even with large changes e.g. Ccnb1, Plk1. Treatment with Dex gave relatively small changes in transcript level when compared to glucose starvation and electrical stimulation. Even when changes were found to be significant the changes were less than 2-fold, with the exception of Fbxo32, which was still only 2.6-fold increase with Dex treatment. These relatively small changes are consistent with the fact that Dex treatment gave no significant change in myotube CSA as seen in figure 12.

Transcript changes show a large degree of variation between glucose starvation and electrical stimulation. In only four of the 12 genes the transcripts change in the same direction with each treatment; Lpl, Bcl2l11, Sod2 and Fbxo32. Furthermore, whilst the direction of change is the same, the degree of change is different. In the case of Lpl, glucose starvation gave less than a 3-fold increase in transcript level, whereas electrical simulation produced an almost 6-fold increase. This degree of variation in transcript level change is evident in each of the four groups of genes. In particular in the regulation of cell cycle group (figure 17, panel C). Here Ccnb1 shows an almost 6.5-fold decrease in transcript level on treatment with glucose-free media, but a 3.5-fold increase with electrical stimulation. Also, Plk1 shows around a 7.5-fold decrease in transcript level with treatment with glucose starvation but around a 3.5-fold increase with electrical stimulation. The differences in transcript changes with glucose starvation and electrical stimulation and possible explanations for them are discussed in detail in 3.5.3.

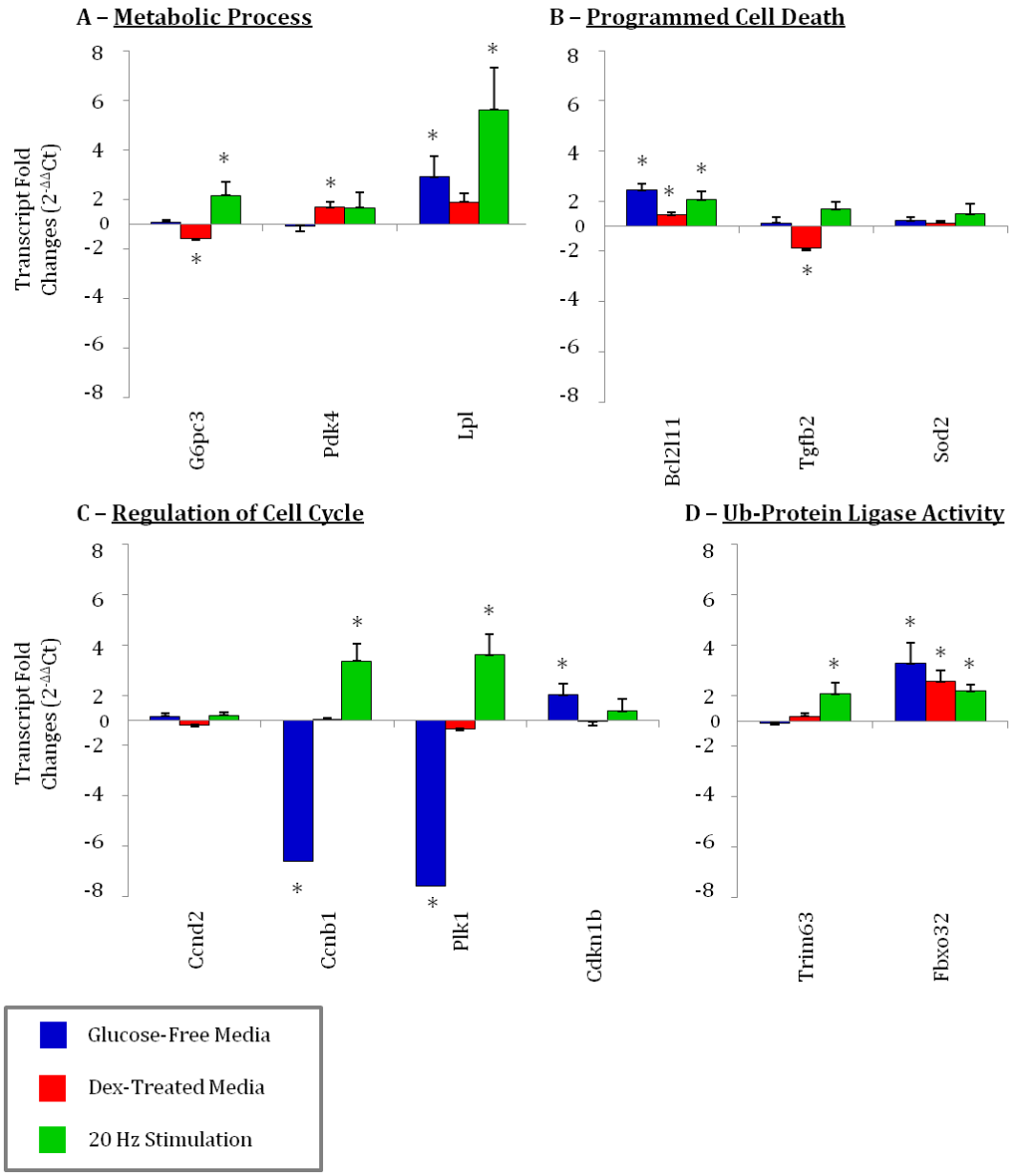

Figure 17 Comparison of Transcript Levels for Foxo1 Target Genes Following Atrophy Inducing Treatment in *In-Vitro* & *In-Vivo* Models

Mean fold changes following treatment are shown for transcripts measured using qRT-PCR and normalised to the mean of two housekeeping genes (Rn18s and Polr2a). *In-vitro* atrophy of C2C12 myotubes was induced by starvation via glucose free media for 24 hours (Blue) or treatment with 1μM dexamethasone for 24 hours (Red). Graphs show fold changes in transcripts relative to the control group cultured for 24 hours in normal media. *In-vivo* results relate to TA muscle tissue which was electrically stimulated at 20Hz continuously for 7 days (Green). Graphs shows fold changes relative to the unstimulated, contralateral control TA. Genes were grouped according to their biological processes defined by associated Gene Ontology Terms; Metabolic Process (A), Programmed Cell Death (B), Regulation of Cell Cycle (C) and Ubiquitin-Protein Ligase Activity (D). Each treatment group contains an *n* number of 6, with error bars indicating standard error. Statistically significant fold changes ($p<0.05$ following ANOVA statistical test) are indicated by *. Error bars indicate SEM.

3.5 Discussion

In vivo and *In vitro* models of atrophy were established; Incubation of myotube cell cultures for 24 hours with glucose-free media and 24 hours with 1μM Dexamethasone (Dex), as well as 7 days of continuous electrical stimulation at a frequency of 20Hz on the rat *Tibialis anterior* muscle *in vivo*. The transcriptional profile of Foxo1 target genes following treatment *in vitro* and *in vivo* were measured in order to compare the effects of the different models and determine whether the models show signs of convergence.

3.5.1 Glucose Starvation but not Dex Treatment Induced Atrophy in C2C12 Myotubes

Incubation for 24 hours in glucose-free media produced a significant 56% decrease in mean CSA in C2C12 myotubes (figure 12). This model was adapted from the study conducted by Sandri *et al* in which they 'starved' myotube cultures by replacing the culture media with PBS for 6 hours (Sandri et al., 2004). They noted a 60% decrease in myotube diameter following treatment. This approach was tested in a pilot study but the level of apoptosis present following treatment, made evident by large numbers of free-floating and single cells, might have interfered with any results produced by this model. 'Starvation' of myotubes by removal of growth media and replacement with PBS for 6 hours has been repeated in studies subsequently (Lagirand-Cantaloube et al., 2009), showing atrophy induction without mention of apoptosis. Atrophy has also been observed in studies that have used serum starvation of myotubes to investigate insulin signalling (Giraud et al., 2007). Others have used a model where the differentiation media is not replenished (Stevenson et al., 2005) leading to a 53% reduction in diameter. Surprisingly, the removal of only glucose from cultured myotubes with the aim of studying muscle atrophy has not been studied before now. The induction of atrophy in myotubes using this model is a novel finding. Interestingly, other studies have also shown that high glucose culture media stimulated protein degradation through the ubiquitin–proteasome pathway and also inhibited protein synthesis (Russell et al., 2009) suggesting that the levels of extracellular glucose may play a central role in the balance of protein synthesis and degradation within the muscle fibre.

In contrast, treatment with 1μM Dex for 24 hours gave no significant reduction in myotube CSA (figure 12). This is in contrast findings from other studies; Sandri *et al* observed a 40% decrease in myotube diameter following the same treatment (Sandri et

al., 2004). However other studies have used increasing concentrations of Dex for 24 hours and confirmed our finding that there was no significant decrease in myotube diameter with 1μM Dex (Stitt et al., 2004) and that significant decreases in myotube CSA were apparent following treatment with 10μM and above (Stitt et al., 2004). This suggests that in this study the concentration of Dex used was not high enough to induce atrophy, and if repeated a concentration of 10 or even 100μM may be more suitable and would be more likely to induce atrophy. As a result of this the transcriptional changes seen with treatment of 1μM Dex were negligible (figure 17) and not be discussed further.

3.5.2 Continuous Electrical Stimulation Produces Atrophy Without Damage to the Muscle

Very little evidence of nerve damage was observed in any of the Haematoxylin and eosin stained histological sections following stimulation (figure 13). Continuous electrical stimulation at a frequency of 20Hz for 7 days produced a significant 12.64% decrease in muscle weight when compared to the unstimulated contra-lateral control (figure 14). When the CSA of muscle fibres was analysed a difference of 17.18% in the mean values was found between the stimulated and control muscles (figure 15). Previous studies have shown that stimulation at 20Hz revealed no damage to muscle after 9 and up to 61 days (Jarvis et al., 1996). This study also showed that this stimulation pattern produced atrophy of the *Tibialis anterior* muscle with a 51% mean reduction in weight following 55-61 days of stimulation. The conclusion from this study stated that there was a switch in muscle fibre type with continuous electrical stimulation from fast to slow. This switch in fibre type has been shown subsequently in unpublished data produced by Dr. Lauren Fisher (Fisher, 2010), and apparent as early as only one week of stimulation. Slow twitch fibres are inherently smaller in cross section (Jarvis et al., 1996) and the switch of some fibres from fast to slow may go some way to explain the change in size of the muscle as a whole. However, Jarvis *et al* also showed a decrease in mean fibre CSA in the fast twitch fibres following stimulation. One explanation for this change in size may be to facilitate diffusion of oxygen and nutrients, whose demand increases with electrical stimulation (Eisenberg et al., 1984, Hepple et al., 2000). This theory was further strengthened by the observation of increased capillary density, with many fibres deeply indented by capillaries (Joplin et al., 1987, Shen et al., 2009). The idea of the muscle adapting due to functional demands

during electrical stimulation prompted the phrase 'functional atrophy'. To the best of our knowledge, the use of electrical stimulation with the aim of producing and studying skeletal muscle atrophy is a novel model.

3.5.3 Transcriptional Changes Reveal Differences in the Models of Atrophy

While it was observed that treatment with glucose-free media *in vitro* and 20Hz continuous electrical stimulation of skeletal muscle *in vivo* both induce atrophy, the differences in the changes in key transcripts suggested that the mechanisms behind these modes of atrophy are different (figure 17). This was not completely unexpected as the *in vitro* model employed a calorie restricting state on immature muscle cells whereas the electrical stimulation model employed an increase in contractile activity in an animal model, where the diet was non-restricted. Although for the muscle itself the great increase in activity must lend to greatly increase the demand and usage of fuel, and thus potentially cause a relative 'starvation'. Additionally, the maturation state of the cells involved in each of the models i.e. *in vitro* cells being immature multinucleate precursors of muscle fibres where as *in vivo* the muscle fibres are fully mature and form part of a larger tissue with a mixed population of cells, may go some way to explaining the differences observed in the transcript changes with each treatment.

A marked difference was observed in transcripts which were functionally involved in the regulation of cell cycle. Transcript levels of each of the four genes (Ccnd2, Ccnb1, Plk1 and Cdkn1b) showed no significant change following treatment with Dex for 24 hours. This is most likely a reflection of the concentration of Dex used to treat the myotubes, discussed in 3.5.1. However treatment of myotubes with glucose-free media and electrical stimulation of skeletal muscle in rat produced very different results, in particular with Ccnb1 and Plk1. Glucose starvation produced a significant 6.5- and 7.5-fold decrease in transcript levels of Ccnb1 and Plk1 respectively. However electrical stimulation produced an opposing 3.5-fold increase in the transcript levels of these genes following treatment. Cyclin B1 (Ccnb1) is a regulatory protein involved in mitosis and contributes to the switch-like all or none behaviour of the cell in deciding to commit to mitosis. Once activated, Ccnb1 promotes several of the events of early mitosis. Before mitosis almost all Ccnb1 in the cell is located in the cytoplasm, but in late prophase it relocates to the nucleus following phosphorylation (Hagting et al., 1999). Phosphorylation also prevents export from the nucleus by blocking the nuclear

export signal (Yang et al., 2001). Ccnb1 is phosphorylated by Polo kinase (Plk1) (Hagting et al., 1999).

Ccnd2 transcript levels showed no significant change following any of the treatments *in vitro* or *in vivo*. However, Cdkn1b showed a significant 2-fold increase with glucose starvation compared to no significant increase with electrical stimulation. Cdkn1b (also known as $p27^{kip1}$) encodes a protein which belongs to the Cip/Kip family of cyclin dependent kinase (Cdk) inhibitor proteins. The encoded protein binds to and prevents the activation of cyclin E-CDK2 or cyclin D-CDK4 complexes, and thus controls the cell cycle progression at G1. It is often referred to as a cell cycle inhibitor protein because its major function is to stop or slow down the cell division cycle (Polyak et al., 1994).

The transcriptional changes in these genes following glucose starvation indicate a down regulation of mitosis. This cell cycle arrest has been observed in other studies involving starving myotubes by non replacement of differentiation media (Stevenson et al., 2005). Mitotic figures are rarely seen in muscle fibers *in vivo*, because myonuclei are postmitotic and unable to proliferate (Lash et al., 1957, Collins and Partridge, 2005). However, satellite cells have long been recognized as reserve myoblasts and a source of new myonuclei during growth and regeneration (Moss and Leblond, 1971, Collins and Partridge, 2005). Studies have shown that the number of myonuclei decreases upon denervation *in vivo* (Schmalbruch and Lewis, 2000). This may be due to the reduction in protein synthesis associated with muscle atrophy. Indeed it has been noted previously that protein synthesis does increase with continuous electrical stimulation, even though there must be a more than compensatory increase in protein degradation, since the total mass of the muscle declines (Joplin et al., 1987). This increase in protein synthesis may be due to the fibre type switch discussed in 3.5.2. This increase in protein synthesis requires an increase in ribosomal RNA, which already accounts for 80% of all RNA present in the muscle. This would be facilitated by an increase in myonuclei number, which has been observed with continuous electrical stimulation in previous studies (Joplin et al., 1987).

The transcripts for genes involved in metabolic processes were also likely to give different changes in transcript following treatments as the metabolic demands placed upon the cells in each model were almost opposite. An *in vitro* environment where the muscle cells have not began to contract and the model then involves starving the cells was bound to have opposing metabolic effects to those in a model where the cells form

part of mature muscle fibre and are being activated to contract above and beyond normal physiological levels. This increase in the metabolic demands was reflected in an increase in the transcript levels of each of the three genes involved in metabolic processes following electrical stimulation, including those involved in carbohydrate (G6pc3) and in particular lipid (Lpl) metabolism, where Lpl showed an almost 6-fold increase. This increase in fatty acid oxidation has been demonstrated in previous studies following continuous electrical stimulation for 7 days (Bonen et al., 1999). However, Lpl was the only transcript from the metabolic process group to increase with glucose starvation of cultured myotubes. This may have been due to the lack of available glucose and so the cells look for alternative fuel sources. The reduction in transcript level of G6pc3 is further evidence to support this observation. Indeed, other studies have shown an increase in fatty acid oxidation in myotubes following starvation, which is mediated by AMPK; a protein known to maintain the energy balance in cells (Carling, 2004).

The transcript levels of the E3 ubiquitin ligases Trim63 and Fbxo32 both increase following 20Hz stimulation, suggesting they play a part in the protein breakdown associated with the functional changes involved in this model. This observation that Trim63 and Fbxo32 increase in expression following continuous electrical stimulation is a novel finding. There have been studies using electrical stimulation to try and counteract the effects of denervation (Russo et al., 2010). These reported a blunting of the over expression of Trim63 and Fbxo32, which is normally present with denervation when electrical stimulation is added. However the stimulation pattern used in that study was different from the pattern we used (20Hz continuously for 7 days). The electrical stimulation sessions were applied daily for 6 days, beginning 24 h after denervation, and produced 200 maximal contractions of the TA muscle. These maximal contractions were divided into four sets of 50 contractions, with a duration of 3.2 min per set and 10 min rest (without ES) between sets. This pattern was chosen to minimise muscle fatigue and may explain the differences seen in the changes in expression of Trim63 and Fbxo32.

Following glucose starvation of myotubes Fbxo32 transcript levels increase but not Trim63. This is in agreement with other studies where an increase in Fbxo32 is reported following starvation of myotubes (Sandri et al., 2004). Although studies have shown that Trim63 expression increases with Dex treatment of myotubes (Stitt et al., 2004), there is no evidence in the literature that it is involved in the atrophy process induced via starvation. The control of Trim63 and Fbxo32 expression may involve

Myog and the Hdac dependent pathway as shown in figure 6, and the effectors of Myog may differ between the *in vitro* and *in vivo* models of atrophy in response to different physiological conditions.

3.6 Summary

The data has shown that two very different methods can produce atrophy in muscle, one which is based on calorific restriction (treatment with glucose free media) and one which involves artificially increased activity (electrical stimulation). The transcriptional profiling of tissue taken from both these models suggests that the mechanisms by which the atrophy is induced may be different, based on the differential response of key target genes linked to atrophy pathways.

However, neither model accurately reflects the physiological state of clinical muscle atrophy, where the most common cause is inactivity of muscle. Thus it was concluded from these findings that a model based on muscle inactivity was required in order to gain a greater insight into the mechanisms behind muscle atrophy in a more clinically relevant state.

Chapter 4: Development of An *In-Vivo* Atrophy Model Incorporating Tetrodotoxin (TTX) Block of the Common Peroneal Nerve

4.1 Introduction

In chapter 3, glucose starvation of C2C12 myotubes and electrical stimulation of skeletal muscle were used to induce atrophy. There was evidence that these two models produced atrophy via contrasting cellular mechanisms, despite some concordant transcriptional changes in foxo1 target genes. Although calorific restriction and imposed electrical stimulation have both been shown to induce atrophy neither is representative of a physiological state of inactivity in muscle. As discussed in 1.4.1 *in vitro* models of atrophy provide excellent models to highlight some of the mechanisms involved. However, the study of the *in vivo* response is vital in directing research towards a therapeutic target for muscle atrophy. *In vivo* models that represent specific physiological states such as functional atrophy via electrical stimulation or atrophy associated with specific disease states such as rodent models of cancer cachexia (Busquets et al., 2004) are limited in translating their findings across other clinical causes of atrophy. However an *in vivo* model of muscle inactivity, which can be used to investigate the molecular mechanisms of atrophy independent of a specific disease state, could give a clearer picture of the normal processes involved in the changes in muscle size. The mechanisms involved may translate over a larger range of atrophy models, and move us closer to the development of rational therapeutic interventions.

Other studies have adopted *in vivo* models of disuse atrophy including denervation (Tang and Goldman, 2006), hindlimb suspension (Stevenson et al., 2003) or joint immobilisation (Yasuda et al., 2005). However, each of these models has drawbacks. Denervation may still impact on muscle through neurotrophic factors released with nerve damage (Midrio, 2006), and is limited in its capacity to investigate recovery from atrophy. Hindlimb suspension involves unloading of the muscle without restriction of activity and it has been suggested that this model may be better suited to study muscle changes with microgravity during spaceflight (Holecek, 2012). Joint immobilisation, such as limb casting has been shown to cause systemic stress responses, which may interfere with changes induced on the muscle by immobilisation (Holecek, 2012).

The aim of this chapter was to set up an *in vivo* model of atrophy which avoids these drawbacks. A tetrodotoxin (TTX) nerve block model would not damage the nerve while completely blocking muscle activity and without imposing undue stress upon the animal. The block could also be time-limited in order to study recovery from atrophy. Once established, tissue samples collected from this experiment could be analysed in

order to elucidate the cellular and molecular changes involved in inactivity induced atrophy.

4.2 Pilot Study of TTX Nerve Block Atrophy Model

A pilot study was designed in order to verify the TTX experimental model, and established that muscle atrophy was evident in the absence of muscle damage and without detriment to the animal. The pilot study consisted of 4 animals, which had a nerve block in place for 7 days (n=2) or 14 days (n=2). The nerve cuffs were assembled in-house. Full details of the nerve cuff implant, surgical procedures and the protocol used can be found in section 2.3.

4.2.1 Efficiency of Delivery of TTX by Osmotic Pump

As this model relies on the continuous delivery of TTX to the nerve cuff, initial tests were carried out to ascertain whether the mini osmotic pump was functioning at the correct flow rate. This was achieved by calculating the amount of TTX that was ejected from the pump over the experimental period. Table 10 details the efficiency of each of the four pumps used in the pilot study. The volume of TTX contained in the pump at day 0 was calculated by weighing the empty and full pump prior to implantation. Upon cessation of the nerve blockade the pumps were removed from the animal. The remaining liquid was then removed from the pump via a 1 ml syringe and blunt-tipped, 27 gauge needle and weighed. Comparing the volume at day 0 and the volume at termination gave the volume of liquid ejected from the pump during the experimental period. From this, the flow rate could be calculated (µl/hour). The desired flow rate was 0.5 µl/hour, the actual flow rates were between 0.48 and 0.51 µl/hour, which was acceptable. The flow rates were monitored for each of the pumps used in any subsequent implants.

Rat	Volume at Day 0 (µL)	Volume at Termination (µL)	Volume Used (µL)	Hours Run	Flow Rate (µL/Hour)
1	265	184	81	168	0.48
2	277	192	85	168	0.51
3	268	101	167	336	0.50
4	275	104	171	336	0.51

Table 10 Review of Osmotic Pump Efficiency
Calculated flow rate for osmotic pumps over experimental period. Volumes at day 0 were calculated by weighing the empty and full pump. Volumes at termination show remaining weight of TTX solution after the pump had been removed from the animal.

4.2.2 Histological Examination of Muscle Showed Little Evidence of Nerve Damage

Analysis of histological sections of both treated and untreated muscle tissue allowed evidence of nerve damage to be quantified. Frozen sections were stained with Haematoxylin and eosin (See 2.5.1), which distinguishes muscle fibres and nuclei. Evidence of nerve damage would appear in the sections as the migration of nuclei from the periphery of the fibre into the interior of the fibre (as shown in figure 13, panel C) as well as areas of small, non-uniformly shaped fibres or the infiltration of inflammatory cells. Figure 18 shows histological sections from each of the four pilot study animals. Very little evidence of nerve damage was observed in any of the histological sections with most sections containing no denervated fibres, meaning that our methods of implantation caused no significant damage to the muscle fibres.

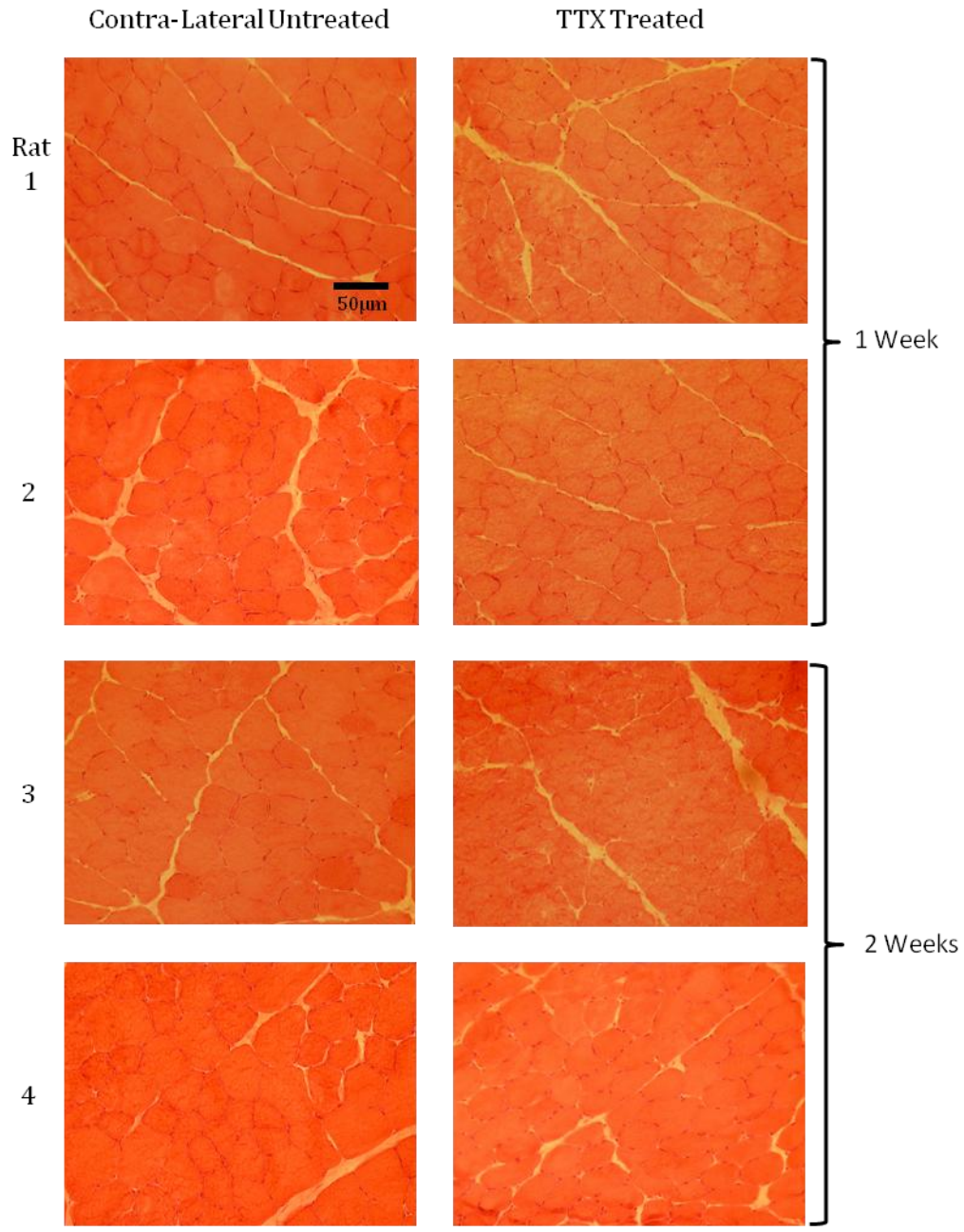

Figure 18 Cross Sectional Photomicrographs of Untreated and TTX Treated TA Muscle
Haematoxylin and eosin stain on sectioned muscle tissue (10µm) from rats 1 and 2, where the TTX block was in place for 1 week and rats 3 and 4 where the TTX block was in place for 2 weeks. No significant morphological changes indicative of nerve damage were evident in fibres from muscle subjected to nerve block by TTX.

4.2.3 Nerve Block Induces Progressive Muscle Atrophy

In order to assess the degree of muscle atrophy induced during the TTX nerve block, the changes in weight and cross sectional area were measured in treated muscles and

compared to control. TA muscles were weighed immediately after harvesting. Figure 19 A shows the weight of both the untreated control and treated muscles of the four pilot study animals. The differences in muscle weight between treated and contra-lateral control limbs are also expressed as a percentage in Figure 19 B.

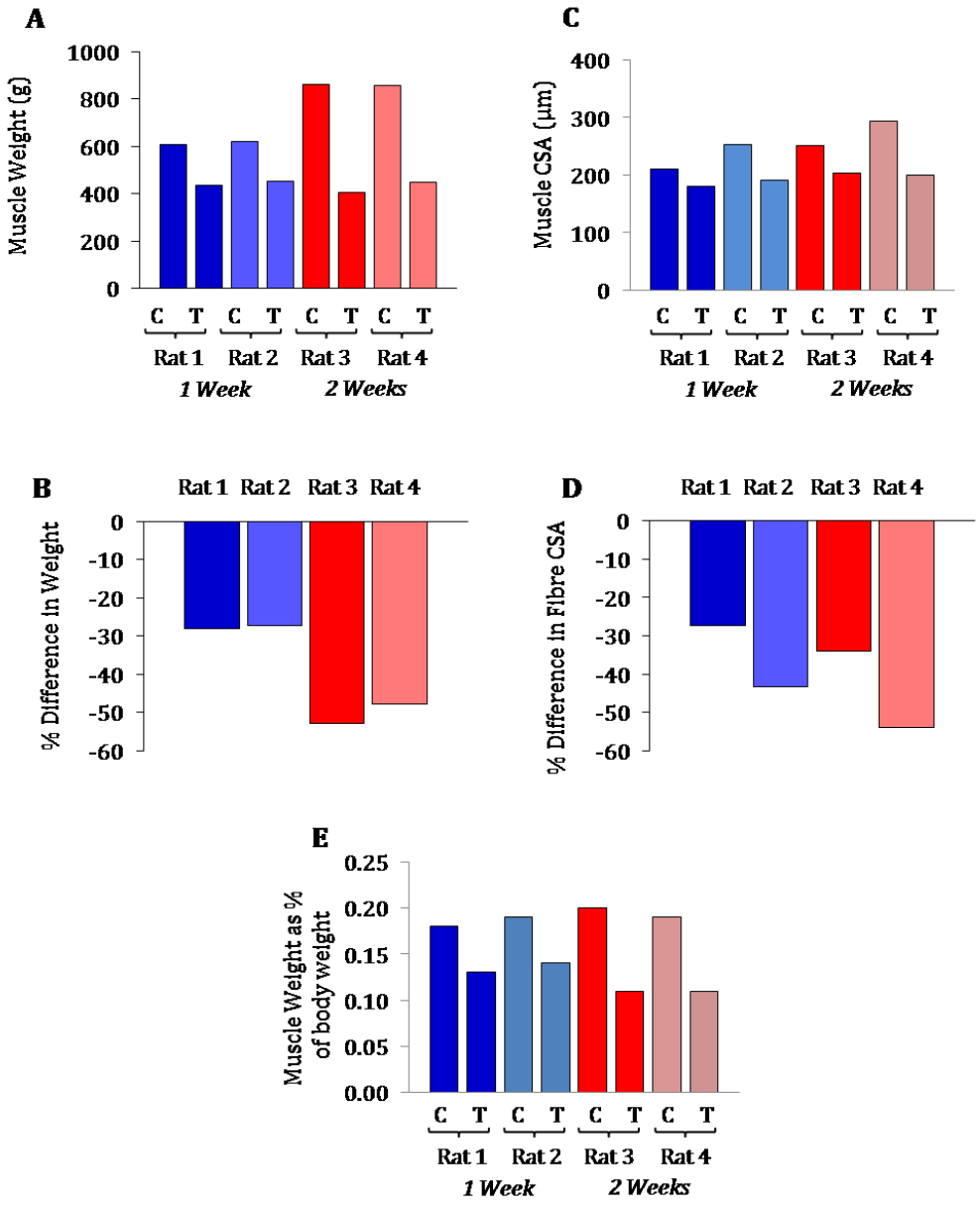

Figure 19 Progressive Muscle Fibre Atrophy Over 2 weeks of TTX Treatment
Graphs show changes in TA muscle weight following TTX nerve block for 1 week (blue) and 2 weeks (red). A; Individual muscle weights of control (C) and treated (T) TA muscles. Panel B; Percentage difference in weight, comparing untreated and treated TA muscles in each animal. Panel C; Individual Mean CSA of control (C) and treated (T) TA muscles. Panel D; Percentage difference in cross sectional area (CSA) of muscle fibres comparing untreated and treated TA muscles. Fibre Cross Sectional Areas (CSA) were calculated by measuring the diameter of fibres from photomicrographs of Haematoxylin and eosin stained muscle sections (10µm). Panel E; Individual muscle weights normalised to animal body weight.

Following 7 days of nerve block, a decrease of 28.1% and 27.3% was observed in rats 1 and 2 respectively. Following 14 days a greater reduction in muscle weight was observed, with a decrease of 52.85 and 47.84% in rats 3 and 4 respectively. From these values it can be seen that TTX nerve block induced a progressive muscle atrophy over the experimental time period. Figure 19, panel A shows that the contra-lateral control TA muscles in rats 3 and 4 were larger than the equivalent in rats 1 and 2. Therefore to try to normalise these values, muscle weights were normalised to whole body weight to ensure that these differences would not result in misleading data (figure 19 E). Expression of the muscle weights as a percentage of whole body weight showed that in rats that were blocked for 7 days, the treated TA muscles were 0.13 and 0.14% of whole body weight, whereas the treated muscles in rats that were blocked for 14 days were both 0.11% of whole body weight. This suggests a progressive decrease in muscle weight regardless of the differences in the weight of the control TA muscles, and therefore a progressive increase in muscle atrophy after a further 7 days of the TTX nerve block .

Cross sectional areas (CSA) of fibres were also measured from Haematoxylin and eosin stained muscle sections as outlined in 2.5.2, (figure 19 D). The values are expressed as a percentage difference between treated and contra-lateral control muscles. All four animals showed a decrease in fibre CSA following nerve block, ranging from 27.3% to 53.9%. The progression in the degree of atrophy is less clear when looking at fibre CSA compared with muscle weights, as the inter-individual variation is greater. However, the mean percentage decrease in CSA for the two animals blocked for 7 days was 35.2%, compared with 43.9% following 14 days block, suggestive of a progression in muscle atrophy after a further 7 days of nerve block.

4.2.4 Transcript Levels of Trim63 and Fbxo32 Increase with Muscle Atrophy

As the aim of the subsequent nerve block study was to analyse the transcriptomic response to muscle inactivity, it was important to ascertain whether the nerve block model induced changes in transcript levels of known atrophy genes. The transcript levels of two ubiquitin E3 ligases (Fbxo32 and Trim63), which are known to be fundamental in the process of skeletal muscle atrophy, were measured using qRT-PCR using the methods outlined in 2.6.8. The results (shown in figure 20) are displayed using the $2^{-\Delta CT}$ method, where differences between the mean reference genes C_T values and the target gene C_T value was quantified individually for each muscle sample.

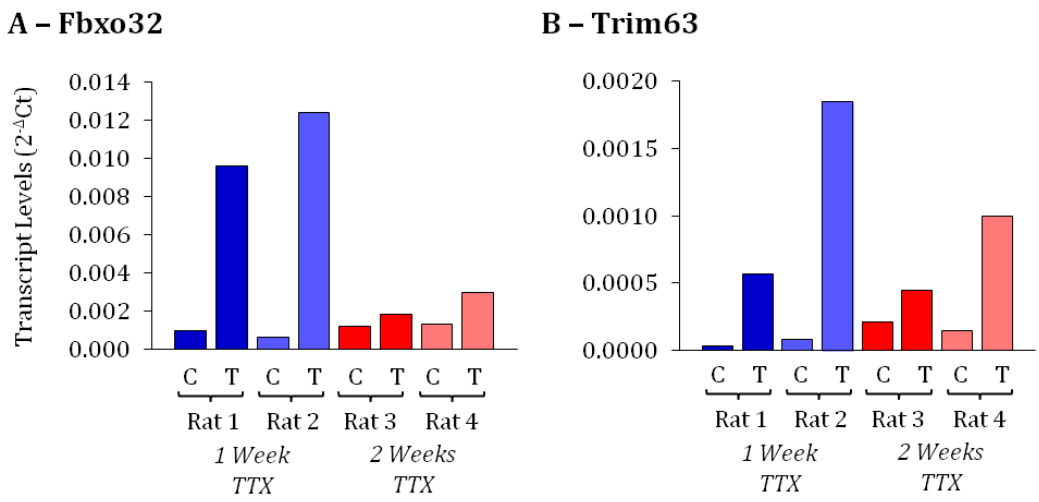

Figure 20 Transcript Levels of Fbxo32 and Trim63 Increase In Response to a TTX block

Transcript levels of Fbxo32 (A) and Trim63 (B) in individual TA muscle samples, measured using qRT-PCR and normalised to the mean of two housekeeping genes (Rn18s and Polr2a). Bars indicate untreated control TA levels (C) and levels following treatment with TTX (T) for 1 week (blue) or 2 weeks (red).

The transcript levels of Fbxo32 (figure 20 A) increase markedly following 7 days of nerve block (mean 14-fold over control muscle). However, after 14 days of block Fbxo32 levels fall back to around 2-fold that of control. Transcript levels of Trim63 (figure 20 B) showed greater variation between individuals than those of Fbxo32. An increase in Trim63 was evident after both 7 and 14 days nerve block, with some indication this may also reduce during the second week. This was surprising as muscle weight and morphology (4.2.3) suggested that the degree of atrophy is progressive during the second week of block. However, figure 20 shows that the transcript levels of the two ubiquitin ligases does not increase progressively over the two weeks. This result did confirm that nerve block altered transcript levels and also hinted at temporal differences in those changes. Furthermore, it demonstrates that transcriptional responses are not a simple transition from a control pattern to an atrophy pattern but rather a dynamic process that requires sampling at more than one time point.

4.3 Full Scale *In-Vivo* TTX Nerve Block Study

Following the successful pilot study in which progressive muscle atrophy was induced by TTX nerve block over the experimental time period without damage or degeneration of the muscle fibres, the experimental numbers and time periods were increased. The subsequent study consisted of animals where the nerve block was in place for 3, 7 or 14 days (n=6). The study also included a TTX nerve block for 14 days following which the block was reversed, allowing the muscle to recover without detriment over the subsequent 7 days.

4.3.1 Histological Analysis of Muscle Revealed Little Evidence of Nerve Damage

Analysis of histological sections of both treated and untreated muscle tissue allowed evidence of nerve damage to be quantified. Frozen sections were stained with Haematoxylin and eosin (See 2.5.1) to assess evidence of nerve damage (as described in 4.2.2). Figure 18 shows representative histological sections for each of the full scale experimental groups. Very little evidence of nerve damage was observed in any of the histological sections with most sections containing no denervated fibres, confirming that our methods of implantation caused no significant damage to the muscle fibres in this larger study.

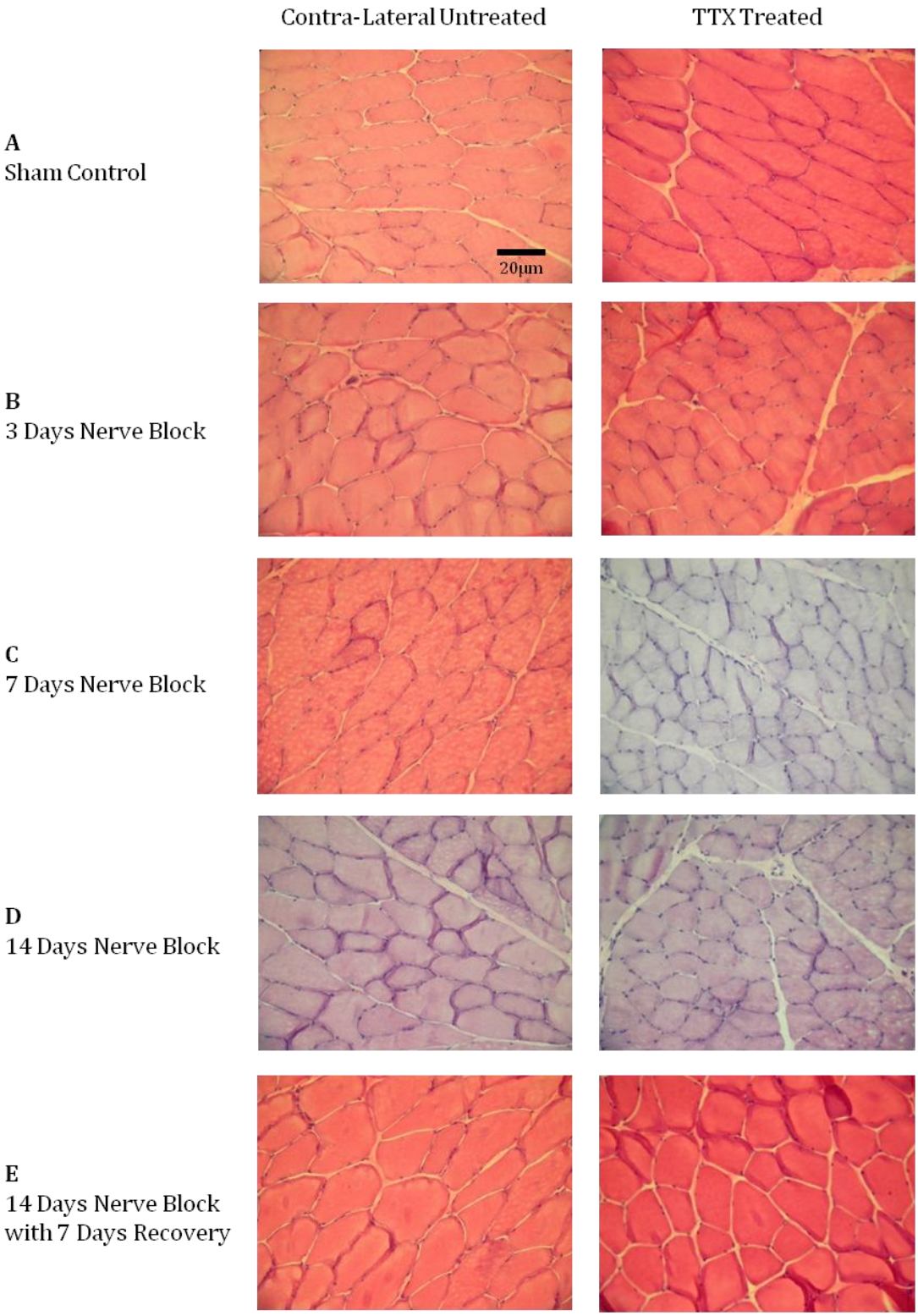

Figure 21 Cross Sectional Photomicrographs of Untreated and TTX Treated TA Muscle

Haematoxylin and eosin stain on sections of untreated and treated TA muscle tissue (10µm) from sham control (A), 3 days nerve block (B), 7 days nerve block (C), 14 days nerve block (D) and 14 days nerve block with 7 days recovery (E). No significant morphological changes indicative of nerve damage were evident in fibres from muscle subjected to nerve block by TTX.

4.3.2 Evidence of Muscle Atrophy In Full TTX Nerve Block Study

The degree of muscle atrophy was measured by changes in muscle weight and cross sectional area. Mean weights for untreated and treated muscles in each experimental group are expressed as a percentage of whole body weights of animals to normalise measurements to differing animal sizes (figure 22 A) (*n*=6). Untreated muscles showed no significant change throughout the experimental time period when compared with the sham-operated control. TTX nerve block produced a statistically significant decrease in muscle weight, which progresses following 3, 7 and 14 days of nerve block. When values are expressed as a percentage difference between untreated and treated muscles (figure 22 C) it can be seen that mean muscle weights decrease following treatment by 7% (+/- 1%), 29% (+/- 2%) and 51% (+/- 1%) after 3, 7 and 14 days nerve block respectively. These changes can be compared to a 13% decrease in muscle weight following 20Hz continuous electrical stimulation for 7 days. This is less than half of the atrophy produced with TTX nerve block.. With 7 days of recovery from 14 days TTX treatment, the muscle weight returns to only 24% less than the control. The level of recovery confirms that the nerve block induces muscle atrophy without detrimental effects on the muscle tissue as it was possible for the muscle to recover over the 7 days and for the effects of atrophy to be reversed to a degree. Furthermore the data shows that the process of atrophy and restoration of mass follow a similar time course.

The level of muscle atrophy could also be determined by analysing cross sectional areas of fibres, measured from Haematoxylin and eosin stained muscle sections as outlined in 2.5.2. These are expressed as mean CSAs of the untreated and treated muscles in each of the experimental groups (*n*=6) in figure 22 B and also as a percentage difference between treated and untreated muscles in figure 22 D. The effect of the nerve block on CSA was comparable to the effect on muscle weight. The mean CSA decreased following treatment by 18%, 42% and 69% with 3, 7 and 14 days nerve block respectively, and with 7 days of recovery the CSA recovered to only 26% less than control. When comparing panels C and D in figure 22 the patterns of change are remarkably similar.

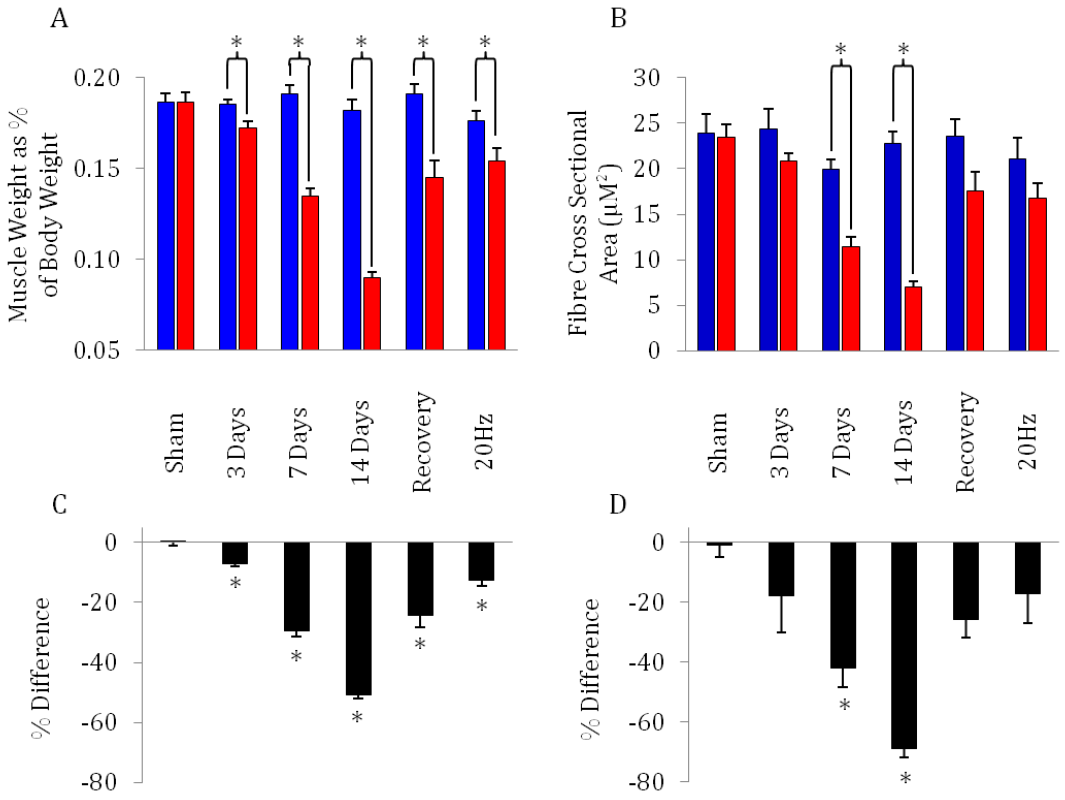

Figure 22 Nerve Block Treatment *In-Vivo* Induces Progressive Decrease in Muscle Weight and Fibre Cross Sectional Area that Can Recover Upon Cessation of Block

TA Muscle weight is expressed as a percentage of whole body weight to normalise measurements to differing animal sizes (A). The mean TA weights of the 6 animals used in each of the experimental groups with untreated contra-lateral control (Blue) and treated (Red). The difference between untreated and treated TA weights is also expressed as a percentage difference (C). Differences in Fibre Cross Sectional Areas (CSA) between untreated and treated TA samples (B) were calculated by measuring the diameter of fibres from photomicrographs of haematoxylin and eosin stained muscle sections (10μm). The differences are also expressed as a percentage difference (D). *n*=6, statistically significant (P<0.01 following ANOVA test) differences are indicated with *. Measurements from electrically stimulated (20Hz, 1 week) samples seen in figure 14 and 15 have been included for comparison. Error bars indicate SEM.

4.4 Discussion

To achieve the aim set out in 1.6, a pilot study was designed in which muscle atrophy was induced via a TTX nerve cuff which was in place for 7 or 14 days. Muscle atrophy was evident in all four animals in the absence of muscle damage. This atrophy was progressive from 7 to 14 days. Transcript levels of protein ubiquitin ligases known to

be integral to muscle atrophy increased in treated muscles compared to the contra-lateral controls, providing evidence that our model influences atrophic transcripts within the muscle tissue.

Following a successful pilot study the experimental numbers and time periods were increased in order to produce a more thorough profile. The main study consisted of TTX muscle blocks for 3, 7 and 14 days (n=6). The study also included a TTX nerve block for 14 days following which the block was reversed, allowing the muscle to recover without detriment over the subsequent 7 days. Progressive muscle atrophy was produced while the nerve block was in place, to a maximal 51% loss of muscle weight after 14 days. Following 7 days of recovery the treated muscles regained weight to a level of 24% less than the untreated. Measurement of CSA of muscle fibres in each experimental group showed concomitant changes with muscle weight, both in response to nerve block and during recovery upon cessation of the nerve block.

4.4.1 TTX Nerve Block Induces Progressive, Recoverable Atrophy

TTX nerve block for 14 days resulted in a maximal 51% loss in mass of the treated TA muscle compared to that in the untreated contralateral-control limb (figure 22). This can be compared to a smaller 39% loss in rat TA muscle following 21 days of denervation (Adhihetty et al., 2007) and only 25% following 14 days of hindlimb suspension (Stump et al., 1997). This less severe atrophy induced by hindlimb suspension is due to the fact that this model does not restrict movement of the limb. Although the muscle is unloaded, the unrestricted movement may act to maintain some muscle mass. The atrophy observed over the experimental time period of the TTX block was progressive with 3 and 7 days of block reducing the weight of the muscle by 7% and 29% respectively (figure 22). Other studies using TTX nerve block to induce atrophy reported a 19% reduction in TA weight following 7 days of block (Dupont Salter et al., 2003), slightly less than reported here. However, although the study by Dupont Salter *et al* used the same dosage of TTX, the TTX nerve cuff was applied on the sciatic nerve, rather than the common peroneal nerve. The sciatic nerve is a larger, less peripheral nerve that supplies additional muscles including the *Lateral gastrocnemius* (LG), which also atrophied in their study. This additional supply as well as the increased size of the nerve may have served to dilute the potency of the TTX and reduced the effect on the TA muscle.

The atrophy produced by the common peroneal TTX nerve cuff model was achieved in the absence of any histological signs of damage or degeneration of the muscle fibres, following analysis of H&E stained muscle sections (figure 21). It was therefore possible to block muscle activity for 14 days, and then reverse the blockade, allowing the muscle to recover without detriment over the subsequent 7 days. The muscle recovered to show a reduction of muscle weight of 24% (figure 22). This represents less atrophy than the equivalent 7 days of TTX block, suggesting that the process of recovery may be faster than that of atrophy.

4.4.2 Summary

Although studies have used TTX nerve block to induce atrophy in skeletal muscle previously (Buffelli et al., 1997, Dupont Salter et al., 2003), these studies have focused on the fibre-type changes produced with the atrophy (Dupont Salter et al., 2003) or the contractile property changes (Buffelli et al., 1997). To our knowledge, this is the first study to use the TTX nerve block model of atrophy with the aim of analysing the molecular and cellular changes involved during atrophy and in the recovery from atrophy. In order to achieve this aim samples from the main nerve block study were analysed using microarray. To provide a genome-wide and time-resolved profile of the transcriptional changes involved in inactivity atrophy and recovery. These studies are described in chapter 5.

Chapter 5: Microarray Analysis of *In Vivo* Skeletal Muscle Atrophy Via Nerve block and Electrical Stimulation

5.1 Introduction

Both the 'functional' atrophy and TTX nerve block *in vivo* models of muscle atrophy undoubtedly produce a decrease in muscle weight. However, whether there is a universal mechanism involved in the molecular pathways leading to muscle atrophy in both models is presently unknown. Identification of key players in the control of muscle atrophy and their response to the different models is fundamental if these pathways are to be delineated and therapeutic targets identified.

Previously studies have used microarray analysis to study in vivo models of atrophy. Several have focused on single time points during atrophy (Bey et al., 2003, Stein et al., 2002), while other have looked over a time course (Stevenson et al., 2003). However these studies employ the hindlimb suspension model which, as previously discussed has several drawbacks when investigating inactivity induced atrophy including the fact that the limbs are allowed to move freely throughout. Furthermore, perhaps surprisingly, there are no experimental reports directed towards uncovering the transcriptional response during the process of recovery from atrophy.

Microarray analysis was used to compare genome-wide transcript changes following 3, 7 and 14 days of nerve blockade, in addition to 14 days of nerve block with 7 days of recovery, or 7 days electrical stimulation at 20Hz. In collaboration with Pfizer, microarray analysis using the Affymetrix GeneChip® Rat Genome 230 2.0 Array was used to measure over 30,000 transcripts and variants from over 28,000 well-substantiated rat genes. The aim of this analysis was to identify cellular signalling pathways that were integral to the process of skeletal muscle atrophy.

5.2 Normalisation & Quality Control of Microarray Data

Untreated and TTX treated muscle samples from the pilot study of four animals, two having the nerve bock in place for 7 days and two for 14 days, were initially sent for processing. Following completion of the main study, only the treated muscle samples from each animal and a sham-operated control sample group (n=4) were subject to microarray analysis. The untreated control samples from the pilot study were only included in the initial quality control stages of the microarray analysis and were excluded from subsequent analysis. Full details of all samples subject to microarray

analysis can be found in table 5. In the main TTX nerve block study outlined in 4.3 an *n* of 6 was obtained for real time PCR analysis. Based on previous experience of Affymetrix data (Pfizer) an *n* of 4 is sufficient for microarray. For each experimental group, the animals that showed the largest and smallest changes in muscle weight following TTX nerve block or 20Hz electrical stimulation were excluded from the microarray study.

The RAW data in the form of .CEL files was read into the bioconductor package within R (full details of the software used for analysis can be found in 2.7.2). Data was normalised via the RMA (Robust Multichip Average) method (Irizarry et al., 2003) which consists of three steps; a background adjustment, quantile normalization and finally summarization. The quality of the arrays both before and after normalisation was assessed using arrayQualityMetrics within Bioconductor (5.2.1-3) and were found to be of sufficient quality for subsequent analysis.

5.2.1 Spatial Distribution of Feature Intensities

A false colour representation of the spatial distribution of feature intensities prior to normalisation for each array (figure 23) was used to identify spatial effects that may be caused by, for example, gradients in the hybridization chamber, air bubbles or printing problems. There were no such anomalies observed in any of the array data sets.

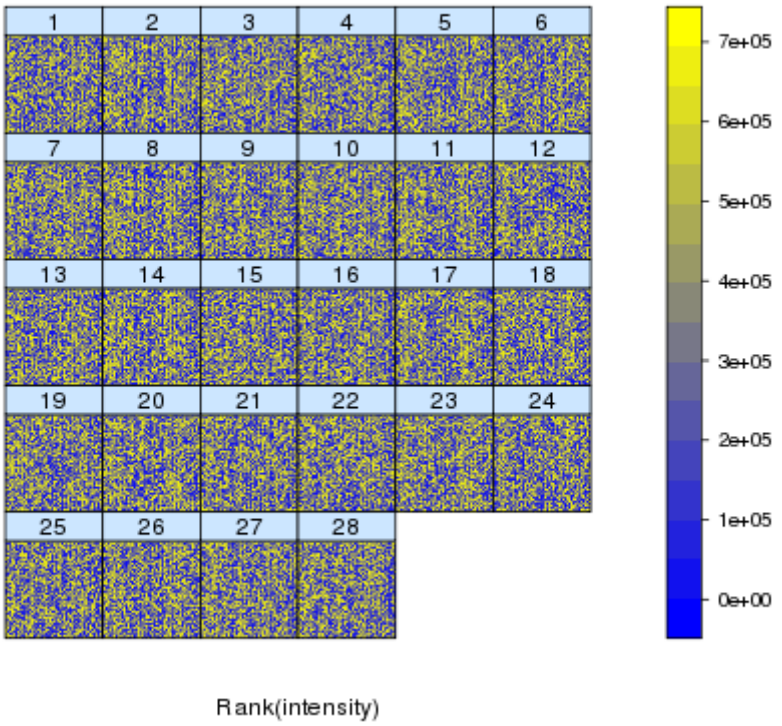

Figure 23 False Colour Representations Showing Spatial Distributions of Feature Intensities on Each of the 28 Arrays
The colour scale is shown in the panel on the right, and it is proportional to the ranks of the probe intensities. Normally, when the features are distributed randomly on the arrays, one expects to see a uniform distribution; sets of control features with particularly high or low intensities may stand out. No Anomalies were observed on our array sets.

5.2.2 Inter Array Intensity Distributions

The package arrayQualityMetrics produces boxplots of the $\log_2$ intensities of each of the arrays (figure 24) in order to assess the homogeneity between the arrays pre- and post-normalisation.

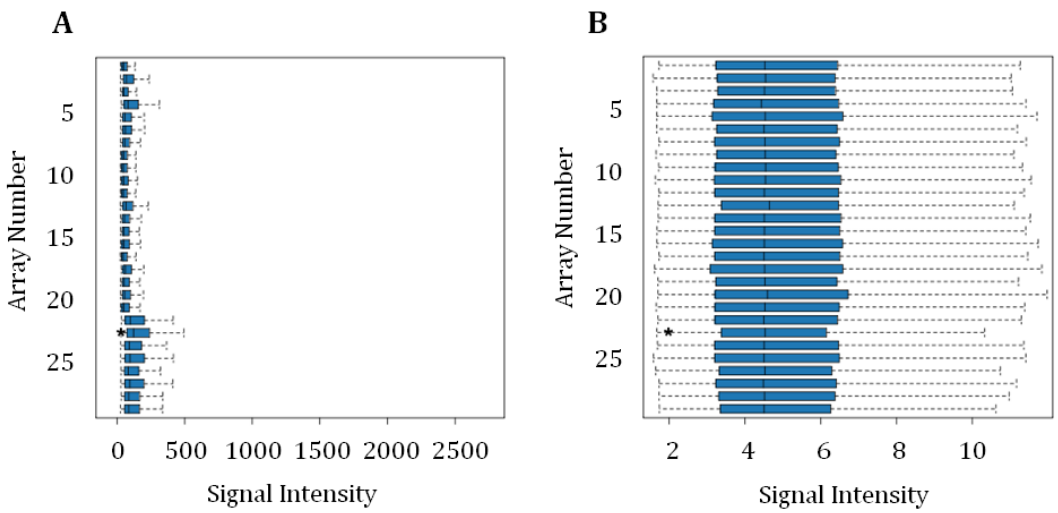

Figure 24 Boxplots Representing Summaries of the Signal Intensity Distributions for Affymetrix Gene Chips
Each box corresponds to one array. Values are shown pre (A) and post (B) normalisation. Typically, one expects the boxes to have similar positions and widths. If the distribution of an array is very different from the others, this may indicate an experimental problem. Outliers, according to the Kolmogorov-Smirnov statistic between each array's distribution and the distribution of the pooled data are marked by an asterisk (*). Array 22, marked with an asterisk represents an array that was not included in subsequent analysis. Normalisation removes batch differences between arrays from the main study (1-20) and the pilot arrays (21-28).

Boxes are expected to have similar positions and widths. If the distribution of an array is very different from the others, this may indicate an experimental problem. In figure 24, arrays 1-20 represent the main TTX study while arrays 21-28 are the untreated and TTX treated samples from the pilot study. It was observed that the batch effect from combining data from two separate experiments, which is evident in figure 24 panel A, is removed following normalisation (panel B). The outlier marked with an asterisk represents an array that was removed from subsequent analysis as this was hybridised with a sample from one of the untreated contralateral control muscles of the pilot study group. In later analysis the sham control group of the main TTX study was used as the control.

5.2.3 Between Array Comparisons

The 'Between array comparison' session within arrayQualityMetrics produces a heatmap of between array distances (figure 25), computed as the mean absolute difference of the M-value for each pair of arrays.

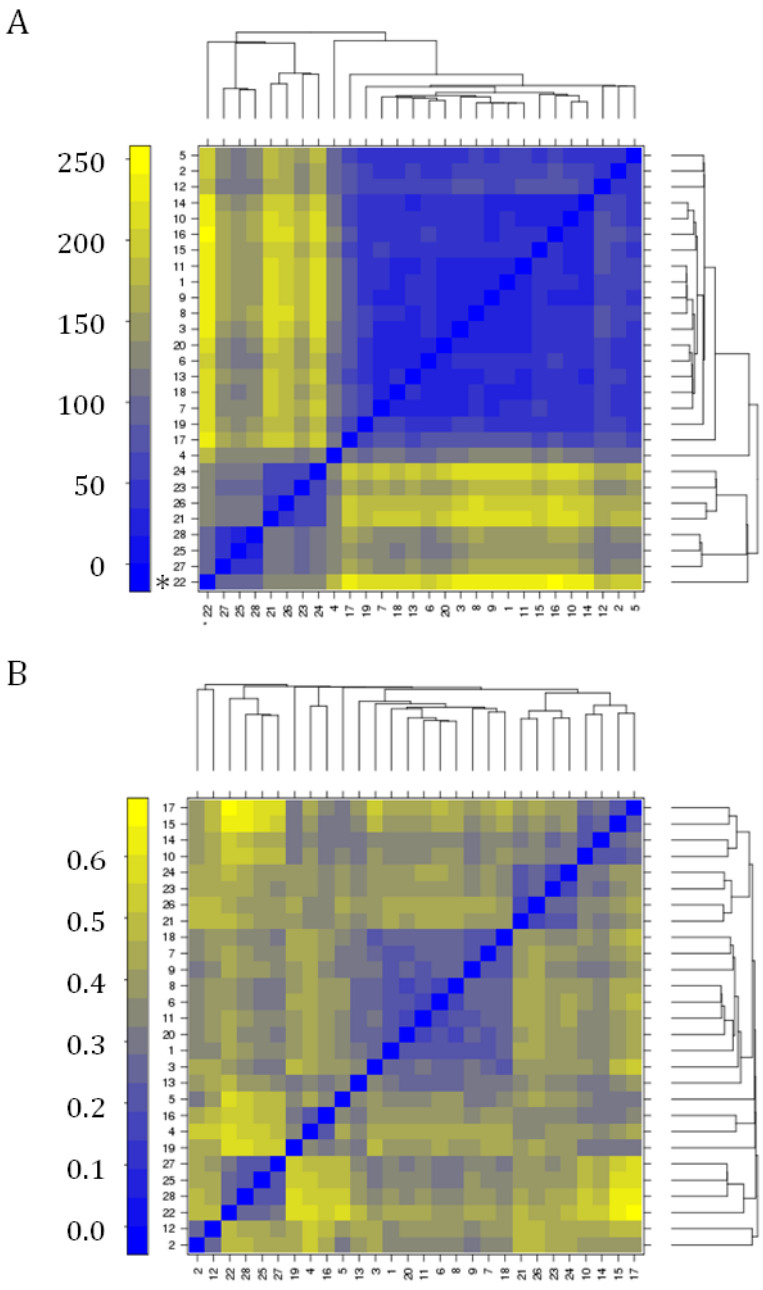

Figure 25 Between Array Comparisons
False colour heatmap representation of between arrays distances before (A) and after (B) normalisation, computed as the median absolute difference of the M-value for each pair of arrays. The colour scale is chosen to cover the range of distances encountered in the dataset. Arrays for which the sum of the distances to the others is significantly different are detected as outliers (marked by an asterisk).

The dendrogram on this plot can help to find batch effects, as well as reveal clustering of the arrays according to biological effects. Here normalisation removes the batch effect which can be seen in panel A where chips 1-20 (main study) show a clear distance from chips 21-28 (pilot study). The outlier array (array 22), marked with an

asterisk, which was highlighted previously in figure 24 was removed following normalisation. However since sham controls were available, as discussed in 5.2.2 this array was removed from further analysis.

5.3 Preliminary Data Analysis Confirms Clustering of Experimental Groups

Following normalisation and review by arrayQualityMetrics the dataset was put forward for preliminary analysis. The untreated contralateral control samples from the pilot study were removed from any subsequent analysis. This decision was made as one of the contralateral controls was highlighted as an outlier in 5.2 and the sham control group were deemed of sufficient number and quality to act as the experimental control. This preliminary analysis takes an unbiased view of all the experimental arrays and looks for correlations within the data that can be mapped to biological effects.

5.3.1 Chip Correlation Heatmap

Expression intensities of all probe sets within an array were compared to intensities on all the other arrays to produce an unbiased correlation heatmap of probe set expression (Figure 26). The dendogram revealed two major clusters consisting of samples that had undergone nerve block induced atrophy (3, 7 and 14 days) and those that had not (sham, recovery and 20Hz electrical stimulation). The arrays marked with an asterisk and highlighted in bold, 3 days atrophy (rat 1745) and recovery (rat 1770), seemed to correlate less well with data for the other animals within their experimental groups. However, these animals showed no outlying anomalies in muscle weight changes or in the arrayQualityMetrics analysis of the chips, therefore were not excluded from subsequent analysis.

Overall the experimental groups seemed to correlate well; with groups that have been exposed to nerve blockade showing a clear difference in transcriptional profile from controls and recovery, as well as those that have undergone electrical stimulation.

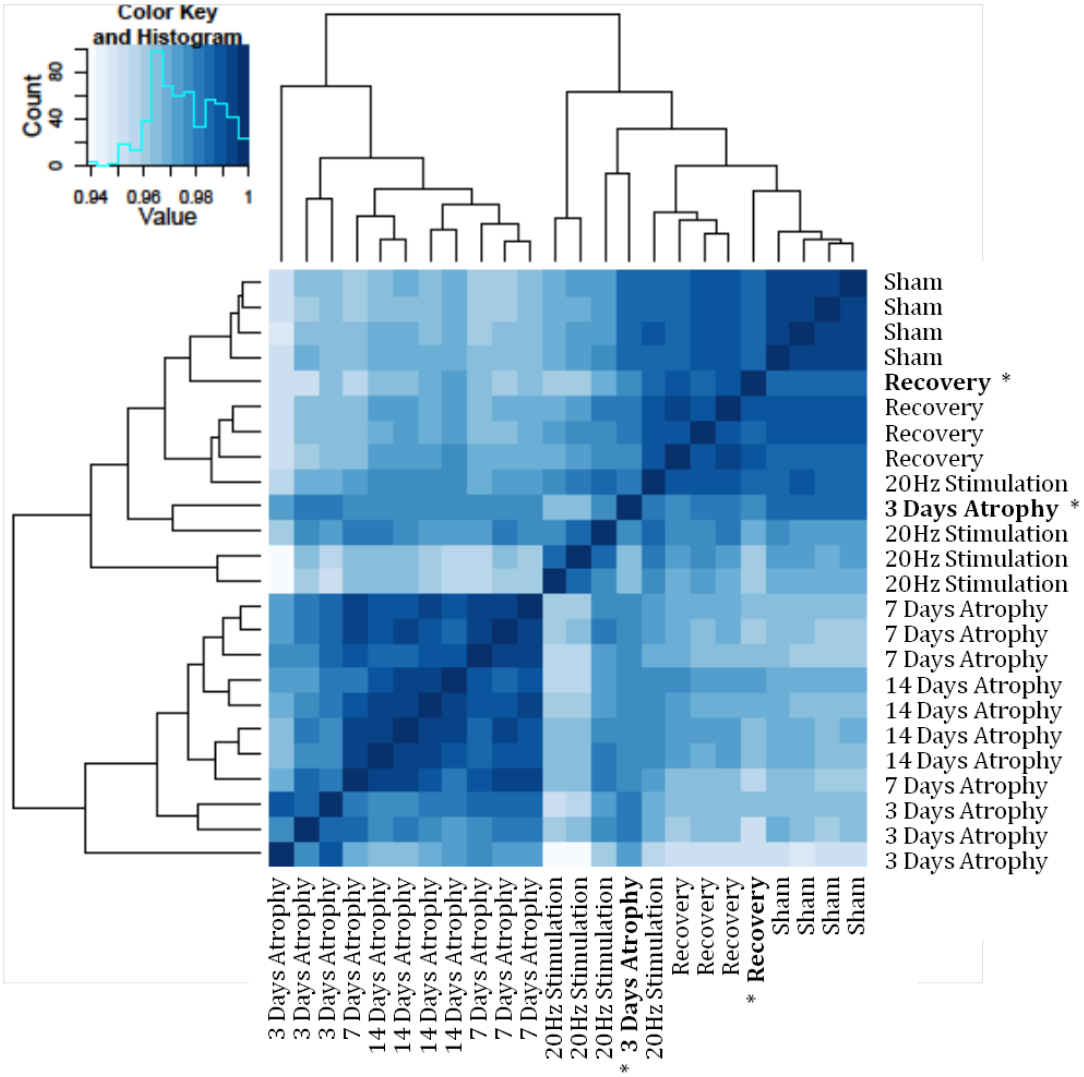

Figure 26 Unbiased Correlation Heatmap of Probe Set Expression Across the Whole Genome for Each Array

Colour scale moves to a darker blue as the correlation coefficient approaches 1 (perfect correlation). Arrays that do not correlate with their experimental groups are marked with an asterisk.

5.3.2 Principal Component Analysis

Principal component analysis was used in order to investigate further how the experimental groups clustered together. This involves a mathematical procedure that uses an orthogonal transformation to convert a set of observations of possibly correlated variables into a set of values of uncorrelated variables called principal

components. Plots in figure 27 show the first two components on the x and y axis respectively, which together account for 98.5% of the variance in the data.

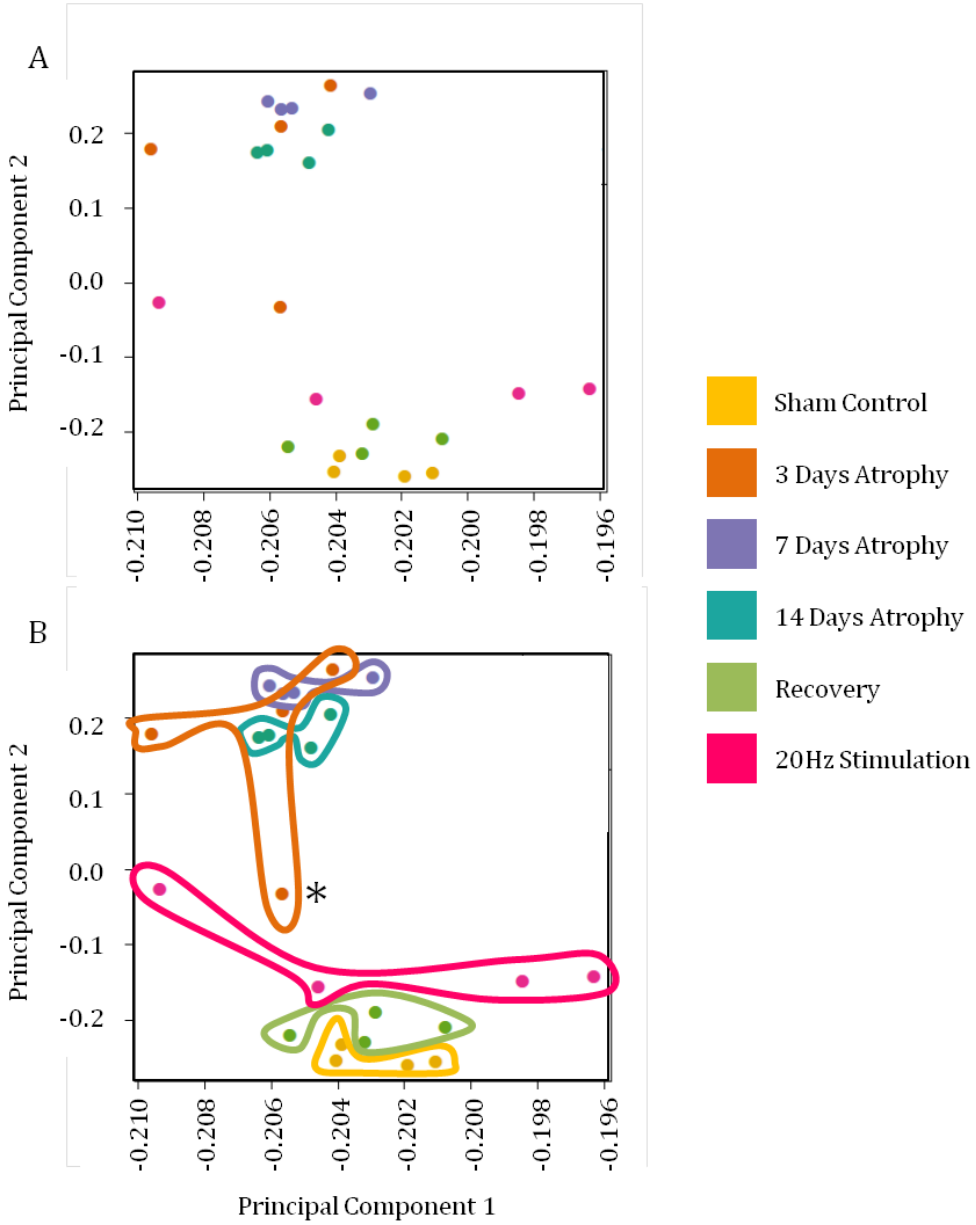

Figure 27 Principal Component Analysis of Experimental Arrays
Plot showing the first two principal components which account for 98.5% of the variance in the data. B shows the same plot with experimental groups enclosed with coloured lines and the outlier marked with an asterisk.

The arrays clustered into two distinct groups based on principal component 2, which corresponds to the two major hierachical clusters observed in figure 26. The 3, 7 and

14 days of nerve block groups clustered together. However, the 3 day nerve block group showed more variation than 7 and 14 days, with the outlier marked with an asterisk which was also previously observed in figure 26. Sham control, recovery and 20Hz electrical stimulation cluster together, as previously observed (figure 26). However these groups are also separated along the vertical axis, representing principal component 2. The 20Hz electrical stimulation group showed the widest variation along the x-axis (principal component 1) and formed a separate, disperse cluster.

The findings of the principal component analysis confirmed the observations from the correlation heatmap in 5.3.1 that the experimental groups seemed to correlate well, with groups that have been exposed to nerve blockade showing a clear difference in transcriptional profile from controls and recovery, which clustered more closely. Again the 20Hz electrical stimulation formed a distinct group from the nerve blockade groups as well as the control and recovery groups, which correlated closely while remaining as two distinct groups.

5.4 Differential Expression Analysis Reveals Atrophy to be a Dynamic Process

Differential expression analysis using the limma package within bioconductor allowed whole genome comparisons between experimental groups. Limma is an R package for the analysis of gene expression microarray data for the assessment of differential expression. Empirical Bayesian methods are used to provide stable results even when the number of arrays is small. The package was used to compare the experimental groups shown in table 11 below.

Comparison Number	First Experimental Group in Comparison	Second Experimental Group in Comparison
1	3 Days Nerve Block	Sham Control
2	7 Days Nerve Block	Sham Control
3	14 Days Nerve Block	Sham Control
4	20Hz Electrical Stimulation	Sham Control
5	14 Days Block with 7 Days Recovery	Sham Control
6	14 Days Block with 7 Days Recovery	14 Days Nerve Block
7	20Hz Electrical Stimulation	7 Days Nerve Block
8	14 Days Nerve Block	3 Days Nerve Block
9	14 Days Nerve Block	7 Days Nerve Block

Table 11 Experimental Groups Compared Within Limma

For each of these comparisons a table was generated which contained an average fold change and adjusted P value for each probe set. The probe sets within these tables were ranked by P value and the most statistically significant differentially expressed probe sets examined.

5.4.1 Number of Differentially Expressed Probe Sets Between Experimental Groups

The tables generated using the limma software in 5.4 for each of the comparisons was restricted to contain only probe sets whose p value was less than 0.05 and whose fold change was greater than 2. The number of probe sets (genes) contained in each of the adjusted tables were plotted on a bar graph (figure 28).

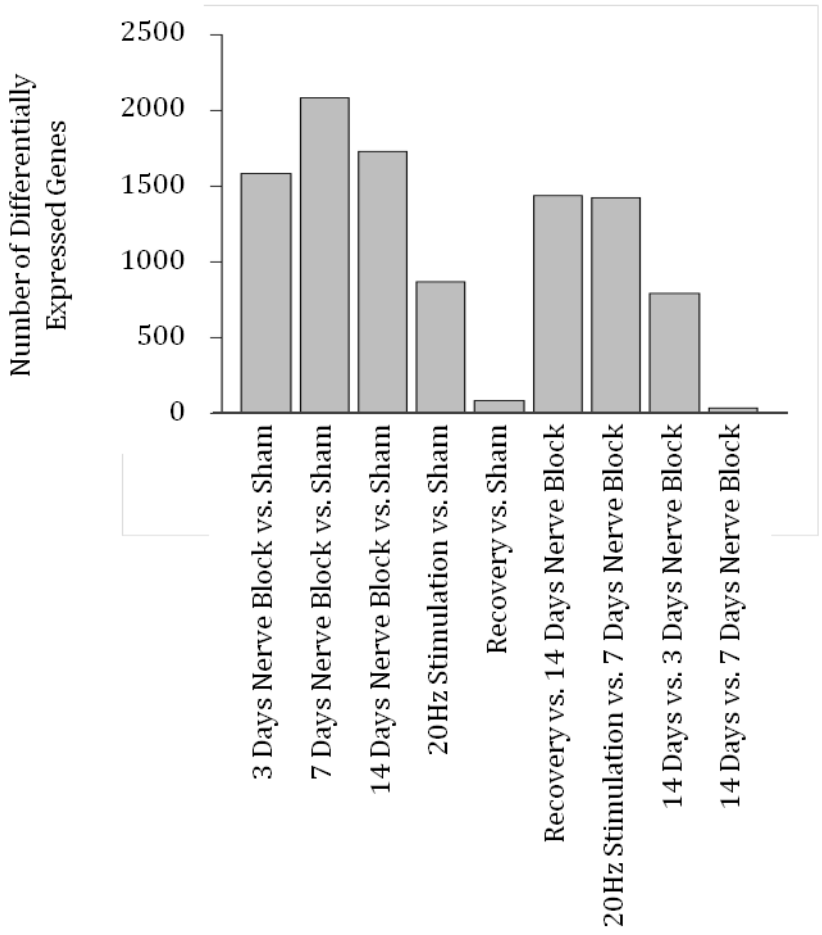

Figure 28 Number of Statistically Significant Differentially Expressed Genes Bars indicate the number of statistically significant ($p<0.05$) differentially expressed (fold change>2) genes when comparing two experimental groups using limma software package.

Comparing 3, 7 or 14 days of nerve block with sham controls, there were over 1500 statistically significant differentially expressed genes in each comparison. When comparing 7 days of nerve block with sham controls there were 2085 statistically significant differentially expressed genes, equating to almost 10% of the entire transcriptome. This analysis confirms that the nerve block model of skeletal muscle atrophy does effect the transcript levels within muscle significantly. Interestingly, the recovery group was almost identical to sham control with only 85 differentially expressed genes, suggesting that the transcriptional profile of the muscle has almost completely recovered within 7 days of reversing the nerve block. On comparison of 14 days of nerve block with 7 days there were only 34 differentially expressed genes. However, when comparing 14 days with 3 days there were 791 differentially expressed genes. These data suggest that the transcriptional reprogramming during atrophy is a dynamic process, with distinct early (3 days) and later (14 days) phases. When comparing 7 days of 20Hz stimulation with 7 days of nerve block there were 1426 statistically significant differentially expressed genes, suggesting the modes of action of producing atrophy in these two models is different.

5.4.2 Analysis of the Top 500 Most Statistically Significant Differentially Expressed Genes

A table was produced using the limma software showing the most statistically significant differentially expressed probe sets across all the comparisons (table 12). In this analysis, Histone deacetylase 4 (Hdac4) was the most statistically significant differentially expressed probe set (gene) across all the comparisons. It was noted that this table also contained the ubiquitin ligase Trim63, as well as the transcription factor myogenin.

Probe Set ID	Gene Symbol	Entrez Gene ID	Full Gene Name	Adjusted P Value
1376761_at	Hdac4	363287	histone deacetylase 4	7.00E-12
1389151_at	Adam19	303068	a disintegrin and metallopeptidase domain 19 (meltrin beta)	1.20E-11
1368342_at	Ampd3	25095	adenosine monophosphate deaminase 3	3.48E-11
1372305_at	Copz2	360611	coatomer protein complex, subunit zeta 2	3.48E-11
1398295_at	Slc29a1	63997	solute carrier family 29 (nucleoside transporters), member 1	4.11E-11
1373421_at	Tgif1	316742	TGFB-induced factor homeobox 1	5.27E-11
1382234_at	Pdhx	311254	pyruvate dehydrogenase complex, component X	5.27E-11
1370210_at	Tmem158	117582	transmembrane protein 158	5.27E-11
1387804_at	Trim63	140939	tripartite motif-containing 63	5.27E-11
1368310_at	Myog	29148	myogenin	5.27E-11

Table 12 The Top 10 Most Statistically Significant Differentially Expressed Probe Sets Over All Comparisons
Generated using the limma package in Bioconductor and ranked according to adjusted p value.

The table of the most statistically significant differentially expressed genes across all the comparisons was ranked by adjusted p value and restricted to include only the top 500 genes. The intensity values of these 500 genes across all the arrays was analysed using an unsupervised hierarchical clustering method within bioconductor, which was plotted on a correlation heatmap (figure 29). The intensity values on the heatmap were scaled for absolute expression and the degree of expression so patterns of change between arrays can be observed more clearly. In all cases the replicate samples within each experimental group cluster together. The dendogram shows that samples subject to 3, 7 and 14 days atrophy cluster together with 3 days being the least similar to 7 and 14 days. Sham, recovery and 20Hz electrical stimulation cluster together before separating into distinct groups.

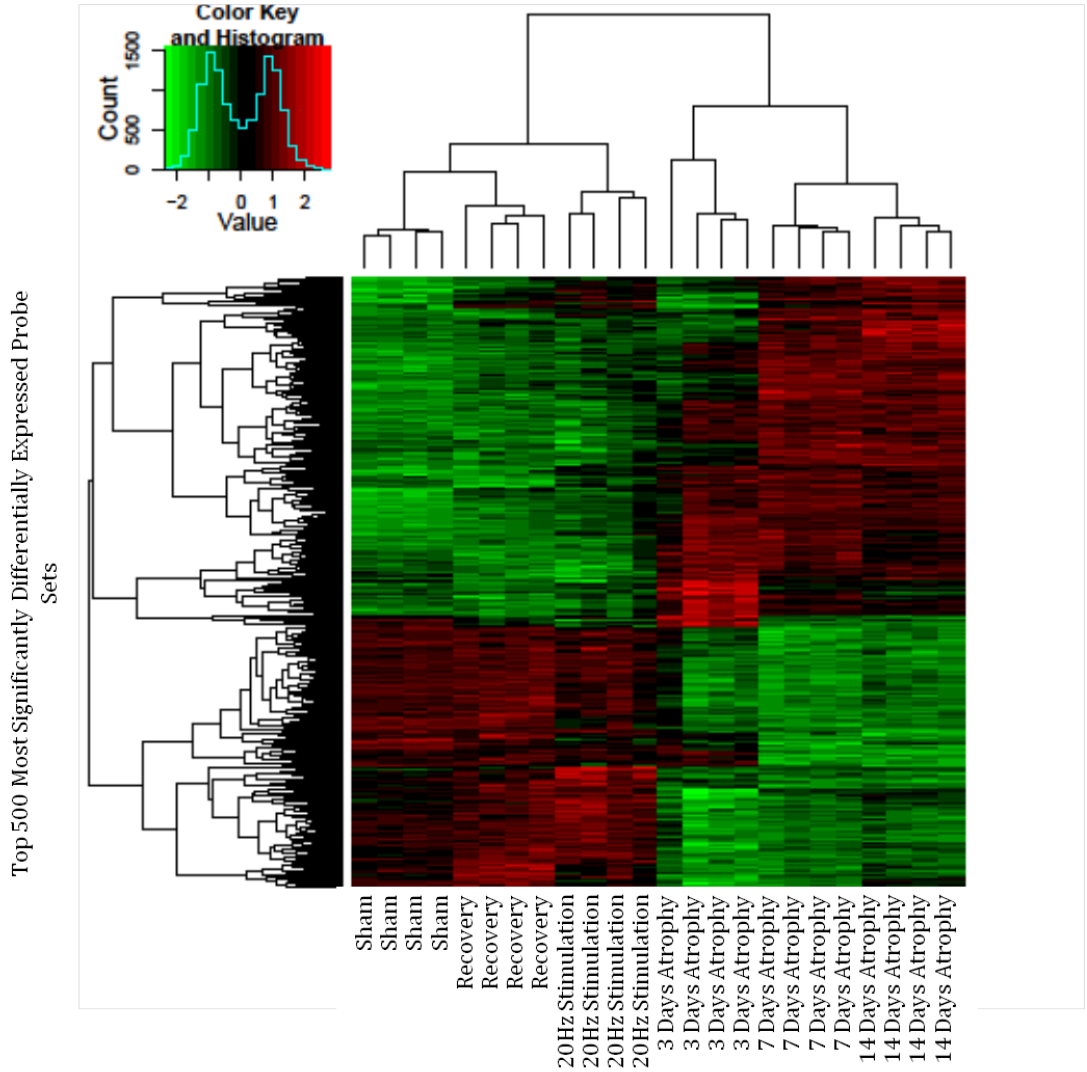

Figure 29 Unsupervised Hierarchical Clustering of Top 500 Most Statistically Significant Differentially Expressed Genes

'Limma' software compared all probe sets across all experimental groups using an ANOVA test. The probe sets are then ranked by adjusted P value. The top 500 most statistically significantly probe sets are plotted on an unsupervised correlation heat map, which is scaled to remove absolute expression and the degree of expression.

5.4.3 Genes Cluster Into Dynamic Groups

In order to investigate further the relationship between the duration of TTX nerve block and the changes in transcript levels, the top 500 most statistically significant differentially expressed genes across all comparisons were subject to temporal clustering analysis within bioconductor. A time line was established with sham control

becoming day 0 and recovery from nerve block becoming day 21 (14 days of nerve block plus 7 days without nerve block). The 20Hz electrical stimulation group was not considered in this analysis. The software analysed the number of statistically significant clusters of genes according to patterns of change in expression over the experimental time period. This was found to be two i.e. genes that increase and genes that decrease upon TTX block. However the software could also be used to separate the 500 genes into any number of clusters to be examined further. Figure 47 shows how the genes were separated into 5 distinct temporal clusters. This number was chosen as the genes formed interesting groups while still remaining large enough for further analysis.

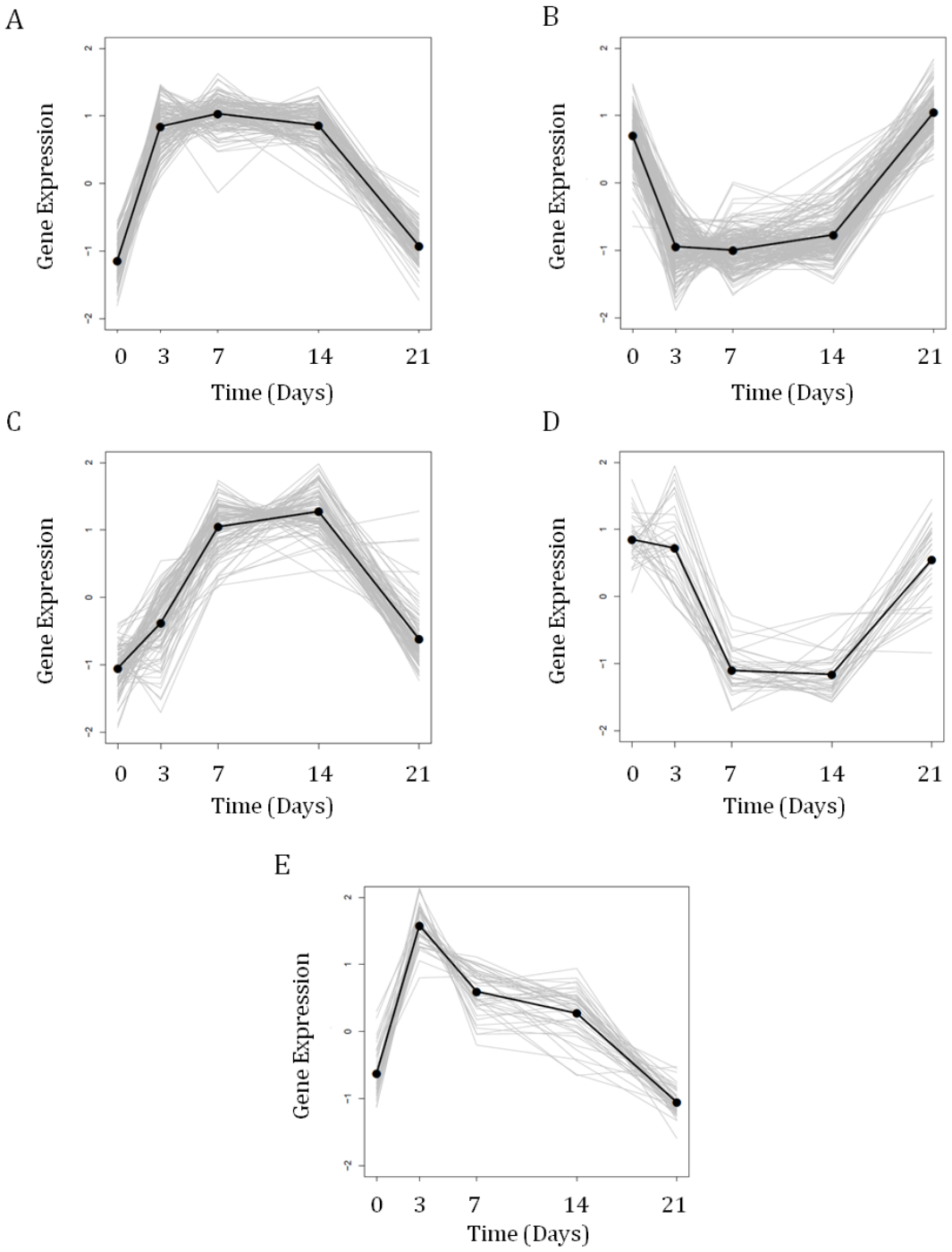

Figure 30 The Top 500 Most Statistically Significant Differentially Expressed Genes Organised Into 5 Distinct Temporal Clusters

Each Panel (A-E) shows the scaled expression of each probe set over the experimental time course as a joined grey line with the median values of all the genes within each cluster added as a black line.

The clusters consisted of genes which increase (figure 30 A) or decrease (B) in expression by the earliest time point and maintain this throughout the atrophy time

course, genes which displayed a delayed increase (C) or decrease (D) in expression that is established later in atrophy, and genes which showed a spike increase in expression in early atrophy and although still elevated fall back towards the sham control levels as atrophy progresses (E). Genes in all clusters returned towards sham control levels during the 7 day period following removal of the nerve block (21 days). This analysis shows that in the context of a transcriptional response, atrophy is a highly dynamic process. The data also showed that the expression of genes did not change in the same direction during muscle atrophy.

The clusters isolated in this analysis, shown in figure 30 A-E, were mapped back onto the heatmap in figure 29. The clusters are highlighted within blue boxes and each shows the patterns of change of that cluster of genes over the experimental time period. This figure highlights a clear distinction between the 3 day block group and the 7 day/14 day block group in the genes within clusters C, D and E. Also, within cluster C there seems to be a delayed recovery of genes, with a number of genes showing a persistent upregulation from sham control group. Interestingly, this cluster is also induced in the functional atrophy group.

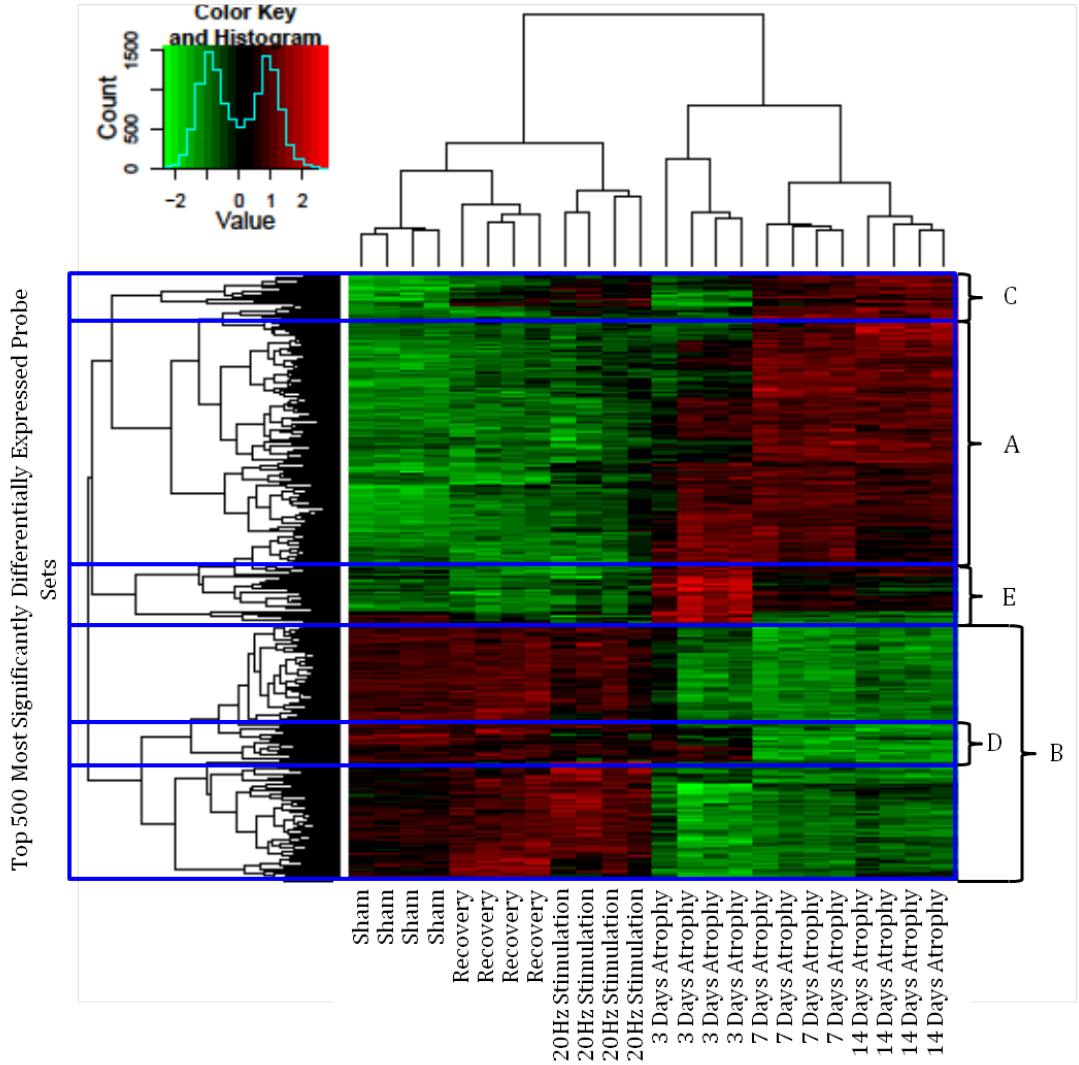

Figure 31 Unsupervised Hierarchical Clustering of Top 500 Most Statistically Significant Differentially Expressed Genes With Gene Clusters Highlighted

'Limma' software compares all genes across all experimental groups using an ANOVA test. The genes are then ranked by adjusted P value. The top 500 most statistically significantly genes are plotted on an unsupervised correlation heat map, which is scaled to remove absolute expression and the degree of expression. The genes can be organised into 5 distinct clusters according to patterns of change in expression over time. These clusters are highlighted within each of the blue boxes (A-E, details outlined in figure 30).

5.5 Gene Ontology Terms Analysis

The Gene Ontology (GO) project (Ashburner et al., 2000) is a major bioinformatics initiative with the aim of standardizing the representation of gene and gene product attributes across species and databases. The project provides a controlled vocabulary of terms for describing gene product characteristics and gene product annotation data from GO Consortium members, as well as tools to access and process this data. (GOConsortium, 2008).

The hypergeometric test is the standard gene enrichment test applied by GoStats (Falcon and Gentleman, 2007) within Bioconductor. It is used to isolate statistically signficantly enriched GO terms for further scrutiny. It is a statistical test calculated for a set of genes, in this case each of the nine comparisons outlined in table 11 and the five gene clusters outlined in figure 30. The hypergeometric test specifies whether each gene set is enriched for any annotations out of the 'gene universe', which was defined as any genes that had an Entrez Gene ID and some GO Term annotation. This analysis produced 14 tables of GO terms, one for each of the nine comparisons and one for each of the five temporal clusters. Each table consisted of the GO Terms which were found to be statistically significantly enriched ($p<0.2$). An example of one of these tables is shown below in table 13. The table shows the top 10 most statistically significant enriched GO Terms within the comparison of 3 days of nerve block vs sham control. Interestingly, with the exception of number 9 'glycolysis', all the GO terms are based around the ubiquitin ligase system.

	GO Term ID	P value	Exp Count	Count	Size	Term Name
1	GO:0051436	4.14E-05	4.7	15	61	negative regulation of ubiquitin-protein ligase activity involved in mitotic cell cycle
2	GO:0010498	5.29E-05	12.7	28	165	proteasomal protein catabolic process
3	GO:0051248	6.91E-05	17.7	35	230	negative regulation of protein metabolic process
4	GO:0031145	7.54E-05	4.9	15	64	anaphase-promoting complex-dependent proteasomal ubiquitin-dependent protein catabolic process
5	GO:0051352	9.12E-05	4.9	15	65	negative regulation of ligase activity
6	GO:0051437	9.12E-05	4.9	15	65	positive regulation of ubiquitin-protein ligase activity involved in mitotic cell cycle
7	GO:0031398	0.000105	7.4	19	96	positive regulation of protein ubiquitination
8	GO:0031397	0.000275	6.1	16	79	negative regulation of protein ubiquitination
9	GO:0006096	0.000369	3.4	11	44	glycolysis
10	GO:0051351	0.000419	5.7	15	74	positive regulation of ligase activity

Table 13 The Top 10 Most Statistically Significant Enriched GO Terms When Comparing 3 Days Nerve Block to the Sham Control
For Each GO Term the table details the GO Term ID, the P value indicating how statistically significantly enriched the GO term is in this analysis, the experimental count (Exp Count) which shows the number of genes within the GO term that a random selection would reveal given the number of genes within the test, the actual number of enriched genes the test revealed within the GO Term (Count), the number of genes contained within the whole GO Term (Size) and the term name.

The 14 tables were scrutinised using knowledge of the surrounding literature. Firstly, GO Terms were identified that might be expected to be enriched within this experimental model. These GO Terms were used to validate the model before pursuing novel findings.

5.5.1 Method Validation

The tables were initially scrutinised for enriched GO terms that were most obviously related to skeletal muscle. Numerous examples of such enriched GO terms were seen across the tables. Two examples were chosen; GO:0007515 'Muscle Organ Development' (figure 32) and GO:0055001 'Muscle Cell Development' (figure 33). The figures show correlation heatmaps of the statistically significant genes within the enriched GO Term analysed using unsupervised hierarchical clustering over the experimental time period. Each row shows the expression intensity of one gene on each of the 24 arrays from sham control to electrical stimulation having been scaled to remove absolute expression and the degree of expression. This allowed the changes in patterns of change to be more easily recognised.

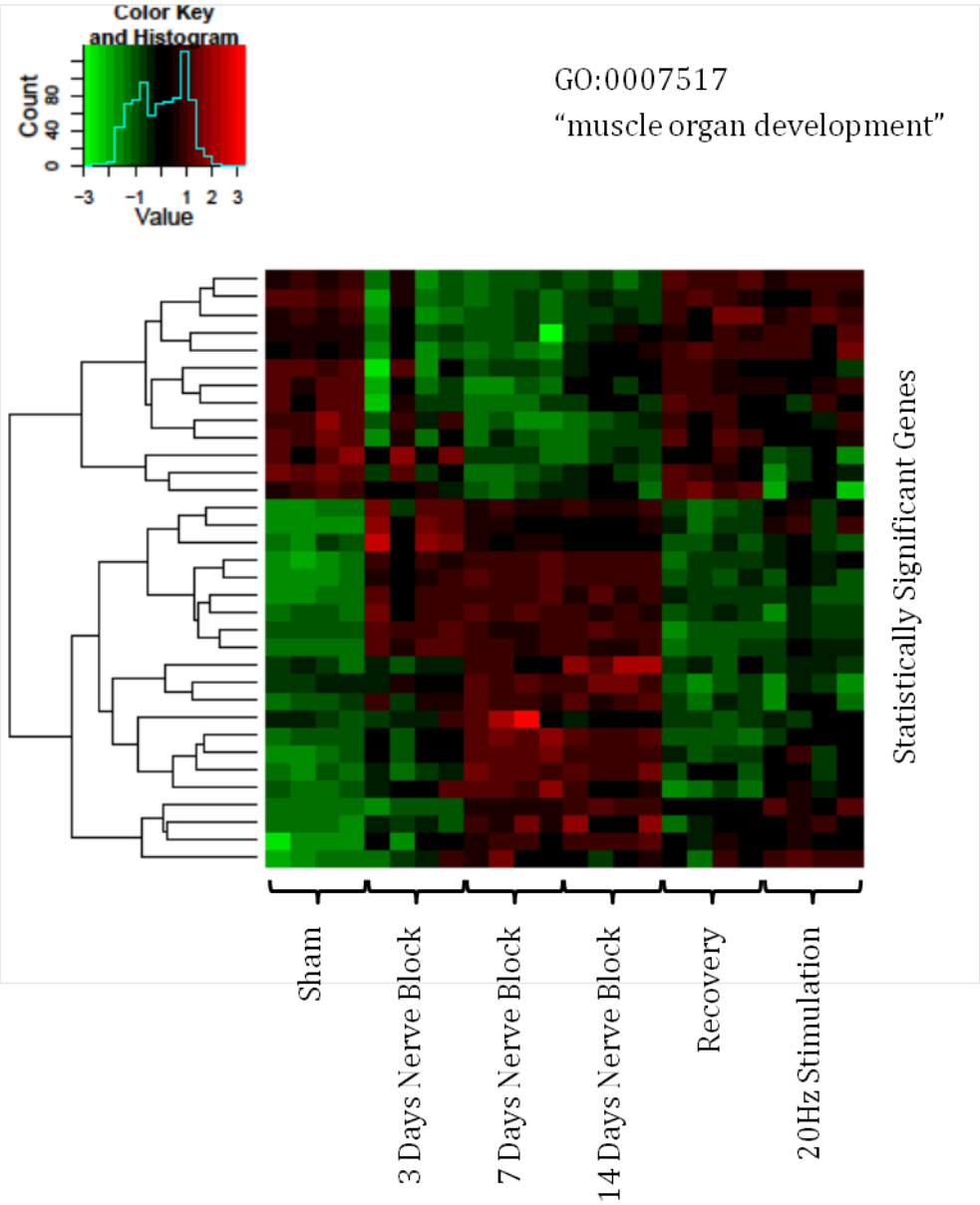

Figure 32 A Correlation Heatmap of the Statistically Significant Genes Within the Go Term 'Muscle Organ Development'

A correlation heatmap of the statistically significant ($p<0.2$) genes that are shown within one enriched GO (Gene Ontology) term , 'GO:0007515', identified following a hypergeometric test for all GO terms on each gene set.

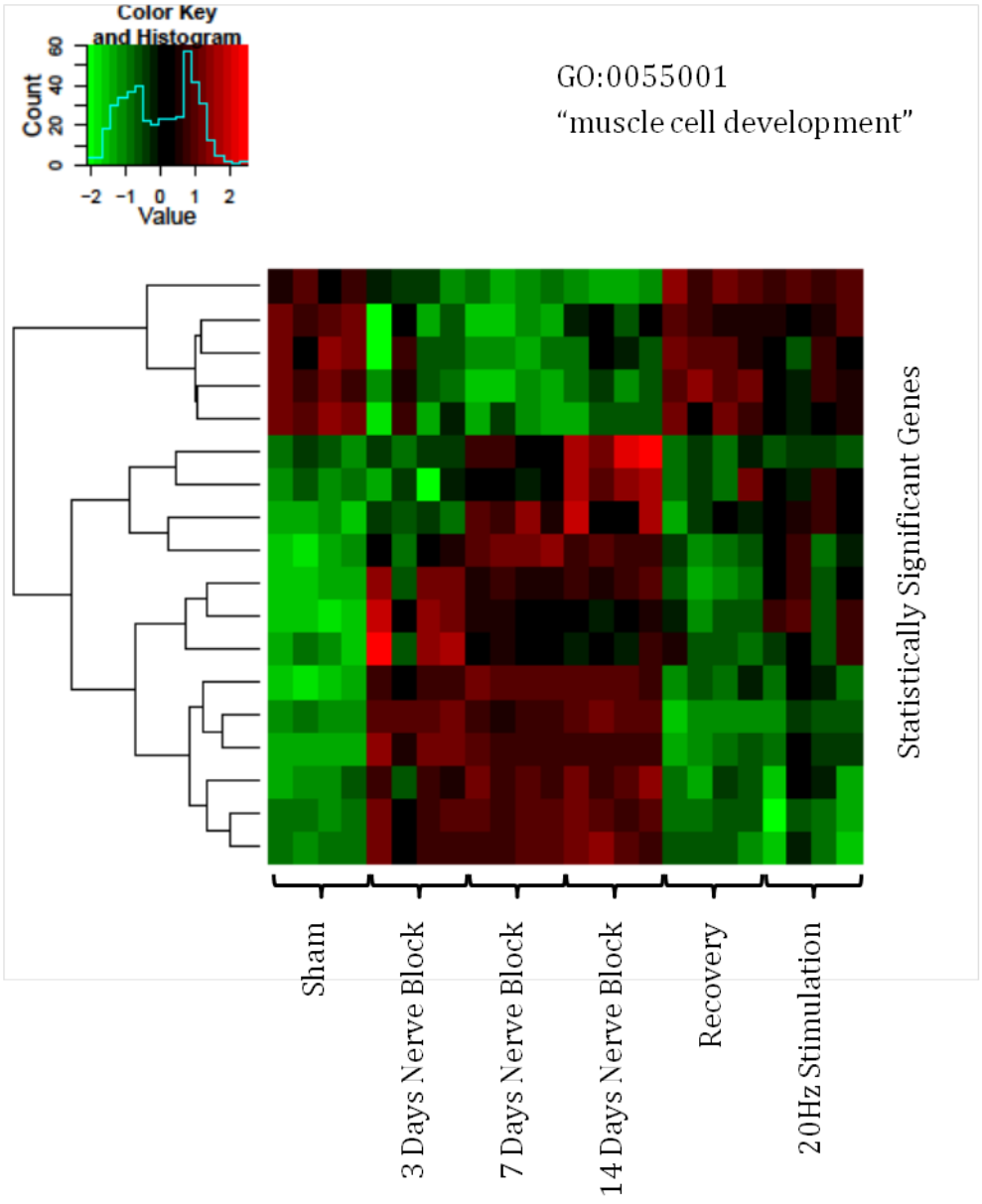

Figure 33 A Correlation Heatmap of the Statistically Significant Genes Within the Go Term 'Muscle Cell Development'

A correlation heatmap of the statistically significant ($p<0.2$) genes that are shown within one enriched GO (Gene Ontology) term , 'GO:0055001', identified following a hypergeometric test for all GO terms on each gene set.

Both Figures 32 and 33 show sets of genes that show significant patterns of change within GO Terms based around skeletal muscle. The individual gene names are excluded from the figure as the focus is on the pattern of change within the set of genes rather than the changes and significance of individual genes.

The focus of the analyses moved next to investigating enrichment within the GO Terms that would be expected on the basis of physiological effects following application of our experimental model. The GO Term 'cellular respiration' was enriched within a number of the comparisons and gene clusters. A correlation heatmap of the statistically significant genes within the enriched GO Term 'cellular respiration' is shown in figure 34 panel A. The mean intensity values for all the genes within in each experimental group are shown as a bar plot on figure 34 panel B. Genes associated with cellular respiration showed an overall drop in expression during nerve blockade. This is consistent with a fall in cellular respiration rate concomitant with decreased muscle activity. A rise in respiration rates would be expected upon recovery from nerve block, and is indeed observed Also in line with expectations was the rise in cellular respiration with the increased muscle activity associated with electrical stimulation (figure 34).

Therefore initial analysis of the expression data confirmed that enriched GO terms are consistent with the tissue type and its physiological condition. The next stage was to scrutinise the enriched GO term tables for terms that could be used in subsequent analysis to shed light on the process of skeletal muscle atrophy through the generation of new hypotheses.

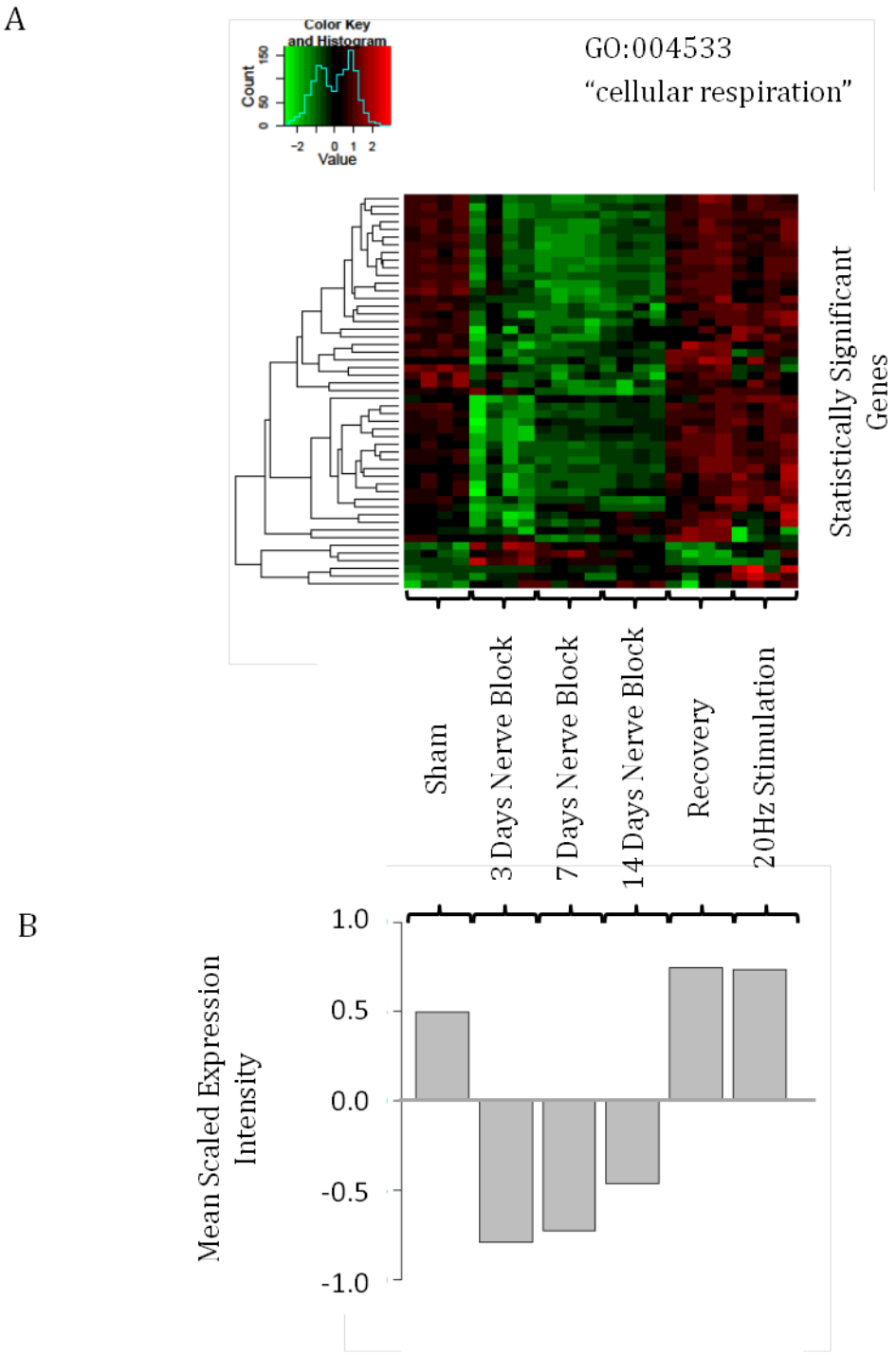

Figure 34 Patterns of Changes in Expression Over Experimental Groups of Statistically Significant Genes Within the Go Term 'Cellular Respiration'

Panel A shows a correlation heatmap of the statistically significant ($p<0.2$) genes that are shown within one enriched GO (Gene Ontology) term , 'GO:004533', identified following a hypergeometric test for all GO terms on each gene set. The mean values for all genes in each experimental group are displayed in panel B.

5.5.2 The Role of The Neuromuscular Junction in *In Vivo* Muscle Atrophy

The GO term GO:0031594 'neuromuscular junction' was enriched following TTX nerve block. As the TTX block model stops all activity at the neuromuscular junction (NMJ) changes of associated transcripts may be expected. A correlation heatmap of the statistically significant genes within this GO Term, analysed using unsupervised hierarchical clustering over the experimental time period is shown in figure 35 panel A. The mean intensity values for all the genes within in each experimental group are shown as a bar plot on figure 35 panel B. Overall, an increase in expression of the genes associated with the term 'neuromuscular junction' was observed during nerve blockade, compared to a relatively low basal level in the sham controls. This finding suggested that when the nerve block was in place and the activity of the NMJs within the muscle was silenced, a negative feedback loop in the muscle increases the expression of genes associated with the NMJ.

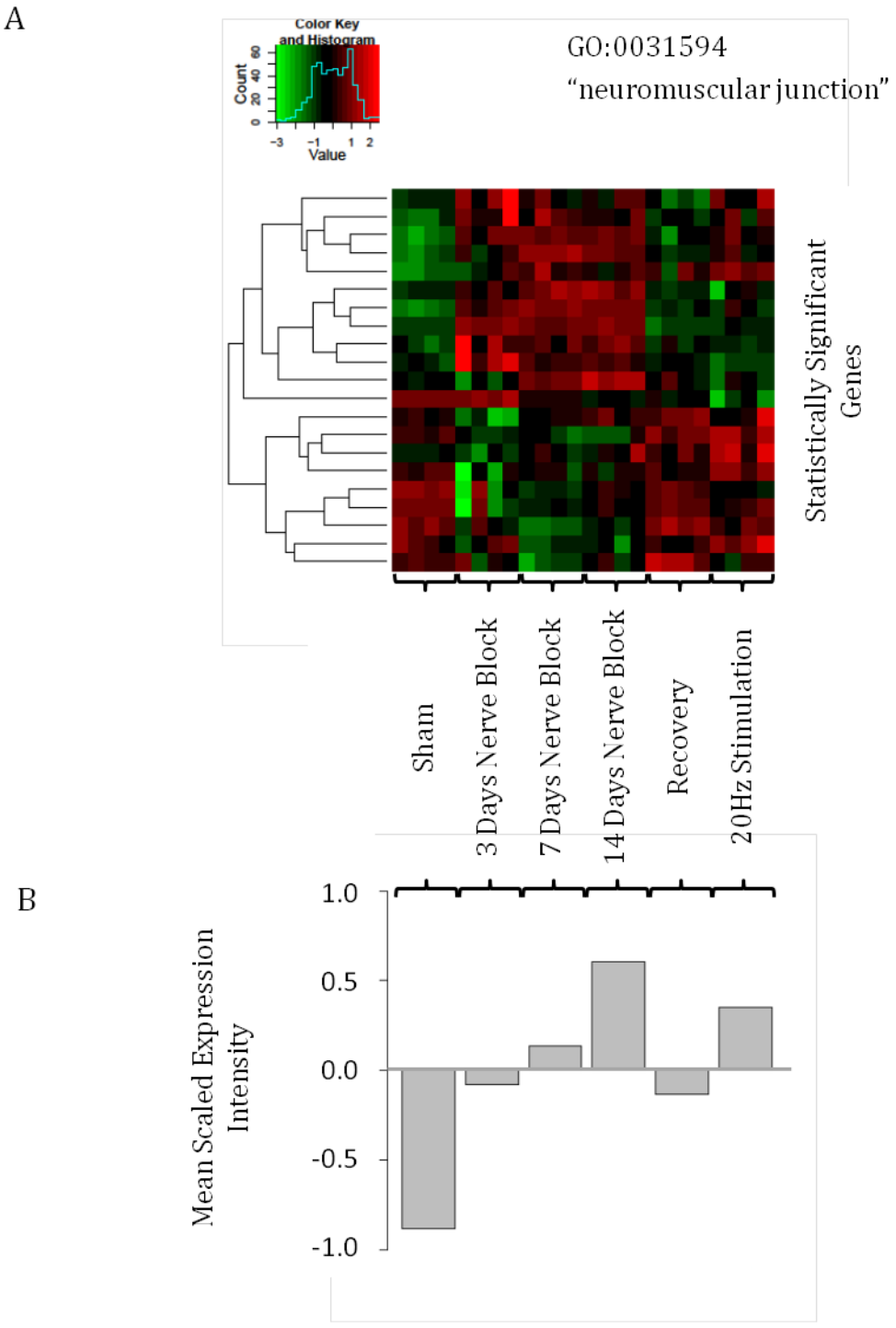

Figure 35 Patterns of Changes in Expression Over Experimental Groups of Statistically Significant Genes Within the Go Term 'Neuromuscular Junction'
Panel A shows a correlation heatmap of the statistically significant ($p<0.2$) genes that are shown within one enriched GO (Gene Ontology) term , 'GO:0031594', identified following a hypergeometric test for all GO terms on each gene set. The mean values for all genes in each experimental group are displayed in panel B.

The muscle specific nicotinic acetyl choline receptor (nAchR) subunit alpha 1 (Chrna1) was one of the genes within the enriched GO term 'neuromuscular junction', shown in figure 35. This result was investigated further by isolating the expression intensities of the other subunits that make up the nAChRs within the NMJ. Nicotinic receptors are made up of five subunits, arranged symmetrically around a central pore. In the muscle-type receptors, found at the neuromuscular junction, receptors are either the embryonic form consisting of, α1, β1, δ, and γ subunits in a 2:1:1:1 ratio, or the adult form composed of α1, β1, δ, and ε subunits in a 2:1:1:1 ratio. The mean expression intensities in experimental groups of each of the subunits, are shown in figure 36.

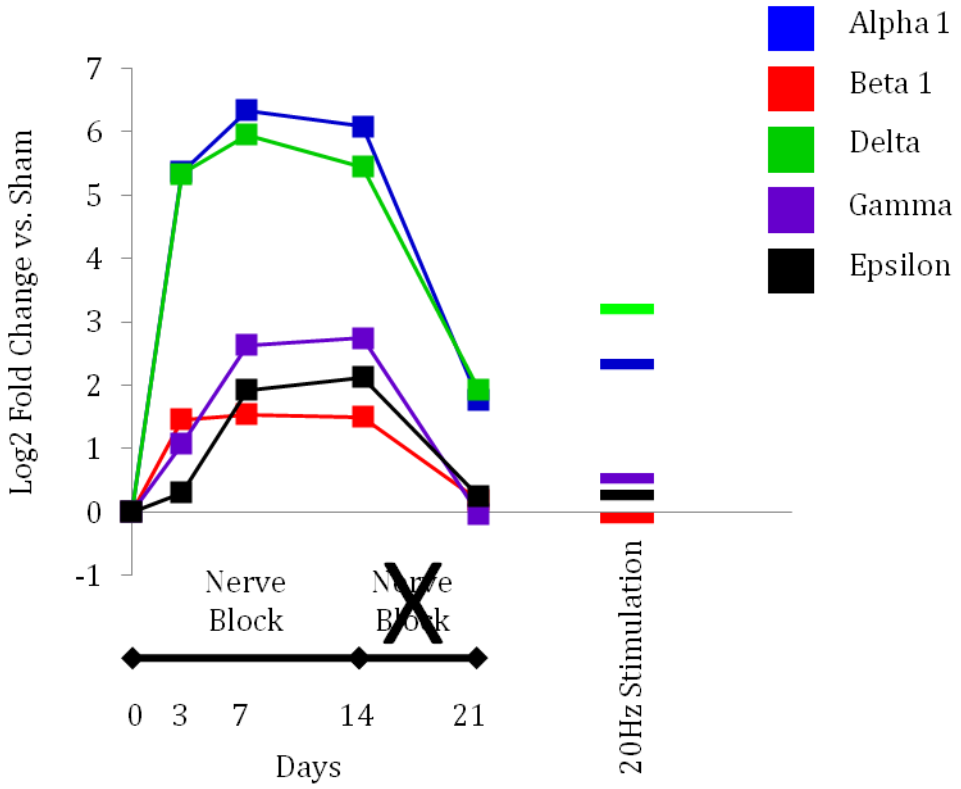

Figure 36 Mean Expression Intensity Levels of Nicotinic Acetyl Choline Receptor (nAChR) Subunits Over Experimental Groups
Mean (*n*=4 per experimental group) expression intensity from arrays over the experimental time course of induced atrophy and recovery, with 20Hz electrical stimulation shown as a separate value. All data are expressed as a $\log_2$ fold change relative to expression in the sham controls.

All 5 subunits showed an increase in expression during nerve block. The largest increases were observed in the alpha and delta subunits, which increased between 2

and 3 fold upon nerve blockade. Expression levels of all the subunits fell back towards sham control levels upon recovery. Only the alpha and delta subunits showed a substantial increase in transcript expression in response to electrical stimulation at 20Hz.

5.5.3 The Role of Cytokine Signalling in *In Vivo* Muscle Atrophy

Next, the ontology analysis was refined further by restriction of the GO terms to those involved in cellular signalling. This restriction generated further tables of enriched GO terms, based upon the original comparisons outlined in table 11. The GO term GO:0019221 'cytokine-mediated signalling pathway' was present in several of the tables including 7 days of TTX block vs. sham control. A correlation heatmap of the statistically significant genes within this enriched GO Term using unsupervised hierarchical clustering over the experimental groups is shown in figure 37.

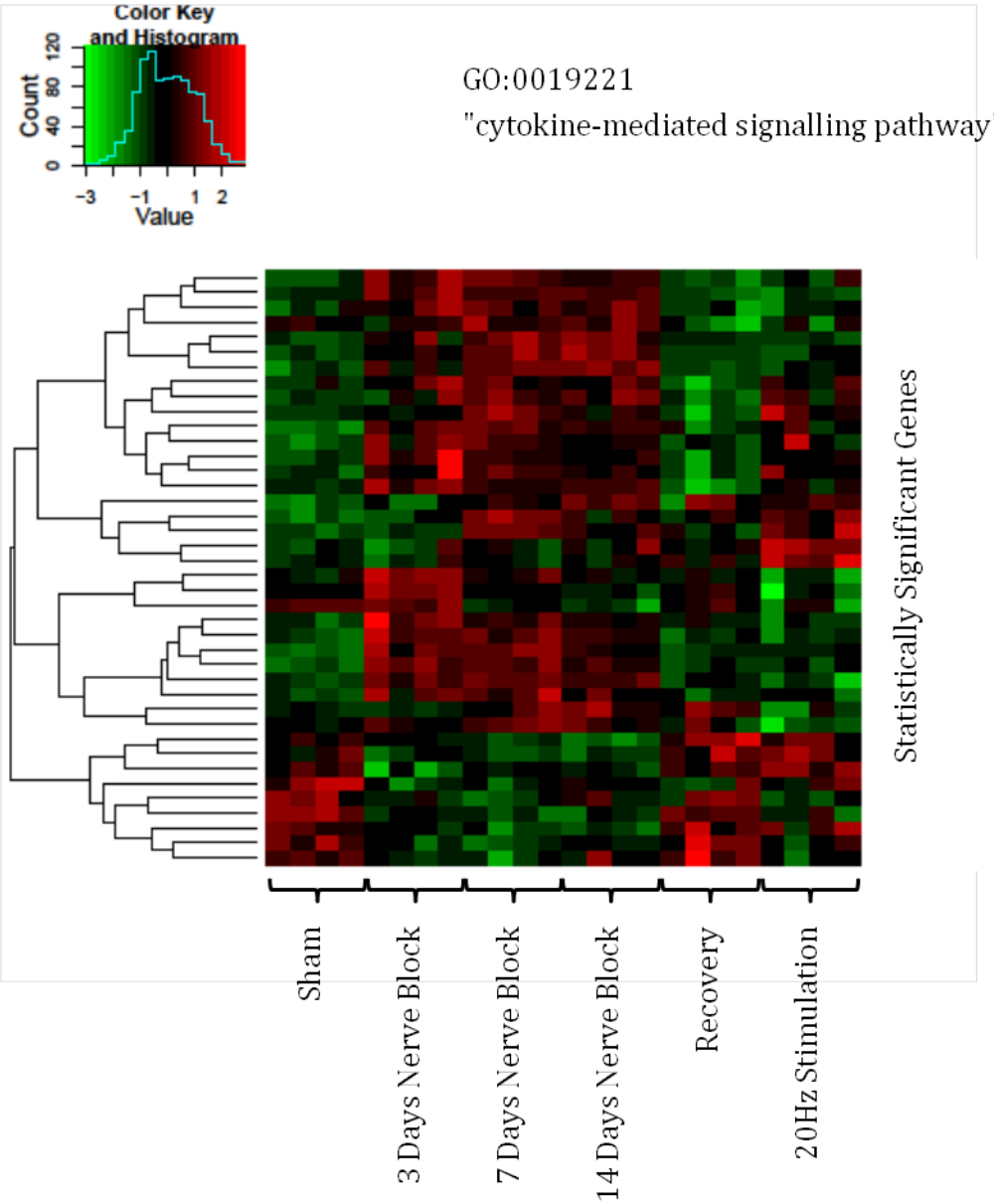

Figure 37 A Correlation Heatmap of the Statistically Significant Genes Within the Go Term ' Cytokine-Mediated Signalling Pathway'

A correlation heatmap of the statistically significant ($p<0.2$) genes that are shown within one enriched GO (Gene Ontology) term , ' GO:0019221', identified following a hypergeometric test for all GO terms on each gene set.

The statistically significant genes whose expression changed upon nerve blockade (figure 37) included a number that map to the Janus Kinase (Jak)/ Signal-Transducer and Activator of Transcription (Stat) pathway, specifically Jak1, Jak2, Stat3 and Stat5b. The mean expression intensities in experimental groups of each of the Jak family members (Jak1, 2 and 3) are shown in figure 38.

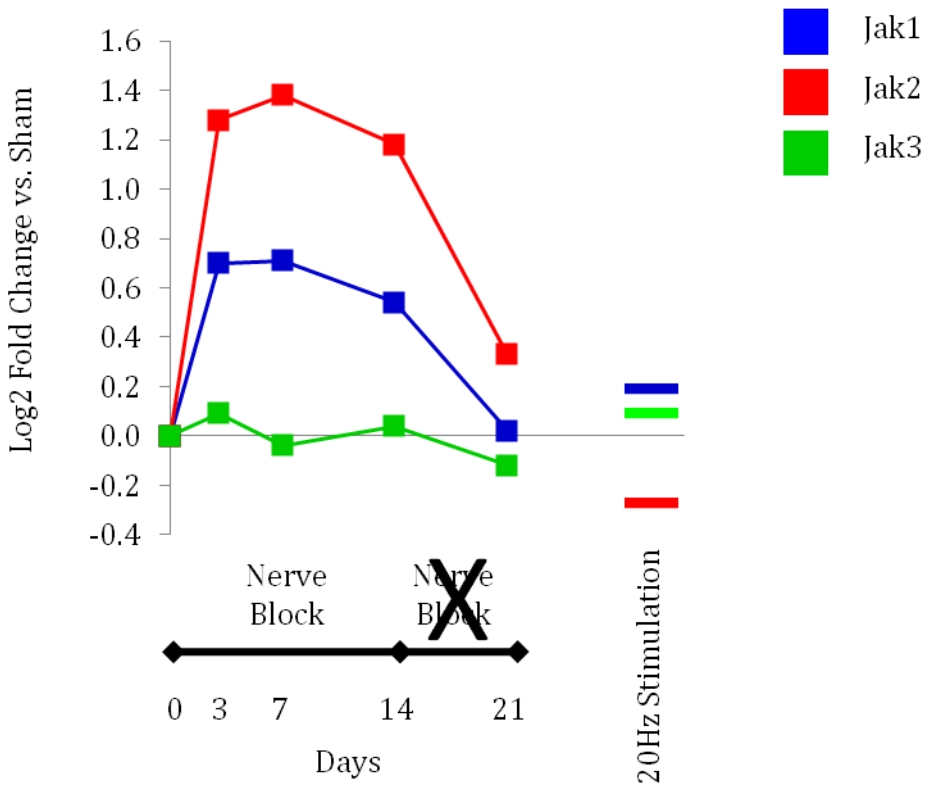

Figure 38 Mean Expression Intensity Levels of Janus Kinases (Jaks) Over Experimental Time Period

Mean (n=4 arrays per experimental group) expression intensity from arrays over the experimental time course of induced atrophy, recovery and 20Hz electrical stimulation as a separate value all expressed as a $\log_2$ fold change from sham control levels.

Jak1 and 2 showed an increase in expression of around 2 fold during nerve blockade which fell back towards sham control levels upon cessation of the nerve block. Interestingly, this increase in Jak1/2 expression was not observed by electrical stimulation in the functional atrophy model.

The mean expression intensities in experimental groups of each of the Stat family members (Stat 2, 3, 4, 5a, 5b and 6) are shown in figure 39. Stat2, 3 and 5b all showed an increase in expression during nerve block with Stat2 showing a delayed response. Stat3 expression levels increased by up to 3 fold with 7 days of nerve block. Stat2 and 3 also showed an increase in expression with 20Hz electrical stimulation.

The transcript changes of the members of the Jak/Stat pathway observed in figures 38 and 39 indicated that this pathway may play a role in skeletal muscle atrophy. To our knowledge, this was a novel finding and merited further investigation

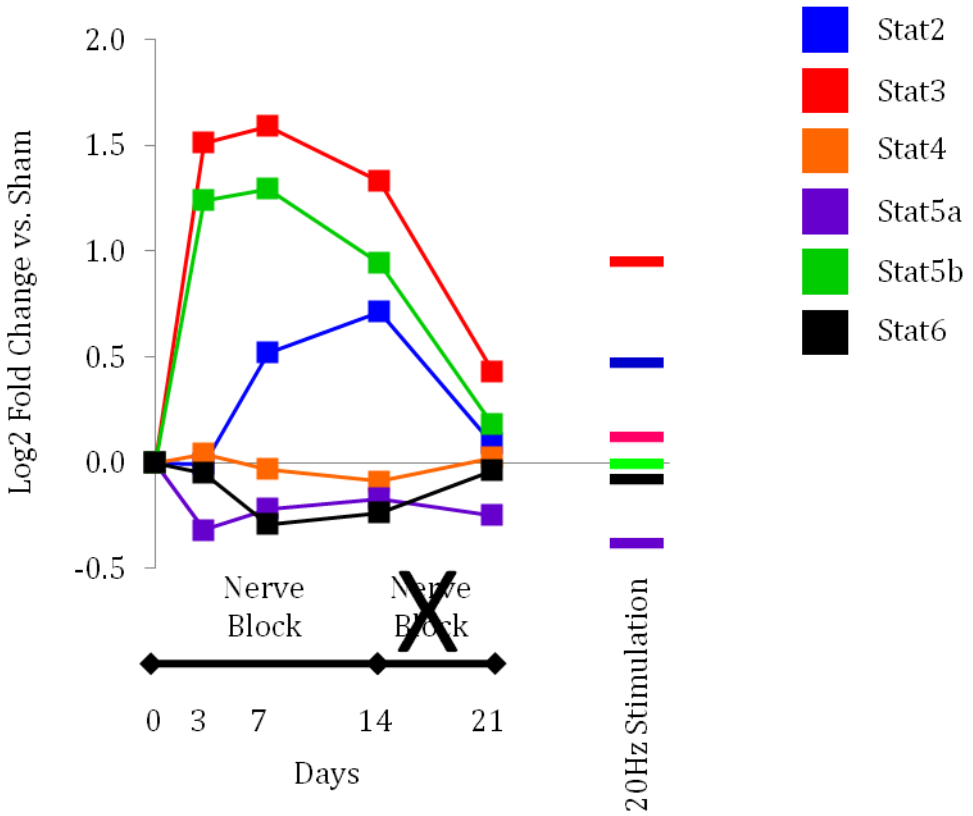

Figure 39 Mean Expression Intensity Levels of Signal-Transducer and Activator of Transcription (Stat) 2, 3, 4, 5a, 5b and 6 Over The Experimental Time Period
Mean (n=4 arrays per experimental group) expression intensity from arrays over the experimental time course of induced atrophy, recovery and 20Hz electrical stimulation as a separate value all expressed as a $\log_2$ fold change from sham control levels.

5.5.4 Modelling Atrophy Signalling Pathways From Transcriptome Profiling

By integrating current knowledge of cellular signalling pathways with the results of the microarray analysis presented in this chapter a working hypothesis was developed for the regulation of the expression of key atrophy genes. This is diagrammatically represented in figure 40. The hypothesis presents the NMJ as an integral activity sensor that controls the transcriptional expression of key genes related to atrophy through the transcription factor myogenin (Myog).

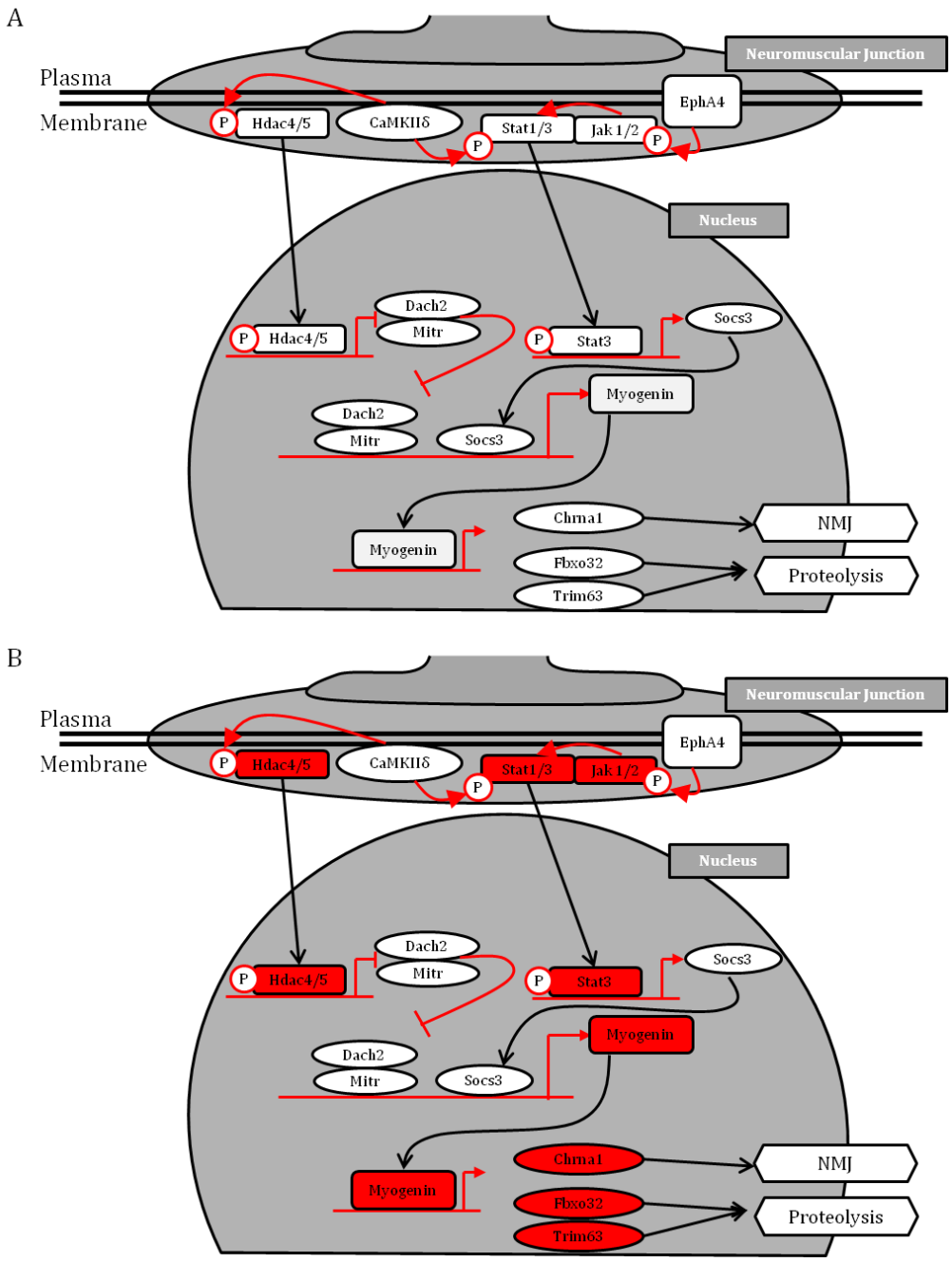

Figure 40 Transcriptome Profiling Reveals Cellular Signalling Pathways Controlling Transcriptional Expression of Genes Integral to Atrophy

A; Diagram of cellular signalling pathways centred on myogenin. Proteins are represented in text boxes with movements denoted by black arrows and red lines indicating actions. B; Transcriptional changes in this signalling network in response to atrophy stimulus measured by microarray. Red indicates an increase in transcript levels for that protein. Abbreviations - EphA4; Eph receptor A4, Jak1/2; Janus kinase 1/2, Trim63; tripartite motif-containing 63, Stat3; signal transducer and activator of transcription 3, CaMKIID; calcium/calmodulin-dependent protein kinase II delta, Hdac4; histone deacetylase 4, Hdac5; histone deacetylase 5, Mitr; a histone deacetylase 9 splice variant, Dach2; dachshund 2, Fbxo32; F-box protein 32, Trim63; tripartite motif-containing 63, Chrna1; nicotinic cholinergic receptor nicotinic (alpha polypeptide 1), Socs3; suppressor of cytokine signaling 3.

The first arm of the hypothesised signalling pathway involves the regulation of Myog by the histone deacetylase Hdac4, which was the most statistically significant differentially expressed probe set across the entire dataset (see table 12). Myog also appeared on this table as the 10th most statistically significant differentially expressed probe set across the dataset. Tang et al showed that a calcium/calmodulin-dependent protein kinase (CaMKII)-dependent phosphorylation of Myog contributes to activity-dependent suppression of nAChR gene expression in developing rat myotubes (Tang et al., 2004). Calcium/calmodulin-dependent protein kinases are serine/threonine-specific protein kinases that are regulated by the calcium/calmodulin complex, which regulates calcium signal transcduction by binding calcium ions and then modifying its interactions with various target proteins. The group linked intracellular calcium levels with the regulation of expression of nAChR subunits. The GO term 'neuromuscular junction' was found to be significantly enriched (figure35) with nerve block atrophy and the nAChR subunits were shown to increase in expression, with marked changes in the alpha and delta subunit in particular (figure 36). Studies in 2009 by the same group showed that the histone deacetylase Hdac4 was an intermediary stage in this signalling pathway (Tang et al., 2009), being phosphorylated by CaMKII, which determined its location within the muscle fibre. As calcium levels drop with number of muscle contractions, CaMKII phosphorylates Hdac4 allowing it to move into the nucleus. Here it acts to suppress the expression of a histone deacetylase 9 splice variant (Mitr) and dachshund 2 (Dach2), whose normal role is to suppress the transcription of Myog. Hence the increased expression and activity of Hdac4 increases expression of Myog. These findings were confirmed in a mouse model of skeletal muscle atrophy involving denervation (Cohen et al., 2007).

The second arm of the signalling pathways involve the regulation of Myog via the Jak/Stat signalling pathway. This pathway was highlighted as the GO term 'cytokine-mediated signalling pathway' was found to be significantly enriched (figure 37). Further investigation of the Jak and Stat family members revealed that Jak1 and 2 (figure 38) as well as Stat2, 3 and 5b (figure 39) increased in expression following nerve block. Lai et al have previously linked the ephrin type-A receptor 4 (EphA4) with Jak/Stat proteins as novel downstream targets (Lai et al., 2004). Eph receptors and their cognate ligands, the ephrins, are important players in axon guidance and neural patterning during development of the nervous system and have been shown previously to be localised in the neuromuscular junction in adult skeletal muscle (Lai et al., 2001). Suppressor of cytokine signalling 3 (Socs3) is a member of the Stat-induced Stat inhibitor family. These are cytokine-inducible negative regulators of cytokine

signalling. Socs3 mRNA expression has previously been shown to increase during myogenesis (Diao et al., 2009) with a concomitant increase in Stat3 phosphorylation and Myog expression (Spangenburg, 2005). Additionally, overexpression of Socs3 further enhanced Myog mRNA expression (Spangenburg, 2005). In turn, Macpherson et al showed in 2011, through denervation of a Myog null mouse model, that Myog can regulate the expression of the ubiquitin E3 ligases Fbxo32 and Trim63 (Macpherson et al., 2011). Trim63 was found to be the 9th most statistically significant differentially expressed probe set across the dataset (table 12).

Figure 40 panel A shows a diagrammatic representation of this combined signalling pathway. Panel B shows this diagram with each of the genes that are represented on the Affymetrix GeneChip® Rat Genome 230 2.0 Array coloured either, representing a gene whose transcripts increased during nerve block. To validate the microarray data, these changes in expression levels were confirmed using qRT-PCR as outlined in 5.6.

5.6 Confirmation of Transcriptional Changes in the Myogenin Pathway Using qRT-PCR

In order to confirm the transcript changes revealed by microarray analysis, primers were designed to key genes of interest and their transcript levels measured using qRT-PCR.

5.6.1 End Point RT-PCR Validation of Primer Sets for Microarray Genes

Forward and reverse primers were designed in rat for the genes integral to the cellular pathways as previously outlined in section 3.4. Primers for Fbxo32 and Trim63 were as previously described (see section 3.4). RT-PCR followed by 2% agarose gel electrophoresis (outlined in 2.6.6) confirmed that all primer pairs amplified a PCR product of the correct size at an optimum annealing temperature of 61 °C (figure 41 A). An RT- template was tested with each primer set to ensure there was no amplification from genomic DNA (figure 41 B). No genomic DNA contamination was found to interfere with amplification for any of the primer sets.

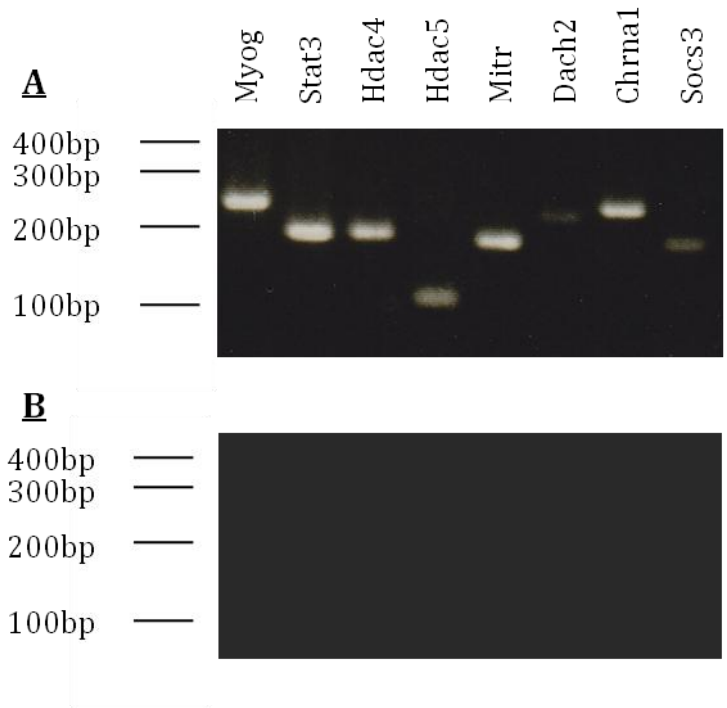

Figure 41 Specificity of Rat-Specific Primer Sets For Transcripts in Interest Identified by Microarray

End-point RT-PCR Followed by 2% agarose gel electrophoresis shows single bands of the correct size for each of the primer sets (A). An RT- template was tested with each primer set to ensure there was no amplification from genomic DNA (B). Each gel was run with a molecular weight hyperladder, whose band positions for 100-400 base pairs (bp) are shown next to each.

5.6.2 Determination of Primer Efficiency in qRT-PCR

The efficiency of the primer sets was tested using the method described in 3.4.3. The efficiency of each primer set is shown in table 14 was determined that the efficiency of all the primer sets was between 90 and 110% as recommended for use in qRT-PCR by BioRad, with the exception of Dach2. This efficiency reading could be explained by the extremely low levels of transcript, as evidenced by a weak band following end-point RT-PCR and agarose gel electrophoresis (figure 41). In subsequent analysis, Dach2 transcript levels were not able to be analysed using qRT-PCR.

Primer Name	Efficiency
Rat Myog	104.08
Rat Stat3	104.36
Rat Hdac4	100.57
Rat Hdac5	100.89
Rat Mitr	102.18
Rat Dach2	1183.39
Rat Chrna1	107.56
Rat Socs3	95.43

Table 14 Efficiency of Product Amplification During qRT-PCR for Each Primer Set
2-fold serial dilutions of a template cDNA (from control, untreated tissue) were used to generate a standard curve for each primer set. Amplification efficiency was calculated from the gradient of the linear regressions line of these curves. For subsequent analysis an optimum efficiency of between 90% and 110% was required and achieved with the exception of Dach2.

5.6.3 Comparative Transcript Changes Determined by Microarray and qRT-PCR analyses

The transcript levels for the genes involved in cellular pathway outlined in figure 40 were measured using qRT-PCR. The results, shown in figures 42, 43 and 44, are displayed using the $2^{-\Delta\Delta CT}$ method, where differences between the mean of the reference genes CT values and the target gene CT value in each muscle sample was quantified individually, then the difference between the untreated and treated samples was calculated as a fold-change. In each of the figures the transcript levels measured using qRT-PCR (n=6) are displayed alongside the mean expression intensity values which were extrapolated from the microarray data (n=4).

Figure 42 shows that transcript levels measured using both analytical methods were very similar for Hdac4 and Hdac5 with each experimental treatment. Hdac4 expression

increased with nerve blockade and remained at an increased level throughout the nerve block, returning to sham control levels upon recovery. Although the activity of Hdac4 has been reported to be controlled by phosphorylation (Tang et al., 2009), the increase in transcript level by 13.6-fold (+/- 4.5) with 14 days of nerve block will likely contribute to an increase in activity. In contrast, Hdac5 transcript levels remain relatively unchanged following nerve block by TTX treatment. These data therefore confirm the expression level changes seen following the microarray analysis. However, for the other arm of the cellular pathways outlined in 5.5.4 involving Stat3, qRT-PCR did not completely validate the microarray data. Stat3 expression levels increased when analysed using qRT-PCR in response to nerve block, however this increase seemed relatively small when compared to changes measured using microarray (figure 42, panel F). It should be noted that the changes in transcript levels measured using microarray are less quantifiable than those measured using qRT-PCR and should be used to look for patterns of change rather than absolute levels of expression. Morey et al investigated the correlation between qRT-PCR and microarray results (Morey et al., 2006) concluding that even though each method has pitfalls, the use of qRT-PCR to validate microarray was sound and the correlation was statistically significant. In the case of the Stat3 the primers used in qRT-PCR were designed to include the exon complementary to the probe sets on the microarray and were validated using end point PCR and sequenced. The seemingly different levels in change of transcriptional expression following TTX nerve block were down to the analytical methods adopted.

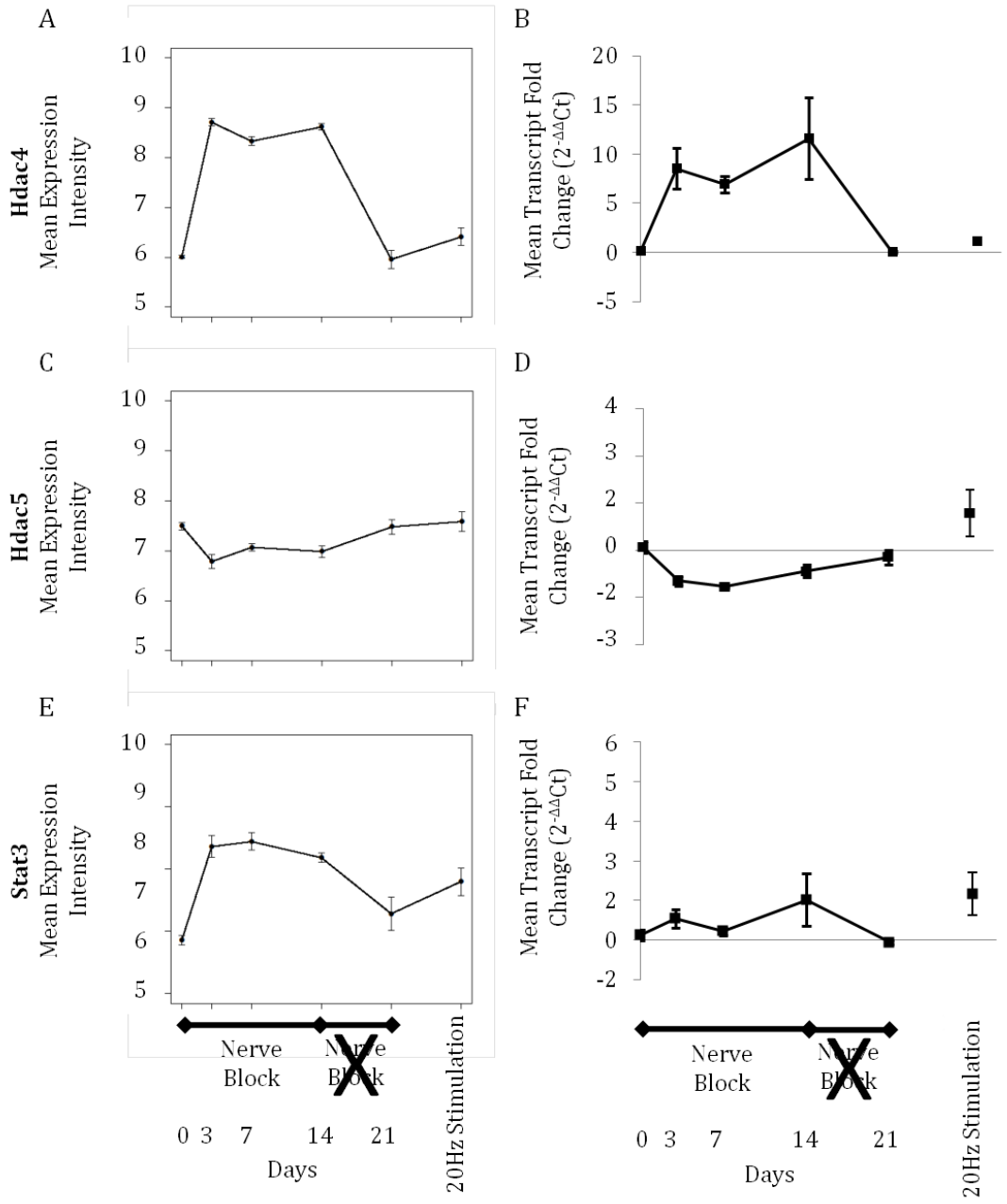

Figure 42 Comparison of Gene Transcript Levels Represented by Microarray Expression Intensity and Quantitative Reverse Transcription PCR (qRT-PCR) of Hdac4, Hdac5 & Stat3

Mean microarray expression intensity (*n*=4) of Hdac4; histone deacetylase 4 (A), Hdac5; histone deacetylase 5 (C) and Stat3; signal transducer and activator of transcription 3 (E) over the experimental groups including atrophy, recovery from atrophy and 20Hz electrical stimulation. These are compared with transcript levels of Hdac4 (B), Hdac5 (D) and Stat3 (E) in the same experimental groups measured using qRT-PCR and normalised to the mean of two housekeeping genes (Rn18s and Polr2a). Levels are expressed as fold changes from contralateral untreated control TA to treated TA sample levels (*n*=6). Error bars indicate SEM.

Further downstream in the signalling pathway (figure 43) the two forms of analysis recorded very similar transcript profiles for Socs3 and Myog. This confirmed that Socs3 transcript levels remained unchanged in response to nerve block treatment or electrical stimulation. However, Myog transcript levels show a marked increase in expression following nerve block, with expression peaking sharply 3 days after TTX treatment at a 34.1-fold (+/- 13.8) higher level in treated compared to untreated muscle. This was observed with both analysis methods. The effectors of Hdac4, Mitr and Dach2, which act as Myog supressors were harder to measure. Dach2 was not available on the Affymetrix microarray plus the transcript levels were at too low a level to measure using qRT-PCR. Data for Mitr was also not available from the microarray analysis due to the absence of probe sets for the gene on the Affymetrix GeneChip® Rat Genome 230 2.0 Array. However, qRT-PCR analysis revealed a sharp 2.8-fold (+/- 0.1)decrease in transcript levels at 3 days of nerve block. This decrease in expression was present throughout nerve block and upon cessation of the nerve block transcript levels were found to return to control levels. This decrease in Mitr would be consistent with the role in the pathway outlined in figure 40. Here the increased activity of Hdac4 reduces the transcription of Mitr, a supressor of Myog, which in turn increases the transcription of Myog.

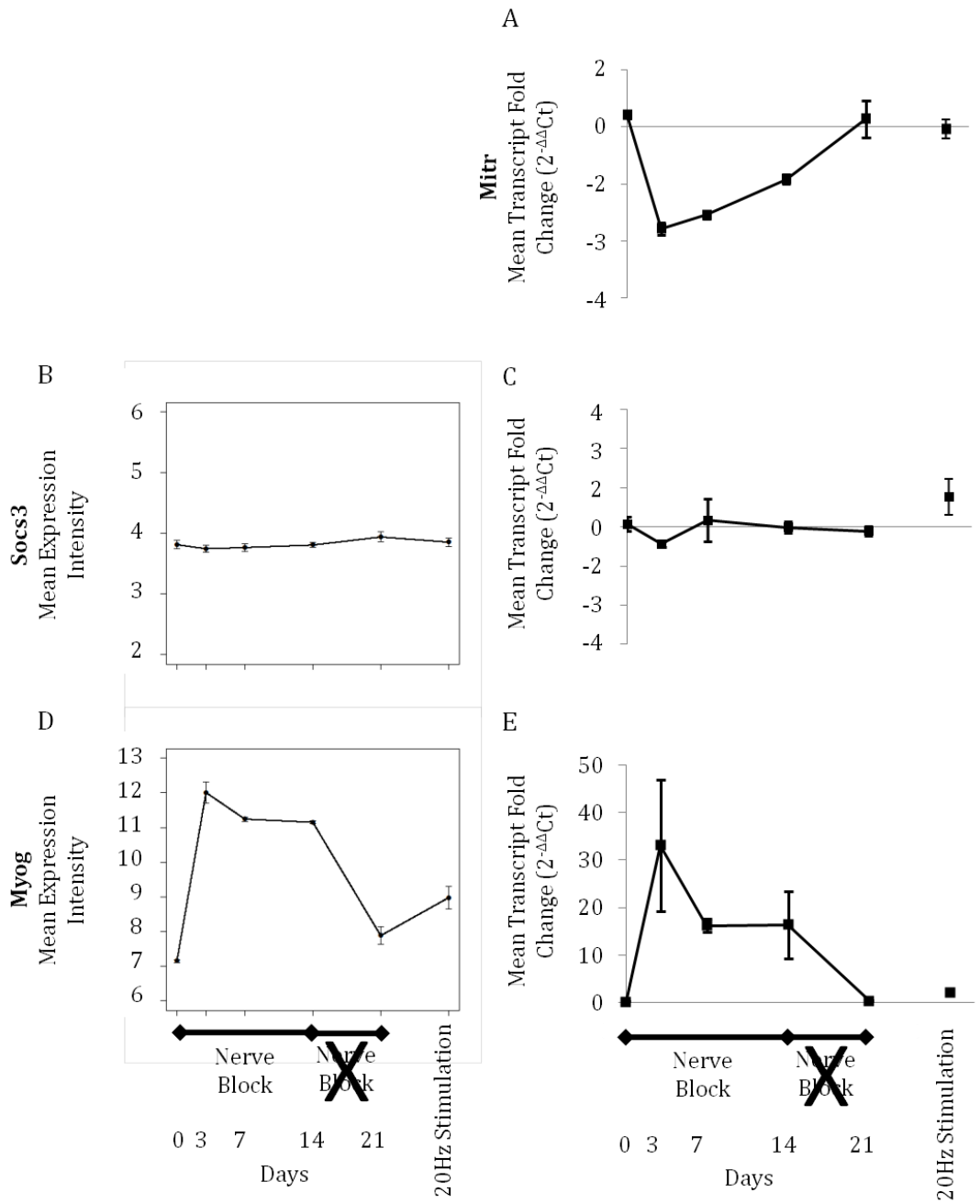

Figure 43 Comparison of Gene Transcript Levels Represented by Microarray Expression Intensity and Quantitative Reverse Transcription PCR (qRT-PCR) of Mitr, Socs3 & Myog

Mean microarray expression intensity (n=4 arrays for each experimental group) of Socs3; suppressor of cytokine signalling 3 (B) and Myogenin (D) over the experimental time period including atrophy, recovery from atrophy and 20Hz electrical stimulation. These are compared with transcript levels of Socs3 (C) and Myogenin (E) in the same experimental groups measured using qRT-PCR and normalised to two housekeeping genes (Rn18s and Polr2a). Levels are expressed as fold changes from contralateral untreated control TA to treated TA sample levels (*n*=6). Transcript levels observed using RT-PCR of Mitr; a histone deacetylase 9 splice variant, are shown in A, a probe set from this gene was not present in the microarray. Error bars indicate SEM.

Figure 44 shows the transcript levels of the Myog target genes Chrna1, Fbxo32 and Trim63, as analysed using microarray and qRT-PCR. The two methods of analysis showed similar changes in transcript levels, as well as the pattern of changes with treatment. Expression of Chrna1 increases markedly following nerve block, with qRT-PCR showing a 43.4-fold (+/- 18.4) increase in expression after 3 days rising to a 133.5-fold (+/- 15.8) and a 177.5-fold (+/-83.8) increase by 7 and 14 days respectively. Expression levels of Chrna1 measured using microarray show an increase in expression after 3 days of nerve block which is maintained at 7 and 14 days. This slight difference in pattern is due to the limited dynamic range of this detection method. The expression of Fbxo32 also increased following nerve block with a peak 4.0-fold (+/- 1.0) induction of the transcript 3 days after instigation of the nerve block. The expression levels were increased throughout the period of blockade, returning to sham control levels upon cessation of the nerve block. Both analysis methods confirmed that increases in Fbxo32 expression were most marked in the early period of nerve block. This pattern is also present in the expression of Trim63. Trim63 showed a peak increase in expression at 3 days of nerve block with a 5.1-fold (+/- 1.1) increase in transcript. The degree of increased expression with nerve block was less marked in the later period of atrophy and returned to sham control levels upon cessation of the block.

As shown in figures 42, 43 and 44, 20Hz electrical stimulation produced relatively small changes in the expression of these transcripts compared to nerve block treatment.

Figures 42, 43 and 44 show that transcript levels measured using qRT-PCR confirmed changes observed using microarray analysis. This strengthened the hypothesis set out in figure 40 that the NMJ acts as a sensor within the muscle fibre, acts through Hdac4 and the Jak/Stat signalling pathway to alter the transcriptional expression of Myog and ultimately it target genes, which are integral to muscle atrophy.

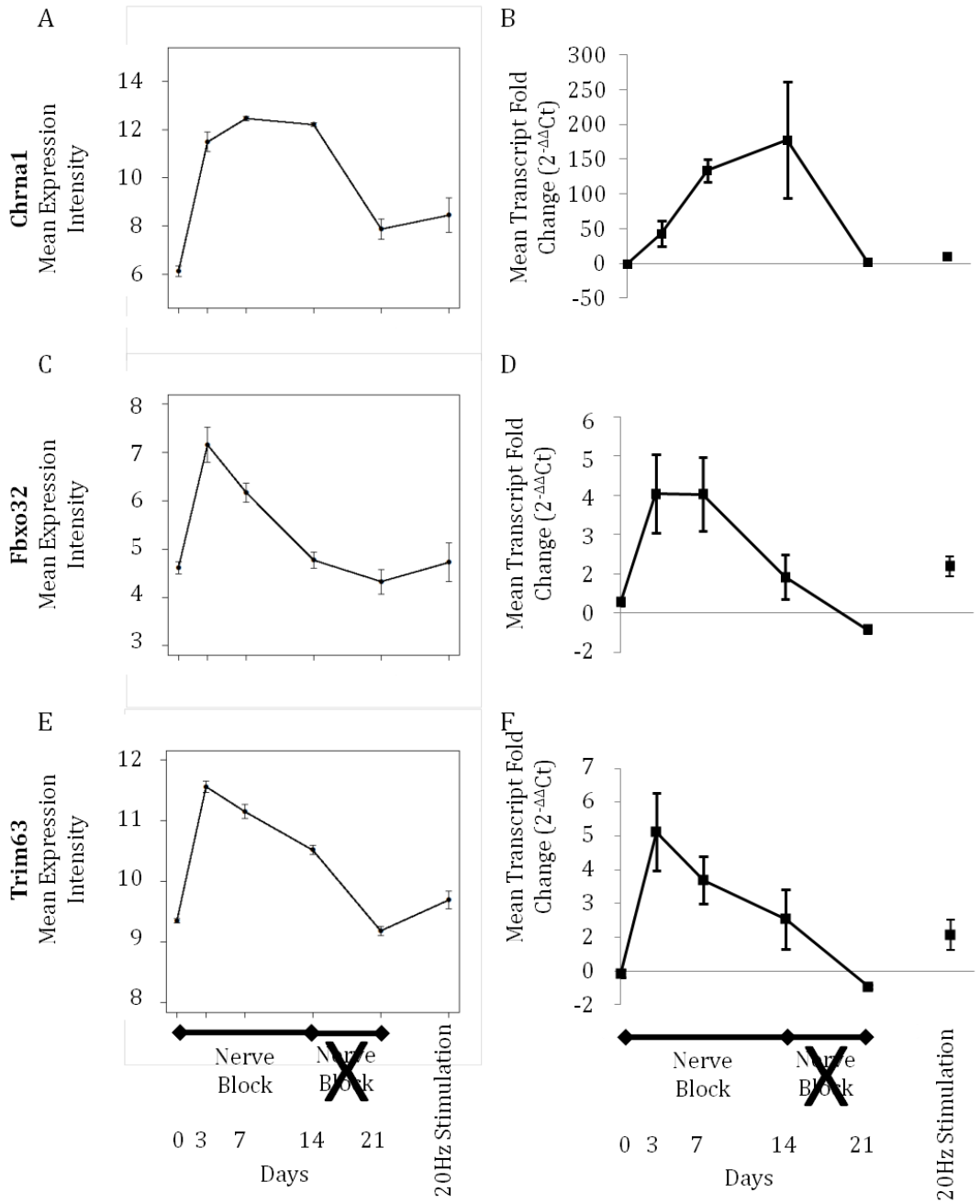

Figure 44 Comparison of Gene Transcript Levels Represented by Microarray Expression Intensity and Quantitative Reverse Transcription PCR (qRT-PCR) of Chrna1, Fbxo32 & Trim63

Mean microarray expression intensity (*n*=4 arrays for each experimental group) of Chrna1; nicotinic cholinergic receptor nicotinic (alpha polypeptide 1) (A), Fbxo32; F-box protein 32 (C) and Trim63; tripartite motif-containing 63 (E) over the experimental time period including atrophy, recovery from atrophy and 20Hz electrical stimulation. These are compared with transcript levels of Chrna1 (B), Fbxo32 (D) and Trim63 (F) in the same experimental groups measured using qRT-PCR and normalised to two housekeeping genes (Rn18s and Polr2a). Levels are expressed as fold changes from contralateral untreated control TA to treated TA sample levels (*n*=6). Error bars indicate SEM.

5.7 Discussion

Microarray analysis was used to compare genome-wide transcript changes following 3, 7 and 14 days of nerve blockade, in addition to 14 days of nerve block with 7 days of recovery, or 7 days electrical stimulation at 20Hz. Raw array data was assessed for quality using arrayQualityMetrics and normalised using the RMA method. Data was further analysed using Bioconductor within R.

5.7.1 Preliminary Analysis Reveals Nerve Block Atrophy to be a Dynamic Process with Transcript Levels Recovering Upon Cessation of Block

Unbiased correlation of probe set expression across the whole genome distinguishes the nerve block atrophy groups from the electrical stimulation, recovery and sham control groups (figure 26). We can infer from this that atrophy produced using a nerve block does transcriptionally program skeletal muscle. Upon cessation of the block the transcriptional profile of the recovery group after only 7 days was strikingly more similar to that of the control than to the nerve block group. Further separation of the recovery and control groups is evident from the dendogram. This relatedness within each group was confirmed by using principal component analysis (figure 27). With this analytical approach the recovery and sham samples from distinct groups that are closely related and separate from the nerve block groups. Here we can also see that the transcriptional response over the different periods of nerve block is stratified. Samples subjected to 7 days or 14 days nerve block form distinct groups whereas the 3 day group showed greater variation but remained distinct from the sham and recovery groups. The differences between the groups were quantified using differential expression analysis (figure 28). Nerve block atrophy induced over 1500 genes to be significantly ($p<0.05$) differentially expressed (fold change>2) when compared to a sham control group. 7 days of nerve block induced 2085 genes to be differentially expressed, which is nearly 10% of the entire genome. This is compared to less than 5% of probe sets analysed by Stevenson *et al*, where hindlimb suspension was analysed by microarray (Stevenson et al., 2003). It was also observed that when comparing recovery and sham control groups there were only 85 significantly differentially expressed genes. Considering the analysis included transcript levels of nearly 30,000

genes the recovery and sham control groups can be considered near identical on this basis.

This analysis also revealed that there are different phases of the transcriptional change that occurs in response nerve block. When 14 days of atrophy was compared with the 3 day group there were 791 differentially expressed genes. However when 14 days was compared to 7 days only 34 were differentially expressed. These data suggests that there may be early (3 days) and established (7-14 days) phases of transcriptional change during nerve block atrophy. Temporal changes in gene transcripts with continued atrophy stimulus have been observed previously in hindlimb suspension model (Stevenson et al., 2003) but nothing has been previously reported with total inactivity due to nerve block. This dynamic response to nerve block was investigated further by separating the top 500 most statistically significant differentially expressed genes into clusters dependant on their patterns of change over the experimental time period (figure 30). The clusters consisted of genes which increase or decrease in expression throughout atrophy, genes which displayed a delayed increase or decrease in expression which is established later in atrophy, and genes which showed a spike increase in expression during early atrophy which is still elevated but closer to sham control levels in later atrophy(Fig 30). Almost all genes moved towards sham control levels upon recovery (21 days).

5.7.2 Microarray Analysis Distinguishes In Vivo Models of Atrophy

Global analysis of microarray data begins to distinguish the transcriptional response during nerve block atrophy, or an atrophic electrical stimulation pattern. Using both unbiased correlation heatmaps of probe set expression across the whole genome (figure 26) and principal component analysis (figure 27) it is clear that the changes in gene expression following these two treatments are markedly different. Indeed, when using differential expression analysis to compare electrical stimulation with 7 days of nerve block there were 1426 statistically significant ($P<0.05$) differentially expressed (fold change>2) genes (figure 28). Using Gene Ontology (GO) term analysis the differences between the two models were explored further. When looking at the GO term 'cellular respiration' (figure 34) nerve block and electrical stimulation had opposite effects on transcript levels of the majority of the genes within this GO term. Almost all of the 51 genes which were significantly differentially expressed within this

GO term showed a reduction in expression with nerve block compared to an increase in expression intensity with electrical stimulation. There were also marked differences in the genes associated with the signalling pathways controlling Myog after nerve block atrophy or electrical stimulation, including myogenin itself (34-fold increase with nerve block measured using qRT-PCR, no significant change with electrical stimulation; figure 43) and Chrna1 (177-fold increase with nerve block using qRT-PCR, no significant change with electrical stimulation; figure 43). These results suggest that the atrophy produced via electrical stimulation does not utilise Myog induction, but potentially exploits another pathway which ultimately produces a reduction in muscle size.

5.7.3 Myogenin May Play a Key Role in Nerve Block Atrophy

GO term analysis along with current knowledge of molecular and signalling pathways in the literature was used to generate a working hypothesis (See 5.5.3 for full details). The cellular pathway consists of two arms which originate within the neuromuscular junction and converge on the transcription factor Myog, which in turn controls the transcriptional expression of genes involved in neuromuscular junction formation and proteolysis. The first arm of the signalling pathway involves the regulation of Myog through the histone deacetylase Hdac4. The second arm of the signalling pathways involve the regulation of Myog via the Jak/Stat signalling pathway (see figure 40). The transcriptional changes, analysed from the microarray data (figure 40 panel B), were then confirmed using qRT-PCR (5.6.3).

qRT-PCR data generally correlated well with the transcriptional changes (observed by microarray analysis), following nerve block. The main exception was Stat3, which showed a smaller degree of increase in transcript levels during the nerve block when measured using qRT-PCR (figure 42) compared to the fluorescence levels measured using microarray analysis. All suitable steps had been taken to ensure the specificity of the primers used in qRT-PCR and this slight difference in levels of transcript induction recorded by the two methods of analysis was probably due to the limited quantification of fluorescence in microarray analysis. Socs3 transcript levels did not show any increase following nerve block following analysis by microarray or qRT-PCR. Thus the hypothesis that Socs3 links Stat3 activity with Myog expression (Caldow et al., 2011) was not confirmed in our analysis of the Socs3 transcript changes. However in this

study Caldow et al overexpressed Socs3 using adenovirus in primary myoblast cultures taken from human muscle tissue. These cells were not cultured in atrophy inducing differentiation media and this study simply showed a concomitant overexpression of Myog as a result of Socs3 overexpression. However, our observation from the nerve block model that Socs3 transcript levels remain unchanged during atrophy does not rule out the possibility that Socs3 could be regulated at a level other than transcription, and so still impact on the expression of Myog.

qRT-PCR validation for the transcripts of other genes of interest did however reflect the changes seen in microarray analysis. Myog transcript levels were observed to increase markedly following nerve block, with a 34-fold increase after 3 days of block (figure 43). This confirms previous studies (Macpherson et al., 2011, Moresi et al., 2010, Tang and Goldman, 2006, Tang et al., 2009) that have implied that Myog has a role in skeletal muscle atrophy. The possible control of Myog expression through the Hdac pathway was also observed following analysis using qRT-PCR. The transcript levels of Hdac4 increased through nerve block to a peak induction of almost 14-fold over control following 14 days of block. This was expected, as previous studies have shown that Hdacs are activated with denervation *in vivo* (Cohen et al., 2007, Moresi et al., 2010, Tang et al., 2009) and *in vitro* (Tang and Goldman, 2006). qRT-PCR also provided some further evidence for the Hdac4 pathway that was not evident in the original microarray data set. Importantly, the repressor of Myog expression Mitr was shown to be downregulated following nerve block (figure 43); this was not seen by microarray analysis, as there was no probe set on the genechip. This suggests that Hdac activity is indeed linked to Myog expression through Mitr as seen in other studies (Tang and Goldman, 2006, Tang et al., 2009). The levels of Hdac5 were not increased during nerve block (figure 42). Although previous studies have shown that it is the phosphorylation state that determines the activity of the Hdacs (Tang et al., 2009), the relative differences in transcript changes in Hdac4 and Hdac5 indicate that during nerve block atrophy Hdac4 expression is more dynamic, perhaps suggesting that it may play a more important role than Hdac5. This would need to be confirmed with further analysis of the phosphorylation state of both Hdac4 and Hdac5, and their localisation within the muscle fibre.

Several potential targets of Myog including Chrna1, the nAChR subunit, and the E3 ubiquitin ligases, Fbxo32 and Trim63 all increased in expression during nerve block induced atrophy when measured using microarray analysis and qRT-PCR (figure 44). The levels of Chrna1 increased by 178-fold (+/- 84) following 14 days of nerve block.

This massive fold change is due to fact that Chrna1 levels are very low in control muscle. However the induction of this gene is marked. This suggests that new NMJ formation is not active in mature muscle. However, in response to silencing of the neuronal input, the muscle begins to produce new NMJs and hence increase the sensitivity of the muscle to nerve impulses. Both Fbxo32 and Trim63 transcript levels show a peak in expression at the early phases of atrophy (4- and 5-fold respectively following 3 days block, figure 44). Although still elevated after 14 days of nerve block (2- and 2.5-fold respectively), their expression is diminished compared to that seen in the earlier phases. Upregulation of these E3 ubiquitin ligases is thus a rapid response to atrophy stimuli.

5.7.4 Summary

Microarray analysis has shown that the two *in vivo* models of atrophy utilise different cellular pathways in order to reduce muscle size. TTX nerve block produces atrophy as a dynamic process, in which the transcriptome measured using microarray analysis moves towards the control state after 7 days of recovery. Following validation using qRT-PCR, it was observed that Myog may play a central role in nerve block atrophy. Its transcription levels may be regulated through the Hdac and Jak/Stat pathways, controlled through the NMJ. Myog ultimately controls the transcription levels of genes integral to the process of muscle atrophy.

Chapter 6: Chemical Inhibition of *In Vitro* Muscle Atrophy and Comparisons With The *In Vivo* Models

6.1 Chapter Introduction

Microarray analysis of an *in vivo* atrophy model reliant on blocking muscle innervation using TTX (chapter 5) supported a cellular mechanism centred on regulating the expression of Myog through Hdac4 and/or Jak/Stat3. The two convergent pathways are detailed in section 5.5.4 and are represented in figure 45 panel A. In order to investigate the role of these same cellular pathways in other models of muscle atrophy the impact of chemical inhibitors targeted to each pathway in cultured C2C12 myotubes would be assessed.

The first arm of the pathway relies on an inducible nuclear translocation of phosphorylated Hdac4/5 into the nucleus, where it represses transcription of Dach2 and Mitr, two negative regulators of Myog. MC1568, a class II specific Hdac inhibitor (Mai et al., 2005) would inhibit the activity of Hdac4, allowing Dach2 and Mitr to suppress the transcription of Myog (as shown diagrammatically in figure 45 panel B). Previously, studies have used MC1568 in myotubes to study differentiation (Nebbioso et al., 2009), but none have studied its effect on atrophy induction. The Class I specific Hdac inhibitor MGCD0103 (Fournel et al., 2008) was used as this would not inhibit Hdac4 (Fournel et al., 2008). If, in the absence of a NMJ, a similar key cellular mechanism exists whereby Myog expression is controlled by a class II Hdac (Hdac4), the pathway should be blocked by MC1568 but unaffected by the addition of a Class I Hdac inhibitor. Previously trichostatin A (TSA) has been used to demonstrate a link between the Hdac pathway and Myog *in vitro* (Tang et al., 2009) and *in vivo* (Bricceno et al., 2012, Tang and Goldman, 2006). However TSA is a broad spectrum inhibitor that targets both Class I and Class II Hdacs. The use of specific Class I or Class II Hdac inhibitors would give greater insight into the specific Hdacs involved in the atrophy of cultured myotubes.

The second arm of the pathway initiates with phosphorylated Stat3 moving into the nucleus and activating transcription of Socs3 which in turn activates transcription of Myog (figure 45 panel C). S3I-201, inhibits Stat3 DNA-binding activity and diminishes Stat3 phosphorylation (Siddiquee et al., 2007). This would prevent the transcriptional upregulation of Socs3 and so the transcription of Myog. Stat3 inhibitors have not, to our knowledge, been previously tested in either *in vivo* or *in vitro* studies of skeletal muscle atrophy.

Through the utilisation of class II Hdac and Stat3 inhibitors the aim of this study was to selectively interfere with each of the pathways upstream of their convergence on Myog. Ultimately these chemical interventions may inhibit the atrophy process generated by glucose deprivation in cultured C2C12 myotubes, which may translate to other models of skeletal muscle atrophy.

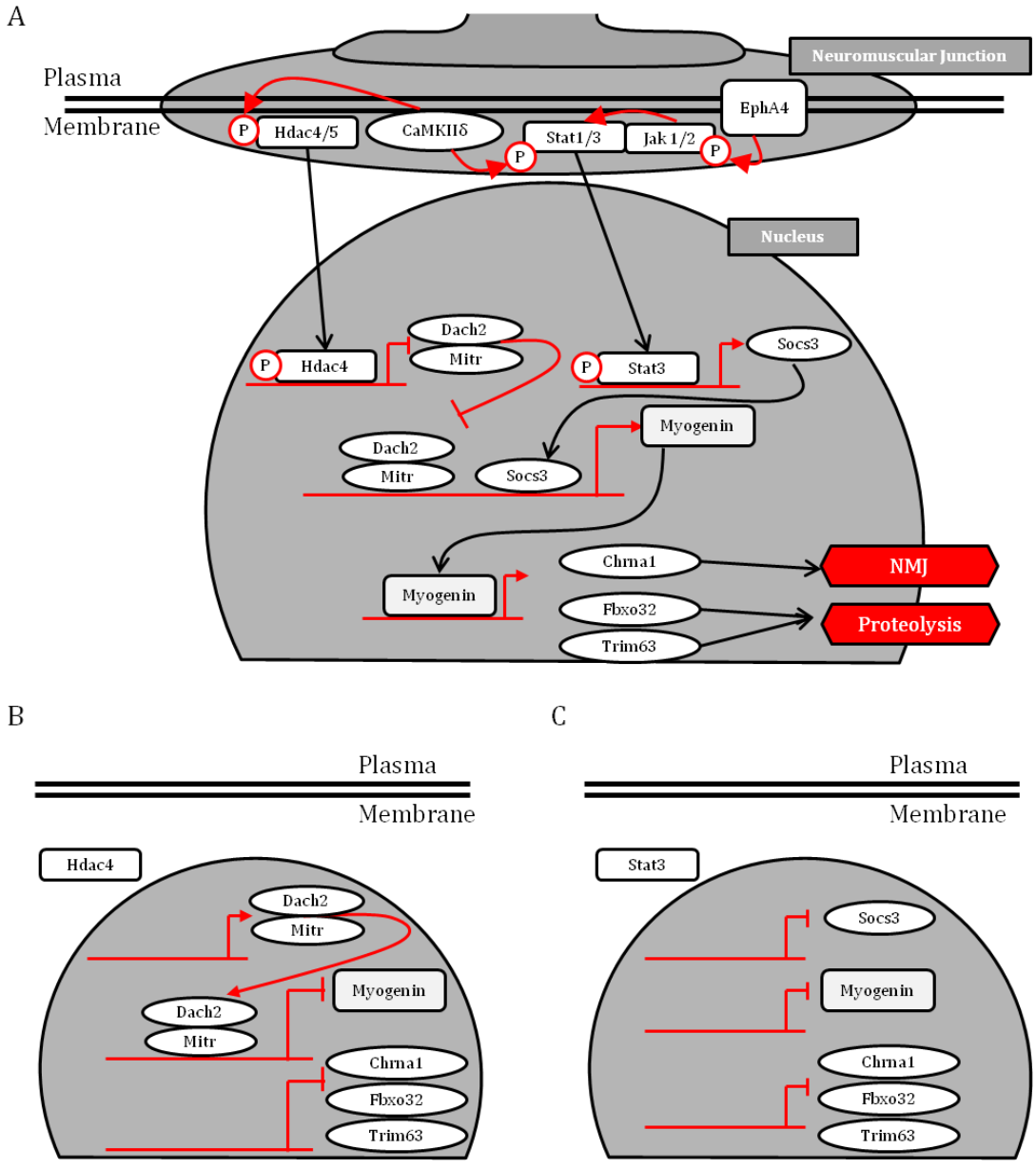

Figure 45 Chemical Inhibition of Cellular Pathways Regulating Myogenin and Its Targets

A; Two branches of the signalling pathway proposed from the *in vivo* TTX study to control the levels of transcription of myogenin and ultimately genes associated with atrophy. Possible Effects of the Hdac class II inhibitor MC1568 (B) and the Stat3 inhibitors S3I-201 (C) on myotubes undergoing glucose starvation. Abbreviations can be found in figure 40.

6.2 Atrophy Measurement Following Glucose Starvation of Myotubes

C2C12 mouse myoblasts were cultured to induce myotube formation as outlined in 2.1.1. 6 plates were treated by replacing the culture media for 24 hours with DMEM supplemented with 2% HS (Normal Media Control) and 6 were treated with DMEM, no glucose supplemented with 2% HS (Glucose Free Media) to give a total of 12 plates in the study. This experimental group was replicated a further 4 times, producing 48 plates in total. In each of these experimental groups there was an addition of a chemical inhibitor; histone deacetylase (Hdac) Class I inhibitor MGCD0103 (Selleck) at 10μM, the Hdac class II inhibitor MC1568 (Selleck) at 10μM, or the Signal Transducer and Activator of Transcription (Stat3) inhibitor S3I-201 (Selleck) at 50μM, as well as a combination of MC1568 and S3I-201 at the same concentrations. The optimal concentrations of the inhibitors were determined by a cell viability test on cultured C2C12 myotubes, using a CellTiter 96® AQueous Non-Radioactive Cell Proliferation Assay (Promega) as per the manufacturer's instructions (2.1.3).

In the main study, the degree of atrophy was measured by changes in myotube cross sectional area (CSA). The transcriptional changes in the genes integral to the working hypothesis were measured by qRT-PCR following treatment in order to further analyse the effects of the chemical inhibitors.

6.2.1 Phase Contrast Microscopy of Chemically Treated Myotubes Shows Healthy Cultures

Phase contrast microscopy was used as described in 3.2.1 to confirm intact myotubes with little evidence of apoptosis following any of the treatments (Figure 46).

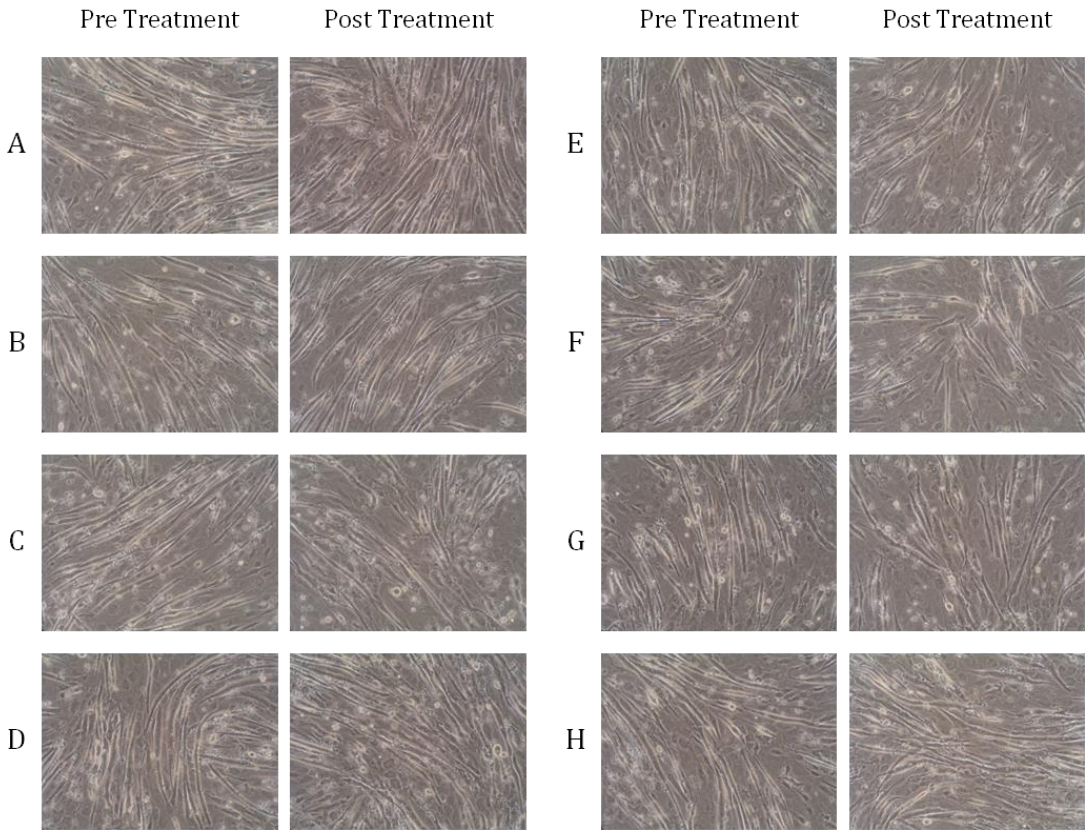

Figure 46 Phase Contrast Microscopy Showing Viable Cultured C2C12 Myotubes Before and After Each Treatment With Each Chemical Inhibitor
Photographs were taken before and after treatment for each of the 48 plates of cultured C2C12 myotubes, a representative example from each group is shown. Plates were treated for 24 hours with normal media and 10μM MC1568 (A), with glucose deficient media and 10μM MC1568 (B), normal media and 10μM MGCD0103 (C), glucose deficient media and 10μM MGCD0103 (D), normal media and 50μM S3I-201 (E), glucose deficient media and 50μM S3I-201 (F), normal media with 10μM MC1568 and 50μM S3I-201 (G) and with glucose deficient media and 10μM MC1568 and 50μM S3I-201 (H). All myotubes remained intact with little evidence of apoptosis of damage.

6.2.2 The Effects of Chemical Inhibition on Atrophy Induced by Glucose Starvation

In order to measure the degree of *in vitro* atrophy attributable to each chemical treatment, the CSA of the myotubes in culture were measured before and after treatment, and comparisons were made. The full method is outlined in 2.1.3. Figure 47 shows the effects of each chemical treatment on the degree of atrophy due to glucose starvation observed in cultured myotubes as well as the effects in myotubes cultured in normal media.

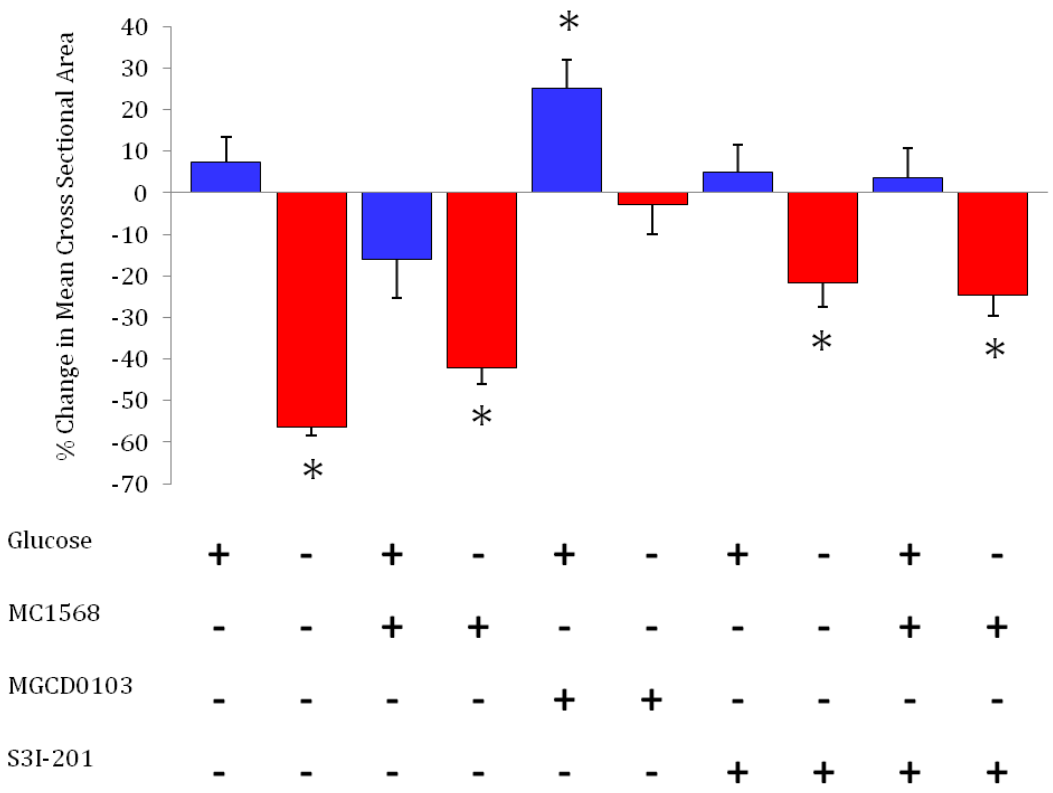

Figure 47 The Response of Myotube Cross Sectional Area (CSA) to Glucose Starvation and Inhibition of the Hdac and Jak/Stat3 Pathway
C2C12 myotubes were cultured for 24 hours in media containing glucose (blue) or no glucose (red), with MC1568, MGCD0103 and S3I-201 as indicated below each bar. CSAs were calculated by measuring the diameter of myotubes from photomicrographs. Bars indicate mean (*n*=6) changes in CSA following treatment and statistically significant ($p<0.05$) changes are indicated by an asterisk. Error bars indicate SEM.

24 hours growth in normal media containing glucose and no additional chemicals gave no significant increase in mean CSA. Incubation in glucose-free media produced a 56.36% (+/- 2.01) decrease in mean CSA compared to the same culture at time zero (Figure 47), which was shown to be statistically significant following an ANOVA test ($p<0.05$).

Myotubes cultured in normal media supplemented with the Hdac Class II inhibitor MC1568 at 10μM showed a non significant ($p=0.072$) 16.12% (+/- 9.15) decrease in CSA following treatment. However, on combining glucose starvation with 10μM MC1568, the myotube CSA still decreased significantly but now only by 42.23% (+/- 3.74). Thus the degree of atrophy produced by glucose starvation, as measured by

myotube CSA, was significantly inhibited by 14.13% by the addition of MC1568 (p= 0.008, following an ANOVA test). This is in line with the predications set out in 6.1 figure 45, if Hdac4 plays a role in atrophy in this *in vitro* starvation atrophy model.

Myotubes treated with normal media supplemented with the Stat3 inhibitor S3I-201 at 50μM showed no significant difference in changes in CSA following treatment when compared with normal media alone (p= 0.939). However, when myotubes were glucose starved with the addition of S3I-201, the CSA decreased by only 21.76% (+/- 5.71), compared to 56.36% without chemical inhibition. This difference was found to be significant following statistical testing (p= 0.00007), showing that Stat3 also plays a role in starvation atrophy.

When myotubes were treated with a combination of S3I-201 and MC1568 in normal media there was no significant change in CSA following treatment (3.66% increase +/- 7.06). However, on glucose starvation this combination treatment produced a significant (p=0.001) decrease in CSA of myotubes of 24.51% (+/- 5.15). This decrease in CSA was not significantly different from the change in CSA observed with S3I-201 alone (p=0.671), suggesting that Stat3 signalling might play a more dominant role than Hdac4 in starvation atrophy.

The addition of the class I Hdac inhibitor MGCD0103 to myotubes was intended as a control for the specifity of class II Hdacs in atrophy. However MGCD0103 at 10μM in normal media surprisingly produced a significant increase in myotube diameter of 25.19% (+/- 6.73). Even more noteably, on glucose starvation the degree of atrophy was markedly reduced in the presence of MGCD0103, which showed only a non significant (p=0.557) 2.93% (+/- 6.93) decrease in CSA. Thus chemical inhibition by MGCD0103 effectively blocked atrophy due to glucose starvation. This was in contrast to the expected effects of the chemical proposed in 6.1.

6.3 Transcriptional Changes of Cellular Pathway Genes

In order to investigate the effects of glucose starvation, as well as chemical inhibition of the Class I or Class II Hdacs and the Jak/Stat3 pathway, on cultured myotubes the transcriptional changes in genes integral to the cellular pathways outlined in figure 45 were measured using qRT-PCR.

6.3.1 End Point RT-PCR Validation of Murine Primer Pairs

As C2C12 myoblasts are murine in origin, new mouse specific RT-PCR primers were designed for the genes integral to the cellular pathways outlined in figure 45 as outlined in section 3.4. These included Hdac4, Hdac5, Stat3, Mitr, Socs3, Myogenin and Chrna1. Primers for Fbxo32 and Trim63 were designed previously (see section 3.4). RT-PCR followed by 2% agarose gel electrophoresis (outlined in 2.6.6) confirmed that all primer pairs amplified a PCR product of the correct size at an optimum annealing temperature of 61 °C (figure 48 A). An RT- template was tested with each primer pair to ensure there was no amplification from genomic DNA (figure 48 B). No genomic DNA contamination was found to interfere with amplification for any of the primer pairs.

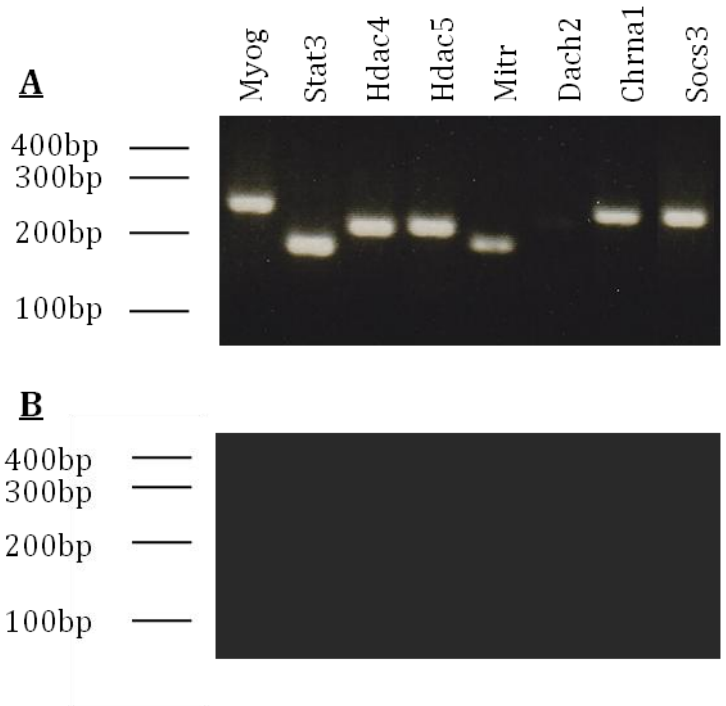

Figure 48 Specificity of Murine PCR Primer Pairs For Microarray Genes
End-point RT-PCR Followed by 2% agarose gel electrophoresis shows single bands of the correct size for each of the primer Pairs (A). An RT- template was tested with each primer pair to ensure there was no amplification from genomic DNA (B). Each gel was run with a molecular weight hyperladder, whose band positions for 100-400 base pairs (bp) are shown next to each.

6.3.2 Determination of Primer Efficiency in qRT-PCR

The amplification efficiency of all primer pairs for microarray genes was assessed using qRT-PCR as previously outlined in 3.4.3. The standard curves generated for each of the primer pairs can be found in appendix 7. It was determined that the efficiency of all the primer pairs was between 90 and 110% as recommended for use in qRT-PCR by BioRad, with the exception of Dach2. This efficiency reading could be explained by the extremely low levels of transcript, making it difficult to detect. This very low level can also be observed in figure 41, where a weak band was evident following end-point RT-PCR and agarose gel electrophoresis. In subsequent analysis, it was not possible to determine Dach2 transcript levels using qRT-PCR. The efficiency of each primer pair is shown in table 15.

Primer Name	Efficiency
Mouse Myog	105.00
Mouse Stat3	102.78
Mouse Hdac4	100.15
Mouse Hdac5	98.70
Mouse Mitr	90.62
Mouse Dach2	277.78
Mouse Chrna1	95.58
Mouse Socs3	103.36

Table 15 Efficiency of Amplification During qRT-PCR for Each Primer Pair
2-fold serial dilutions of a template cDNA (from control, untreated tissue) were used to generate a standard curve for each primer pair. Amplification efficiency was calculated from the gradient of the linear regression line of these curves. For subsequent analysis an optimum efficiency of between 90 and 110% was required, and was achieved with the exception of Dach2.

6.3.3 Overview of Transcriptional Changes

The transcript levels of each of the target genes were measured using qRT-PCR. The results were analysed by the $2^{-\Delta CT}$ method, where differences between the mean of the reference genes C_T values and the target gene C_T value in each sample was quantified individually. Figure 49 shows the transcript levels of each of the genes in each of the experimental treatment groups, in order to highlight the differences in abundance of transcripts. Evidently, Chrna1 and Myog transcript levels are relatively more abundant than the other transcripts under both normal growth conditions and glucose starvation.

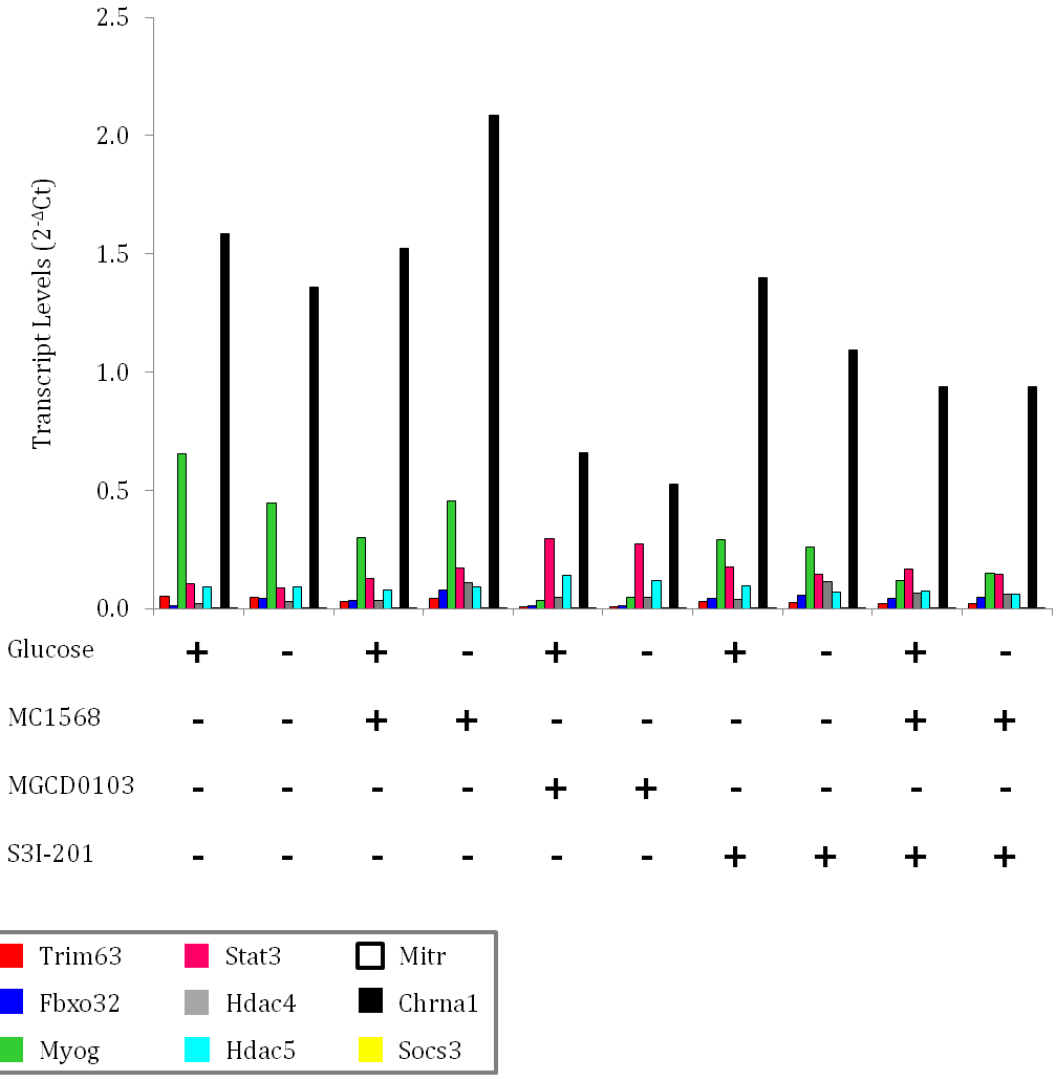

Figure 49 Mean Transcript Levels of Genes of Interest following Each Treatment *In Vitro*

C2C12 myotubes were cultured for 24 hours in media containing glucose, MC1568, MGCD0103 or S3I-201 as indicated below each set of transcripts. mRNA transcript levels were measured using qRT-PCR and normalised to the mean of two housekeeping genes (Rn18s and Polr2a) (*n*=6).

Further analysis used the $2^{-\Delta\Delta CT}$ method, where the difference between the transcript levels of each of the genes was calculated as a fold change in the treated group, compared to treatment with normal media containing no chemical inhibitors. The results from this analysis are shown in Figure 50, where the fold changes of each of the genes are displayed following each treatment. The fold change of these transcripts was highly divergent and thus the response these transcripts was further analysed by considering each of the chemical inhibitors and their effects separately (section 6.3.5, 6.3.6 and 6.3.7).

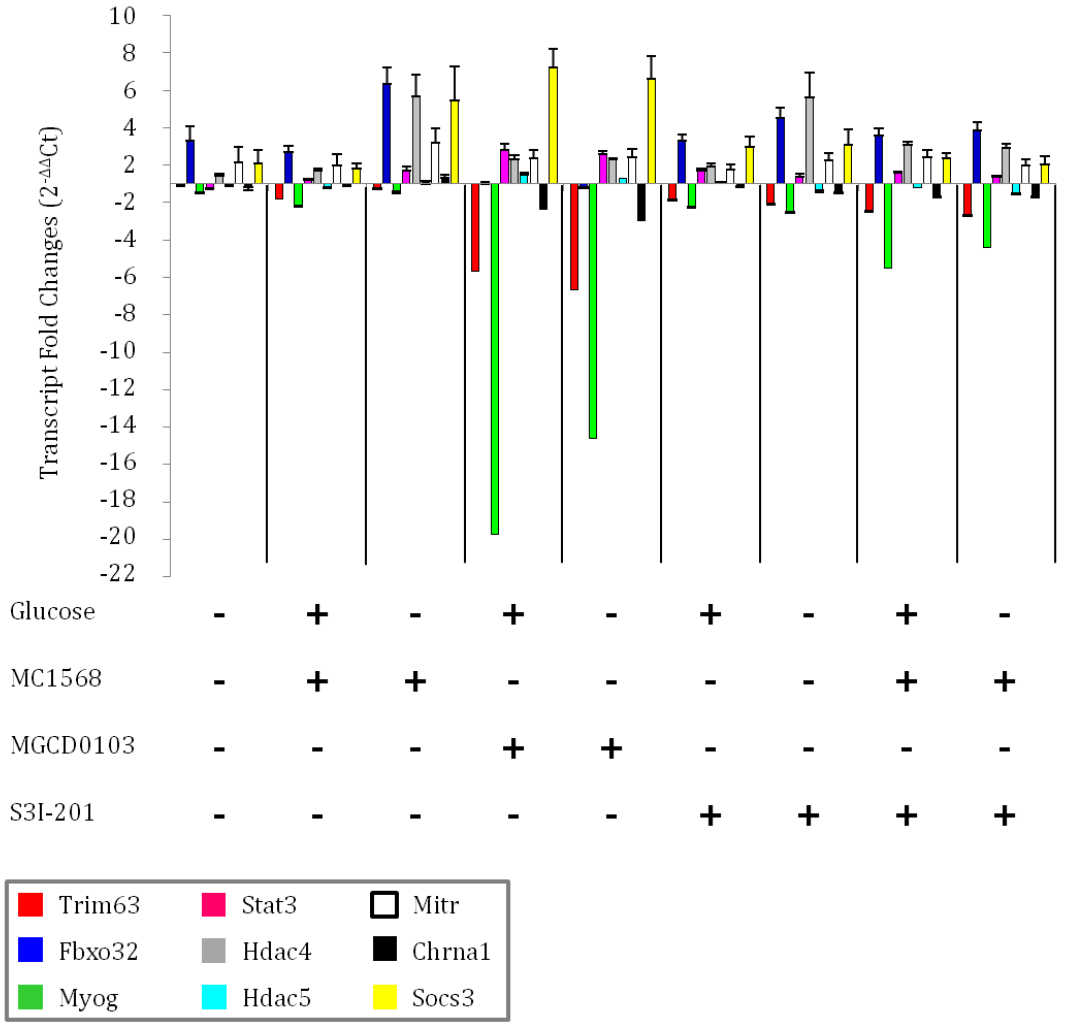

Figure 50 Mean Changes in Transcript Levels Following Treatment *In Vitro*
Treatment of cultured C2C12 myotubes included 24 hours of media containing glucose, MC1568, MGCD0103 and S3I-201, as indicated below each set of transcripts. Mean fold changes in transcript levels following treatment from normal media were measured using qRT-PCR and normalised to two housekeeping genes (Rn18s and Polr2a) (*n*=6). Error bars indicate SEM.

6.3.4 Does Glucose Starvation in Myotubes Utilise Hdac4 or Stat3 Regulation of Myogenin?

Gene expression on glucose starvation of myotubes might be expected to decrease the Myog suppressor Mitr, leading to an increase in expression of Myog and of its potential targets Fbxo32, Trim63 and Chrna1. However, when the transcript levels of these genes were analysed following glucose starvation these predicted changes were not

observed (figure 50). In fact, Mitr expression actually increased following glucose starvation with a concomitant decrease in the levels of Myog. There was however an increase in Fbxo32 levels, but no significant change in Trim63 or Chrna1 levels. These results suggest that Myog expression levels may not play a role in the myotube starvation model of atrophy, in contrast to the results found following TTX nerve block *in vivo*. The difference in the response of Myog in the *in vivo* and *in vitro* models may be related to the absence of the NMJ in the latter. Thus, it may still be possible to determine a role for Myog in the *in vitro* model of muscle atrophy with the use of chemical inhibitors which act on genes further downstream of the NMJ.

6.3.5 The Class II Hdac Inhibitor MC1568 Significantly Reduces Atrophy in Myotubes Cultured in Glucose-Free Media

When considering the effect of MC1568 on glucose starvation we compared the transcript changes following glucose starvation, with and without MC1568 (figure 51).

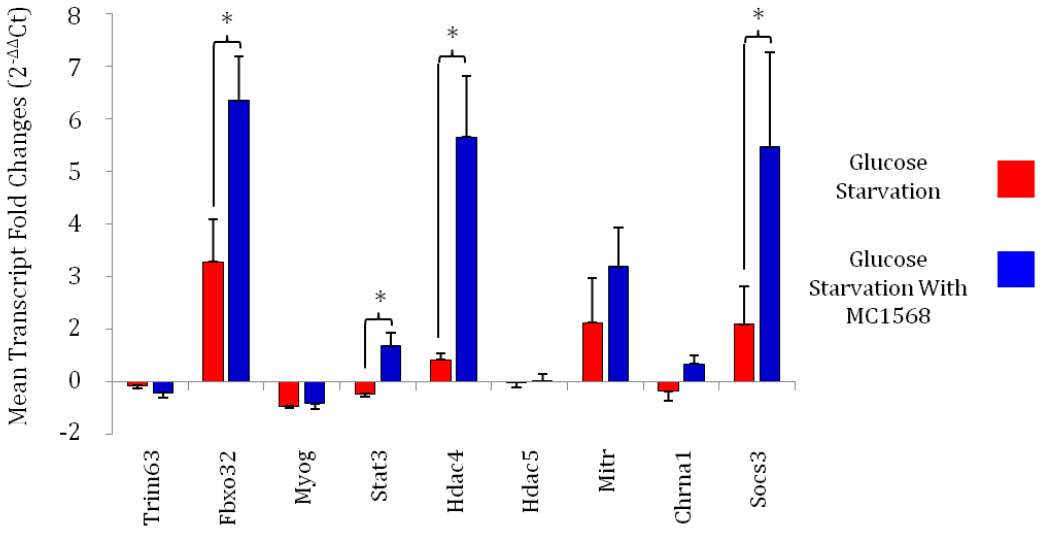

Figure 51 The Transcriptional Response of Myotubes Following Glucose Starvation with and without MC1568

Mean transcript levels were measured using qRT-PCR and normalised to the mean of two housekeeping genes (Rn18s and Polr2a). Transcript levels are represented as a fold change from myotubes treated with normal media, without chemical inhibition. Statistically significant ($p<0.05$) differences in changes in transcript levels following an ANOVA test are marked with *(n=6). Error bars indicate SEM.

There were significant increases in several genes in the presence of MC1568. Hdac4 transcript levels significantly increased after the addition of MC1568. This may be the result of a positive feedback mechanism following the inhibition of Class II Hdac activity. The significant increase in both Stat3 and Socs3 may suggest that the two arms of the cellular signalling pathways are linked. For example, the increase in the expression of Stat3 and Socs3 may be a compensatory mechanism in response to the decreased activity of the Hdac pathway. However, Myog levels remain unchanged with the addition of MC1568, suggesting that whilst the Hdac and Jak/Stat3 pathways may be affected by chemical inhibition in myotubes, there may be other downstream targets that are involved in the control of atrophy without the involvement of Myog. Furthermore, the transcript levels of the E3 ligases, targets of Myog, do not change as predicted. Levels of Trim63 remain unchanged following MC1568 treatment and Fbxo32 levels increase. As MC1568 has been shown to reduce the degree of atrophy following glucose starvation in myotubes, a decrease in the levels of these E3 ligases would be expected. However, the failure to suppress Trim63 and Fbxo32 transcript levels suggests they are not integral to the atrophy process induced by glucose starvation in myotubes, and that there is potentially an alternative mechanism governing atrophy that does not utilise the Myog pathway.

6.3.6 The Class I Hdac Inhibitor MGCD0103 Inhibits Atrophy Through Altered Myogenin Expression

Surprisingly, the most striking effects of chemical inhibition were for MGCD0103 which strongly inhibited glucose starvation atrophy, and demonstrated a hypertrophic affect under normal growth conditions (Figure 47). These changes in myotube size were accompanied by significant changes in some transcript levels, most notably the Myog, Trim63 and Chrna1 transcripts, which all decreased on addition of MGCD0103 (Figures 49 and 50).

Changes in Myog, Trim63 and Chrna1 have been considered earlier, where significant increases in these genes were observed in the TTX *in vivo* model of atrophy (Figures 43 and 44). Thus, a central role for Myog and its targets has been highlighted in both *in vivo* and *in vitro* models of atrophy. More detailed comparisons between these two models and the response of Myog and its targets are discussed further here.

Figure 52 shows the relative transcript levels of myogenin in control muscle tissue and C2C12 myotube cultures that have been grown in normal media to make comparisons between the two models at the transcript level.

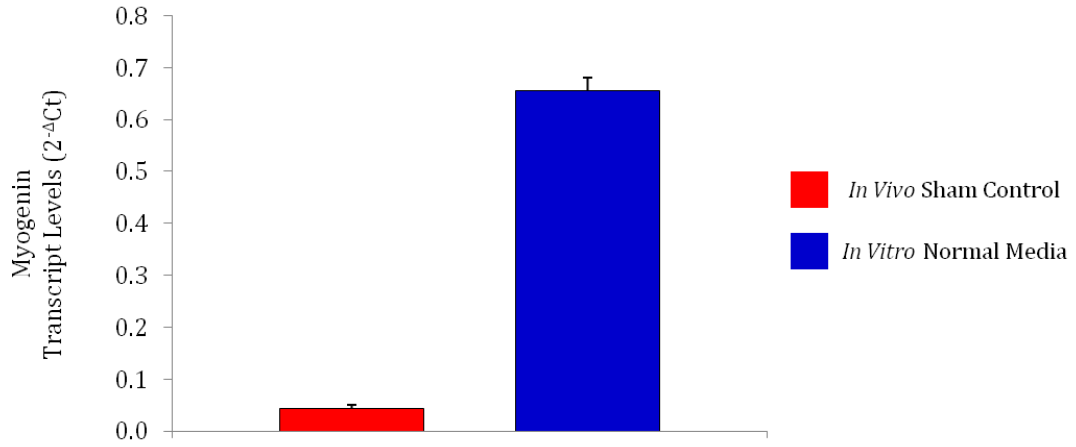

Figure 52 Myogenin Transcript Levels in *In Vivo* and *In Vitro* Models of Atrophy
Mean transcript levels were measured using qRT-PCR and normalised to the mean of two housekeeping genes (Rn18s and Polr2a). Levels were calculated using the $2^{-\Delta CT}$ method to show the relative abundance of each transcript (n=6). Error bars indicate SEM.

Lower relative basal transcript levels of Myog were observed in the *in vivo* sham control group (0.034 +/- 0.002) when compared with the *in vitro* normal media control group (0.656 +/- 0.024). This represents an 18-fold (+/- 2.61) higher transcript level of Myog in the *in vitro* control group. This difference was not unexpected as Myog is known to be involved in the differentiation of muscle cells (Hasty et al., 1993). Thus a higher expression of Myog *in vitro* is likely to be indicative of the developmental stage of the myotubes in comparison with fully differentiated muscle tissue *in vivo*. The potential consequences of this difference were explored further, to investigate whether basal transcript levels of Myog have any effect on the response of Myog during atrophy. Changes in myotube or fibre CSA were measured to determine the degree of muscle atrophy, and correlated with changes in Myog expression, to investiage further the importance of basal Myog expression.

Figure 53 shows the correlation between Myog transcript levels and the CSA of muscle fibres *in vivo* (panel A) and myotubes *in vitro* (panel B) across all the treatment groups.

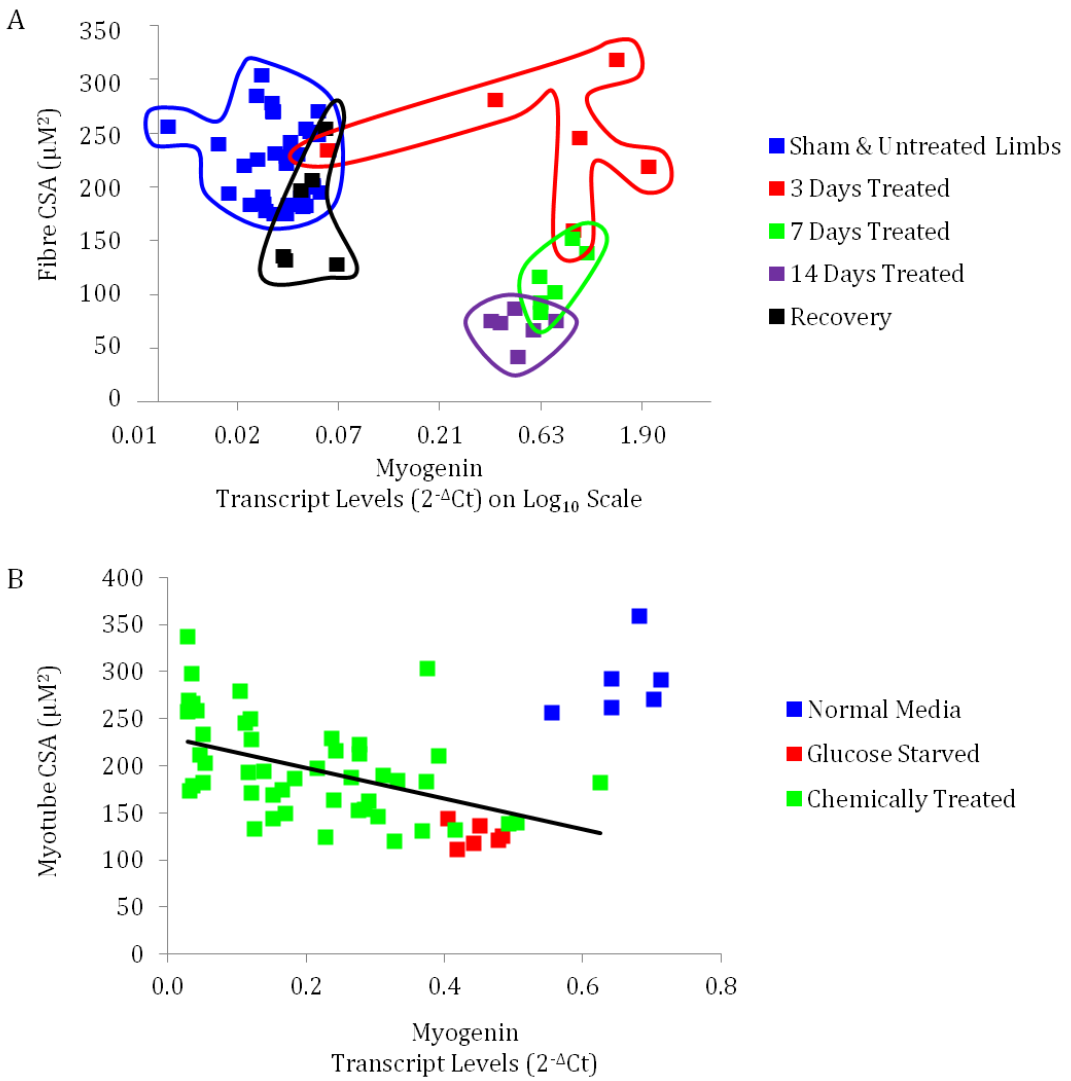

Figure 53 The Relationship Between Myogenin Transcript Levels and CSA in Muscle (A) and Myotubes (B)
Transcript levels were measured using qRT-PCR and normalised to the mean of two housekeeping genes (Rn18s and Polr2a) and are shown on the x axis of each graph. CSAs (y axis) were calculated by measuring the diameter of myotubes/muscle fibres from photomicrographs using ImageJ and scaled using a graticule.

It was observed that as Myog transcript levels increase from a relatively low basal control level *in vivo* (A) there is a delayed concomitant decrease in CSA. Following 3 days of nerve block Myog levels generally increase without a significant change in CSA. By day 7 of the nerve block the levels of Myog remain elevated with a decrease in the fibre CSA. This is further exacerbated at day 14 of the nerve block, where Myog levels remain elevated and a further decrease in CSA is observed. The delay in changes in CSA compared with changes in Myog transcript expression levels is logical since changes in transcript levels are part of the early response mechanisms which eventually lead to changes in muscle structure and function.

The *in vitro* model of atrophy revealed a pattern of negative correlation between Myog transcript levels and myotube CSA only when the myotubes were treated with inhibitors or subjected to glucose starvation (figure 53). Under normal growth conditions (which was taken as a control) the Myog/CSA correlation appears as an outlying group.

The relationship between Myog and its transcriptional targets, which significantly altered during chemical inhibition by MGCD0103, was then considered. Interestingly, both Trim63, a ubiquitin ligase, and Chrna1 transcript levels were found to decrease with a decrease in Myog (figure 50). However, the ubiquitin ligase Fbxo32 did not change, despite evidence that it is a downstream target of Myog (Moresi et al., 2010). Figure 54 shows the correlations between Myog transcript levels and the levels of each ubiquitin ligase, Trim63 and Fbxo32, both *in vitro* and *in vivo* across all experimental groups, to compare the relationship between Myog transcript levels and expression of these target genes.

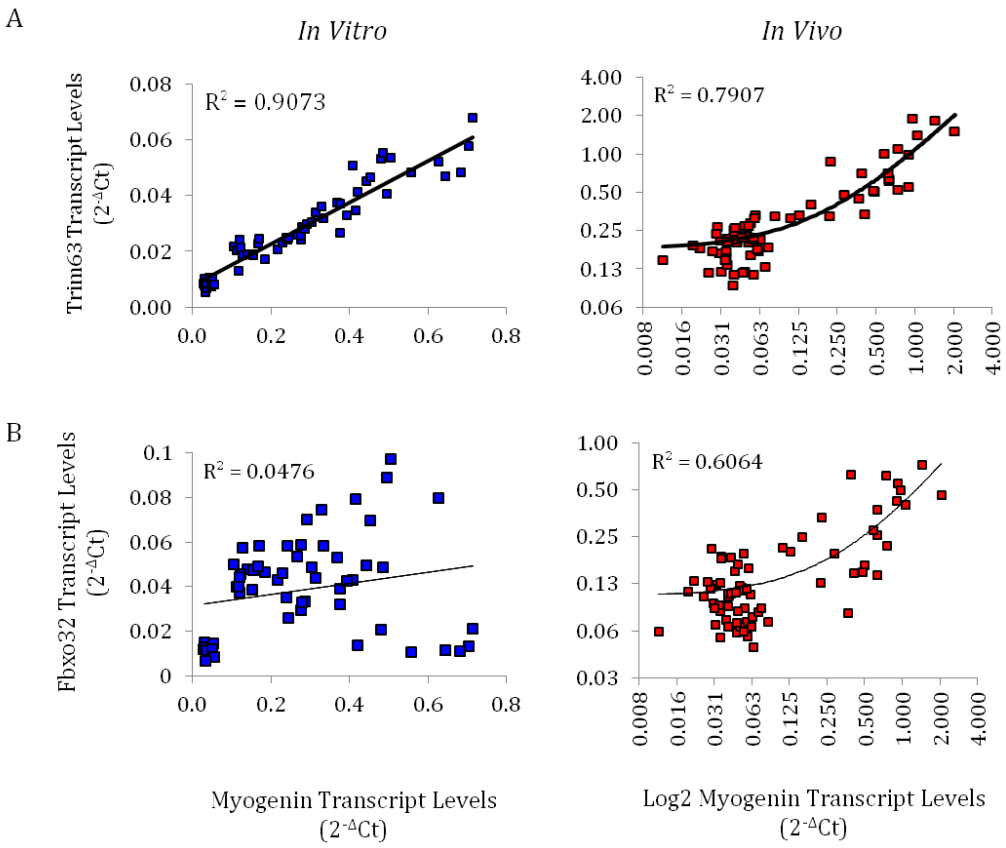

Figure 54 The Relationship Between Transcript Levels of Myog and The Ubiquitin Ligases Trim63 and Fbxo32 Both *In Vitro* and *In Vivo*
Correlations between Myog and Trim63 (A) and Myog and Fbxo32 (B) were analysed in both the *in vitro* and *in vivo* models of atrophy. Transcript levels were measured using qRT-PCR and normalised to the mean of two housekeeping genes (Rn18s and Polr2a). Correlations are determined by the coefficient of determination (R^2).

A strong positive correlation (R^2=0.9) can be seen between Myog and Trim63 transcript levels *in vitro*, which is evident to a lesser extent *in vivo* (R^2=0.7907). In contrast. Myog transcript levels showed no correlation with Fbxo32 transcript levels *in vitro*, although *in vivo* some degree of correlation was evident (R^2 0.6064). Thus the data suggests a relationship between Myog and Trim63 transcription. However, Fbxo32 may be subject to control by other upstream effectors, particularly in the *in vitro* setting.

Figure 55 shows the relationship between myogenin transcript levels and transcript levels of Chrna1 *in vitro* and *in vivo*.

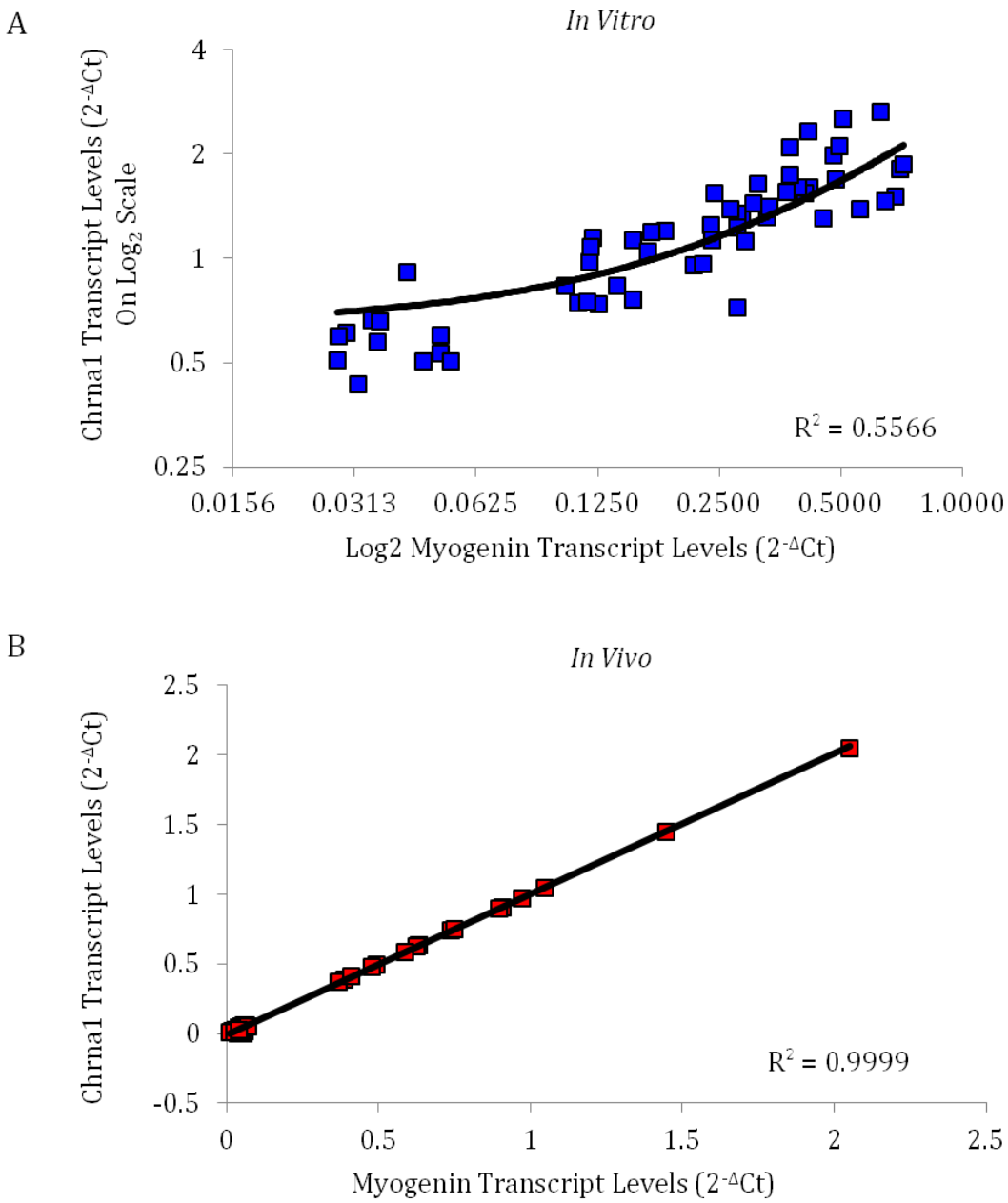

Figure 55 The Relationship Between Transcript Levels of Myog and Chrna1 *In Vitro* and I*n Vivo*

Correlations between Myog and Chrna1 Transcript levels *in vitro* (A) and *in vivo* (B) were measured using qRT-PCR and normalised to the mean of two housekeeping genes (Rn18s and Polr2a). Correlation is determined by the coefficient of determination (R^2).

A very strong correlation between Myog and Chrna1 transcript levels is evident *in vivo* with an R^2 value of 0.999, with a weaker relationship apparent *in vitro* ($R^2$0.5566). The difference between the correlation in the *in vitro* and *in vivo* models may be related to the absence of the NMJ in cultured myotubes and the role of Chrn1 as an AchR subunit in the NMJ.

The chemical inhibition of *in vitro* muscle atrophy with MGCD0103, characterised by a lesser reduction in myotube CSA, was a surprising result. The addition of MGCD0103 to myotubes cultured under conditions of glucose starvation appears to affect the basal levels of Myog transcript, which is relatively high in the *in vitro* model when compared with the *in vivo* model. A concomitant decrease in Trim63 and Chrna1, downstream targets of Myog, was also evident. Further scrutiny of the data revealed strong correlations between Myog and Trim63 transcript levels, as well as Myog and Chrna1, in both *in vitro* and *in vivo* models of atrophy. However, the correlation between Myog and another of its downstream targets, Fbxo32, was absent in the *in vitro* model, suggesting that Myog may act only on specific downstream targets in different conditions of muscle atrophy, or that Fbxo32 is controlled by upstream effectors other than Myog in cultured myotubes.

6.3.7 Comparisons of The Effects of S3I-201 on Atrophy and Combination Therapy with MC1568

The addition of S3I-201 to myotubes incubated in glucose free media resulted in the decrease of myotube CSA by 21.76% (+/- 5.71), compared to a decrease of 56.36% in response to glucose starvation alone (figure 47). When the transcripts were analysed (figure 56) there were significant decreases in Trim63 and Myog expression in the presence of S3I-201, and increases in Stat3 and Hdac4 expression. The Reduction in the level of atrophy in response to S31-201 indicates an important role for the Jak/Stat3 pathway in the control of myotube size, and the decrease in the expression of Myog and its downstream target Trim63 suggests that the Jak/Stat3 pathway is indeed regulating Myog expression in this model. Interestingly, an increase in Stat3 was observed, potentially indicative of a positive feedback mechanism in response to a severe decrease in Stat3 activity. Furthermore, the increase in Hdac4 may be the result of a compensatory mechanism to permit control of muscle size via a pathway that does not require Stat3 activation. The data shown in Figure 51, where increases in Stat3 were observed following inhibition of the Hdac pathway by MC1568, also support compensatory cross talk between the two arms of the pathway.

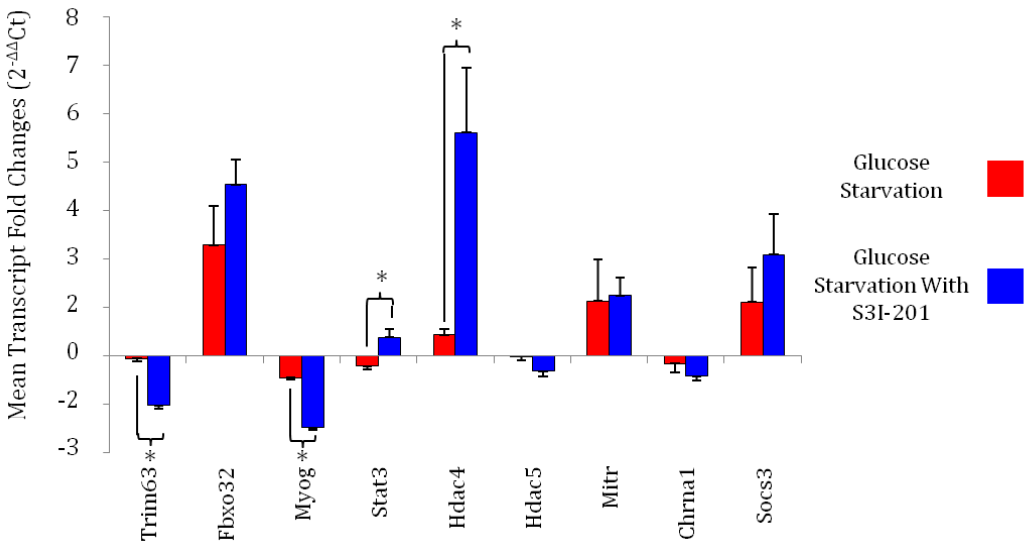

Figure 56 Fold Transcript Level Changes in Myotubes Following Glucose Starvation with and without S3I-201

Mean transcript levels were measured using qRT-PCR and normalised to the mean of two housekeeping genes (Rn18s and Polr2a). Statistically significant ($p<0.05$) differences in changes in transcript levels following an ANOVA test are marked with * (n=6). Error bars indicate SEM.

The rescue in CSA caused by S31-201 combined with MC1568 and glucose starvation was not significantly different to that seen with S3I-201 alone ($p=0.671$). Decreases in Trim63 and Myog were observed in myotubes cultured in glucose free media with the addition of S31-201, when compared to those cultured in normal media with S31-201 (figure 56). The addition of MC1568 to both normal and glucose free cultures, in combination with S31-201, did not appear to effect the changes in these transcripts any further (figure 57). This was unsurprising result since an earlier study showed that the addition of MC1568 alone did not change the expression of either of these genes (Figure 51). Thus it would appear that the Hdac Class II inhibitor has no effect on the transcription of these genes, irrespective of whether the Stat3 pathway is inhibited.

An increase in Hdac4 expression was observed following the addition of S31-201 in myotubes cultured in glucose free media compared with normal media. Intriguingly though, the response of Hdac4 to a combined therapy of S31-201 and MC1568 in myotubes cultured in glucose free media, was a significant decrease in transcript compared with that when cultured in normal media . The response of Hdac4 to the combined therapy further illustrates the complexity of the pathways that may interlink to control Myog expression and ultimately muscle size.

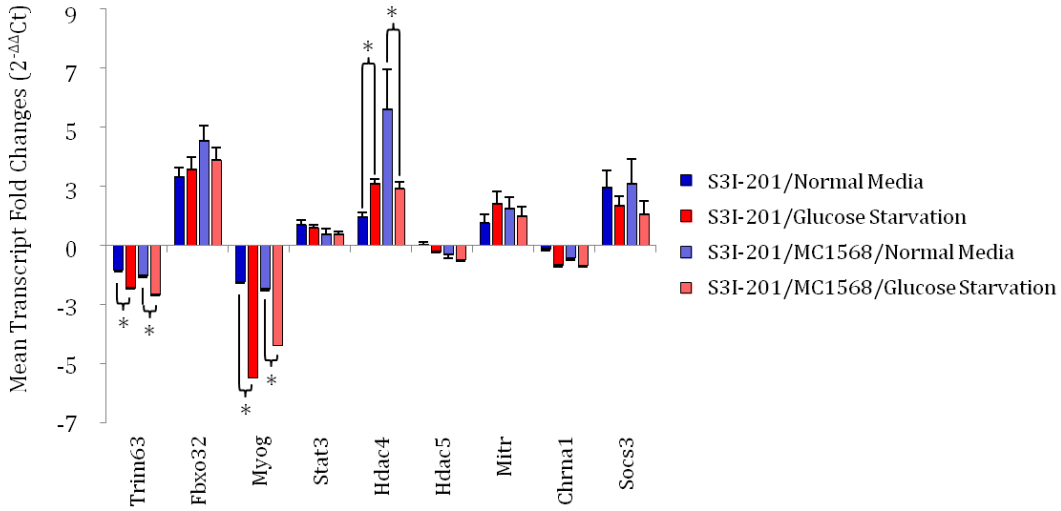

Figure 57 Mean Transcript Levels Following Treatment With S3I-201, and a combination of S31-201 and MC1568, Cultured in Normal and Glucose Free Media
Mean transcript levels were measured using qRT-PCR and normalised to the mean of two housekeeping genes (Rn18s and Polr2a). Transcript levels are shown as mean fold changes compared to myotubes cultured in normal media. Significant differences ($p<0.05$) in fold changes following an ANOVA test are marked with * ($n=6$). Error bars indicate SEM.

6.3.8 The Differential transcriptional response to *In Vitro* Glucose Starvation and *In Vivo* Nerve Block

The transcript levels following glucose starvation *in vitro* and after 14 days of nerve block *in vivo* were considered in order to compare the two models of muscle atrophy. The transcript levels are shown as fold changes following each of the treatments (figure 58).

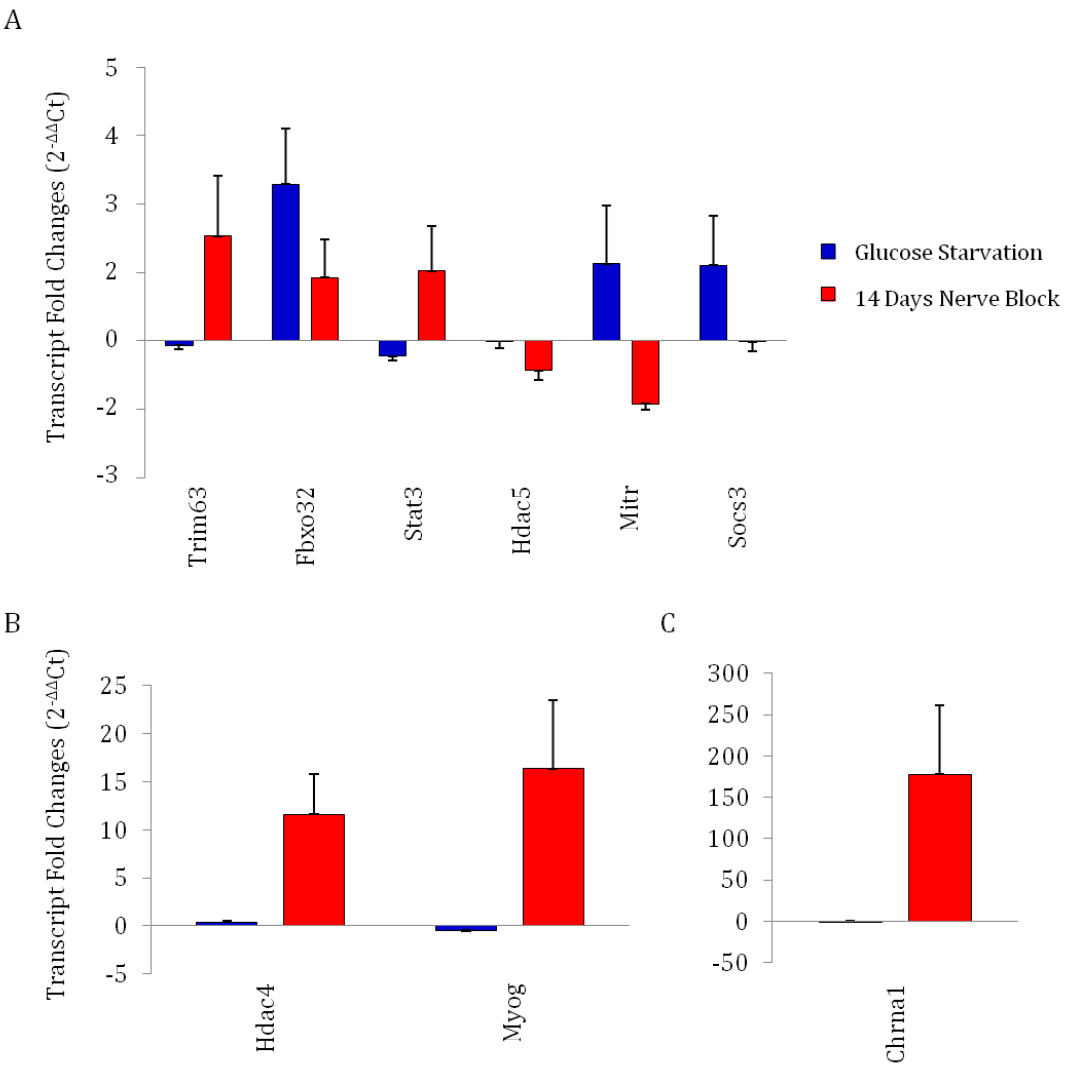

Figure 58 Comparison of Transcript Changes with Glucose Starvation *In Vitro* and Muscle Block *In Vivo*

Transcript levels were measured using qRT-PCR and normalised to the mean of two housekeeping genes (Rn18s and Polr2a). Transcript levels are represented as fold changes, glucose starved from normal media treated myotubes and 14 days atrophy from the untreated contraleteral control. The transcripts are shown in 3 panels (A-C) to allow for differences in scale of change (*n*=6). Error bars indicate SEM.

Comparisons between changes in key transcripts in the *in vitro* and *in vivo* models of atrophy have highlighted the differential responses between the two. Increases in Stat3 and Hdac 4 were observed in the *in vivo* nerve block study, whilst myotubes cultured *in vitro* in glucose-free conditions showed no change in Hdac4 and a very small decrease in Stat3. Similarly, increases in Myog transcript and its downstream targets Trim63 and Chrna1 were also observed in the *in vivo* model but not in the *in vitro* model. Thus it would appear that the Myog dependent pathway is involved in muscle atrophy in fully

differentiated tissue in vivo, but perhaps an alternative pathway exists *in vitro*, where different transcripts are required to induce changes in myotube size.
Interestingly, the ubiquitin ligases Trim63 and Fbxo32 appear to respond differently in different conditions of atrophy at the transcript level. Whilst Trim63 seems to be more involved in the *in vivo* nerve block model of atrophy, Fbxo32 showed a greater response in the *in vitro* glucose starvation model. The data therefore indicates that while Myog may contribute to the control of the expression of these ubiquitin ligases, there may well be other upstream effectors which are involved in different conditions of atrophy.

6.4 Discussion

Myotube cultures incubated in normal differentiation media or in media lacking glucose in order to induce atrophy were used to investigate the response of chemical inhibitors of Hdac class I and II and Stat3. The Hdac Class II inhibitor MC1568 was used in order to target the Hdac arm of the Myog transcriptional network. It has been suggested that the Class II Hdacs that are involved with the regulation of Myog expression in muscle atrophy (Moresi et al., 2010). If this is true then the Class II inhibitor has the potential to have an effect on the degree of atrophy (figure 45 panel B). The class I Hdac inhibitor MGCD0103 was chosen as a control under the premis that this may not have an effect on Myog expression during atrophy. Lastly the Stat3 inhibitor S3I-201 was chosen to investigate the role of Stat3 in muscle atrophy. If Stat3 is playing a major role in atrophy then S31-201 would be expected to reduce the expression of Myog and ultimately inhibit the atrophy process (figure 45 panel C).

6.4.1 A Potential Role for Class I or II Hdacs in Control of Myotube Size

The class II Hdac inhbitor MC1568 significantly blunted atrophy in myotubes cultured in glucose free media by 14%. This confirms the role of Hdac Class II proteins in muscle atrophy, (figure 47) which have been observed in previous studies (Moresi et al., 2010). This result was interesting in light of the fact that Hdac4 was previously described as a transcriptional sensor located at the NMJ, whilst myotubes in culture do not have NMJs. However, subsequent analyses of transcriptional changes suggest a more complex role for the class II Hdacs. Figure 51 analysed transcript changes

following glucose starvation dependent on the Hdac Class II inhibitor MC1568. The chemical inhibition of the Class II Hdacs might be expected to reduce the expression of Myog through the transcriptional induction of its suppressor Mitr. However, the addition of MC1568 produced no significant changes in Myog or Mitr transcript levels, or the targets of Myog; Trim63 and Chrna1. Additionally, Fbxo32 levels actually increased with the addition of MC1568. The expression of Hdac4 increased suggesting a positive feedback mechanism to produce more Hdac4 to compensate for the inhibition of existing Hdac4. The addition of MC1568 to myotubes cultured in normal media, produced a 16.12% (+/- 9.15) decrease in CSA. Whilst this was found to be non-significant (p=0.072), the analysis of the data may be abnormally skewed. For five experimental replicates a decrease in CSA of between 38% and 13% was observed, but one replicate instead showed an increase in CSA of 25% following treatment. Interestingly, the inhibition of Hdac4/5 in this replicate did effect Myog transcript levels, with a decrease in expression and a concomitant increase in its repressor Mitr and its hypothesised target Trim63 (figure 50). There is the possibility that human error may account for this discrepancy on the basis that the rest of the data followed a similar pattern of response. Further repetitions of these experiments are required to determine the reproducibility and frequency of outlier samples.

In contrast to the other Myog target genes, MC1568 produced a significant increase in Fbxo32, which may go some way to explain the atrophy this inhibitor caused even without concomitant glucose starvation. So how can inhibition by MC1568 produce opposing effects under different culture conditions? MC1568 blunts the atrophy produced by glucose starvation but in normal cells produces atrophy. This implies a dual role for the Hdac Class II proteins in normal and atrophy inducing states. This could be exacerbated by the fact that in our model, the myotubes are still differentiating, even when they are cultured in normal media in the presence of glucose. To date, the effects of class II Hdac specific inhibition *in vivo* have not yet been investigated, to look for differences between differentiating muscle and fully differentiated tissue. It should be noted whilst MC1568 has been shown to specifically inhibit Class II Hdacs in other studies (Cenik et al., 2011, Munkacsi et al., 2011), and the results show that it undoubtedly has an effect on the myotube cultures, there is no direct evidence in this assay that Class II Hdacs specificity is certain. This is also true for the use of the Class I Hdac inhibitor MGCD0103.

The most surprising result of our *in vitro* study came from the addition of MGD0103 to myotubes cultured in both normal and glucose free conditions. The addition of

MGCD0103 produced marked changes in myotube size and transcriptional output. Addition to myotubes cultured in normal media produced a significant increase in myotube diameter by 25% and in myotubes cultured in glucose-free conditions showed no significant decrease in CSA. Thus MGCD0103 effectively blocked atrophy caused by glucose starvation. When the transcript changes were analysed, the changes in Myog were marked and are discussed below in 6.4.2.

6.4.2 Further Evidence for The Role of Myog in Muscle Atrophy

Data produced from the nerve block study (discussed in 5.7.3) indicate that an increase in Myog expression may play a central role in this *in vivo* model of atrophy. This is in line with other *in vivo* studies (Moresi et al., 2010, Tang et al., 2009). We have also shown a less significant role for Myog in glucose starvation induced atrophy *in vitro*, with no significant increase in expression of most targets (6.3.4). However, chemical inhibition of the Class I Hdacs essentially blocked glucose-starvation induced atrophy. This was accompanied by a 14-fold (+/- 0.005, $p < 0.0001$) decrease in Myog transcript levels when compared to myotubes cultured in normal media (figure 50). When myotubes were cultured in normal media, the addition of MGCD0103 alone induced hypertrophy and a 19-fold (+/- 0.003, $p < 0.0001$) decrease in expression level of Myog (figure 50). This indicates a link between Myog transcript level and myotube size, and thus a potential role for Myog in the control of myotube size in culture.

One plausible explanation for the differential response of Myog across the different atrophy models may be related to its role in myotube development. The *in vitro* model of atrophy is based on immature, differentiating myotubes and thus the role of Myog in these conditions may lean towards the control of differentiation. Alternatively, the in *vivo* model employs fully differentiated muscle, and thus Myog may be recruited to help regulate muscle size under different physiological conditions. Figure 52 shows a comparison between Myog expression in control samples *in vitro* and *in vivo*, highlighting the differential responses. The addition of MGCD0103 to C2C12 myotube cultures may alter the role of Myog even in differentiating muscle cells. This idea was investigated further in figure 53. Here, comparisons were made between Myog transcript levels and fibre CSA in vivo, and myotube CSA in vitro, across all treatment groups. The *in vivo* data showed that an increased level of Myog transcript is associated with in a decrease in fibre CSA (figure 53 A), with a delayed response in the 3 day block

group. However, in vitro, a relationship between increased Myog levels and decreased myofibre CSA was evident, but only with either the addition of a chemical inhibitor or in glucose free culture conditions. The data appears to strengthen the theory that Myog is recruited into its role in regulating myotubes under conditions of glucose starvation or in response to chemical inhibition.

The mechanisms underlying the role of Myog in regulating muscle size are yet to be fully elucidated. Previous studies have shown that Myog regulates the expression of the E3 ubiquitin ligases Fbxo32 and Trim63 (Moresi et al., 2010, Tang et al., 2009). However, the data shown in figure 54 suggests that the regulation of both E3s may not be the sole responsibility of Myog. Whilst comparisons of Myog transcript levels with Trim63 and Fbxo32 transcript levels does not provide direct evidence (figure 54), it does highlight a stronger relationship between Myog and Trim63 than between Myog and Fbxo32. Further evidence comes from the data showing that during glucose starvation of myotubes, Myog transcript levels are not significantly changed (figure 50) but Fbxo32 transcript levels increase. One possible explanation for this could be that the E3 ubiquitin ligase is under the control of Foxo transcription factors in this model. Although the transcript levels of Foxo1 showed no significant change with any of the *in vitro* treatments (data not shown), it is the phosphorylation state of the protein that is known to dictate its activity (Van Der Heide et al., 2004), and thus it is still possible that Foxo activation effects Fbxo32 transcription. Further investigation into the phosphorylation state and cellular location of Foxo1 during these treatments would be required in order to make links between Foxo1 and Fbxo32.

The use of Hdac inhibitors in muscle atrophy has so far focused upon their effects on Myog, without consideration of their effects on Foxo. One study using human lung cancer cell lines has shown a link between Class I Hdacs, but not Class II Hdacs, in the regulation of Foxo1 (Yang et al., 2009). This may help to explain the relatively small effect of the Hdac Class II inhibitor in our models, but when considering the large effect of the Hdac Class I inhibitor, further investigation is required to make sense of the potential role for Foxo1. Studies using the broad-spectrum Hdac inhbitor Trichostatin A (TSA) in both *in vivo* (Bricceno et al., 2012) and *in vitro* models (Tang et al., 2009) have focused on its effects on the Class II Hdacs in blunting atrophy. However, TSA inhibits all Classes of Hdacs, making it difficult to isolate which are involved in the atrophy process.

6.4.3 Does the Jak/Stat pathway play a role in Atrophy?

The addition of the Stat3 inhibitor S3I-201 to myotubes cultured under glucose free conditions blunted the atrophy produced from a 56% to a 22% reduction in myotube CSA. The predicted changes in transcript levels in line with a role for Myog included a decrease in Socs3 and Myog and a subsequent decrease in Trim63, Fbxo32 and Chrna1. Although the addition of S3I-201 did significantly reduce the expression of Myog and Trim63 (figure 56) there was no significant reduction in the expression of Fbxo32 or Chrna1. In fact, Fbxo32 transcript levels increased, although this was not statistically significant. This further reinforces the idea that in the myotube model of glucose starvation-induced atrophy, Myog is more strongly linked to Trim63 than Fbxo32. Socs3 expression did not significantly change with the addition of S3I-201. This suggests that if Stat3 does regulate Myog, as our data implies, then it does not do so through the action of Socs3. The addition of S3I-201 also increased the expression of Stat3 and Hdac4. Stat3 induction could be the result of a feedback mechanism within the cell in an attempt to compensate for the blocked activity of Stat3. A similar response was seen with the Hdac Class II inhibitor, when inducing Hdac4 expression (figure 51). Blocking Stat3 activity may also feedback to the Hdac4 pathway, as seen in an induction of Hdac4 expression.

Further investigations are required in order to clarify these theories and confirm that the Stat3 inhibitor is effectively blocking the activity of Stat3 in our model, and that this functionally induces activity of the Hdac4 pathway by analysis of Hdac4 protein levels, phosphorylation state and sub-cellular localisation. However, inhibition by S3I-201 did significantly blunt atrophy and it's mode of action requires further investigation. Stat inhibitors have not been evaluated in muscle atrophy previously and when comparing their effects with the Class II Hdac inhibitors they seem to be more effective in modulating the atrophy pathway. This is illustrated in figure 57, showing that transcript changes, along with changes in CSA (figure 47) are not significantly affected with the addition of the class II Hdac inhibitor in combination with the Stat3 inhibitor.

6.4.4 Myotube Starvation & Nerve Block Atrophy Utilise Different Cellular Pathways

We have already discussed the differences between the *in vitro* glucose starvation and *in vivo* electrical stimulation models of atrophy in 3.5.3, as well as the differences between both *in vivo* models of atrophy: 20Hz electrical stimulation and nerve block in 5.7.2 (available comparisons are made in table 16).

Gene	Gene Transcriptional Changes in Each Atrophy Model		
	Glucose Starvation	Functional Atrophy	TTX Nerve Block
Hdac4	-	↑	↑
Hdac5	-	-	-
Mitr	↑	-	↓
Stat3	-	-	-
Socs3	↑	-	-
Myog	-	↑	↑
Chrna1	-	↑	↑
Fbxo32	↑	↑	↑
Trim63	-	-	↑

Table 16 Gene Transcriptional Changes Across Atrophy Models
↑; Upregulation of gene transcript levels, ↓; downregulation, -; no significant change

Finally, comparisons must be made between the glucose starvation model and nerve block atrophy. 6.3.8 outlines the differences in transcriptional changes following the two treatments. There are significant differences in 5 out of the 9 genes analysed including a marked 17-fold increase following nerve block and no significant change following glucose starvation. Thus whilst all 3 models of atrophy (glucose starvation *in vitro*, nerve block and electrical stimulation *in vivo*) undoubtedly produce a reduction in muscle or myotube size, the evidence here indicates that the cellular pathways utilised may differ between different models. Consequently, considering the model used when investigating skeletal muscle atrophy is of great importance.

6.4.5 Summary

The novel discovery that the chemical inhibition of the class I hdacs effectively blocked the atrophy caused by glucose starvation in myotubes is an exciting finding. Whilst cellular pathways involving Hdac4/5 or Stat3 converging on Myog to regulate its transcription have been implicated in several studies previously, the data from the *in vitro*, glucose starvation model of muscle atrophy strengthens the hypothesis that these

two pathways cross talk at several levels. Most importantly, the role of Class I Hdacs in muscle atrophy has not been considered previously. Furthermore, the data suggest that whilst Myog and its downstream targets may play an important role in the control of muscle size, this is not the only mechanism by which muscle atrophy is regulated. Comparisons of the *in vitro* myotube glucose starvation and *in vivo* TTX nerve block models of atrophy highlighted differences in the transcriptional, suggestive of a more complex, multi-dimensional regulation of muscle mass under different physiological conditions.

Chapter 7: Thesis Conclusions and Further Work

A number of conditions lead to skeletal muscle atrophy, including disease states such as cancer cachexia, age-related sarcopenia and muscle disuse. The latter can also contribute in a secondary manner to muscle atrophy, primarily in response to the impact on mobility of many of these debilitating disorders. Whilst there is a large body of research directed towards muscle atrophy, the complexity of the signalling pathways involved in the regulation of muscle mass have resulted in large gaps in the understanding of these pathways. One contributing factor may be the fact that there are numerous events that can initiate muscle atrophy, and that regulation of protein synthesis may be unique in each case. A more in-depth knowledge of the cellular and molecular mechanisms that govern muscle size is vital in identifying therapeutic targets to prevent muscle breakdown and encourage muscle growth.

An important role for the transcription factors Myog and Foxo in muscle atrophy has been highlighted in several studies through their regulation of the E3 ubiquitin ligases Trim63 and Fbxo32. Both E3 ligases have been shown to be upregulated in several models of muscle atrophy and consequently have been used as markers of muscle breakdown (Clarke et al., 2007). In contrast to the control of Foxo activity, which involves phosphorylation and cellular localisation, control of Myog occurs through transcriptional expression. Consequently, our study of the transcriptional response to muscle atrophy has involved analyses of Myog and a number of its downstream targets linked to muscle atrophy.

Comparisons of *in vitro* models of muscle atrophy, using glucose starvation or dexamethasone treatment of myotubes, with an *in vivo* model of 'functional atrophy' showed remarkably different responses in terms of transcriptional regulation. Target genes of Foxo transcription factors were selected and a transcriptional profile was analysed in response to each of the models of atrophy. The data from our comparative study suggested that each model of atrophy potentially has a unique transcriptional profile and highlighted the need for a more physiologically relevant *in vivo* model in order to identify the transcriptional pathways involved in muscle disuse atrophy. Data obtained from a more clinically accurate muscle disuse model could have a greater potential to provide information which would lead to a therapeutic target for the prevention of muscle atrophy.

We developed an *in vivo* model of muscle atrophy, utilising TTX to block nerve activity and provide a model of complete muscle disuse. The model permitted a time course analysis of muscle disuse with the option of recovery. Progressive muscle atrophy was

observed in response to TTX nerve block over a 14 day period, without damage to the muscle tissue. Removal of the nerve block resulted in partial recovery, characterised by an increase in muscle mass. Interestingly, our study indicates that the time scale for muscle atrophy is similar, if not the same as, the time scale of muscle recovery from atrophy.

Comparative microarray analysis of both the 'functional atrophy' and TTX nerve block *in vivo* models showed remarkable differences in the transcriptional profile of the two models. This is unsurprising in light of previous studies in which comparisons of transcriptional profiles have suggested a unique regulation of protein loss in response to the different events initiating the atrophy pathway (Kandarian and Jackman, 2006). The importance of studying the time course of transcriptional changes in response to muscle disuse was highlighted by the temporal changes in gene transcripts over a 14 day period. 'Early responders' were identified following 3 days of muscle disuse, whilst after 7-14 days gene transcripts involved in the 'established' phase of muscle atrophy were highlighted. Many studies have previously focused on a single time point when considering the transcriptional response to muscle atrophy, potentially overlooking the response of key genes involved in the initiation of signalling pathways leading to muscle protein breakdown (Bey et al., 2003, Stein et al., 2002).

Data from the microarray analysis supported data available in the current literature and was used to link together two potential cellular pathways controlling the expression of Myog, originating within the NMJ and acting as a sensor for changed muscle activity. The intermediaries of this pathway, which consisted of two branches, could be targeted to potentially interfere with the process of muscle atrophy. Subsequently, we designed an *in vitro* study which involved inhibition of the two arms of the pathway, the class II Hdacs, Hdac4/5 and Jak/Stat3, which are thought to converge on the regulation of Myog. Our findings indicated a role for these pathways in the control of Myog expression in conditions of glucose starvation in myotubes, where addition of the chemical inhibitors of the class II Hdacs, MC1568, and Stat3, S3I-201, showed a reduction in the degree of atrophy produced in the absence of chemical inhibition. However, the response to chemical inhibition of the class I Hdacs with MGCD0103 was the most surprising and interesting result. The class I Hdac inhibitor was selected as a control, under the premise that it would selectively block class I Hdac activity and thus it would not affect either of the arms of the cellular pathway. Treatment of myotubes cultured in glucose-free media with MGCD0103 showed a significant reduction in the atrophy evident without chemical inhibition, to produce a

non-significant reduction in myotube CSA, effectively blocking atrophy. Furthermore, Myog transcript levels were shown to dramatically decrease in this *in vitro* model, highlighting a potential link between Myog transcript and atrophy. Whilst this is a preliminary study that must be repeated in order to verify the data, the results provide an exciting new avenue of potential research. Future studies should confirm the specificity of the class I Hdac inhibitor to determine selective blocking of class I, and not class II, Hdac activity. Once the *in vitro* model has been validated and established, the chemical inhibition of class I Hdacs must be considered in an *in vivo* model, to see if the mode of action and subsequent response of the muscle translates in physiologically relevant conditions. The potential role for class I Hdacs in the prevention of muscle atrophy is a novel finding that has not been reported in the literature to date.

Finally, comparisons were made between the transcriptional output from the *in vitro* glucose starvation model of atrophy and our *in vivo* TTX nerve block model to determine whether our model showed a similar transcriptional response to the *in vitro* model. Our findings showed distinct differences between the two models in terms of the response of Myog and its downstream targets at the transcript level, reinforcing the theory that the particular cause of muscle atrophy in a given model dictates the response of the muscle by initiating a distinct and unique signalling pathway. Whilst Myog and its key targets genes involved in muscle size regulation appear to play a central role in many models of muscle atrophy, the data produced for this thesis highlights a role for alternative signalling pathways that do not utilise Myog. Foxo transcription factors have been implicated as another key regulator of muscle atrophy and further investigation into the response and regulation of Foxo in different atrophy models could help to further elucidate their role.

The data produced in this cross-model study of muscle atrophy has highlighted the need for care when interpreting the cellular changes that by various routes produce the end result of loss in protein content. Such complex interactions need multivariate or systems analysis to understand fully, but the data contained in this thesis is exactly the type of multi-dimensional data across the genome and across the time course of muscle adaptation that will be required for a complete analysis of the remarkable adaptive capacity of muscle cells.

REFERENCES

ADACHI, M., OSAWA, Y., UCHINAMI, H., KITAMURA, T., ACCILI, D. & BRENNER, D. A. 2007. The forkhead transcription factor FoxO1 regulates proliferation and transdifferentiation of hepatic stellate cells. *Gastroenterology,* 132**,** 1434-46.

ADHIHETTY, P. J., O'LEARY, M. F., CHABI, B., WICKS, K. L. & HOOD, D. A. 2007. Effect of denervation on mitochondrially mediated apoptosis in skeletal muscle. *J Appl Physiol,* 102**,** 1143-51.

ALVAREZ, B., MARTINEZ, A. C., BURGERING, B. M. & CARRERA, A. C. 2001. Forkhead transcription factors contribute to execution of the mitotic programme in mammals. *Nature,* 413**,** 744-7.

ASHBURNER, M., BALL, C. A., BLAKE, J. A., BOTSTEIN, D., BUTLER, H., CHERRY, J. M., DAVIS, A. P., DOLINSKI, K., DWIGHT, S. S., EPPIG, J. T., HARRIS, M. A., HILL, D. P., ISSEL-TARVER, L., KASARSKIS, A., LEWIS, S., MATESE, J. C., RICHARDSON, J. E., RINGWALD, M., RUBIN, G. M. & SHERLOCK, G. 2000. Gene ontology: tool for the unification of biology. The Gene Ontology Consortium. *Nat Genet,* 25**,** 25-9.

AVERSA, Z., ALAMDARI, N. & HASSELGREN, P. O. 2011. Molecules modulating gene transcription during muscle wasting in cancer, sepsis, and other critical illness. *Crit Rev Clin Lab Sci,* 48**,** 71-86.

AYALA, J. E., STREEPER, R. S., DESGROSELLIER, J. S., DURHAM, S. K., SUWANICHKUL, A., SVITEK, C. A., GOLDMAN, J. K., BARR, F. G., POWELL, D. R. & O'BRIEN, R. M. 1999. Conservation of an insulin response unit between mouse and human glucose-6-phosphatase catalytic subunit gene promoters: transcription factor FKHR binds the insulin response sequence. *Diabetes,* 48**,** 1885-9.

BEY, L., AKUNURI, N., ZHAO, P., HOFFMAN, E. P., HAMILTON, D. G. & HAMILTON, M. T. 2003. Patterns of global gene expression in rat skeletal muscle during unloading and low-intensity ambulatory activity. *Physiol Genomics,* 13**,** 157-67.

BODINE, S. C., LATRES, E., BAUMHUETER, S., LAI, V. K., NUNEZ, L., CLARKE, B. A., POUEYMIROU, W. T., PANARO, F. J., NA, E., DHARMARAJAN, K., PAN, Z. Q., VALENZUELA, D. M., DECHIARA, T. M., STITT, T. N., YANCOPOULOS, G. D. & GLASS, D. J. 2001. Identification of ubiquitin ligases required for skeletal muscle atrophy. *Science,* 294**,** 1704-8.

BONEN, A., DYCK, D. J., IBRAHIMI, A. & ABUMRAD, N. A. 1999. Muscle contractile activity increases fatty acid metabolism and transport and FAT/CD36. *Am J Physiol,* 276**,** E642-9.

BRICCENO, K. V., SAMPOGNARO, P. J., VAN MEERBEKE, J. P., SUMNER, C. J., FISCHBECK, K. H. & BURNETT, B. G. 2012. Histone deacetylase inhibition suppresses myogenin-dependent atrogene activation in spinal muscular atrophy mice. *Hum Mol Genet*.

BUFFELLI, M., PASINO, E. & CANGIANO, A. 1997. Paralysis of rat skeletal muscle equally affects contractile properties as does permanent denervation. *J Muscle Res Cell Motil,* 18**,** 683-95.

BUSQUETS, S., FIGUERAS, M. T., FUSTER, G., ALMENDRO, V., MOORE-CARRASCO, R., AMETLLER, E., ARGILES, J. M. & LOPEZ-SORIANO, F. J. 2004. Anticachectic effects of formoterol: a drug for potential treatment of muscle wasting. *Cancer Res,* 64**,** 6725-31.

CALDOW, M. K., STEINBERG, G. R. & CAMERON-SMITH, D. 2011. Impact of SOCS3 overexpression on human skeletal muscle development in vitro. *Cytokine,* 55**,** 104-9.

CALLAHAN, L. A. & SUPINSKI, G. S. 2009. Sepsis-induced myopathy. *Crit Care Med,* 37**,** S354-67.

CALURA, E., CAGNIN, S., RAFFAELLO, A., LAVEDER, P., LANFRANCHI, G. & ROMUALDI, C. 2008. Meta-analysis of expression signatures of muscle atrophy: gene interaction networks in early and late stages. *BMC Genomics,* 9**,** 630.

CARLING, D. 2004. The AMP-activated protein kinase cascade--a unifying system for energy control. *Trends Biochem Sci,* 29**,** 18-24.

CARLSON, B. M. 2008. The Denervated Muscle: 45 years later. *Neurol Res,* 30**,** 119-22.

CENIK, B., SEPHTON, C. F., DEWEY, C. M., XIAN, X., WEI, S., YU, K., NIU, W., COPPOLA, G., COUGHLIN, S. E., LEE, S. E., DRIES, D. R., ALMEIDA, S., GESCHWIND, D. H., GAO, F. B., MILLER, B. L., FARESE, R. V., JR., POSNER, B. A., YU, G. & HERZ, J. 2011. Suberoylanilide hydroxamic acid (vorinostat) up-regulates progranulin transcription: rational therapeutic approach to frontotemporal dementia. *J Biol Chem,* 286**,** 16101-8.

CHARGE, S. B. & RUDNICKI, M. A. 2004. Cellular and molecular regulation of muscle regeneration. *Physiol Rev,* 84**,** 209-38.

CHOUDHARY, C., KUMAR, C., GNAD, F., NIELSEN, M. L., REHMAN, M., WALTHER, T. C., OLSEN, J. V. & MANN, M. 2009. Lysine acetylation targets protein complexes and co-regulates major cellular functions. *Science,* 325**,** 834-40.

CLARKE, B. A., DRUJAN, D., WILLIS, M. S., MURPHY, L. O., CORPINA, R. A., BUROVA, E., RAKHILIN, S. V., STITT, T. N., PATTERSON, C., LATRES, E. & GLASS, D. J. 2007. The E3 Ligase MuRF1 degrades myosin heavy chain protein in dexamethasone-treated skeletal muscle. *Cell Metab,* 6**,** 376-85.

COHEN, S., BRAULT, J. J., GYGI, S. P., GLASS, D. J., VALENZUELA, D. M., GARTNER, C., LATRES, E. & GOLDBERG, A. L. 2009. During muscle atrophy, thick, but not thin, filament components are degraded by MuRF1-dependent ubiquitylation. *J Cell Biol,* 185**,** 1083-95.

COHEN, T. J., WADDELL, D. S., BARRIENTOS, T., LU, Z., FENG, G., COX, G. A., BODINE, S. C. & YAO, T. P. 2007. The histone deacetylase HDAC4 connects neural activity to muscle transcriptional reprogramming. *J Biol Chem,* 282**,** 33752-9.

COLLINS, C. A. & PARTRIDGE, T. A. 2005. Self-renewal of the adult skeletal muscle satellite cell. *Cell Cycle,* 4**,** 1338-41.

CSIBI, A., CORNILLE, K., LEIBOVITCH, M. P., POUPON, A., TINTIGNAC, L. A., SANCHEZ, A. M. & LEIBOVITCH, S. A. 2010. The translation regulatory subunit eIF3f controls the kinase-dependent mTOR signaling required for muscle differentiation and hypertrophy in mouse. *PLoS One,* 5**,** e8994.

DE RUIJTER, A. J., VAN GENNIP, A. H., CARON, H. N., KEMP, S. & VAN KUILENBURG, A. B. 2003. Histone deacetylases (HDACs): characterization of the classical HDAC family. *Biochem J,* 370**,** 737-49.

DEGENS, H. & ALWAY, S. E. 2006. Control of muscle size during disuse, disease, and aging. *Int J Sports Med,* 27**,** 94-9.

DESCHENES, M. R. 2011. Motor unit and neuromuscular junction remodeling with aging. *Curr Aging Sci,* 4**,** 209-20.

DESHAIES, R. J. & JOAZEIRO, C. A. 2009. RING domain E3 ubiquitin ligases. *Annu Rev Biochem,* 78**,** 399-434.

DIAO, Y., WANG, X. & WU, Z. 2009. SOCS1, SOCS3, and PIAS1 promote myogenic differentiation by inhibiting the leukemia inhibitory factor-induced JAK1/STAT1/STAT3 pathway. *Mol Cell Biol,* 29**,** 5084-93.

DUPONT SALTER, A. C., RICHMOND, F. J. & LOEB, G. E. 2003. Effects of muscle immobilization at different lengths on tetrodotoxin-induced disuse atrophy. *IEEE Trans Neural Syst Rehabil Eng,* 11**,** 209-17.

EDDINS, M. J., MARBLESTONE, J. G., SURESH KUMAR, K. G., LEACH, C. A., STERNER, D. E., MATTERN, M. R. & NICHOLSON, B. 2011. Targeting the ubiquitin E3 ligase MuRF1 to inhibit muscle atrophy. *Cell Biochem Biophys,* 60**,** 113-8.

EDDINS, M. J., VARADAN, R., FUSHMAN, D., PICKART, C. M. & WOLBERGER, C. 2007. Crystal structure and solution NMR studies of Lys48-linked tetraubiquitin at neutral pH. *J Mol Biol,* 367**,** 204-11.

EISENBERG, B. R., BROWN, J. M. & SALMONS, S. 1984. Restoration of fast muscle characteristics following cessation of chronic stimulation. The ultrastructure of slow-to-fast transformation. *Cell Tissue Res,* 238**,** 221-30.

ELDRIDGE, A. G. & O'BRIEN, T. 2010. Therapeutic strategies within the ubiquitin proteasome system. *Cell Death Differ,* 17**,** 4-13.

FALCON, S. & GENTLEMAN, R. 2007. Using GOstats to test gene lists for GO term association. *Bioinformatics,* 23**,** 257-8.

FINSTERER, J., PAPIC, L. & AUER-GRUMBACH, M. 2011. Motor neuron, nerve, and neuromuscular junction disease. *Curr Opin Neurol,* 24**,** 469-74.

FISHER, L. M. 2010. Time- and Activity-Dependence of Transcriptional Changes in Stimulated Rat Skeletal Muscle.

FOURNEL, M., BONFILS, C., HOU, Y., YAN, P. T., TRACHY-BOURGET, M. C., KALITA, A., LIU, J., LU, A. H., ZHOU, N. Z., ROBERT, M. F., GILLESPIE, J., WANG, J. J., STE-CROIX, H., RAHIL, J., LEFEBVRE, S., MORADEI, O., DELORME, D., MACLEOD, A. R., BESTERMAN, J. M. & LI, Z. 2008. MGCD0103, a novel isotype-selective histone deacetylase inhibitor, has broad spectrum antitumor activity in vitro and in vivo. *Mol Cancer Ther,* 7**,** 759-68.

FURUYAMA, T., KITAYAMA, K., YAMASHITA, H. & MORI, N. 2003. Forkhead transcription factor FOXO1 (FKHR)-dependent induction of PDK4 gene expression in skeletal muscle during energy deprivation. *Biochem J,* 375**,** 365-71.

FURUYAMA, T., YAMASHITA, H., KITAYAMA, K., HIGAMI, Y., SHIMOKAWA, I. & MORI, N. 2002. Effects of aging and caloric restriction on the gene expression of Foxo1, 3, and 4 (FKHR, FKHRL1, and AFX) in the rat skeletal muscles. *Microsc Res Tech,* 59**,** 331-4.

GAUTIER, L., COPE, L., BOLSTAD, B. M. & IRIZARRY, R. A. 2004. affy--analysis of Affymetrix GeneChip data at the probe level. *Bioinformatics,* 20**,** 307-15.

GENTLEMAN, R. C., CAREY, V. J., BATES, D. M., BOLSTAD, B., DETTLING, M., DUDOIT, S., ELLIS, B., GAUTIER, L., GE, Y., GENTRY, J., HORNIK, K., HOTHORN, T., HUBER, W., IACUS, S., IRIZARRY, R., LEISCH, F., LI, C., MAECHLER, M., ROSSINI, A. J., SAWITZKI, G., SMITH, C., SMYTH, G., TIERNEY, L., YANG, J. Y. & ZHANG, J. 2004. Bioconductor: open software development for computational biology and bioinformatics. *Genome Biol,* 5**,** R80.

GIGO-BENATO, D., RUSSO, T. L., GEUNA, S., DOMINGUES, N. R., SALVINI, T. F. & PARIZOTTO, N. A. 2010. Electrical stimulation impairs early functional recovery and accentuates skeletal muscle atrophy after sciatic nerve crush injury in rats. *Muscle Nerve,* 41**,** 685-93.

GILLEY, J., COFFER, P. J. & HAM, J. 2003. FOXO transcription factors directly activate bim gene expression and promote apoptosis in sympathetic neurons. *J Cell Biol,* 162**,** 613-22.

GILLIS, T. E., MARSHALL, C. R. & TIBBITS, G. F. 2007. Functional and evolutionary relationships of troponin C. *Physiol Genomics,* 32**,** 16-27.

GIRAUD, J., HAAS, M., FEENER, E. P., COPPS, K. D., DONG, X., DUNN, S. L. & WHITE, M. F. 2007. Phosphorylation of Irs1 at SER-522 inhibits insulin signaling. *Mol Endocrinol,* 21**,** 2294-302.

GLASS, D. J. 2010. Signaling pathways perturbing muscle mass. *Curr Opin Clin Nutr Metab Care,* 13**,** 225-9.

GOCONSORTIUM 2008. The Gene Ontology project in 2008. *Nucleic Acids Res,* 36**,** D440-4.

HABERLAND, M., MONTGOMERY, R. L. & OLSON, E. N. 2009. The many roles of histone deacetylases in development and physiology: implications for disease and therapy. *Nat Rev Genet,* 10**,** 32-42.
HAGTING, A., JACKMAN, M., SIMPSON, K. & PINES, J. 1999. Translocation of cyclin B1 to the nucleus at prophase requires a phosphorylation-dependent nuclear import signal. *Curr Biol,* 9**,** 680-9.
HASTY, P., BRADLEY, A., MORRIS, J. H., EDMONDSON, D. G., VENUTI, J. M., OLSON, E. N. & KLEIN, W. H. 1993. Muscle deficiency and neonatal death in mice with a targeted mutation in the myogenin gene. *Nature,* 364**,** 501-6.
HAWKE, T. J. & GARRY, D. J. 2001. Myogenic satellite cells: physiology to molecular biology. *J Appl Physiol,* 91**,** 534-51.
HEPPLE, R. T., HOGAN, M. C., STARY, C., BEBOUT, D. E., MATHIEU-COSTELLO, O. & WAGNER, P. D. 2000. Structural basis of muscle O(2) diffusing capacity: evidence from muscle function in situ. *J Appl Physiol,* 88**,** 560-6.
HERSHKO, A. & CIECHANOVER, A. 1998. The ubiquitin system. *Annu Rev Biochem,* 67**,** 425-79.
HOLECEK, M. 2012. Muscle wasting in animal models of severe illness. *Int J Exp Pathol,* 93**,** 157-71.
HWANG, D. F. & NOGUCHI, T. 2007. Tetrodotoxin poisoning. *Adv Food Nutr Res,* 52**,** 141-236.
IRIZARRY, R. A., BOLSTAD, B. M., COLLIN, F., COPE, L. M., HOBBS, B. & SPEED, T. P. 2003. Summaries of Affymetrix GeneChip probe level data. *Nucleic Acids Res,* 31**,** e15.
JARVIS, J. C., MOKRUSCH, T., KWENDE, M. M., SUTHERLAND, H. & SALMONS, S. 1996. Fast-to-slow transformation in stimulated rat muscle. *Muscle Nerve,* 19**,** 1469-75.
JARVIS, J. C. & SALMONS, S. 1991. A family of neuromuscular stimulators with optical transcutaneous control. *J Med Eng Technol,* 15**,** 53-7.
JOPLIN, R. E., FRANCHI, L. L. & SALMONS, S. 1987. Changes in the size and synthetic activity of nuclear populations in chronically stimulated rabbit skeletal muscle. *J Anat,* 155**,** 39-50.
KAMEI, Y., MIZUKAMI, J., MIURA, S., SUZUKI, M., TAKAHASHI, N., KAWADA, T., TANIGUCHI, T. & EZAKI, O. 2003. A forkhead transcription factor FKHR up-regulates lipoprotein lipase expression in skeletal muscle. *FEBS Lett,* 536**,** 232-6.
KANDARIAN, S. C. & JACKMAN, R. W. 2006. Intracellular signaling during skeletal muscle atrophy. *Muscle Nerve,* 33**,** 155-65.
KHAN, J., HARRISON, T. B. & RICH, M. M. 2008. Mechanisms of neuromuscular dysfunction in critical illness. *Crit Care Clin,* 24**,** 165-77, x.
LAGIRAND-CANTALOUBE, J., CORNILLE, K., CSIBI, A., BATONNET-PICHON, S., LEIBOVITCH, M. P. & LEIBOVITCH, S. A. 2009. Inhibition of atrogin-1/MAFbx mediated MyoD proteolysis prevents skeletal muscle atrophy in vivo. *PLoS One,* 4**,** e4973.
LAGIRAND-CANTALOUBE, J., OFFNER, N., CSIBI, A., LEIBOVITCH, M. P., BATONNET-PICHON, S., TINTIGNAC, L. A., SEGURA, C. T. & LEIBOVITCH, S. A. 2008. The initiation factor eIF3-f is a major target for atrogin1/MAFbx function in skeletal muscle atrophy. *EMBO J,* 27**,** 1266-76.
LAI, K. O., CHEN, Y., PO, H. M., LOK, K. C., GONG, K. & IP, N. Y. 2004. Identification of the Jak/Stat proteins as novel downstream targets of EphA4 signaling in muscle: implications in the regulation of acetylcholinesterase expression. *J Biol Chem,* 279**,** 13383-92.
LAI, K. O., IP, F. C., CHEUNG, J., FU, A. K. & IP, N. Y. 2001. Expression of Eph receptors in skeletal muscle and their localization at the neuromuscular junction. *Mol Cell Neurosci,* 17**,** 1034-47.

LARSSON, L., LI, X., EDSTROM, L., ERIKSSON, L. I., ZACKRISSON, H., ARGENTINI, C. & SCHIAFFINO, S. 2000. Acute quadriplegia and loss of muscle myosin in patients treated with nondepolarizing neuromuscular blocking agents and corticosteroids: mechanisms at the cellular and molecular levels. *Crit Care Med,* 28**,** 34-45.

LASH, J. W., HOLTZER, H. & SWIFT, H. 1957. Regeneration of mature skeletal muscle. *Anat Rec,* 128**,** 679-97.

LEE, S. W., DAI, G., HU, Z., WANG, X., DU, J. & MITCH, W. E. 2004. Regulation of muscle protein degradation: coordinated control of apoptotic and ubiquitin-proteasome systems by phosphatidylinositol 3 kinase. *J Am Soc Nephrol,* 15**,** 1537-45.

MACPHERSON, P. C., WANG, X. & GOLDMAN, D. 2011. Myogenin regulates denervation-dependent muscle atrophy in mouse soleus muscle. *J Cell Biochem,* 112**,** 2149-59.

MAI, A., MASSA, S., PEZZI, R., SIMEONI, S., ROTILI, D., NEBBIOSO, A., SCOGNAMIGLIO, A., ALTUCCI, L., LOIDL, P. & BROSCH, G. 2005. Class II (IIa)-selective histone deacetylase inhibitors. 1. Synthesis and biological evaluation of novel (aryloxopropenyl)pyrrolyl hydroxyamides. *J Med Chem,* 48**,** 3344-53.

MASKOS, U. & SOUTHERN, E. M. 1992. Oligonucleotide hybridizations on glass supports: a novel linker for oligonucleotide synthesis and hybridization properties of oligonucleotides synthesised in situ. *Nucleic Acids Res,* 20**,** 1679-84.

MAURO, A. 1961. Satellite cell of skeletal muscle fibers. *J Biophys Biochem Cytol,* 9**,** 493-5.

MAYNE, C. N., ANDERSON, W. A., HAMMOND, R. L., EISENBERG, B. R., STEPHENSON, L. W. & SALMONS, S. 1991. Correlates of fatigue resistance in canine skeletal muscle stimulated electrically for up to one year. *Am J Physiol,* 261**,** C259-70.

MCKINSEY, T. A., ZHANG, C. L., LU, J. & OLSON, E. N. 2000. Signal-dependent nuclear export of a histone deacetylase regulates muscle differentiation. *Nature,* 408**,** 106-11.

MCMULLEN, C. A., BUTTERFIELD, T. A., DIETRICH, M., ANDREATTA, R. D., ANDRADE, F. H., FRY, L. & STEMPLE, J. C. 2011. Chronic stimulation-induced changes in the rodent thyroarytenoid muscle. *J Speech Lang Hear Res,* 54**,** 845-53.

MICHEL, R. N. & GARDINER, P. F. 1990. To what extent is hindlimb suspension a model of disuse? *Muscle Nerve,* 13**,** 646-53.

MIDRIO, M. 2006. The denervated muscle: facts and hypotheses. A historical review. *Eur J Appl Physiol,* 98**,** 1-21.

MORESI, V., WILLIAMS, A. H., MEADOWS, E., FLYNN, J. M., POTTHOFF, M. J., MCANALLY, J., SHELTON, J. M., BACKS, J., KLEIN, W. H., RICHARDSON, J. A., BASSEL-DUBY, R. & OLSON, E. N. 2010. Myogenin and class II HDACs control neurogenic muscle atrophy by inducing E3 ubiquitin ligases. *Cell,* 143**,** 35-45.

MOREY, J. S., RYAN, J. C. & VAN DOLAH, F. M. 2006. Microarray validation: factors influencing correlation between oligonucleotide microarrays and real-time PCR. *Biol Proced Online,* 8**,** 175-93.

MOSS, F. P. & LEBLOND, C. P. 1971. Satellite cells as the source of nuclei in muscles of growing rats. *Anat Rec,* 170**,** 421-35.

MUNKACSI, A. B., CHEN, F. W., BRINKMAN, M. A., HIGAKI, K., GUTIERREZ, G. D., CHAUDHARI, J., LAYER, J. V., TONG, A., BARD, M., BOONE, C., IOANNOU, Y. A. & STURLEY, S. L. 2011. An "exacerbate-reverse" strategy in yeast identifies histone deacetylase inhibition as a correction for cholesterol and sphingolipid transport defects in human Niemann-Pick type C disease. *J Biol Chem,* 286**,** 23842-51.

NEBBIOSO, A., MANZO, F., MICELI, M., CONTE, M., MANENTE, L., BALDI, A., DE LUCA, A., ROTILI, D., VALENTE, S., MAI, A., USIELLO, A., GRONEMEYER, H. & ALTUCCI, L.

2009. Selective class II HDAC inhibitors impair myogenesis by modulating the stability and activity of HDAC-MEF2 complexes. *EMBO Rep,* 10**,** 776-82.
PARK, Y., MAIZELS, E. T., FEIGER, Z. J., ALAM, H., PETERS, C. A., WOODRUFF, T. K., UNTERMAN, T. G., LEE, E. J., JAMESON, J. L. & HUNZICKER-DUNN, M. 2005. Induction of cyclin D2 in rat granulosa cells requires FSH-dependent relief from FOXO1 repression coupled with positive signals from Smad. *J Biol Chem,* 280**,** 9135-48.
PICKART, C. M. 2001. Mechanisms underlying ubiquitination. *Annu Rev Biochem,* 70**,** 503-33.
PICKART, C. M. & EDDINS, M. J. 2004. Ubiquitin: structures, functions, mechanisms. *Biochim Biophys Acta,* 1695**,** 55-72.
POLYAK, K., KATO, J. Y., SOLOMON, M. J., SHERR, C. J., MASSAGUE, J., ROBERTS, J. M. & KOFF, A. 1994. p27Kip1, a cyclin-Cdk inhibitor, links transforming growth factor-beta and contact inhibition to cell cycle arrest. *Genes Dev,* 8**,** 9-22.
POTTHOFF, M. J., WU, H., ARNOLD, M. A., SHELTON, J. M., BACKS, J., MCANALLY, J., RICHARDSON, J. A., BASSEL-DUBY, R. & OLSON, E. N. 2007. Histone deacetylase degradation and MEF2 activation promote the formation of slow-twitch myofibers. *J Clin Invest,* 117**,** 2459-67.
PURVES, D. 2008. *Neuroscience*, Sinauer Associates.
RAYMENT, I., HOLDEN, H. M., WHITTAKER, M., YOHN, C. B., LORENZ, M., HOLMES, K. C. & MILLIGAN, R. A. 1993. Structure of the actin-myosin complex and its implications for muscle contraction. *Science,* 261**,** 58-65.
ROMMEL, C., BODINE, S. C., CLARKE, B. A., ROSSMAN, R., NUNEZ, L., STITT, T. N., YANCOPOULOS, G. D. & GLASS, D. J. 2001. Mediation of IGF-1-induced skeletal myotube hypertrophy by PI(3)K/Akt/mTOR and PI(3)K/Akt/GSK3 pathways. *Nat Cell Biol,* 3**,** 1009-13.
ROSENBLATT, J. D., YONG, D. & PARRY, D. J. 1994. Satellite cell activity is required for hypertrophy of overloaded adult rat muscle. *Muscle Nerve,* 17**,** 608-13.
RUSSELL, S. T., RAJANI, S., DHADDA, R. S. & TISDALE, M. J. 2009. Mechanism of induction of muscle protein loss by hyperglycaemia. *Exp Cell Res,* 315**,** 16-25.
RUSSO, T. L., PEVIANI, S. M., DURIGAN, J. L., GIGO-BENATO, D., DELFINO, G. B. & SALVINI, T. F. 2010. Stretching and electrical stimulation reduce the accumulation of MyoD, myostatin and atrogin-1 in denervated rat skeletal muscle. *J Muscle Res Cell Motil,* 31**,** 45-57.
SALMONS, S. 1995. Muscle. *In:* SALMONS, S. (ed.) *Gray's Anatomy.* 38 ed.: Churchill Livingstone.
SAMATAR, A. A., WANG, L., MIRZA, A., KOSEOGLU, S., LIU, S. & KUMAR, C. C. 2002. Transforming growth factor-beta 2 is a transcriptional target for Akt/protein kinase B via forkhead transcription factor. *J Biol Chem,* 277**,** 28118-26.
SANDRI, M., SANDRI, C., GILBERT, A., SKURK, C., CALABRIA, E., PICARD, A., WALSH, K., SCHIAFFINO, S., LECKER, S. H. & GOLDBERG, A. L. 2004. Foxo transcription factors induce the atrophy-related ubiquitin ligase atrogin-1 and cause skeletal muscle atrophy. *Cell,* 117**,** 399-412.
SCHEFFNER, M. & STAUB, O. 2007. HECT E3s and human disease. *BMC Biochem,* 8 Suppl 1**,** S6.
SCHIAFFINO, S. & REGGIANI, C. 1994. Myosin isoforms in mammalian skeletal muscle. *J Appl Physiol,* 77**,** 493-501.
SCHMALBRUCH, H. & LEWIS, D. M. 2000. Dynamics of nuclei of muscle fibers and connective tissue cells in normal and denervated rat muscles. *Muscle Nerve,* 23**,** 617-26.
SENF, S. M., DODD, S. L. & JUDGE, A. R. 2010. FOXO signaling is required for disuse muscle atrophy and is directly regulated by Hsp70. *Am J Physiol Cell Physiol,* 298**,** C38-45.

SHARPLES, A. P. & STEWART, C. E. 2011. Myoblast models of skeletal muscle hypertrophy and atrophy. *Curr Opin Clin Nutr Metab Care,* 14**,** 230-6.
SHEN, M., GAO, J., LI, J. & SU, J. 2009. Effect of stimulation frequency on angiogenesis and gene expression in ischemic skeletal muscle of rabbit. *Can J Physiol Pharmacol,* 87**,** 396-401.
SIDDIQUEE, K., ZHANG, S., GUIDA, W. C., BLASKOVICH, M. A., GREEDY, B., LAWRENCE, H. R., YIP, M. L., JOVE, R., MCLAUGHLIN, M. M., LAWRENCE, N. J., SEBTI, S. M. & TURKSON, J. 2007. Selective chemical probe inhibitor of Stat3, identified through structure-based virtual screening, induces antitumor activity. *Proc Natl Acad Sci U S A,* 104**,** 7391-6.
SMYTH, G. K. 2004. Linear models and empirical bayes methods for assessing differential expression in microarray experiments. *Stat Appl Genet Mol Biol,* 3**,** Article3.
SNOW, M. H. 1978. An autoradiographic study of satellite cell differentiation into regenerating myotubes following transplantation of muscles in young rats. *Cell Tissue Res,* 186**,** 535-40.
SPANGENBURG, E. E. 2005. SOCS-3 induces myoblast differentiation. *J Biol Chem,* 280**,** 10749-58.
ST-AMAND, J., OKAMURA, K., MATSUMOTO, K., SHIMIZU, S. & SOGAWA, Y. 2001. Characterization of control and immobilized skeletal muscle: an overview from genetic engineering. *FASEB J,* 15**,** 684-92.
STEIN, T., SCHLUTER, M., GALANTE, A., SOTEROPOULOS, P., TOLIAS, P., GRINDELAND, R., MORAN, M., WANG, T., POLANSKY, M. & WADE, C. 2002. Energy metabolism pathways in rat muscle under conditions of simulated microgravity. *J Nutr Biochem,* 13**,** 471.
STEVENSON, E. J., GIRESI, P. G., KONCAREVIC, A. & KANDARIAN, S. C. 2003. Global analysis of gene expression patterns during disuse atrophy in rat skeletal muscle. *J Physiol,* 551**,** 33-48.
STEVENSON, E. J., KONCAREVIC, A., GIRESI, P. G., JACKMAN, R. W. & KANDARIAN, S. C. 2005. Transcriptional profile of a myotube starvation model of atrophy. *J Appl Physiol,* 98**,** 1396-406.
STITT, T. N., DRUJAN, D., CLARKE, B. A., PANARO, F., TIMOFEYVA, Y., KLINE, W. O., GONZALEZ, M., YANCOPOULOS, G. D. & GLASS, D. J. 2004. The IGF-1/PI3K/Akt pathway prevents expression of muscle atrophy-induced ubiquitin ligases by inhibiting FOXO transcription factors. *Mol Cell,* 14**,** 395-403.
STUMP, C. S., TIPTON, C. M. & HENRIKSEN, E. J. 1997. Muscle adaptations to hindlimb suspension in mature and old Fischer 344 rats. *J Appl Physiol,* 82**,** 1875-81.
SUN, L. & CHEN, Z. J. 2004. The novel functions of ubiquitination in signaling. *Curr Opin Cell Biol,* 16**,** 119-26.
TANG, H. & GOLDMAN, D. 2006. Activity-dependent gene regulation in skeletal muscle is mediated by a histone deacetylase (HDAC)-Dach2-myogenin signal transduction cascade. *Proc Natl Acad Sci U S A,* 103**,** 16977-82.
TANG, H., MACPHERSON, P., ARGETSINGER, L. S., CIESLAK, D., SUHR, S. T., CARTER-SU, C. & GOLDMAN, D. 2004. CaM kinase II-dependent phosphorylation of myogenin contributes to activity-dependent suppression of nAChR gene expression in developing rat myotubes. *Cell Signal,* 16**,** 551-63.
TANG, H., MACPHERSON, P., MARVIN, M., MEADOWS, E., KLEIN, W. H., YANG, X. J. & GOLDMAN, D. 2009. A histone deacetylase 4/myogenin positive feedback loop coordinates denervation-dependent gene induction and suppression. *Mol Biol Cell,* 20**,** 1120-31.
TINTIGNAC, L. A., LAGIRAND, J., BATONNET, S., SIRRI, V., LEIBOVITCH, M. P. & LEIBOVITCH, S. A. 2005. Degradation of MyoD mediated by the SCF (MAFbx) ubiquitin ligase. *J Biol Chem,* 280**,** 2847-56.
TISDALE, M. J. 2009. Mechanisms of cancer cachexia. *Physiol Rev,* 89**,** 381-410.

TUTEJA, G. & KAESTNER, K. H. 2007. SnapShot: forkhead transcription factors I. *Cell,* 130**,** 1160.
TZIVION, G., DOBSON, M. & RAMAKRISHNAN, G. 2011. FoxO transcription factors; Regulation by AKT and 14-3-3 proteins. *Biochim Biophys Acta,* 1813**,** 1938-45.
VAN DER HEIDE, L. P., HOEKMAN, M. F. & SMIDT, M. P. 2004. The ins and outs of FoxO shuttling: mechanisms of FoxO translocation and transcriptional regulation. *Biochem J,* 380**,** 297-309.
VAN DER MEER, S. F., JASPERS, R. T., JONES, D. A. & DEGENS, H. 2011. Time-course of changes in the myonuclear domain during denervation in young-adult and old rat gastrocnemius muscle. *Muscle Nerve,* 43**,** 212-22.
VAREJAO, A. S., CABRITA, A. M., MEEK, M. F., BULAS-CRUZ, J., MELO-PINTO, P., RAIMONDO, S., GEUNA, S. & GIACOBINI-ROBECCHI, M. G. 2004. Functional and morphological assessment of a standardized rat sciatic nerve crush injury with a non-serrated clamp. *J Neurotrauma,* 21**,** 1652-70.
WEI, M., ONG, L., SMITH, M. T., ROSS, F. B., SCHMID, K., HOEY, A. J., BURSTOW, D. & BROWN, L. 2003. The streptozotocin-diabetic rat as a model of the chronic complications of human diabetes. *Heart Lung Circ,* 12**,** 44-50.
WEISS, A., SCHIAFFINO, S. & LEINWAND, L. A. 1999. Comparative sequence analysis of the complete human sarcomeric myosin heavy chain family: implications for functional diversity. *J Mol Biol,* 290**,** 61-75.
YAFFE, D. & SAXEL, O. 1977. Serial passaging and differentiation of myogenic cells isolated from dystrophic mouse muscle. *Nature,* 270**,** 725-7.
YANG, J., SONG, H., WALSH, S., BARDES, E. S. & KORNBLUTH, S. 2001. Combinatorial control of cyclin B1 nuclear trafficking through phosphorylation at multiple sites. *J Biol Chem,* 276**,** 3604-9.
YANG, Y., ZHAO, Y., LIAO, W., YANG, J., WU, L., ZHENG, Z., YU, Y., ZHOU, W., LI, L., FENG, J., WANG, H. & ZHU, W. G. 2009. Acetylation of FoxO1 activates Bim expression to induce apoptosis in response to histone deacetylase inhibitor depsipeptide treatment. *Neoplasia,* 11**,** 313-24.
YASUDA, N., GLOVER, E. I., PHILLIPS, S. M., ISFORT, R. J. & TARNOPOLSKY, M. A. 2005. Sex-based differences in skeletal muscle function and morphology with short-term limb immobilization. *J Appl Physiol,* 99**,** 1085-92.

APPENDICES

APPENDIX 1

Details of All Experimental Procedures

Rat No.	Animal Weight (g)	Treatment	Untreated TA Weight (µg)	Treated TA Weight (µg)	% Change in TA	Reason For Omission
1673	404	14 Days Atrophy	740	372	-49.7	
1674	373		694	368	-47.0	
1675	445		686	347	-49.4	
1676	394		729	364	-50.1	
1677	434		819	365	-55.4	
1678	393		772	366	-52.6	
1679	396	7 Days Atrophy	742	735	-0.9	Failed Block
1680	409		737	513	-30.4	
1681	392		772	575	-25.5	
1682	407	Sham Control	742	469	-36.8	Nerve Damage
1683	409		728	543	-25.4	Nerve Damage
1684	414		743	722	-2.8	Failed Block
1685	395		629	590	-6.2	Failed Block
1686	410		815	562	-31.0	Nerve Damage
1687	416		731	715	-2.2	Failed Block
1688	411	7 Days Atrophy	810	529	-34.7	
1689	442		847	547	-35.4	
1690	400		842	829	-1.5	Failed Block
1712	385	Sham Control	650	459	-29.4	Nerve Damage
1721	291		857	861	0.5	
1722	473		946	956	1.1	
1723	458		887	850	-4.2	
1724	477		875	879	0.5	
1725	466		890	919	3.3	
1742	438	7 Days Atrophy	754	580	-23.1	
1743	444		818	794	-2.9	Failed Block
1744	428		889	644	-27.6	
1745	460	3 Days Atrophy	870	805	-7.5	
1746	485		888	830	-6.5	
1747	401		781	723	-7.4	
1748	429		776	802	3.4	Failed Block
1749	464		759	783	3.2	Failed Block
1750	449		792	701	-11.5	
1751	457		836	798	-4.5	
1752	460		851	813	-4.5	
1753	548	Sham Control	902	897	-0.6	
1758	413	20Hz Stimulation 7 Days	712	589	-17.3	
1759	425		658	578	-12.2	
1760	416		771	652	-15.4	
1761	387		711	604	-15.0	
1762	367		704	679	-3.6	
1763	391		664	582	-12.3	

1764	412	14 Days Atrophy with 7 Days Recovery	748	476	-36.4	
1765	410		707	351	-50.4	Block Did Not Cease
1766	396		842	800	-5.0	Failed Block
1767	445		899	334	-62.8	Block Did Not Cease
1768	421		771	634	-17.8	
1769	384		808	639	-20.9	
1770	392		802	645	-19.6	
1771	402		741	320	-56.8	Block Did Not Cease
1772	419		759	481	-36.6	
1773	413		767	648	-15.5	

APPENDIX 2

Subbing Slides

Manufacturers;

Slides: Twin frost, BDH premium 406/0184/02

Gelatine: Bovine type B Sigma G-9328

Solutions

0.1% w/v gelatine

0.01% chromium potassium sulphate

Double-distilled water

Protocol

1. Slides were cleaned in 100% alcohol and left to dry for approximately 30 minutes
2. Slides were then dipped in subbing solution and left to dry overnight

APPENDIX 3

H&E Solutions and protocol

Solutions

Erhlich's Haematoxylin

0.65% w/v haematoxylin

33.25% ethanol

32.25% glycerine

32.25% double-distilled water

3.23% acetic acid

4.52% aluminium potassium sulphate

Protocol

1. Dissolve haematoxylin in alcohol and add remainder of ingredients

2. Leave the stain to ripen in a container with a loose lid. The solution must be kept in a warm place for a minimum of 4 months to mature.

Eosin

1% Eosin

APPENDIX 4

Electrophoresis Gels

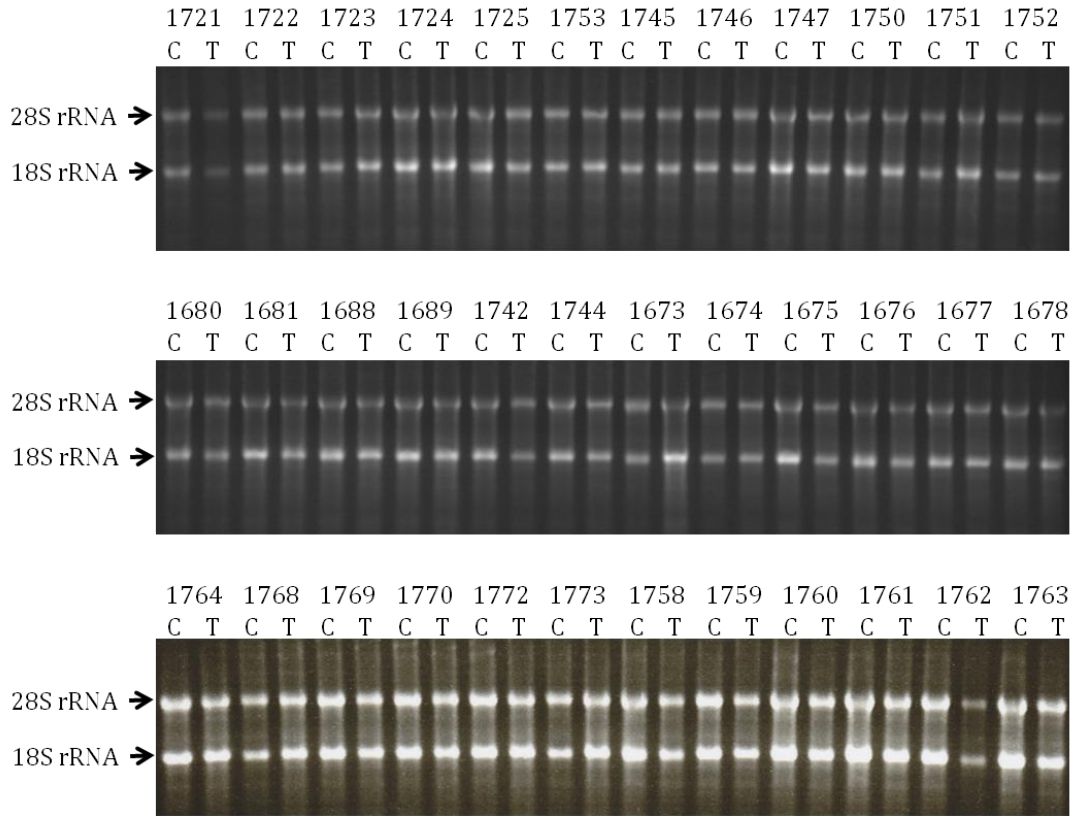

Agarose Gel (1.5%) Electrophoresis of RNA From Each Muscle Sample Showing Consistently Good Quality & Yield

Gel Confirms yield and quality of RNA as represented by clear 18- and 28-S bands. Each of the 36 animals (1721-1763) has both an untreated contralateral control TA sample (C) and a treated TA sample (T).

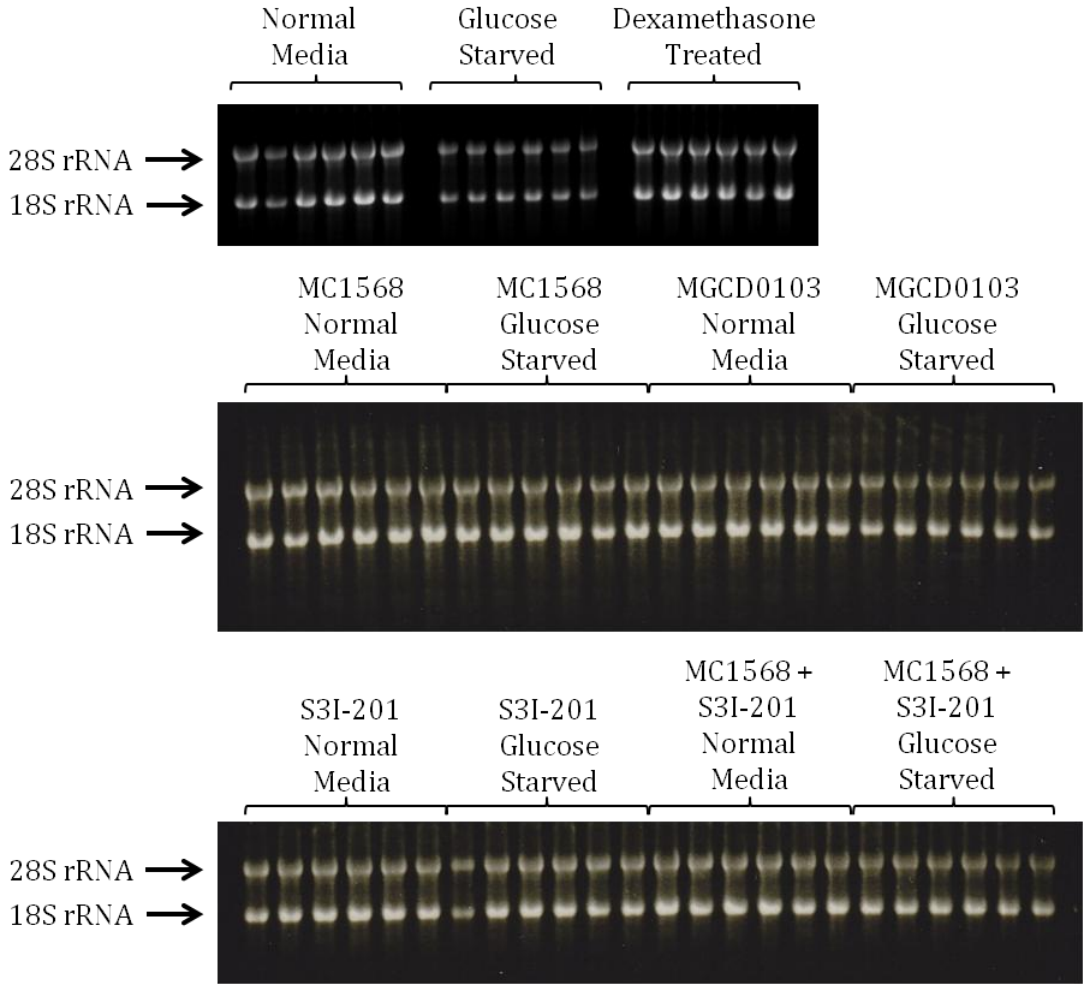

Agarose Gel (1.5%) Electrophoresis of RNA From Each Myotube Sample Showing Consistently Good Quality & Yield

Gel Confirms yield and quality of RNA as represented by clear 18- and 28-S bands. Each Group (Normal Media, Glucose Starved etc.) has 6 samples running 1-6 from left to right.

APPENDIX 5

Details of Nanodrop Readings

Myotubes A

Sample number	Treatment	260nm	280nm	Ratio	conc µg/ml
1	Normal Media	84.256	43.171	1.95	39.41
2		36.164	17.622	2.05	47.29
3		44.123	21.776	2.03	32.94
4		37.326	17.866	2.09	17.79
5		58.380	28.476	2.05	38.72
6		36.594	17.633	2.08	35.60
7	Glucose Starved	61.982	30.601	2.03	87.38
8		69.016	34.424	2.00	89.51
9		65.284	32.548	2.01	97.76
10		58.994	29.197	2.02	106.24
11		18.826	9.285	2.03	126.73
12		23.521	11.623	2.02	86.35
13	Dexamethasone Treated	59.785	29.127	2.05	77.42
14		69.028	33.889	2.04	28.54
15		72.730	35.904	2.03	89.60
16		70.039	34.449	2.03	81.92
17		92.864	48.125	1.93	122.59
18		104.181	58.323	1.79	131.95

Myotubes B

Sample number	Treatment	260nm	280nm	Ratio	conc µg/ml
1	MC1568 Normal Media	23.946	11.967	2.00	1197.31
2		55.320	27.749	1.99	2766.01
3		63.344	31.962	1.98	3167.20
4		81.664	42.200	1.94	4083.18
5		23.863	11.911	2.00	1193.13
6		27.957	13.942	2.01	1397.87
7	MC1568 Glucose Starved	37.917	18.720	2.03	1895.86
8		33.582	16.617	2.02	1679.10
9		81.161	41.707	1.95	4058.04
10		26.151	13.079	2.00	1307.56
11		21.158	10.544	2.01	1057.89
12		23.779	11.868	2.00	1188.94
13	MGCD0103 Normal Media	62.813	31.418	2.00	3140.65
14		35.868	17.755	2.02	1793.40
15		25.662	12.665	2.03	1283.08
16		31.293	15.418	2.03	1564.65
17		23.715	11.627	2.04	1185.75
18		25.196	12.357	2.04	1259.82
19	MGCD0103 Glucose Starved	21.331	10.501	2.03	1066.53
20		44.519	21.941	2.03	2225.96
21		28.532	14.024	2.03	1426.60
22		22.149	10.936	2.03	1107.46
23		20.682	10.113	2.05	1034.08
24		29.361	14.382	2.04	1468.05
25	S3I-201 Normal Media	19.360	9.739	1.99	968.00
26		48.539	24.439	1.99	2426.96
27		55.935	28.137	1.99	2796.73
28		23.041	11.556	1.99	1152.03
29		37.391	18.613	2.01	1869.57
30		34.342	17.099	2.01	1717.12
31	S3I-201 Glucose Starved	11.705	6.092	1.92	585.24
32		24.398	12.257	1.99	1219.91
33		38.145	19.120	1.99	1907.24
34		19.463	9.865	1.97	973.15
35		105.068	62.547	1.68	5253.40
36		27.298	13.600	2.01	1364.91
37	MC1568 + S3I-201 Normal Media	23.369	11.739	1.99	1168.45
38		23.006	11.555	1.99	1150.32
39		23.447	11.715	2.00	1172.33
40		30.024	15.045	2.00	1501.18
41		22.561	11.205	2.01	1128.05
42		23.688	11.846	2.00	1184.42
43	MC1568 + S3I-201 Glucose Starved	22.327	11.154	2.00	1116.35
44		24.992	12.479	2.00	1249.61
45		22.426	11.195	2.00	1121.28
46		23.422	11.668	2.01	1171.11
47		22.016	10.870	2.03	1100.82
48		24.836	12.404	2.00	1241.78

Muscle Samples

Animal Number & Limb Side	Treatment	260nm	280nm	Ratio	conc µg/ml
1721RL	Sham Control	12.955	6.271	2.07	647.77
1721RR		6.936	3.442	2.02	346.81
1722RL		14.889	7.045	2.11	744.46
1722RR		11.789	5.928	1.99	589.47
1723RL		13.906	6.961	2.00	695.28
1723RR		18.397	9.178	2.00	919.83
1724RL		16.565	8.239	2.01	828.27
1724RR		19.337	9.729	1.99	966.84
1725RL		24.017	12.390	1.94	1200.85
1725RR		27.027	13.289	2.03	1351.35
1753RL		17.449	8.781	1.99	872.43
1753RR		17.231	8.591	2.01	861.57
1745RL	3 Days Atrophy	11.894	5.846	2.03	594.69
1745RR		19.981	9.478	2.11	999.03
1746RL		18.334	9.056	2.02	916.70
1746RR		16.770	8.450	1.98	838.48
1747RL		23.051	11.338	2.03	1152.54
1747RR		23.420	11.696	2.00	1171.00
1750RL		19.278	9.570	2.01	963.90
1750RR		33.313	16.396	2.03	1665.66
1751RL		13.673	6.984	1.96	683.64
1751RR		19.511	9.768	2.00	975.54
1752RL		15.649	7.787	2.01	782.45
1752RR		15.616	7.771	2.01	780.82
1680RL	7 Days Atrophy	37.312	17.972	2.08	1865.62
1680RR		11.960	5.968	2.00	597.98
1681RL		21.245	10.439	2.04	1062.24
1681RR		17.473	8.575	2.04	873.64
1688RL		21.064	10.604	1.99	1053.21
1688RR		41.540	20.330	2.04	2077.02
1689RL		25.507	12.752	2.00	1275.33
1689RR		20.742	10.340	2.01	1037.12
1742RL		20.305	10.090	2.01	1015.23
1742RR		13.843	6.888	2.01	692.16
1744RL		18.476	9.260	2.00	923.78
1721RL		12.955	6.271	2.07	647.77

Animal Number & Limb Side	Treatment	260nm	280nm	Ratio	conc µg/ml
1744RR	14 Days Atrophy	16.430	8.255	1.99	821.48
1673RL		13.429	6.525	2.06	671.45
1673RR		27.050	12.846	2.11	1352.48
1674RL		15.103	7.562	2.00	755.15
1674RR		16.553	8.051	2.06	827.64
1675RL		29.779	14.926	2.00	1488.93
1675RR		18.255	9.083	2.01	912.76
1676RL		20.946	10.482	2.00	1047.29
1676RR		34.923	17.219	2.03	1746.17
1677RL		22.172	11.261	1.97	1108.60
1677RR		24.212	11.952	2.03	1210.58
1678RL		21.661	10.945	1.98	1083.03
1678RR	14 Days Atrophy with 7 Days Recovery	23.564	11.638	2.02	1178.18
1764RL		15.605	7.426	2.10	780.23
1764RR		21.398	10.501	2.04	1069.89
1768RL		16.488	8.480	1.94	824.42
1768RR		21.398	10.501	2.04	1069.89
1769RL		19.764	9.843	2.01	988.19
1769RR		18.115	9.094	1.99	905.73
1770RL		18.255	9.083	2.01	912.76
1770RR		20.972	10.397	2.02	1048.58
1772RL		24.040	12.007	2.00	1202.01
1772RR		20.972	10.397	2.02	1048.58
1773RL		17.231	8.591	2.01	861.57
1773RR	20Hz Stimulation for 7 Days	26.863	13.371	2.01	1343.14
1758RL		21.357	10.289	2.08	1067.84
1758RR		15.605	7.426	2.10	780.23
1759RL		17.751	8.779	2.02	887.53
1759RR		17.009	8.407	2.02	850.46
1760RL		27.632	13.743	2.01	1381.60
1760RR		19.991	9.951	2.01	999.53
1761RL		31.000	15.367	2.02	1550.01
1761RR		17.647	8.793	2.01	882.35
1762RL		58.724	29.497	1.99	2936.18
1762RR		7.282	3.737	1.95	364.11
1763RL		26.863	13.371	2.01	1343.14

APPENDIX 6

Sequencing Results

Mouse Rn18s

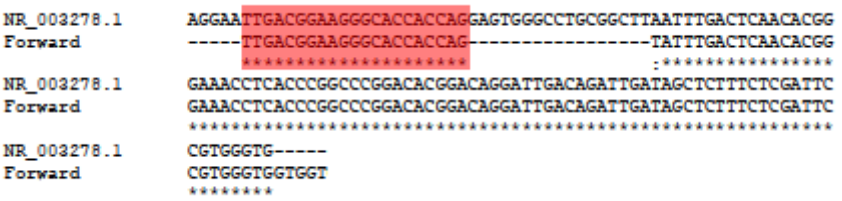

Mouse Polr2a

Mouse G6pc3

Mouse Pdk4

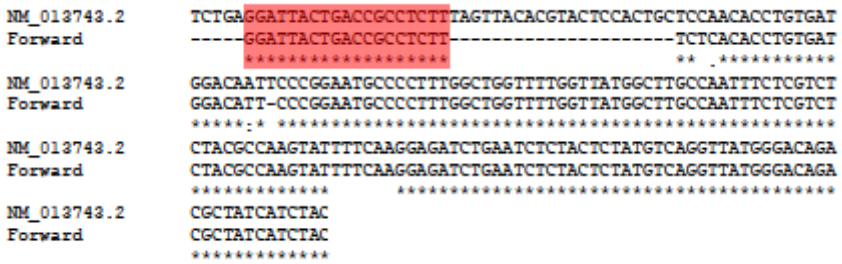

Mouse Lpl

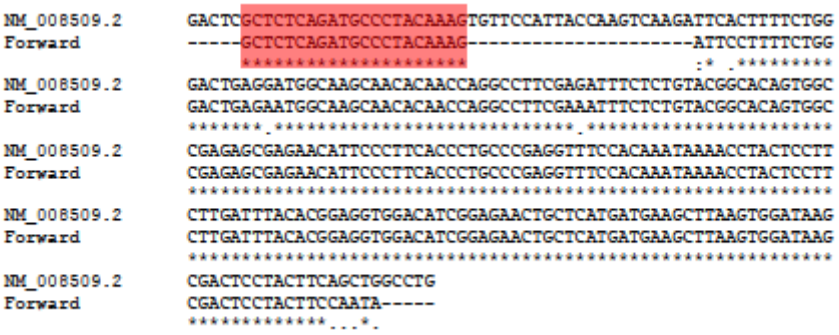

Mouse Bcl2l11

Mouse Tgfb2

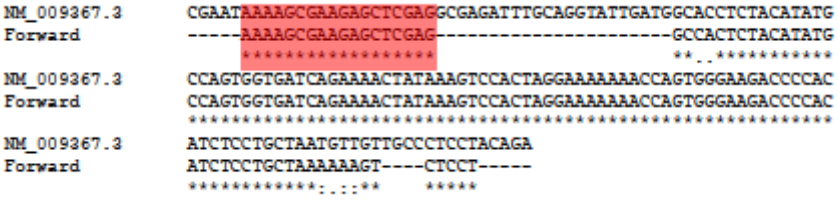

Mouse Sod2

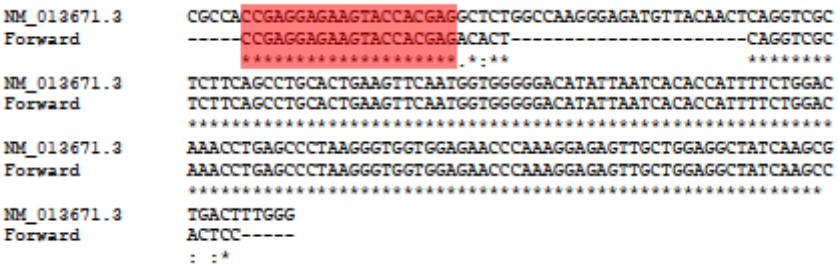

Mouse Ccnd2

Mouse Ccnb1

Mouse Plk1

Mouse Cdkn1b

Mouse Fbxo32

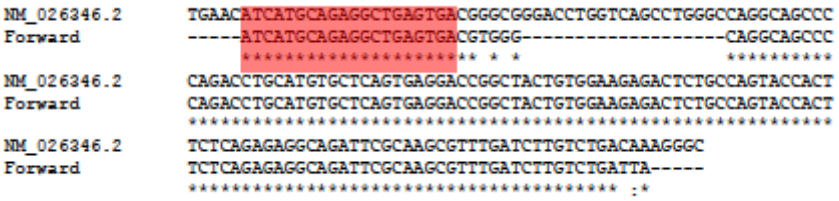

Mouse Myog

Mouse Stat3

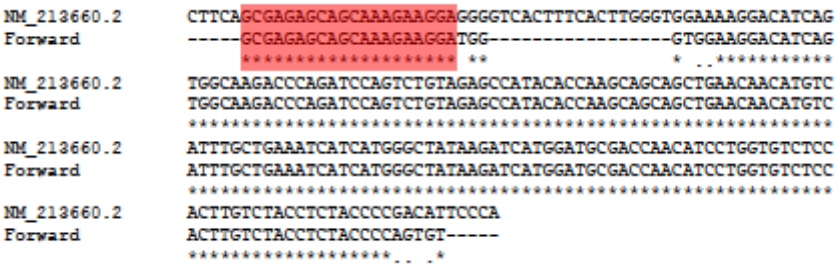

Mouse Hdac4

Mouse Hdac5

Mouse Mitr

Mouse Dach2

Mouse Chrna1

Rat Rn18s

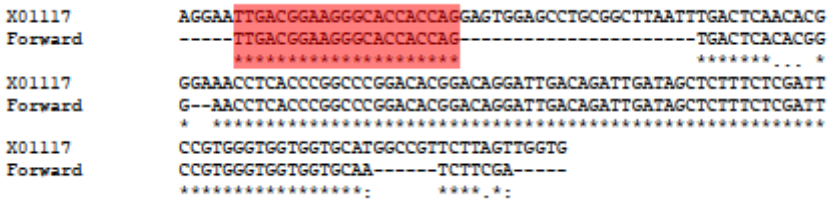

Rat G6pc3

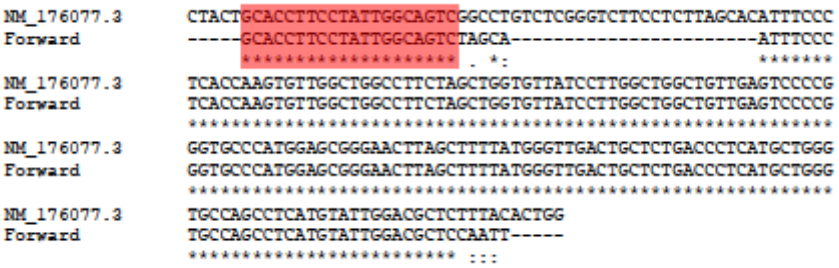

Rat Pdk4

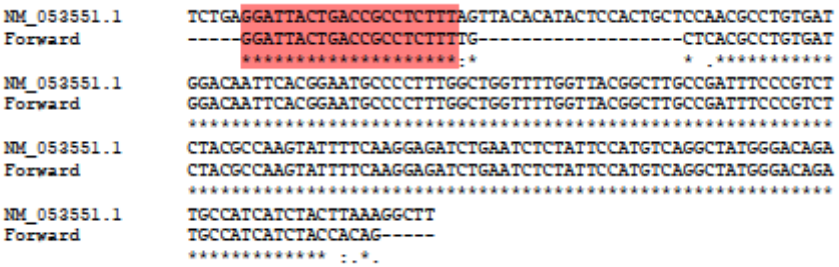

Rat Bcl2l11

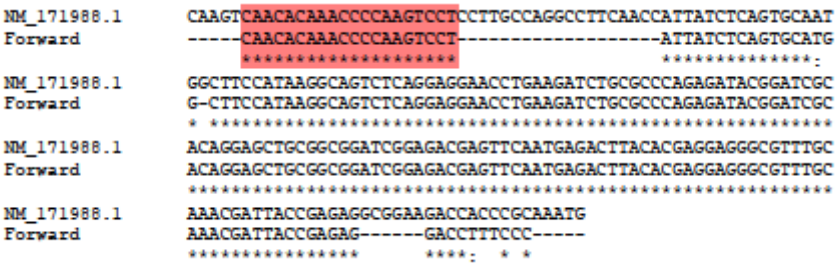

Rat Tgfb2

Rat Sod2

Rat Ccnd2

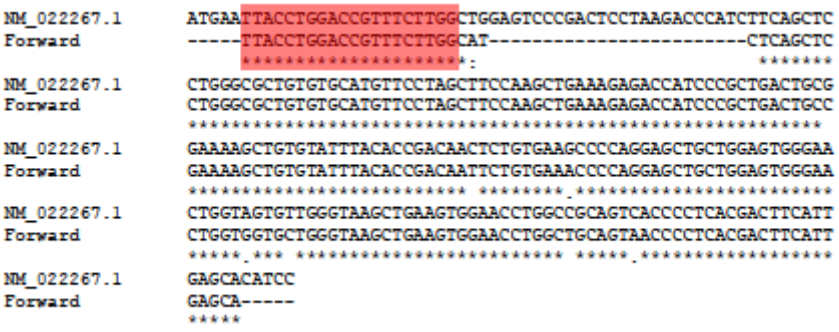

Rat Ccnb1

Rat Plk1

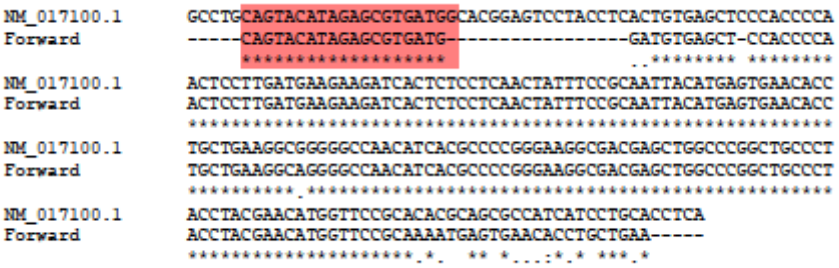

Rat Cdkn1b

Rat Trim63

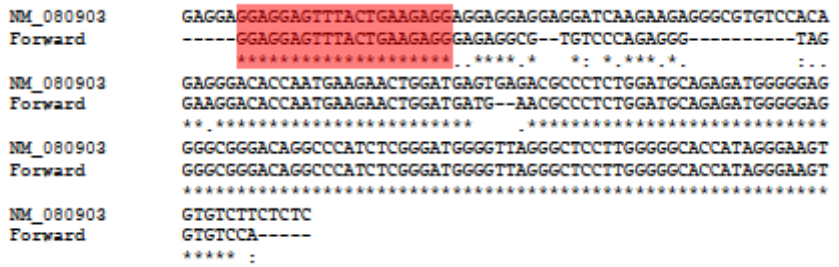

Rat Fbxo32

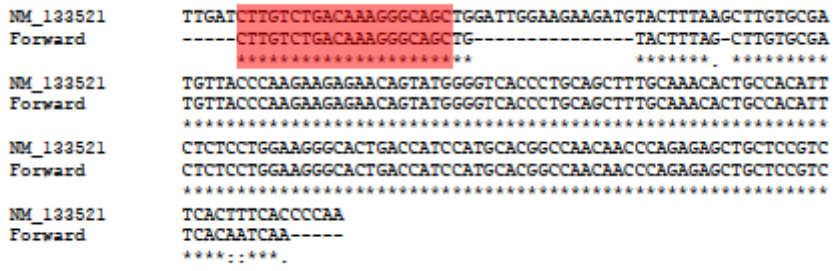

Rat Myog

Rat Stat3

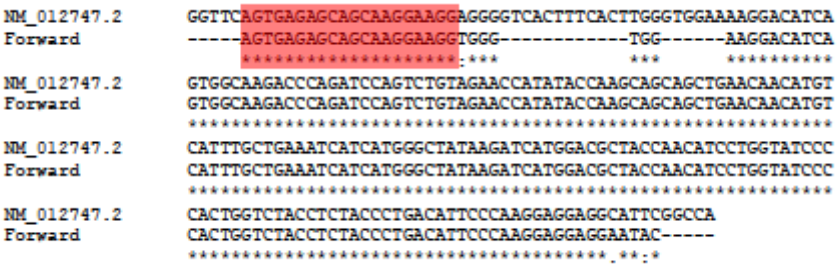

Rat Hdac4

Rat Hdac5

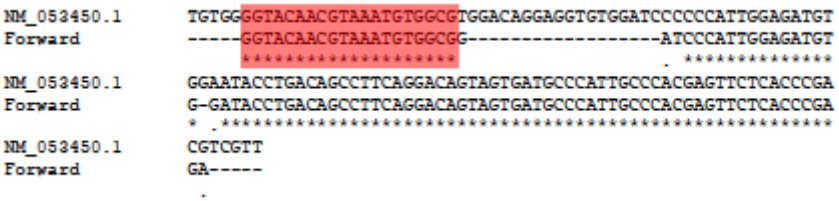

Rat Mitr

Rat Chrna1

APPENDIX 7

Primer Efficiency Curves

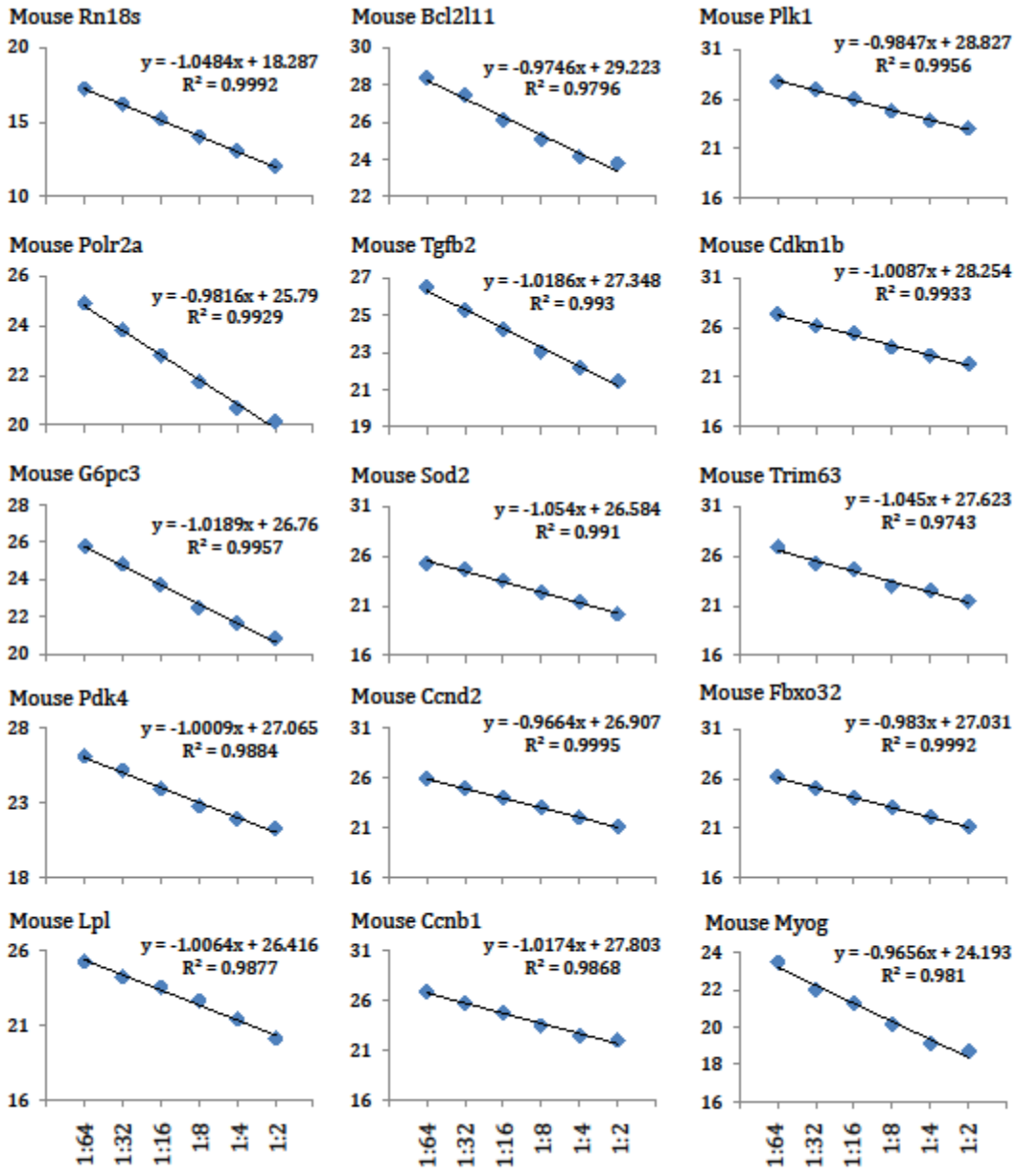

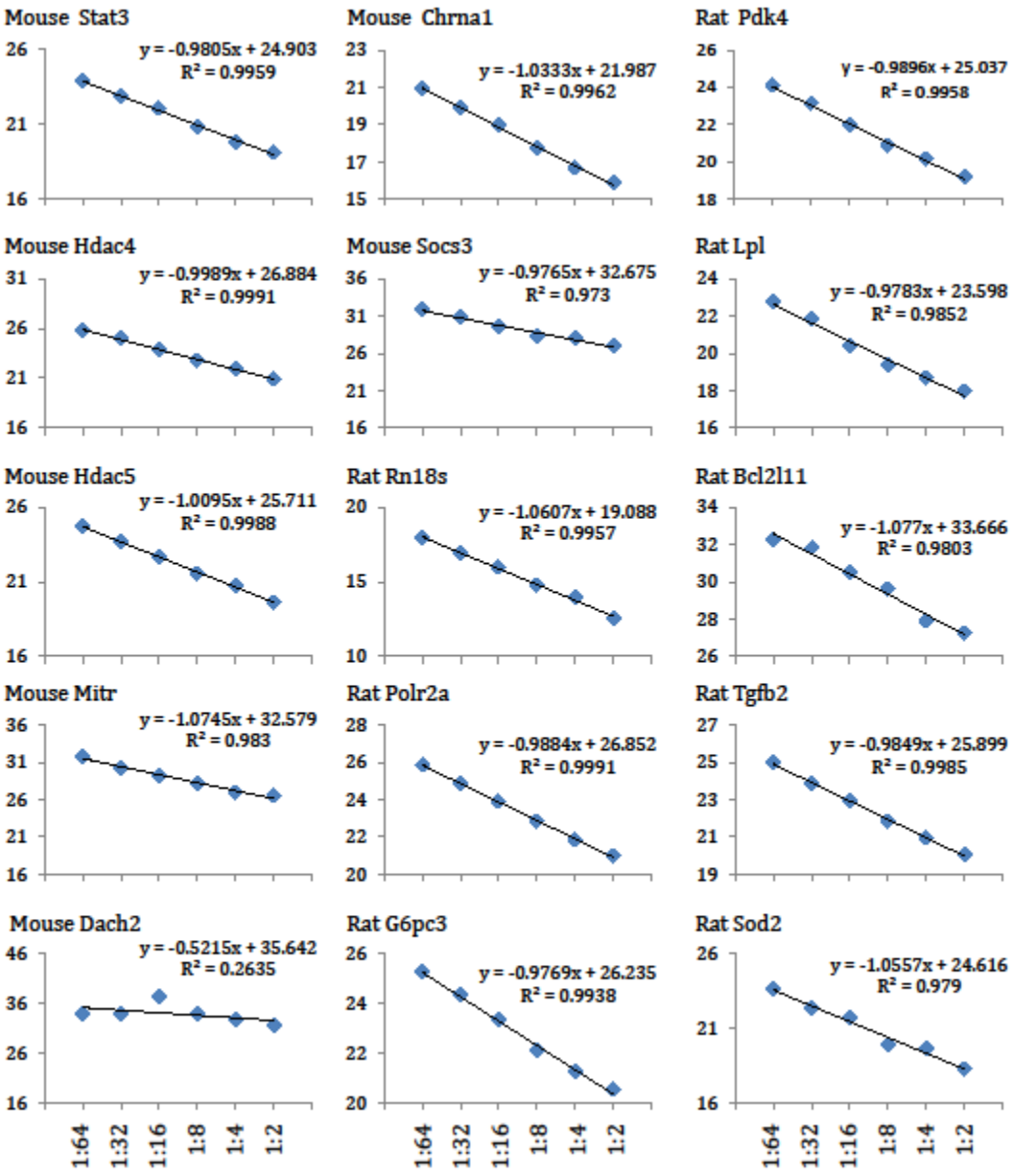
Mouse Stat3
y = -0.9805x + 24.903
R² = 0.9959
Mouse Chrna1
y = -1.0333x + 21.987
R² = 0.9962
Rat Pdk4
y = -0.9896x + 25.037
R² = 0.9958
Mouse Hdac4
y = -0.9989x + 26.884
R² = 0.9991
Mouse Socs3
y = -0.9765x + 32.675
R² = 0.973
Rat Lpl
y = -0.9783x + 23.598
R² = 0.9852
Mouse Hdac5
y = -1.0095x + 25.711
R² = 0.9988
Rat Rn18s
y = -1.0607x + 19.088
R² = 0.9957
Rat Bcl2l11
y = -1.077x + 33.666
R² = 0.9803
Mouse Mitr
y = -1.0745x + 32.579
R² = 0.983
Rat Polr2a
y = -0.9884x + 26.852
R² = 0.9991
Rat Tgfb2
y = -0.9849x + 25.899
R² = 0.9985
Mouse Dach2
y = -0.5215x + 35.642
R² = 0.2635
Rat G6pc3
y = -0.9769x + 26.235
R² = 0.9938
Rat Sod2
y = -1.0557x + 24.616
R² = 0.979
1:64
1:32
1:16
1:8
1:4
1:2

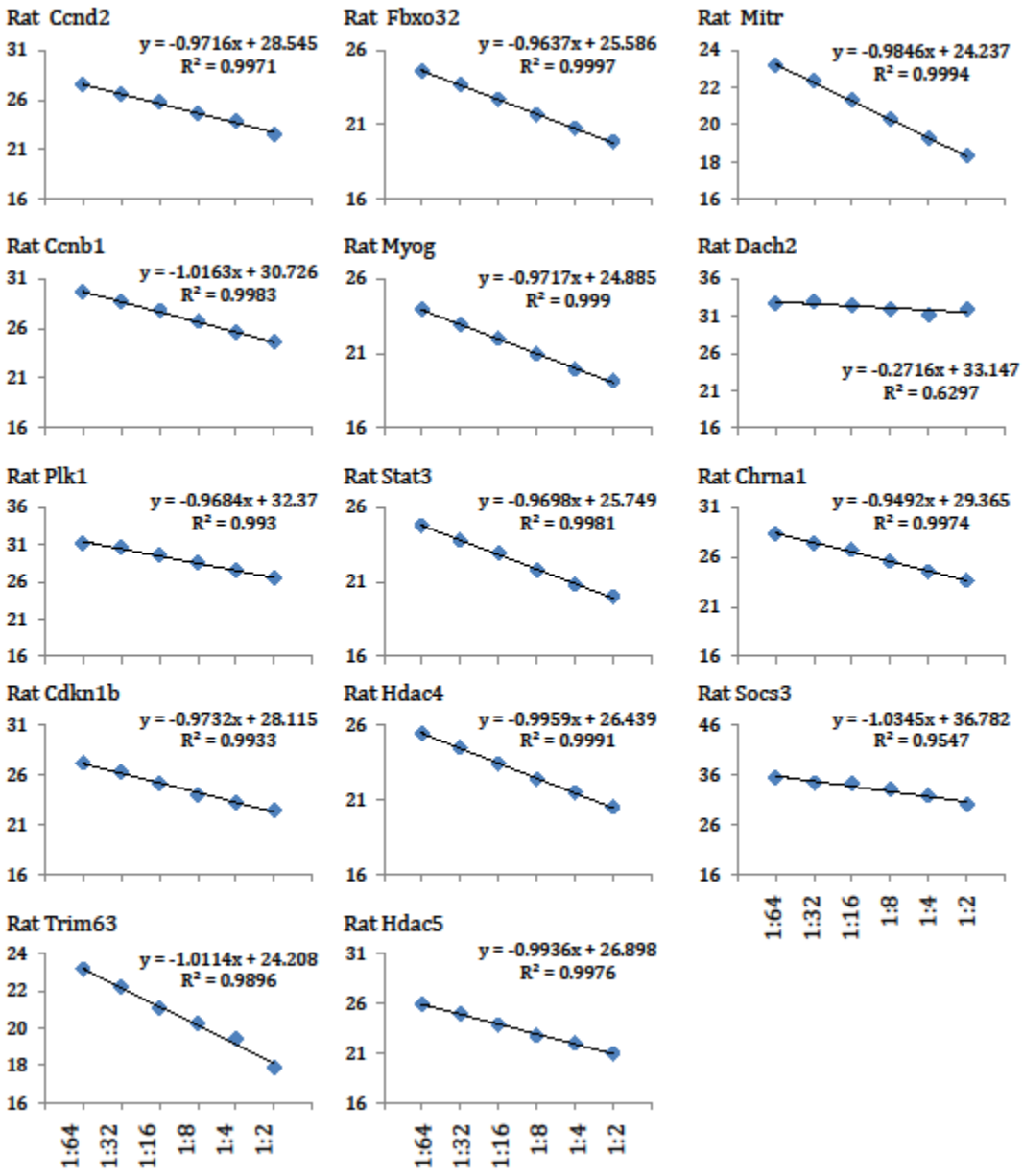
Rat Ccnd2
y = -0.9716x + 28.545
R² = 0.9971
Rat Fbxo32
y = -0.9637x + 25.586
R² = 0.9997
Rat Mitr
y = -0.9846x + 24.237
R² = 0.9994
Rat Ccnb1
y = -1.0163x + 30.726
R² = 0.9983
Rat Myog
y = -0.9717x + 24.885
R² = 0.999
Rat Dach2
y = -0.2716x + 33.147
R² = 0.6297
Rat Plk1
y = -0.9684x + 32.37
R² = 0.993
Rat Stat3
y = -0.9698x + 25.749
R² = 0.9981
Rat Chrna1
y = -0.9492x + 29.365
R² = 0.9974
Rat Cdkn1b
y = -0.9732x + 28.115
R² = 0.9933
Rat Hdac4
y = -0.9959x + 26.439
R² = 0.9991
Rat Socs3
y = -1.0345x + 36.782
R² = 0.9547
Rat Trim63
y = -1.0114x + 24.208
R² = 0.9896
Rat Hdac5
y = -0.9936x + 26.898
R² = 0.9976
1:64
1:32
1:16
1:8
1:4
1:2

APPENDIX 8

Validation of SYBR green reaction by melt curve analysis

Melt curve analyses of the products formed using each primer set. The melt curve is a plot of the total fluorescence as a function of the temperature. The y-axis, represented by -d (RFU)/dT, is the rate of change of fluorescence in the reaction and a significant change in fluorescene accompanies teh melting of the double-stranded PCR products. Thus a plot of -d (RFU)/dT vs. temperature displays the change in fluorescence as a distinct peak.

Mouse Rn18s

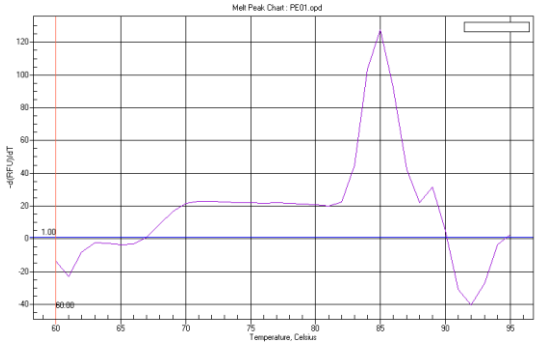

Mouse Pdk4

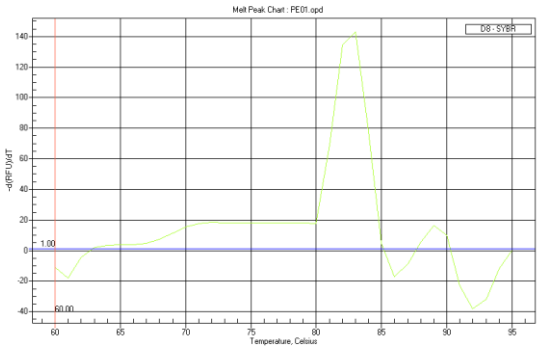

Mouse Polr2a

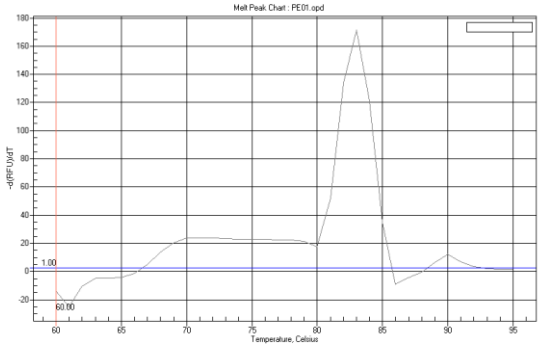

Mouse Lpl

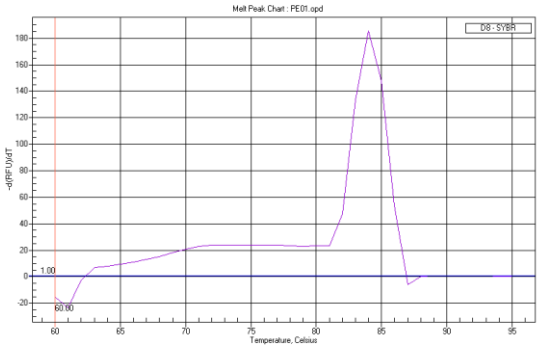

Mouse G6pc3

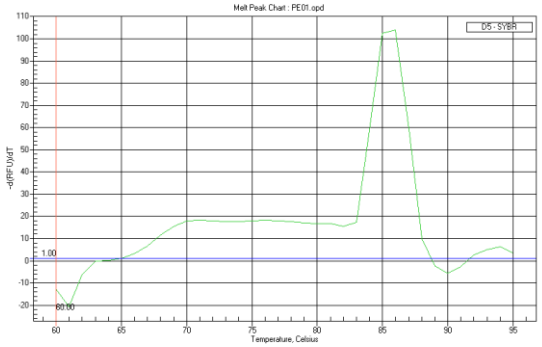

Mouse Bcl2l11

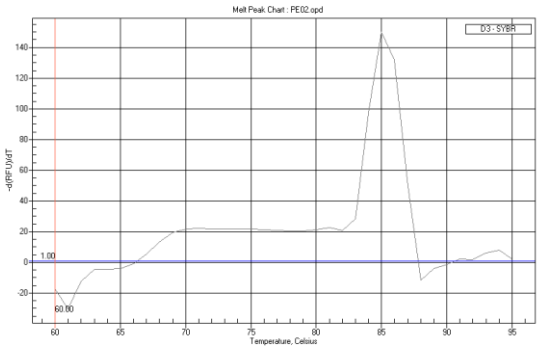

Mouse Tgfb2

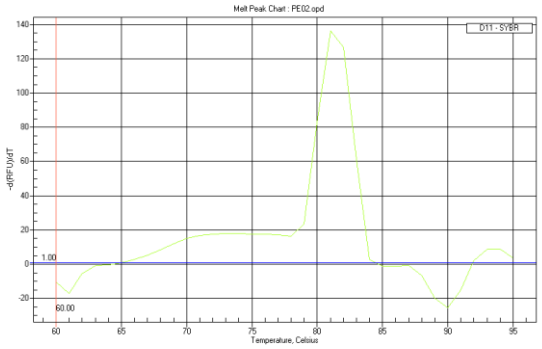

Mouse Plk1

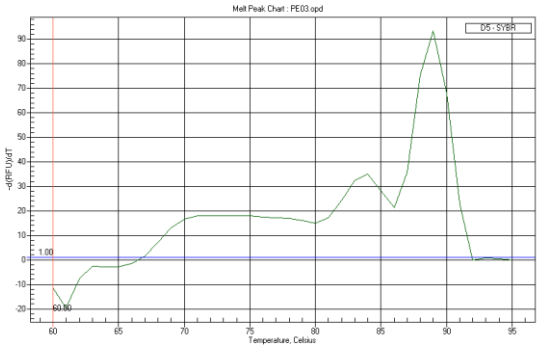

Mouse Sod2

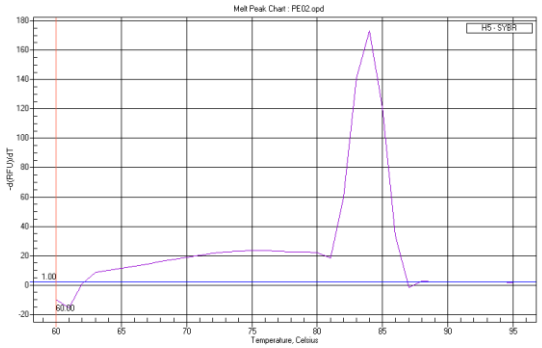

Mouse Cdkn1b

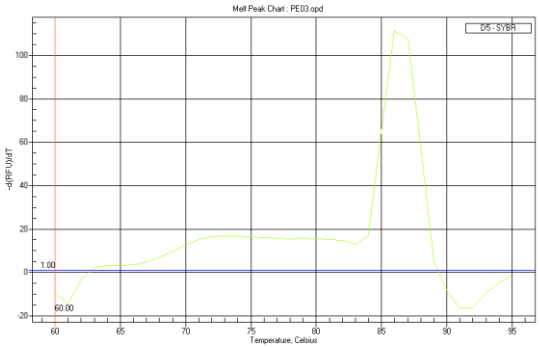

Mouse Ccnd2

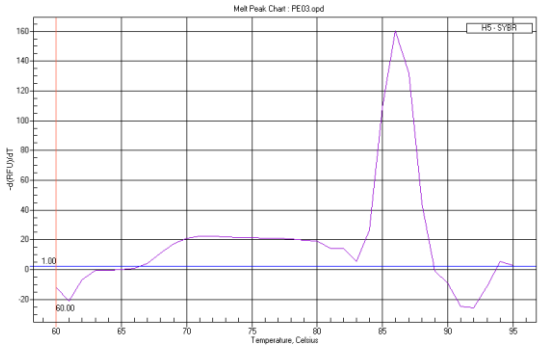

Mouse Trim63

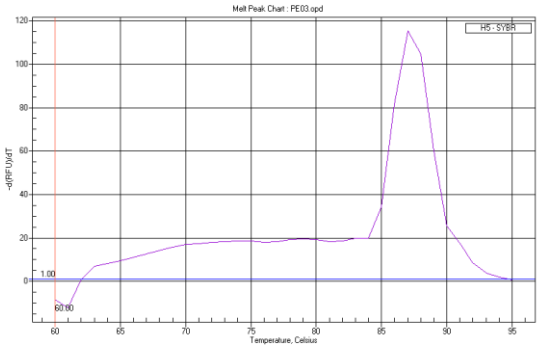

Mouse Ccnb1

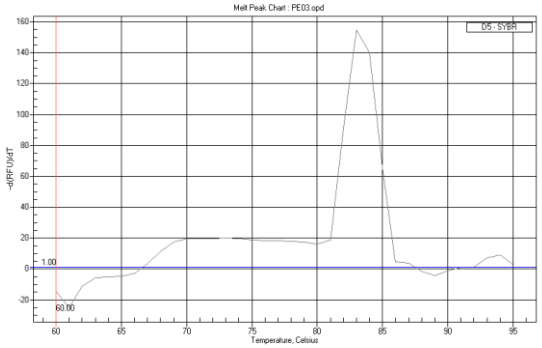

Mouse Fbxo32

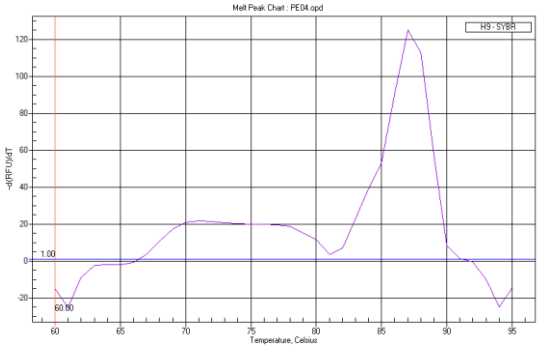

Mouse Myog

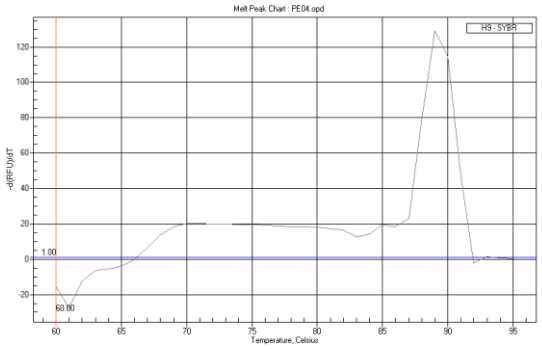

Mouse Mitr

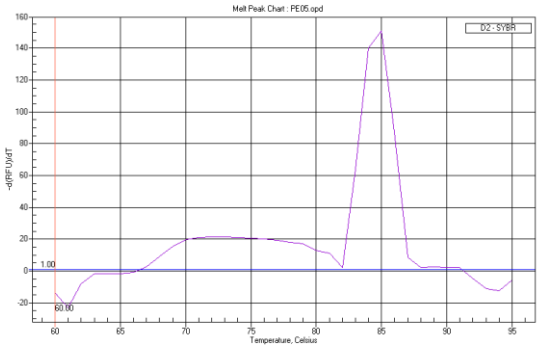

Mouse Stat3

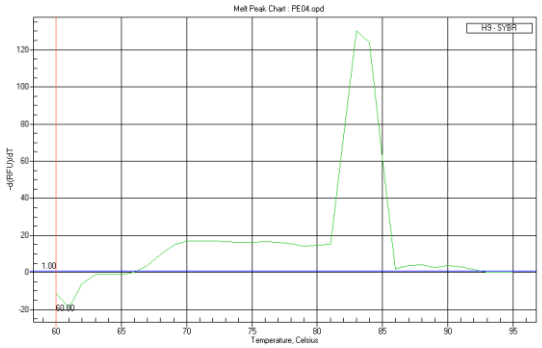

Mouse Chrna1

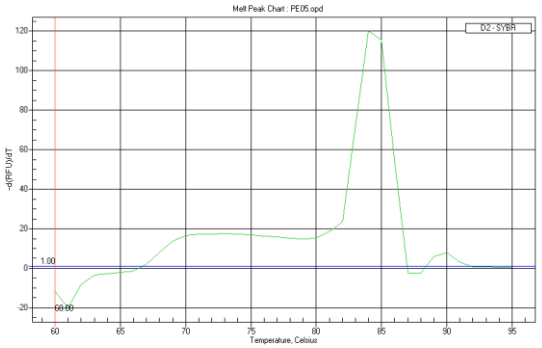

Mouse Hdac4

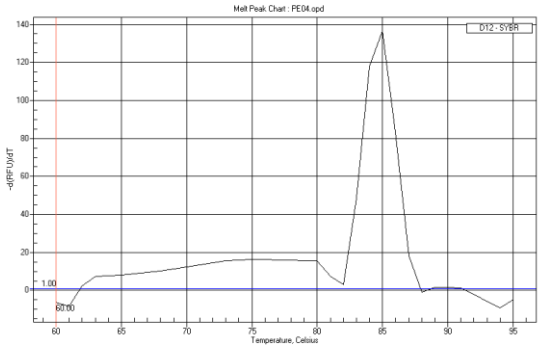

Mouse Socs3

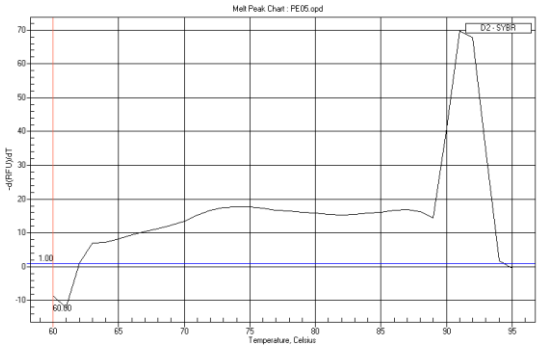

Mouse Hdac5

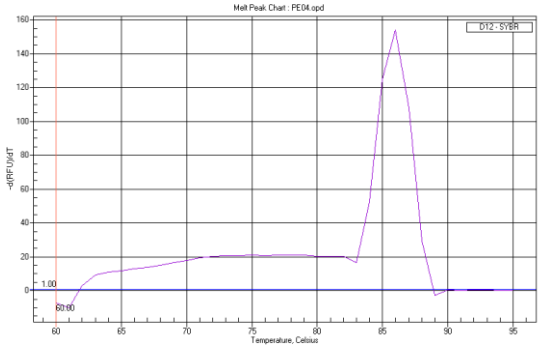

Rat Rn18s

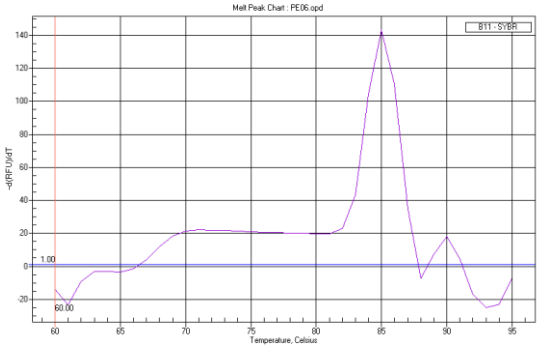

Rat Polr2a

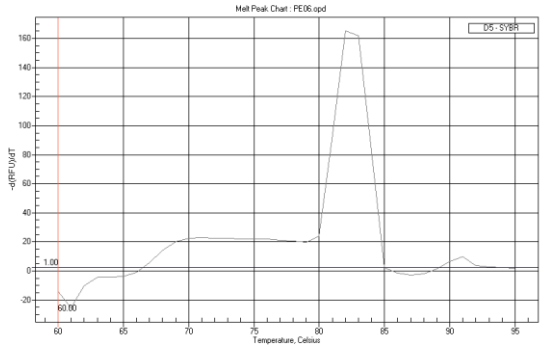

Rat Bcl2l11

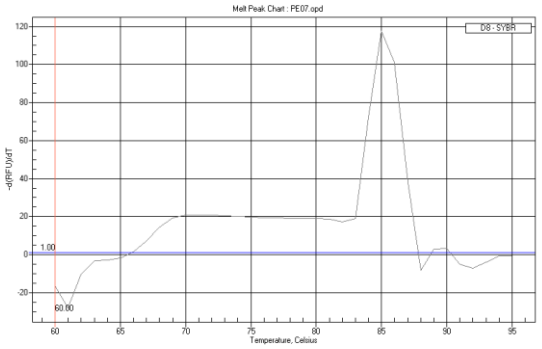

Rat G6pc3

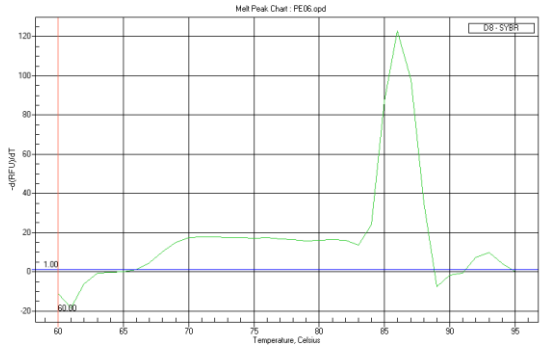

Rat Tgfb2

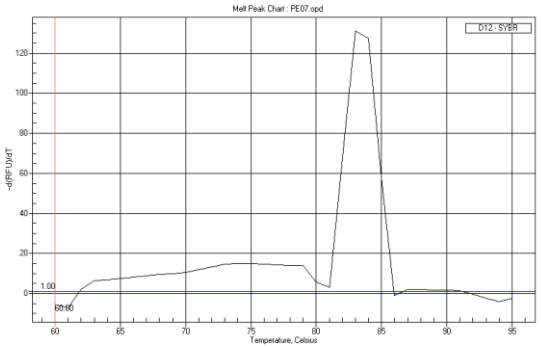

Rat Pdk4

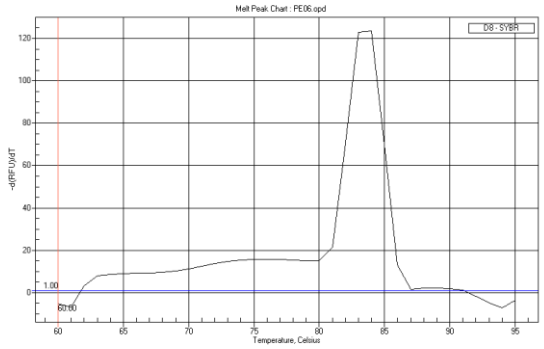

Rat Sod2

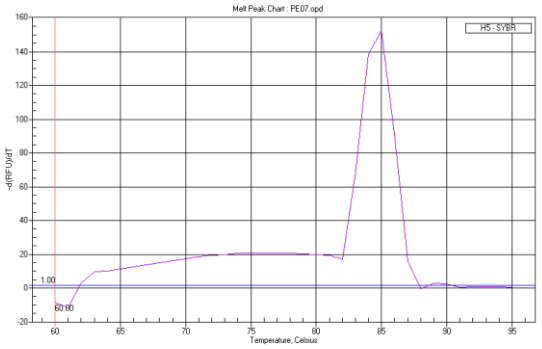

Rat Lpl

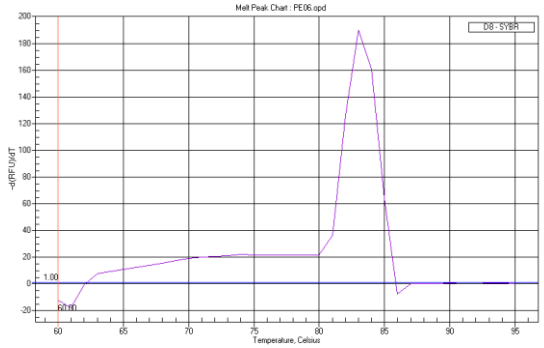

Rat Ccnd2

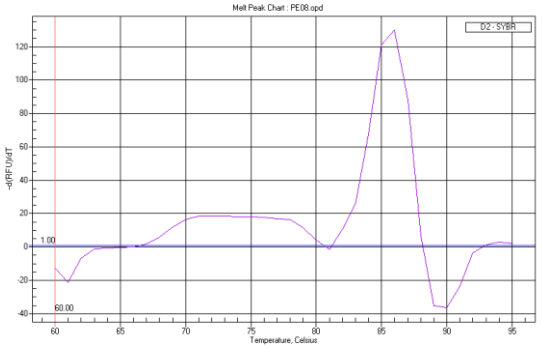

Rat Ccnb1

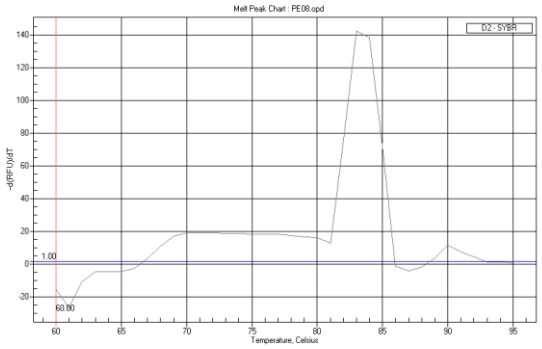

Rat Fbxo32

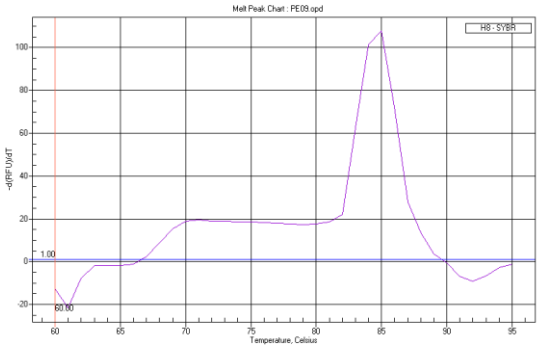

Rat Plk1

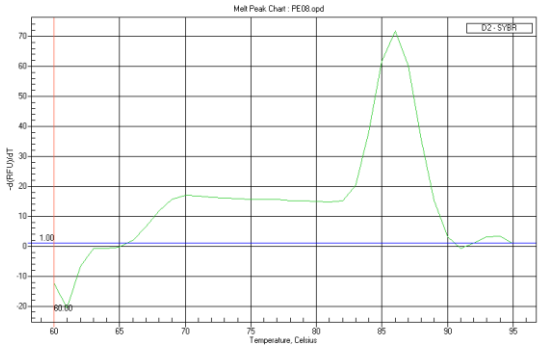

Rat Myog

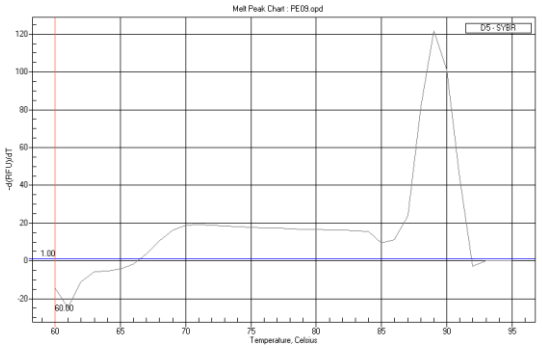

Rat Cdkn1b

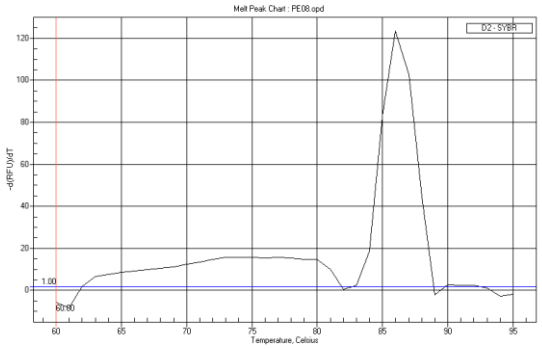

Rat Stat3

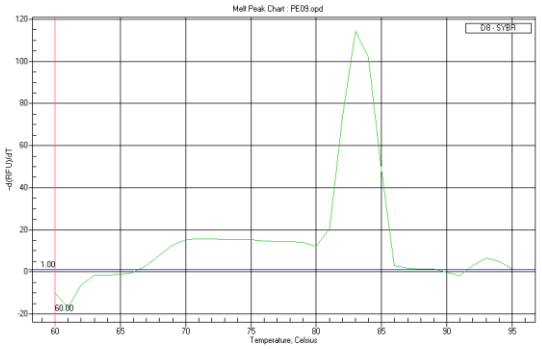

Rat Trim63

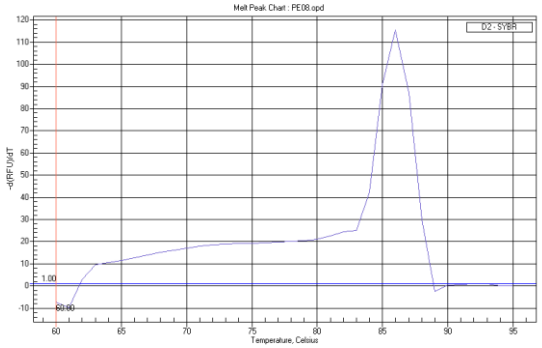

Rat Hdac4

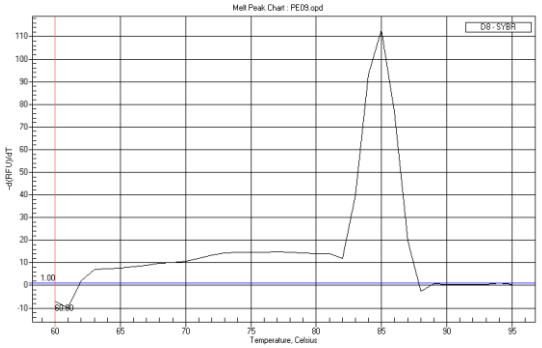

Rat Hdac5

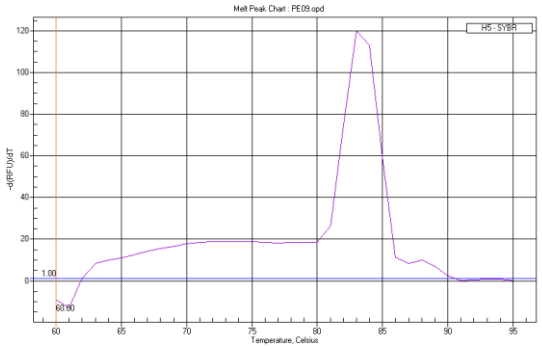

Rat Chrna1

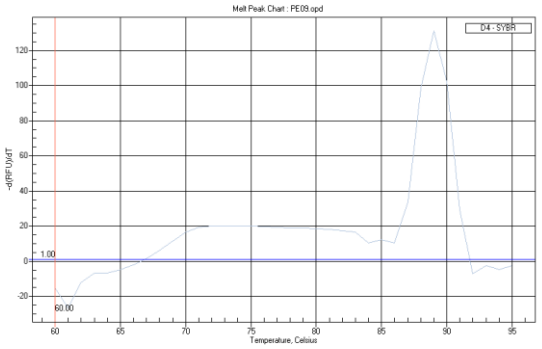

Rat Mitr

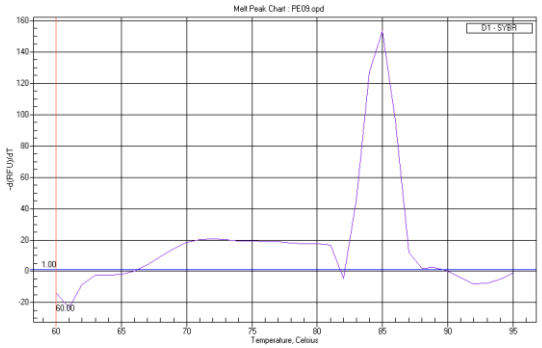

Rat Socs3